MINES PARIS
ParisTech

ED n° 432 : « Sciences des Métiers de l'Ingénieur »

N° attribué par la bibliothèque

|__|__|__|__|__|__|__|__|__|__|

THESE

pour obtenir le grade de
Docteur de l'Ecole des Mines de Paris
Spécialité "Energétique"

présentée et soutenue publiquement par
Elias BOU LAWZ KSAYER

le 12 novembre 2007

ETUDE ET CONCEPTION DE SYSTEMES A EFFICACITE ENERGETIQUE AMELIOREE FONCTIONNANT AU CO_2 COMME FLUIDE FRIGORIGENE

Directeur(s) de thèse : Denis CLODIC

Jury :

M. Francis MEUNIER .... Rapporteur
M. Eckhart GROLL .... Rapporteur
M. Carloandrea MALVICINO .... Examinateur
M. Laurent GAGNEPAIN .... Examinateur
M. Jurgen KOEHLER .... Examinateur
M. Dominique MARCHIO .... Examinateur
M. Denis CLODIC .... Examinateur

Autant les problèmes sont ***`complexes`*** ……..

Autant les solutions sont ***`simples`*** ……...

The more ***`complex`*** *the problems* …....

The ***`simpler`*** *the solutions* …....

Acknowledgements

I realize at the end of this journey that the three years of devotion that led to the present book is due not only to me but to other people to whom I dedicate my acknowledgement.

Denis Clodic, director of CEP-Paris for providing me excellent working conditions and useful thoughts to complete the work.

Eckhard GROLL and ***Francis MEUNIER*** as rapporteurs for evaluating my work. Your presence honors me.

Members of the examination board for the patience you held while reading and evaluating my work, hoping that it had made your task as much a pleasant as an inspiring one.

Anne-Marie Pougin, for always being present when needed, *nursing* the project and particularly through extended meticulous proofreading.

The Center for Energy and Processes working team, who created a suitable environment for me to work, along with endless on field instructions.

Youssef, Mourad for your help that make part of my success.

My ***Parents***, my village ***BEIT CHABAB***, my country ***LEBANON***, for contributing in my formation before coming to France.

Thank you.

Nomenclature

Symbol

a	specific surface	m^2.s / kg
A	surface	m^2
Bo	Boiling number	adim.
c	heat capacity	kJ/kg . K
CF	correction factor	adim.
Co	Convection number	adim.
d, D	diameter	m
DP	pressure drop	MPa
e	error	adim.
E, e	exergy	kj/kg
ettas	surface efficiency	adim.
F	comparison factor	adim.
f	friction factor	adim.
Fr	Froude number	adim.
g	gravity acceleration	m/s^2
G	mass flux	$kg/s.m^2$
h	enthalpy	kj/kg
h	heat transfer coefficient	$W/m^2.K$
h	height	m
k	thermal conductivity	W/m
L	length	m
M	mach number	adim.
m	mass flow rate	in kg/s
N	entropy number	adim.
N	rotation speed	RPM
Nu	Nusselt number	adim.
P	perimeter	m
P	pressure	bar or MPa
Pr	Prandtl number	adim.
q	cooling capacity	W or kj/kg
q	heat power	W or kj/kg
R	ideal gas constant	j/mol.K.
R	radius	m
Re	Reynolds number	adim.
S	suppression factor	adim.
s	entropy	kj/kg. K
s	Laplace variable	adim.
SC	sub-cooling	K
SH, TS	evaporator outlet superheat	K
T	temperature	°C or K
T	constant	adim.
u	control signal	adim.
U	heat transfer coefficient	$W/m^2.K$
V	velocity	m/s
V,v	velocity	m/s
w	entrainment ratio	adim.
W,w	compression work	W or kj/kg
We	Weber number	adim.
x	displacement	adim.
X	Lockart-Martinelli parameter	adim.
x	quality	kg/kg
Y	correction factor	adim.

y	output signal	V
z	elevation	m

Greek letter

ΔT	temperature difference	K
Φ_{lo}	diphase multiplier	adim.
δ	thickness	m
ε	void fraction	adim.
γ	isentropic coefficient = c_p/c_v	adim
η	efficiency	adim.
μ	kinetic viscosity	Pa.s
θ	inclination angle	°
θ	wettability angle	°
ρ	density	kg/m^3
σ	surface tension	N/m
τ	compression ratio	adim.

Subscripts

a	acceleration
a	guessed value
b	boiler
b	bulk
c	control
cal	calculated
cb	convective boiling
comp	compression, compressor
cond	condenser
conv	conventional
cr, crit	critical
cs	cold source
cst atrea	constant area
d	derivative
d	diffuser
de	dry completion
di	dry inception
e,i	exit, inlet
eff	effective
ej	ejector
ev	evaporator, evaporation
ex	exergetic
exp	expansion
exp	experimental, measured
G	Gnielinski
gc	gas cooler
gen	generation
H	homogeneous
h	hydraulic
hs	heat sink
HX	heat exchanger
i	inlet
i	integral
is	isentropic
K	constant
L	low

l, liq	liquid
mix, m	mixture
n	nozzle
nb	nucleating boiling
o	outlet
opt	optimal
p	constant pressure
p	primary flow
p	proportional
pseudo	pseudo-critical
ref	reference
s	isentropic
s	secondary flow
s	surface
sat	saturation
strat	stratified
th	throat
turb	turbine, expander
v	volumetric
v, vap	vapor
w	wall
w	water

Expression

%COP	COP improvement = (F –1)%
1D	one dimensional
CFC	chloro fluoro carbon
CFD	computational fluid dynamic
COP	Coefficient of performance
CWHE	city water heat exchanger
HCFC	hydro chloro fluoro carbon
HFC	hydro fluoro carbon
HTF	heat transfer fluid
IHE	internal heat exchanger
IHX	internal heat exchanger
OE	obrist engineering
TSCDI	Two stage compression with direct injection between the stages
TSCE	Two stage compression with economizer
TSCI	Two stage compression with injection between the stages
TSCII	Two stage compression with indirect injection between the stages
TSCSI	Two stage compression in series with intercooler between the stages
VDC	volt direct current
EEV	Electronic expansion valve
CEV	Compressor electro-valve
EVO	Electronic valve opening

Adimensional numbers

$Bo=\frac{\dot{q}}{G\cdot h_{fg}}$	Boiling number
$Co=\left(\frac{1-x}{x}\right)^{0,8}\left(\frac{\rho_v}{\rho_l}\right)^{0,5}$	Convection number

$Fr_l = \frac{G^2}{\rho_l^2 \cdot g \cdot D}$	Froude liquid number
$Fr_V = \frac{G^2}{gD\rho_V(\rho_L - \rho_V)}$	Froude vapor number
$X = \left(\frac{\mu_{liq}}{\mu_{vap}}\right)^{0,1} \cdot \left(\frac{1-x}{x}\right)^{0,9} \cdot \left(\frac{\rho_{vap}}{\rho_{liq}}\right)^{1/2}$	Lockart-Martinelli parameter
$Nu = \frac{h \cdot d_h}{k}$	Nusselt number
$\Pr = \frac{\mu \cdot c_p}{k}$	Prandtl number
$We = \frac{G^2 D}{\rho\sigma}$	Weber number

CONTENTS

General Introduction 1

Chapter 1. Improvement of energy efficiency of CO_2 transcritical cycles 3
1.1 History of CO_2 in refrigeration 3
1.2 Properties of CO_2 4
  1.2.1 Thermodynamic properties 5
  1.2.2 Trans-critical compression cycle.. 9
1.3 Exergy analysis...12
  1.3.1 Compression : Evolution 3→ 4 13
  1.3.2 Condenser or gas cooler : Evolution 4→ 1 14
  1.3.3 Expansion : Evolution 1→ 2 14
  1.3.4 Evaporator : Evolution 2→ 3 14
  1.3.5 Internal heat exchanger : Evolution 1→ 2 / 4→ 5 15
1.4 Modified cycles for enhancement of CO_2 refrigeration cycle 18
  1.4.1 Internal heat exchanger cycle 18
  1.4.2 Work generating expansion 19
  1.4.3 Staging of compression phase 23
1.5 Comparison of cycles 27
1.6 Conclusions 34
References 35

Chapter 2. Improved expansion cycle and simulation of a refrigeration ejector cycle 39
2.1 Introduction 39
2.2 CO_2 trans-critical cycle with expander turbines 41
2.3 Ejector cycles 46
2.4 1D simulation of an ejector cycle 49
  2.4.1 1D simulation of an ejector with superheated vapor inlet as primary fluid 49
  2.4.2 Results of the superheated vapor inlet model 52
  2.4.3 CFD comparison with R-141b 57
  2.4.4 1D simulation of an ejector cycle with liquid / supercritical inlet as primary fluid 64
  2.4.5 Theoretical results of liquid / supercritical inlet ejector model 69
2.5 Performance comparison of fluids : CO_2 and R-134a 72
2.6 Conclusions 74
Reference 75

Chapter 3. Design of the CO_2 ejector system and test bench 81
3.1 Test bench components.. 81
  3.1.1 Water-cooling loop 81
  3.1.2 CO_2 refrigeration loop 82
  3.1.3 CO_2 compressor and expansion valve... 83
3.2 Heat exchangers 90
  3.2.1 CO_2 evaporation process 90
  3.2.2 CO_2 flow vaporization heat transfer correlations 91
  3.2.3 Evaporation pressure drop 99
3.3 Gas cooler / condenser 101
  3.3.1 One phase correlation of heat transfer and pressure drop 101
  3.3.2 CO_2 condensation correlations 102
  3.3.3 One phase correlations 103
  3.3.4 Water transfer heat coefficient 104
3.4 Heat exchanger design 104
  3.4.1 Evaporator 106
  3.4.2 Gas cooler 107
3.5 Design of a two phase CO_2 trans-critical ejector 109
3.6 Analysis of an ejector 112
3.7 Separator 117
3.8 Acquisition system and measurement elements 117
3.9 Validation of heat exchangers models...119
  3.9.1 Gas cooler / Condenser model validation 119
  3.9.2 Evaporator model validation 121
3.10 Conclusions 122
References 123

Chapter 4. CO_2 system operation: control strategy and experimental results 127
4.1 Introduction 127
4.2 The simple CO_2 refrigeration system 127
4.3 Design of the control strategies of the high pressure and the evaporation temperature 127
  4.3.1 Global system control 127
  4.3.2 PID control description and tuning 129
  4.3.3 Control of the evaporation temperature by the CEV 131
  4.3.4 Control of P_{gc} with EEV 133
  4.3.5 Control of T_{ev} with EEV and control of P_{gc} with CEV 134
  4.3.6 Conclusion 136
4.4 Ejector test results and 1D model adaptation 136
4.5 Tests 137
4.6 Nozzle characterization 137
4.7 Body characterization 141
4.8 Constant pressure chamber length 142
4.9 Experimental result reliability 143
4.10 Effect of η_m on ejector performance 145
4.11 Effect of $d_{cst\ area}$ and d_{th} 147
  4.11.1 Variation of $d_{cst\ area}$ 147
  4.11.2 Variation of d_{th} 148
4.12 Variation of T_{gc}, T_{ev} and SH 149
4.13 Ejector refrigeration system with integral IgHX 153
4.14 Ejector refrigeration system with IHX 155
4.16 ettas improvement 157
4.17 Conclusions 159
References 160

General conclusion 161

ANNEX 1. CO_2 two-stage compression cycles 165

ANNEX 2. Ejector Computational Fluid Dynamics Analysis 207

ANNEX 3. Developed ejectors figures 223

ANNEX 4. Test bench 225

General introduction

Due to the strong increase of the emissions of the global warming gases along the 20th century, the commitment of the European Union to the Kyoto Protocol has led to a number of decisions to limit those emissions. For Mobile Air-Conditioning (MAC) systems, the EU directive 40 /2006 has forbidden the use of refrigerants whose Global Warming Potential is higher than 150 equivalent CO_2 as of 2011.

Carbon dioxide is one of the candidates since it is a refrigerant with a global warning potential of 1. However the CO_2 physical properties are different from currently used refrigerants so research actions have been and are required as well as technical developments in order to develop efficient CO_2 MAC systems.

The objective of this work is to describe and to characterize CO_2 (R-744) as a refrigerant, and to improve the refrigeration cycle performance by introducing an ejector in the refrigeration cycle.

In Chapter 1, the thermo-physical and thermodynamic properties of R-744 are presented and compared to other refrigerants. An exergy analysis of the simple CO_2 refrigeration cycle is performed in order to establish the component exergy losses. different cycle architectures are compared to select the most efficient ones.

In Chapter 2, a bibliography study on isentropic expansion (using different expander types) and refrigeration cycles with ejector is performed. The two types of ejector refrigeration cycles: superheated vapor ejector cycle and sub-cooled/ supercritical ejector cycle are studied. Two 1D models are elaborated to simulate those two ejector refrigeration cycles. The 1D model of the superheated vapor ejector cycle is validated by experimental results from literature and by CFD calculations.

In Chapter 3, the design and sizing of all components of a refrigeration ejector cycle using CO_2 is realized. A test bench to complete the experiments on this system is presented and described. Its purpose is to:

- Characterize the compressor with external control.
- Validate the heat exchanger models: evaporator and gas cooler.
- Control the optimal operation of the CO_2 refrigeration cycle.
- Verify the energy performance improvement due to the ejector compared to the single stage reference cycle.
- Validate and adapt the sub-cooled ejector model.

The 1D model is used to design different ejectors that are realized with three nozzle throat diameters: 0.75, 1.0, and 1.25 mm, and six constant area diameters: 1.5, 2.0, 2.5, 3.0, and 3.5 mm.

In Chapter 4, the experimental results are presented and discussed:

- Test results on the CO_2 refrigeration cycle.
- Test results on four control strategies for the control of the high pressure and the evaporation temperature.
- Test results comparing 18 ejector configurations.

The ejector results are used to adapt the 1D model that is used to characterize the ejector operation with different parameters and different ejector cycle configurations with “integral” heat exchanger and internal heat exchanger.

Chapter 1. Improvement of energy efficiency of CO_2 transcritical cycles

1.1 History of CO_2 in refrigeration

The carbon dioxide is an old refrigerant, one of the first used to produce cold in refrigerated chambers, since water cannot ensure a temperature lower than its triple point 0°C. During the first decades of the 20th century, CO_2 was widely used as a refrigerant, mainly in marine systems but also in air conditioning and stationary refrigeration applications. Alexander Twining has been the first to propose CO_2 as refrigerant in his 1850 British Patent, but the first CO_2 system was built only in the late 1860s by the American Thaddeus S.C. Lowe. Lowe, who received a British Patent in 1867, did not develop his ideas further. In Europe, Carl Linde built the first CO_2 machine in 1881. Franz Windhausen of Germany advanced the technology considerably, and was awarded a British Patent in 1886. The company J.&E. Hall in the United Kingdom purchased the patent rights in 1887, and after having further improved the technology, Hall begun manufacturing in about 1890. Hall made the first two-stage CO_2 machine in 1889. The primary application was in marine refrigeration, a field where CO_2 dominated as a refrigerant until 1950-1960 as shown in Figure 1.1.

In Europe, CO_2 machines were often the only choice due to the legal restrictions on the use of toxic or flammable refrigerants, like NH_3, SO_2 and hydrocarbons. In the United States, CO_2 was used in refrigerating systems from about 1890 and in comfort cooling from about 1900. The refrigeration applications included small cold storage systems, food markets, kitchen and restaurant systems, while comfort cooling systems were installed for instance in passenger ships, hospitals, theatres and restaurants. Most of these systems used calcium chloride solutions as a secondary refrigerant in two-stage systems. Compressors were slow-running double or single-acting crosshead machines with atmospheric crankcase pressure, and expansion valves were usually of the manual-control type. Condensers were often water-cooled double-pipe units.

Safety of use, compared to refrigerants like NH_3 and SO_2, gave CO_2 a preference on board of ships and in public buildings. The commonly reported disadvantages of CO_2 were loss of capacity and low COP at high heat rejection temperature, compared to other common refrigerants. Especially in warm climates, this gave CO_2 a disadvantage. Refrigerant containment at high pressure was difficult with the sealing technology available at that time. By operation at supercritical high-side pressure or by various two-stage arrangements, the capacity and efficiency loss could be reduced.

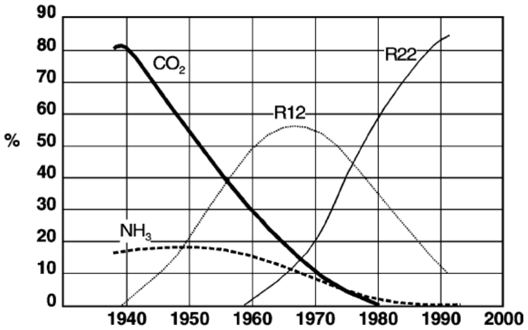

Figure 1.1: Percentage use of main primary refrigerants in existing marine cargo installations classed by Lloyd's Register [LONDON 1992]

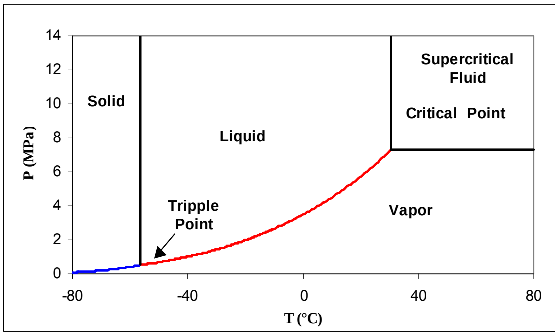

Figure 1.2: Phase diagram of CO_2

The so-called multiple-effect compression as devised by Voorhees in 1905, is one example of the improvements that were made. When supercritical high-side operation was needed, this was obtained by charging more refrigerant into the system to increase the high-side pressure. As the CFC fluids were introduced in the 1930s and 1940s, like

CFC-12 discovered by Midgley and Henne (1928), these 'safe refrigerants' eventually replaced the old working fluids in most applications. Although the major argument in their favor was improved safety compared to fluids like ammonia and sulfur dioxide, CO_2 was also replaced by this transition to CFCs. There is no single reason why the use of CO_2 declined, but a number of factors probably contributed. These factors included high-pressure containment problems, capacity and efficiency losses at high temperature aggravated by the need to use air cooling instead of water, aggressive marketing of CFC products, low-cost tube assembly in competing systems, and a failure of CO_2 system manufacturers to improve and modernize the design of systems and machinery.

The stratospheric ozone depletion led to the international agreement: the Montreal Protocol, which has defined a global schedule for the phase-out of CFCs and then of HCFCs. The whole industry was searching for viable refrigerant alternatives. In Norway, Professor Gustav Lorentzen believed that the old refrigerant CO_2 could have a renaissance. In a 1989 international patent application, he devised a 'transcritical' CO_2 cycle system, where the throttling valve controlled the high-side pressure. One of the intended applications for this system was automobile air conditioning, a sector where CFC refrigerant emissions were huge, and also an application where a non-toxic and non-flammable refrigerant was needed. The potential for more compact components due to high pressure was also an interesting feature.

In 1992, Lorentzen and Pettersen published the first experimental results on a prototype CO_2 system for automobile air conditioning. A comparison was made between a state-of-the-art R-12 system and a laboratory prototype CO_2 system with equal heat exchanger dimensions and design-point capacity. Although simple cycle calculations indicated that the CO_2 system efficiency would be inferior, a number of practical factors made the actual efficiencies of the two systems equal. Based on these and other results, the interest in CO_2 as a refrigerant increased considerably throughout the nineties.

The commitment of the European Union to the Kyoto Protocol has led through a number of events to decide that refrigerant with a GWP (Global Warming Potential) inferior to 150 eq. CO_2 can only be used in mobile air-conditioning (MAC) systems as of 2011 for new vehicle types and progressively until 2017 for the other new vehicles. This decision has been made based on the technical development of CO_2 MAC systems by car makers and their suppliers.

1.2 Properties of CO_2

The carbon dioxide is a non-flammable refrigerant with no ozone depletion potential and a global warming potential of 1 (which is the GWP reference for all other global warming gases). Its vapor pressure is much higher and its volumetric refrigeration capacity is 3 to 10 times larger than CFC, HCFC, HFC and HC refrigerants used in the different refrigeration applications. The critical pressure and temperature are 7.38 MPa and 31°C, so the cooling of CO_2 above 31°C is only a sensible heat cooling of dense gas (no condensation occurs). When the saturating temperature of CO_2 is higher than 31°C on the high-pressure side the cycle is called a transcritical cycle: it is sub-critical on the low-side pressure and supercritical on the high-side pressure. The high pressure and temperature in the supercritical region are no more coupled and need to be regulated independently to obtain the optimum operating conditions.

The phase diagram of CO_2, Figure 1.2, shows that the temperature and pressure for the triple point of CO_2 are –56.6°C and 520 kPa, respectively, and the saturation pressure at 0°C is 3.5 MPa.
The CO_2 P-h and T-s diagrams are shown in Figures 1.3 and 1.4. Table 1.1 presents the comparison between the properties of CO_2 and the three other refrigerants.

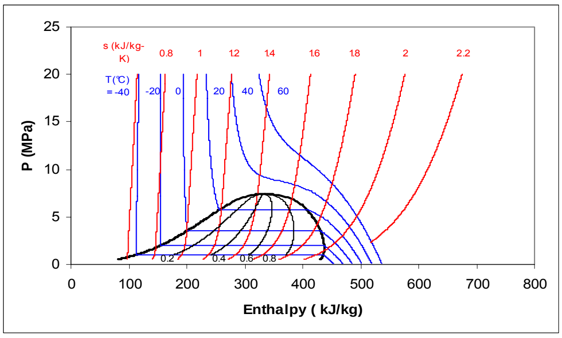

Figure 1.3: Pressure-enthalpy diagram of CO_2.

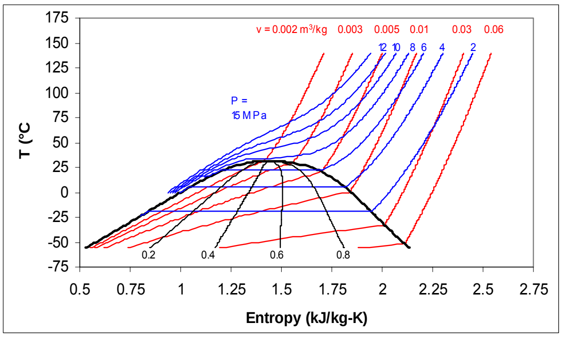

Figure 1.4: Temperature-entropy diagram of CO_2.

Table 1.1: Comparison between different refrigerants and CO_2.

	R-12	R-134a	R-152a	R-744
ODP/GWP	1/8500	0/1300	0/120	0/1
Flammability / toxicity	N/N	N/N	Y/N	N/N
Molecular mass (g/mol)	120.9	102	66.05	44.01
Normal boiling point (°C)	-29.8	-26.1	-24	-78.4
Critical pressure (MPa)	4.13	4.06	4.517	7.38
Critical temperature (°C)	112	101.1	113.26	30.98
Pressure (bar) at 0°C	3.08	2.928	2.64	34.85
Refrigeration capacity (KJ/m^3) at 0°C	2734	2865.4	2567	22545.7
First commercial use as refrigerant	1931	1990	1990	1869

1.2.1 Thermodynamic properties

Many researchers, like Vesovic et al.[1990], Fenghour et al. [1998], Rieberer [1998] studied CO_2,and evaluated equations of state and correlations to describe the CO_2 properties. The NIST Data (Refprop 7) is used to draw the properties of CO_2: the free energy Helmotz equations of state for carbon dioxide has been developed by Span and Wagner (1996), covering a fluid region from the triple point to 1100 K at pressures up to 800 MPa. Those equations are used to calculate different thermodynamic properties with estimated uncertainties ranging from 0.03 to 0.05% for the density, 0.03 to 1% for the speed of sound, and +0.15 to 1.5% for the isobaric heat capacity.

The saturation pressure and slope of the saturation temperature curve of CO_2 compared to other fluids, presented in Figures 1.5 and 1.6, show that the saturation pressure of CO_2 is much higher than other refrigerants, and its higher value near the critical point gives a smaller temperature change for a given pressure change. Thus, the temperature change associated with pressure drop in the evaporator will be smaller, at 0°C, the temperature change of CO_2 for 1 kPa pressure drop is about 0.01 K, on the other hand, the same pressure drop with R-134a gives a temperature change of 0.10 K, about 10 times higher, as shown in Figure 1.6. On the other side, a small variation of temperature brings a large variation of the saturated pressure.

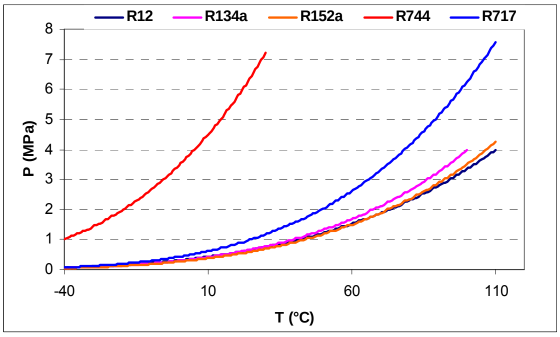

Figure 1.5 : Refrigerants saturation pressure

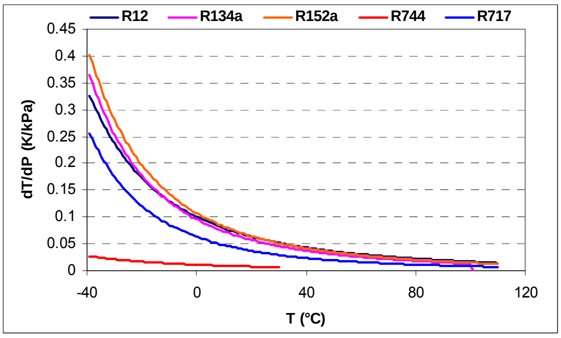

Figure 1.6: Slope of saturation pressure curve dT/dP for refrigerants

The high saturation pressure and closeness to the critical point result in quite different characteristics of liquid and vapor density of CO_2 compared to other refrigerants. The high vapor density may have significant effects on two-phase flow patterns where differences in phase density determine phase separation characteristics. Vapor density influences also the flow momentum of the vapor phase and shear force between vapor and liquid phases. Figures 1.7 and 1.8 show density variation of CO_2 as a function temperature and the ratio of liquid to vapor density for several refrigerants. The density of CO_2 changes rapidly with temperature near the critical point, and the density ratio of CO_2 is much smaller than other refrigerants. At 0°C, for instance, the ratio of liquid (927 kg/m^3) to vapor density (98 kg/m^3) of CO_2 is around 10, whereas the density ratio of R-134a is 89. The vapor density of R-134a is 14 kg/m^3, which are 14% of the CO_2 vapor density. The low-density ratio of CO_2 may give more homogenous two-phase flow than with other refrigerants. The liquid to vapor density ratio plays an important role in an evaporator since it determines the flow pattern and thus the heat transfer coefficient.

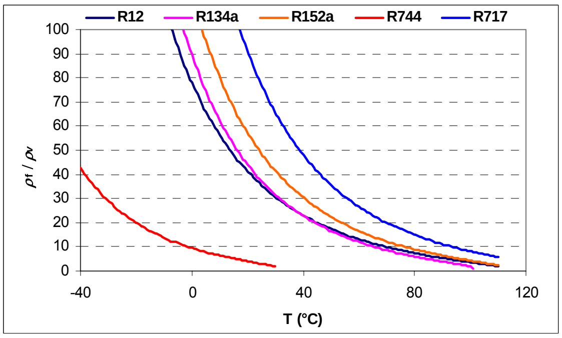

Figure 1.7: Ratio of liquid to vapor density at saturation for refrigerants.

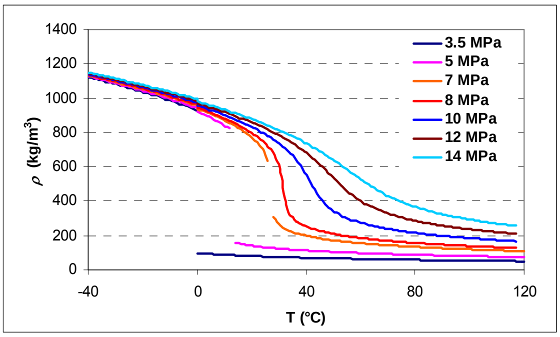

Figure 1.8: Density of CO_2.

The higher vapor density gives the high volumetric refrigeration capacity of CO_2, which is defined as product of vapor density and latent heat of evaporation. The volumetric refrigeration capacity of CO_2, Figure 1.9, increases with temperature, reaches a maximum at 21.7°C, and then decreases again. By definition it is zero at the critical point because the latent heat is nil. The volumetric refrigeration capacity influences the swept volume of compressor in a refrigeration cycle, thus the CO_2 compressor will have a smaller swept volume than for other fluids.

Surface tension of refrigerants influences nucleate boiling and two-phase flow characteristics. A small surface tension reduces the superheat required for nucleation and growth of vapor bubbles, which may positively affect heat transfer. Wetting characteristics of the liquid are affected by surface tension, thus influencing evaporation heat transfer. Reduced liquid surface stability with small surface tension may affect heat transfer negatively due to the increase of small droplet formation (aerosol) and entrainment. Figure1.9 presents the surface tension of saturated CO_2 liquid as a function of temperature, compared to other fluids. The surface tension of refrigerants decreases with temperature and becomes zero at the critical point; the surface tension of CO_2 is smaller than those of other fluids. For instance at 0°C it is 0.0044 N/m, which is 2.5 times smaller than that of R-134a at the same temperature.

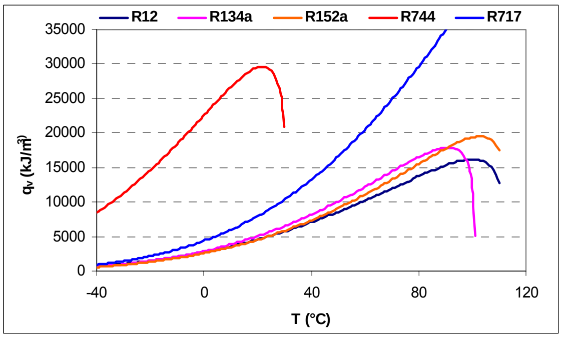

Figure 1.9: Volumetric refrigeration capacity for refrigerants

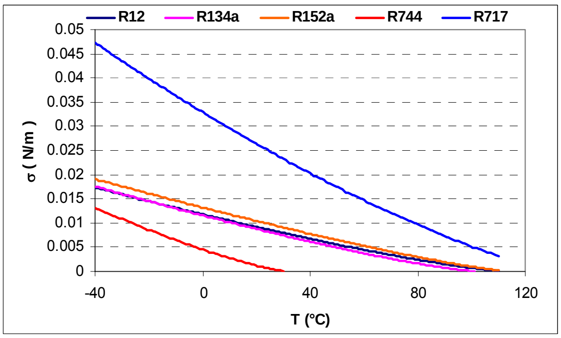

Figure 1.10: Surface tension for refrigerants

The enthalpy and entropy variations with temperature at constant pressure are shown in Figures 1.11 and 1.12. The supercritical region corresponds to a cooling process in a gas cooler, enthalpy and entropy of CO_2 increase with temperature with a large slope near the critical temperature; below the critical temperature, the pressure has small effect on enthalpy and entropy. Above the critical temperature, enthalpy and entropy of CO_2 decrease with pressure.

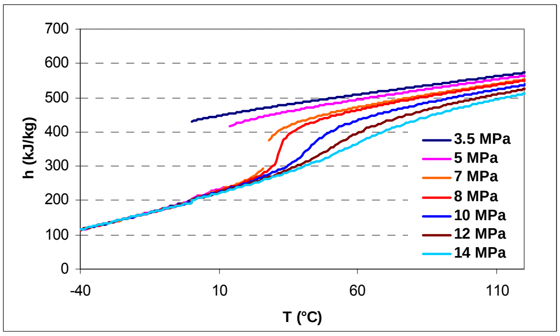

Figure 1.11: Enthalpy changes of CO_2 in gas cooling process.

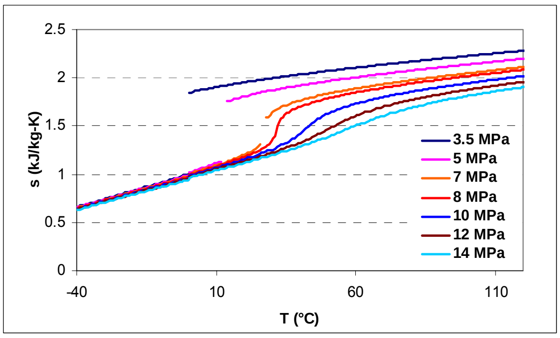

Figure 1.12: Entropy changes of CO_2 in gas cooling process.

The transport properties of refrigerants play an important role in heat transfer and pressure drop characteristics. Figures 1.13 and 1.14 show two transport properties: thermal conductivity and viscosity at sub-critical and supercritical pressures at different temperatures. A high thermal conductivity is essential for heat transfer coefficients both in single-phase and two-phase flows. Viscosity, particularly of the liquid phase, and the ratio of liquid to vapor viscosity, are important parameters for the fluid flow behaviors, convection characteristics, two-phase heat transfer, and pressure drop. The thermal conductivities of CO_2 saturated liquid and vapor at 0°C are 20% and 60% higher than of R-134a saturated liquid and vapor, respectively, while the viscosity of liquid CO_2 is only 40% of R-134a liquid viscosity, and the vapor viscosities of the two fluids are similar.

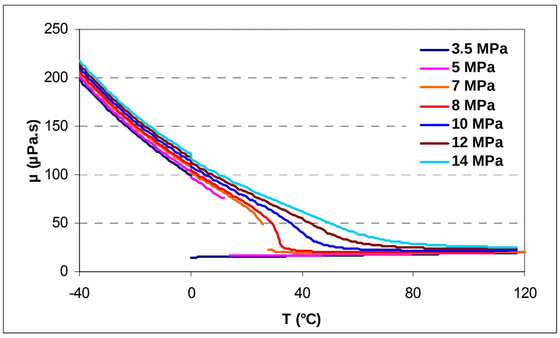

Figure 1.13: Viscosity of CO_2

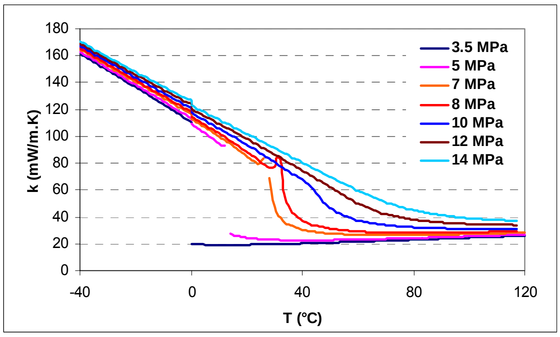

Figure 1.14: Thermal conductivity of CO_2

The Prandtl number is an important parameter for the heat transfer coefficient. Figure 1.15 shows the Prandtl number of supercritical and liquid/vapor CO_2 at varying temperatures. It has a maximum at the pseudo-critical temperature associated with the corresponding heat capacity, and the maximum value decreases with pressure. The effect of the temperature on the Prandtl number depends on pressure. The Prandtl number becomes higher with pressure for temperature above 60°C in the supercritical region, whereas it decreases with pressure when temperature is lower than about 20°C. These values result in a strong variation of local heat transfer coefficients depending on temperature and pressure. In summary, the thermodynamic and transport properties of CO_2 seem to be favorable in terms of heat transfer and pressure drop, compared to other typical refrigerants like R-134a.

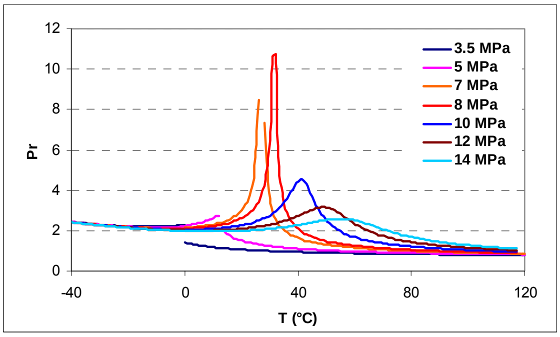

Figure 1.15: Prandtl number of CO_2

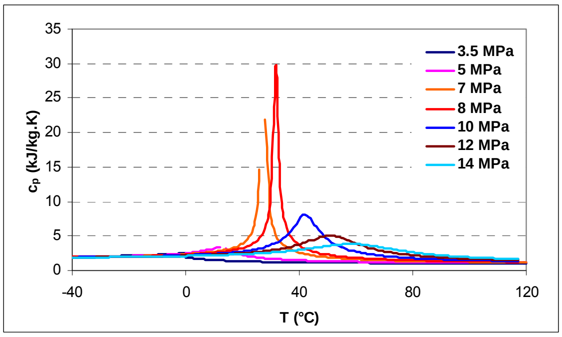

Figure 1.16: Isobaric heat capacity of CO_2

One of the most important characteristics of supercritical fluids near the critical point is that their properties change rapidly with temperature in an isobaric process, especially near the pseudo-critical temperature points (the temperature at which the heat capacity presents a maximum for a given pressure) as shown in Figure 1.16. This may be clearly seen from Figures 1.13 and 1.17, where the isobaric heat capacity and pseudo-critical temperature are presented.

The pseudo-critical temperature of CO_2 can be calculated using the following algebraic equation given by [LIA 00]:

$$T_{pseudo} = -122.6 + 6.124P - 0.1657P^2 + 0.01773P^{2.5} - 0.0005608P^3 \quad ; \; 75 \leq \mathrm{P} \leq 140 \qquad \text{Eq. 1.1}$$

where the temperature T_{pseudo} and pressure P are in°C and bar, respectively.

Using Refprop 7 to calculate T_{pseudo}, a 3rd degree polynomial equation has been elaborated with a maximum relative error of 0.33% that correspond to 0.12 K as a maximum absolute error (see Figure 1.18):

$$T_{pseudo} = 0.000003915\,P^3 - 0.003315\,P^2 + 1.0275\,P - 28.411 ; 75 \leq \mathrm{P} \leq 200 \qquad \text{Eq. 1.2}$$

where the temperature T_{pseudo} and pressure P are in°C and bar, respectively.

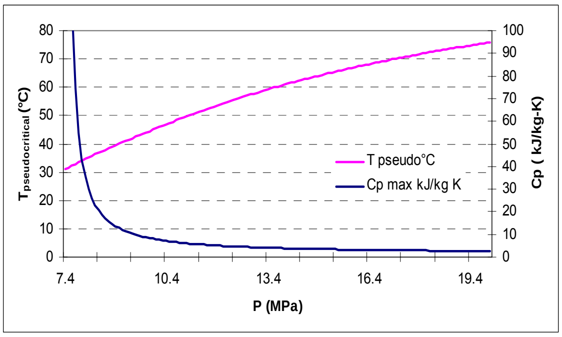

Figure 1.17: Pseudo-critical temperature and maximum isobaric heat capacity of CO_2

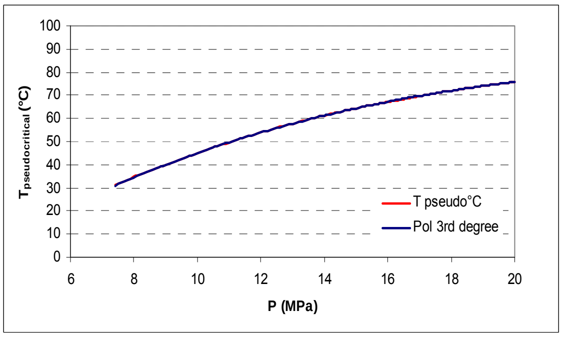

Figure 1.18: Comparison of algebraic polynomial 3rd degree equation with real values.

1.2.2 Transcritical compression cycle

Compared to conventional refrigerants, where the refrigerant condenses at saturation conditions with two-phase state at constant pressure and temperature, the most remarkable property of CO_2 is the low critical temperature of 31.1°C. The vapor compression systems with CO_2 operating at usual outdoor temperatures, will therefore work close to and even above the critical pressure of 7.38 MPa. Heat rejection will, in most cases, take place at a supercritical pressure, causing the pressure levels in the system to be high, and the cycle to be 'transcritical, meaning sub-critical at the low-side pressure and supercritical at the high-side pressure, for a single-stage cycle.

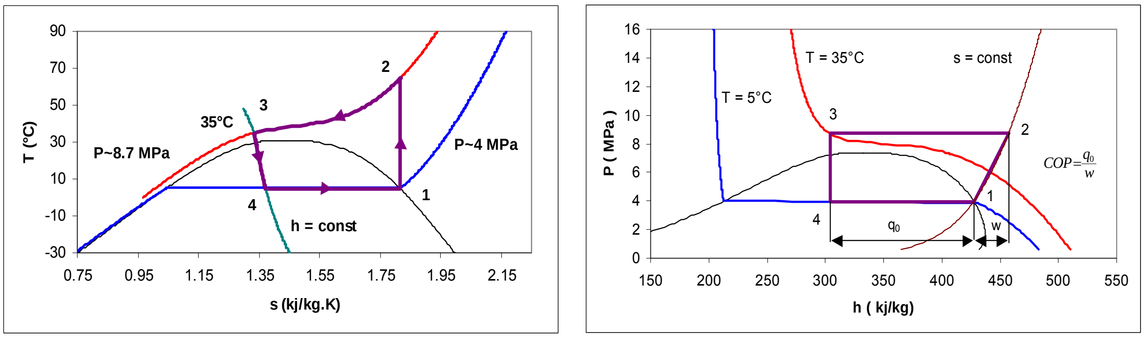

Figure 1.19: Transcritical Evans- Perkins cycle in the CO_2 T-s and P-H diagrams.

In supercritical state, the pressure is independent of the temperature. In conventional sub-critical cycles, the enthalpy at point 3 of Figure 1.19 is mainly a function of temperature, but in supercritical conditions the pressure also has a marked influence on enthalpy. An important consequence is the necessary control of the high pressure, since the pressure at the throttling valve inlet determines the cooling capacity. As in conventional systems, the compressor input power, and thereby the COP will depend on the discharge pressure. However, while the COP tends to drop when increasing the high pressure in conventional cycles, the behavior is quite different in a transcritical cycle.

Figure 1.20 shows the theoretical influence from varying high-side pressure on refrigerating capacity q_0 (in kJ/kg); compressor work W and the cooling COP. The curves are based on ideal cycle calculations, with evaporating temperature at 5°C and a minimum heat rejection temperature T_{ex} of 35°C, and 50°C.

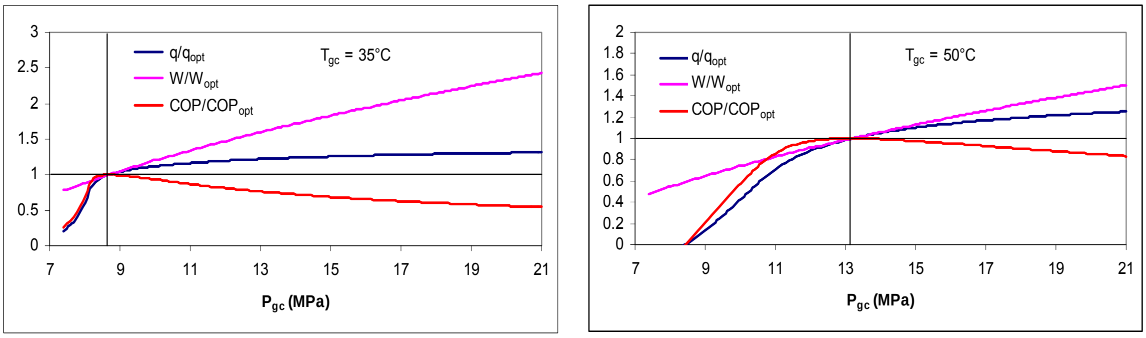

Figure 1.20: Influence of varying high pressure on refrigerating capacity (q), compressor work (W) and COP in a transcritical CO_2 cycle.

Note: the curves are based on isentropic compression (η_{is} = 1), evaporating temperature T_{evap} = 5°C and a refrigerant outlet temperature for the gas cooler of 35°C and 50°C, the sub-cooling and the superheat are nil.

As the high pressure is increased, the COP reaches a maximum above which the added refrigerating capacity no longer compensates the additional work of compression. In Figure 1.19, it may be observed that the isotherm becomes steeper as the pressure increases, thereby reducing the capacity enhancement from a given pressure increment.

In contrast, the isentropic compression line shows a nearly linear shape. Differentiation of cooling COP = (h_1 –h_3)/ (h_2 – h_1) with respect to the high-side pressure gives maximum COP for ∂COP / ∂p = 0 at a pressure p defined by [KIM 04]:

$$\left(\frac{\partial h_3}{\partial p}\right)_T = -COP\left(\frac{\partial h_2}{\partial p}\right)_s \qquad \text{Eq. 1.3}$$

The 'optimum' pressure is reached when the marginal increase in capacity equals COP times the marginal increase in work. High pressure control can be developed to maintain the COP at its maximum and to regulate the cooling or heating capacity.

The optimum pressure increases steadily, almost linearly as T_{gc} raises (Figure 1.21), and the influence from varying evaporating temperature is quite small (Figure 1.22). For -15/15°C evaporating temperature variation and a gas cooler outlet temperature of 35°C, the optimum pressure difference is 520 kPa, at 45°C it is 960 kPa, and for gas cooler outlet temperature of 55°C, the optimum pressure difference is 1.28 MPa.

Heat is rejected from the CO_2 gas cooler under a glide of temperature, while the supercritical pressure single-phase refrigerant is cooled. This glide may be useful in heat pumps for water heating, and may also give advantages in heat recovery from refrigeration or air conditioning systems.

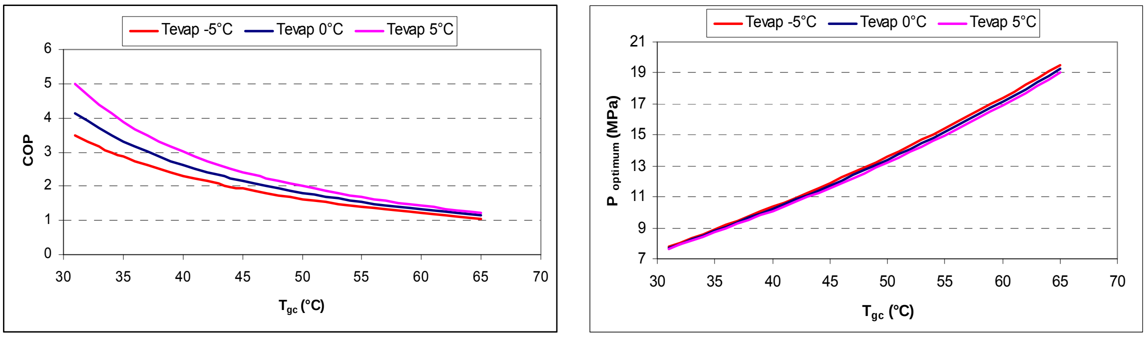

Figure 1.21: Variation of the optimum pressure and COP as a function of the outlet temperature of gas cooler.

Note: the evaporating temperatures are constant, isentropic efficiency η_{is} = 1, the sub-cooling is nil and the superheat is 5 K.

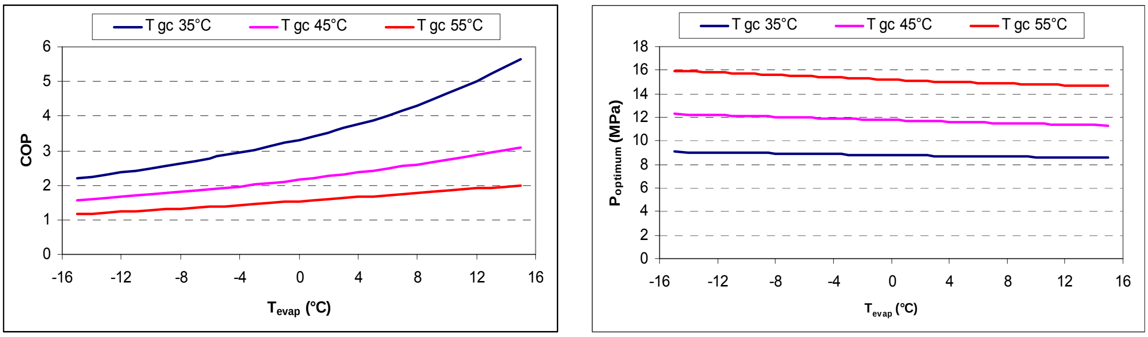

Figure 1.22: Variation of the optimum pressure and COP as a function of the evaporating temperature.

Note: the gas cooler outlet temperatures are constant, isentropic efficiency η_{is} = 1, the sub-cooling is nil and superheat is 5 K.

By comparing the performance of a refrigeration cycle operating with R-134a, R-152a and CO_2 at the same conditions: η_{is}, evaporating temperature, sub-cooling and superheat, as shown in Figure 1.23.a, the CO_2 cycle performance is lower than the ones of the other two fluids. When modifying the isentropic compression efficiencies, 0.8 (or 1.0) for CO_2 cycle and 0.6 for the other cycles as shown in Figure 1.23.b, the CO_2 cycle becomes more efficient for a condensing temperature lower than 21°C (or lower than 28°C). Thus, by improving the compression efficiency, the CO_2 refrigeration cycle may be more efficient than the R-134a cycle. A number of comparisons have been presented in conferences during the last ten years where the compressor efficiencies of R-134a compressors vs. CO_2 compressors were different and so the comparisons were many times biased. In conclusion, for the comparison of refrigeration cycles with different refrigerants, it is necessary to assess the efficiencies, especially of compressors, when making those comparisons.

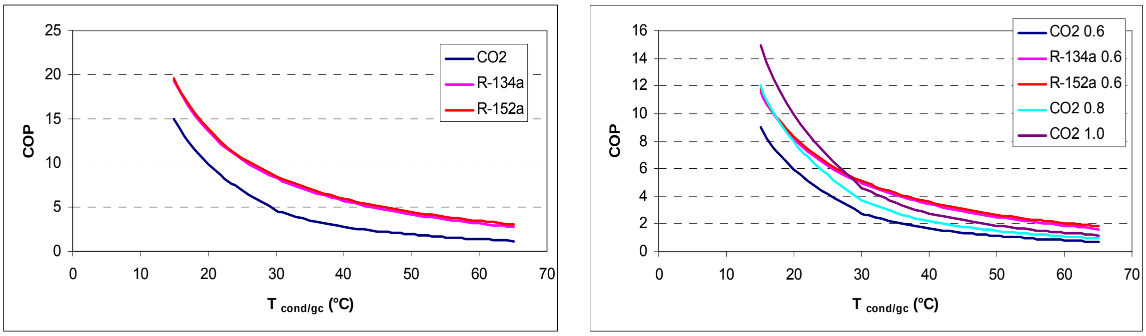

a. $T_{ev} = 2°C$, $\eta_{is} = 1$, SH = 5 K, SC = 0. b. $T_{ev} = 2°C$, SH = 5 K, SC = 0.

Figure 1.23: Comparison of performance between R-134a, R-152a, and CO_2 at constant evaporation temperature 5°C and different conditions of sub-cooling, superheat and isentropic efficiency of compression.

Table 1.2: Performance comparison of the simple refrigeration cycle.

$T_{cond/gc}$°C	COP CO_2 1.0	R-134a 0.6	R-152a 0.6	COP CO_2 0.8
28	5.537	5.419	5.555	4.430
21	9.215	7.279	7.412	7.372

For an ideal simple transcritical cycle, such as the one described in Figure 1.19, the value of the optimum pressure P_{opt} of the gas cooler can be calculated by the equation [LIA 98]

$$P_{opt}=(2.778-0.0157.t_{ev}).t_{gc}+(0.381.t_{ev}-9.34) \qquad \text{Eq. 1.4}$$

Popt is a function of evaporation temperature t_{ev} and temperature at the gas cooler outlet t_{gc}, with t_{ev} and t_{gc} in°C, and P_{opt} in bar, $-40°C \le t_{ev} \le 5°C;\ 31°C \le t_{gc} \le 50°C$.

Note: the compression is isentropic and the CO_2 vapor is saturated at the compressor suction port.

Using Refprop7, the optimum pressure and COP are calculated from the same conditions, and correlations were elaborated for $P_{optimum}$ and $COP_{optimum}$ as a function of t_{ev} and t_{gc}:

$$P_{opt} = (-0.1564 + 0.2271\ t_{ev} - 0.00304\ t_{ev}^2 + 2.6026\ t_{gc} - 0.006085\ t_{gc}^2 + 0.00031\ t_{gc}^3)/(1+0.0049\ t_{ev} - 4.17e\text{-}5\ t_{ev}^2 - 3.153e\text{-}7\ t_{ev}^3 + 0.0029\ t_{gc}) \qquad \text{Eq. 1.5}$$

$$COP_{opt} = (-4.6043 + 0.000281\ t_{ev} + 9.613e\text{-}5\ t_{ev}^2 + 0.0804\ t_{gc} - 0.000555\ t_{gc}^2 + 1.414e\text{-}7\ t_{gc}^3)/(1+0.0227\ t_{ev} - 0.0001404\ t_{ev}^2 - 0.0866\ t_{gc} + 0.001464\ t_{gc}^2 - 1.078e\text{-}5\ t_{gc}^3) \qquad \text{Eq. 1.6}$$

with t_{ev} and t_{gc} in°C, and P_{opt} in bar, $-40°C \le t_{ev} \le 15°C;\ 31°C \le t_{gc} \le 60°C$.

The relative error for P_{opt} is 0.88% and the maximum difference between the calculated value and the formula is 1455 bar. The relative error for COP_{opt} is 1.61% and the maximum difference between the calculated value and the formula is 0.079.
In addition, the optimum pressure of the conventional cycle is independent of the efficiency of the compressor.

1.3 Exergy analysis

The exergy analysis of a cycle identifies the performance of each component of the cycle. Exergy at a given state is equal to the maximum work that can be obtained when operating reversibly between the given state and the reference state:

$$e = (h - h_0) - T_0 (s - s_0) \qquad \text{Eq. 1.7}$$

For Q at constant temperature T, exergy can be also calculated by:

$$E = \left(1 - \frac{T_0}{T}\right) Q \qquad \text{Eq. 1.8}$$

The entropy production is calculated for each component of the system. The number of entropy production allows analyzing the generation of entropy of each component. From the ideal COP (Carnot), the sources of irreversibilities are evaluated to define the real COP of the system under the specified operating conditions.

The first and the second laws of thermodynamics are applied to the reference cycle in steady state operation. The combination of the two laws allows defining the coefficient of performance (COP) and the total number of production of entropy.

The first law of thermodynamic at steady state gives:

$$\dot{W}_{eff} + \dot{Q}_{hs} + \dot{Q}_{cs} = 0 \qquad \text{Eq. 1.9}$$

$$q + w = \sum\left(h_e + \frac{V_e^2}{2} + gz_e\right) - \sum\left(h_i + \frac{V_i^2}{2} + gz_i\right) \qquad \text{Eq. 1.9'}$$

The Second law of thermodynamic in steady state gives:

$$P(S) + \frac{\dot{Q}_{hs}}{T_{hs}} + \frac{\dot{Q}_{cs}}{T_{cs}} = 0 \qquad \text{Eq. 1.10}$$

For a component, it will be:

$$s_{gen} = \sum s_e - \sum s_i + \frac{q_{surr}}{T_0} \qquad \text{Eq. 1.10'}$$

The coefficient of performance is given by:

$$COP_{cold} = \frac{T_{cs}}{T_{hs} - T_{cs}}\left(1 - N_{cold}\right) \qquad \text{Eq. 1.11}$$

$$COP_{hot} = \frac{T_{hs}}{T_{hs} - T_{cs}}\left(1 - N_{hot}\right) \qquad \text{Eq. 1.12}$$

The entropy number is given by:

$$N_{cold} = T_{hs} \frac{P(S)}{\dot{W}_{eff}} \quad \text{and} \quad N_{hot} = T_{cs} \frac{P(S)}{\dot{W}_{eff}} \qquad \text{Eq. 1.13}$$

For the *n* components of the cycle, the exergy number is:

$$N = \sum_{i=1}^{n} N_i \qquad \text{Eq. 1.14}$$

The thermodynamic efficiency of the cycle is expressed as a function of to the total number of entropy generation.

$$\eta = \frac{COP}{COP_{Carnot}} = 1 - N \qquad \text{Eq. 1.15}$$

$$COP_{Carnot,Cold} = \frac{T_{cs}}{T_{hs} - T_{cs}} \; ; \; COP_{Carnot,Hot} = \frac{T_{hs}}{T_{hs} - T_{cs}} \qquad \text{Eq. 1.15'}$$

The refrigeration cycle studied in this section, Figure 1.24, without an internal heat exchanger, is composed of five components: a condenser (gas cooler), an evaporator, an expansion device, and a compressor. Referring to Figure 1.24, the equation of each component is expressed as a function of enthalpy, temperature and entropy.

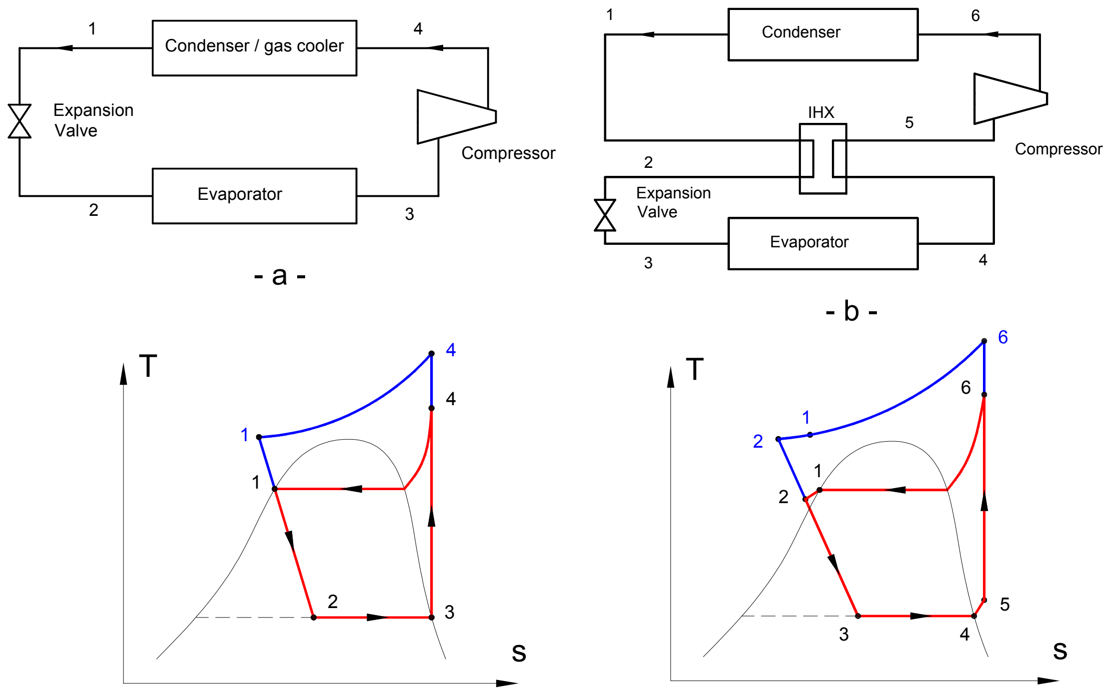

- a -

- b -

- c -

- d -

Figure 1.24: Conventional refrigeration cycle with and without internal heat exchanger.

1.3.1 Compression: Evolution 3 → 4

By neglecting kinetic and potential energies, first law gives:

$$q_{comp} + w_{comp} = h_4 - h_3 \qquad \text{Eq. 1.16}$$

Second law applied to compressor gives:

$$s_{gen,comp} = s_4 - s_3 + \frac{q_{comp}}{T_0} \quad \text{Eq. 1.17}$$

By considering only the work absorbed by the fluid and an isentropic compression, the compressor is adiabatic so the heat of compression is nil, and the entropy generated will be:

$$s_{gen,comp} = s_4 - s_3 \quad \text{Eq. 1.18}$$

$$w_{comp} = h_4 - h_3 \quad \text{Eq. 1.19}$$

$$N_{comp} = T_0 \frac{s_{gen,comp}}{w_{comp}} \quad \text{Eq. 1.20}$$

The coefficient of performance COP is given by:

$$COP = \frac{h_3 - h_2}{h_4 - h_3} \quad \text{Eq. 1.21}$$

1.3.2 Condenser or gas cooler: Evolution 4 → 1

In a supercritical case, in the gas cooler the heat loss will be generated at variable temperature. In sub-critical case, the evolution will be composed of de-superheating at variable temperature, condensing heat loss at constant temperature and sub-cooling at variable temperature. The evolution is isobaric at constant pressure.

By neglecting kinetic and potential energies, first law gives:

$$q_{cond/gc} = h_4 - h_1 \quad \text{Eq. 1.22}$$

Second law applied to condenser/gas cooler gives:

$$s_{gen,cond/gc} = \frac{q_{cond/gc}}{T_{cond/gc,e}} - \left(s_4 - s_1\right) \quad \text{Eq. 1.23}$$

$$N_{cond/gc} = T_0 \frac{s_{gen,cond/gc}}{w_{comp}} \quad \text{Eq. 1.24}$$

The entropy number is always positive.

1.3.3 Expansion: Evolution 1 → 2

Second law applied to the isenthalpic expansion device gives, by considering adiabatic process:

$$s_{gen,\exp} = s_2 - s_1 \quad \text{Eq. 1.25}$$

$$N_{\exp} = T_0 \frac{s_{gen,\exp}}{w_{comp}} \quad \text{Eq. 1.26}$$

When the expansion device is isentropic, the total work and the COP become:

$$w_{comp} = (h_4 - h_3) - (h_1 - h_2) \quad \text{Eq. 1.27}$$

$$COP = \frac{h_3 - h_2}{(h_4 - h_3) - (h_1 - h_2)} \quad \text{Eq. 1.28}$$

1.3.4 Evaporator: Evolution 2 → 3

By neglecting kinetic and potential energies, first law gives:

$$q_{evap} = h_3 - h_2 \qquad \text{Eq. 1.29}$$

Second law applied to the evaporator gives:

$$s_{gen,evap} = s_3 - s_2 - \frac{q_{evap}}{T_{evap}} \qquad \text{Eq. 1.30}$$

$$N_{evap} = T_0 \frac{s_{gen,evap}}{w_{comp}} \qquad \text{Eq. 1.31}$$

1.3.5 Internal Heat exchanger: Evolution 1 → 2 / 4 → 5

Second law applied to the IHX gives:

$$s_{gen,HXI} = (s_5 + s_2) - (s_1 + s_4) \qquad \text{Eq. 1.32}$$

$$N_{HXI} = T_0 \frac{s_{gen,HXI}}{w_{comp}} \qquad \text{Eq. 1.33}$$

By considering all the cycle without IHX as a control volume, the second law gives:

$$s_{gen,cycle} = \frac{(h_4 - h_1)}{T_{gc}} - \frac{(h_3 - h_2)}{T_{evap}} \qquad \text{Eq. 1.34}$$

$$\eta_{ex,cycle} = 1 - \frac{T_0}{w_{comp}} \left(\frac{h_4 - h_1}{T_{gc/cond}} - \frac{h_3 - h_2}{T_{evap}} \right) \qquad \text{Eq. 1.35}$$

The heat of condensation/gas cooling is rejected at $T_{cond\ /\ gc}$ that is taken equal to T_0 to verify Eq. 1.15. The heat of vaporization is absorbed at T_{evap} in all cases that correspond to the inlet temperature of the evaporator, the sub-cooling is nil and so is the superheat. The efficiency of the compressor is fixed at **80%**; the isentropic efficiency of the turbine is fixed at **70%**.

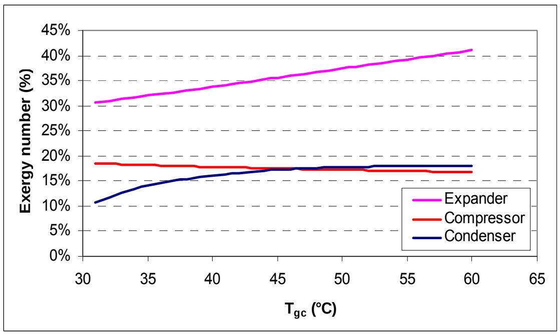

a- Isenthalpic expansion, T_{evap} = 5°C

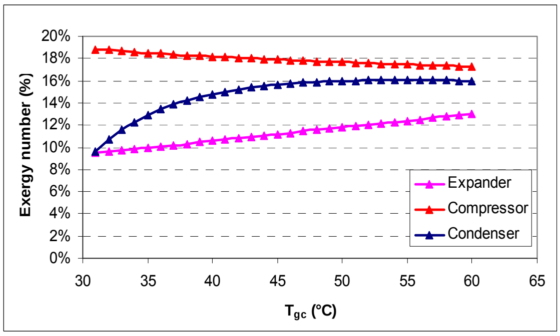

b- Isentropic expansion, T_{evap} = 5°C

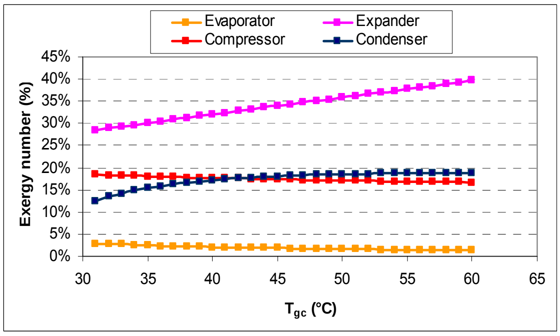

c- Isenthalpic expansion with pressure drop, T_{evap} = 5°C

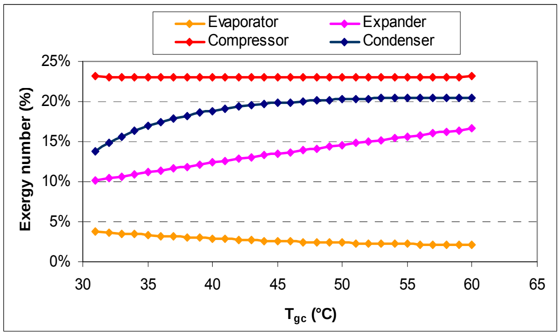

d- Isentropic expansion with pressure drop, T_{evap} = 5°C

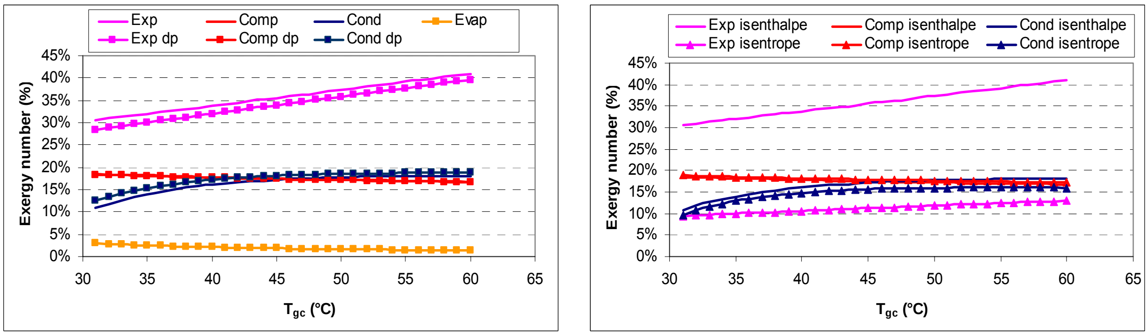

e- Isenthalpic dp / isenthalpic, T_{evap} = 5°C f- Isentropic / isenthalpic, T_{evap} = 5°C

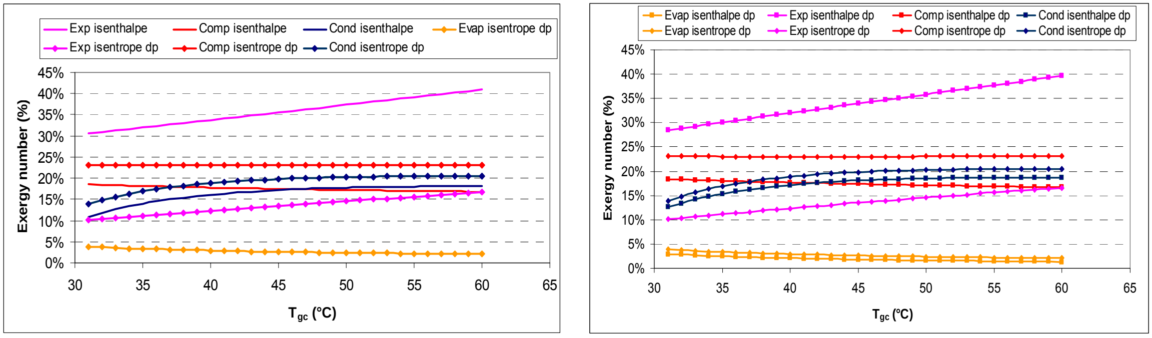

g- Isentropic dp/ isenthalpic, T_{evap} = 5°C h- Isentropic dp/ isenthalpic dp, T_{evap} = 5°C

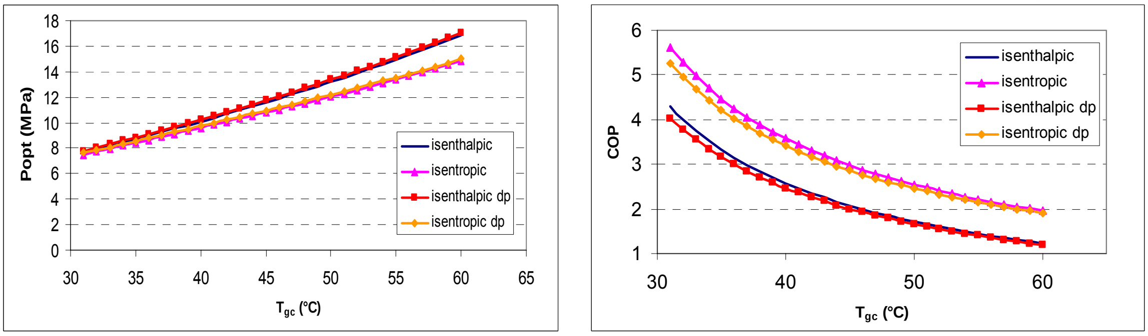

i- Optimum high pressure, T_{evap} = 5°C j- Optimum COP, T_{evap} = 5°C

Figure 1.25: Exergy variation with the gas cooler outlet temperature for different components of a CO_2 refrigeration cycle with different operation modes at 5°C evaporation temperature:

a- isenthalpic expansion,
b- isentropic expansion,
c- isenthalpic expansion with pressure drop,
d- isentropic expansion with pressure drop,
e- comparison of isenthalpic expansion with pressure drop and isenthalpic expansion,
f- comparison of isentropic expansion and isenthalpic expansion,
g- comparison of isentropic expansion with pressure drop and isenthalpic expansion,
h- comparison of isenthalpic expansion with pressure drop and isentropic expansion with pressure drop,
i- variation of optimum pressure as a function of gas cooler outlet temperature,
j- variation of COP as a function of gas cooler outlet temperature.

Table 1.3: Pressure drop in the circuit of refrigeration cycle.

Element	**DP**	**kPa**
Connector evaporator – Compressor	DP 3	0
Connector compressor-condenser	DP 4	0
Condenser/gas cooler	DP 4 -1	100
Connector condenser/gas cooler – Expansion valve / Expander	DP 1	0
Evaporator	DP 2 - 3	100

For a given evaporating temperature and a given minimum heat rejection temperature (gas cooler outlet temperature), the trans-critical cycle exhibits larger thermodynamic losses than a conventional Evans–Perkins cycle with condensation.

Figure 1.25 shows the exergy number variation of different components of a refrigeration cycle with the gas cooler outlet temperature at constant evaporation temperature of 5°C. In Figure 1.25a, the exergy number of the evaporator is nil because there is no superheat, the exergy numbers of expander and condenser (gas cooler) increase with the gas cooler temperature outlet. On the other hand the exergy number of compressor decreases with T_{gc} but the total exergy number increases with T_{gc}, the exergy number of expander is the largest for an isenthalpic expansion.

The pressure drops in evaporator and condenser increase their exergy number except the compression exergy number as shown in Figure 1.25e, and deteriorate the performance of the cycle as shown in Figure 1.25j, because the compression work of the cycle increases due to the pressure drop, and so the discharge enthalpy of the compressor increases. The optimum high pressure of the cycle is not largely affected by the pressure losses as shown in Figure 1.25l, but it depends on the type of the expansion mode. Also the pressure losses in the evaporator create a non-zero exergy number. The pressure drop affects the cycle with isentropic expansion as shown in Figures 1.25g and 1.25h. The pressure drop increases the compression work and decreases the turbine-generated work.

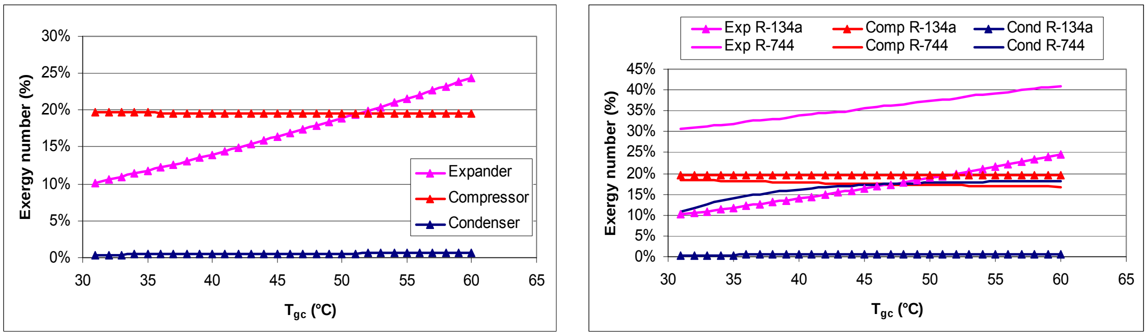

a- R-134a isenthalpic expansion
T_{evap} = 5°C

b- R-744/R-134a isenthalpic expansion
T_{evap} = 5°C

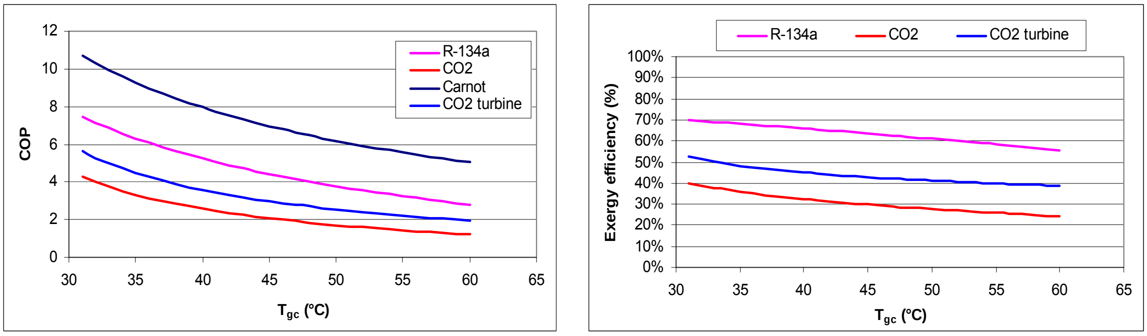

c- R-134a Isenthalpic expansion, T_{evap} = 5°C

d- R-134a Isenthalpic expansion, T_{evap} = 5°C

Figure 1.26: Exergy variation with condensing temperature for different components of a R134a refrigeration cycle at 5°C evaporation temperature:

a- isenthalpic adiabatic expansion,
b- **c**omparison of exergy number with CO_2 refrigeration cycle,
c- **c**omparison of performance,
d- **c**omparison of exergy efficiency.

Figure 1.26-a shows the exergy number variation of R-134a with condensation temperature. The exergy number of the condenser is small because there is not a large superheat. Also the exergy number of compressor is quasi-constant so the performance of the cycle depends largely on the exergy number of the expander. By comparing exergy number of R-134a with CO_2, the exergy number of compressor is close but the exergy

number of condenser and expander of CO_2 are larger than R-134a, therefore the performance of CO_2 cycle could be enhanced by decreasing expansion exergy number: using a turbine (an isentropic expansion) to decrease the expansion exergy number, or by limiting the compressor outlet temperature: using multi-stage compression with inter-cooling or direct cooling of the compressor to decrease the required compression work and the gas cooler exergy number.

On the other hand, the use of the high-temperature heat rejected for domestic hot water in stationary applications and for reheating (or defogging) in mobile applications can enhance the economic viability of the transcritical cycle.

1.4 Modified cycles for enhancement of CO_2 refrigeration cycle

The exergy analysis of the conventional refrigeration cycle using carbon dioxide as refrigerant shows that the major performance losses are in the throttling process and the gas cooling / condensing phase that is mainly affected by the discharge temperature of the compressor; so the cycle improvements consist in modifying these two phases.
In principle, a large number of modifications are possible:

- use of an internal heat exchanger
- work-generating expansion
- staging of compression phase
- cooling of compressor
- use of an ejector.

These modifications can be combined. Every modified cycle has its optimal operation parameters. The purpose of the modified cycle is to increase the CO_2 refrigeration cycle performance so it will be comparable to the other refrigerant performance cycles, such as R-134a for air conditioning.

1.4.1 Internal heat exchange cycle

The performance of a transcritical cycle depends largely on the gas cooler outlet temperature, so, by decreasing the outlet temperature, the performance of the cycle will increase. Since the ambient temperature defines the gas cooler outlet temperature, a cold sink with a temperature lower than the ambient temperature is required, so the compressor suction can be used as internal cold sink. Then by installing an internal heat exchanger IHX between the compressor suction line and the gas cooler outlet, a performance improvement can be achieved.

With an internal heat exchanger, Figure 1.24.b, the cooling capacity increases due to sub-cooling and the compression input power increases due to the higher suction temperature. Thus combining those two effects produces net thermodynamic benefits for some refrigerants such as R-134a, CO_2 and penalties for others such as R-22, according to the shape of the saturation liquid-vapor line and the isentropic line [NAV 05].

The influences of the internal heat exchange on the overall efficiency of the system depend on the working fluids and the operating conditions.

For CO_2, the benefits are substantial because the COP optimized discharge pressure is lower when an internal heat exchanger is installed.

Referring to Figure 1.24.b, the efficiency of an internal heat exchanger is defined by:

$$\eta_{IHX} = \frac{h_1 - h_2}{\min(h(P_5, T_1) - h_4; h_1 - h(P_2, T_4))} \qquad \text{Eq. 1.36}$$

Increasing the IHX efficiency involves an increase of the heat exchange surfaces, which requires an increase of the length and the number of internal fins. As the temperature difference Δt between the flows decreases, the heat transfer coefficients should be increased to provide a high heat transfer. Using Eq. 1.36, Figure 1.27 is drawn. As the IHX efficiency increases, the cycle performance is enhanced of 6% at 0°C evaporation temperature and - 35°C gas cooler outlet temperature (compression efficiency = 1).

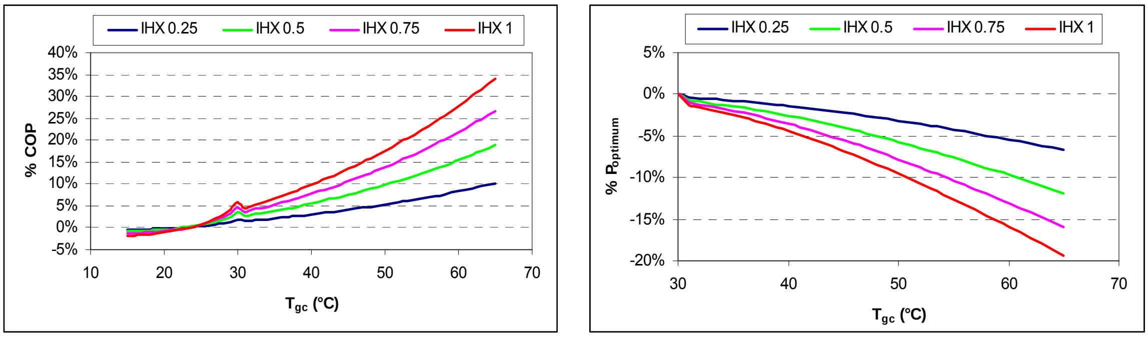

a. η_{comp} = 1, T_{evap} = 0°C, SC = 0 K, SH = 5 K, b. η_{comp} = 1, T_{evap} = 0°C, SC = 0 K, SH = 5 K,

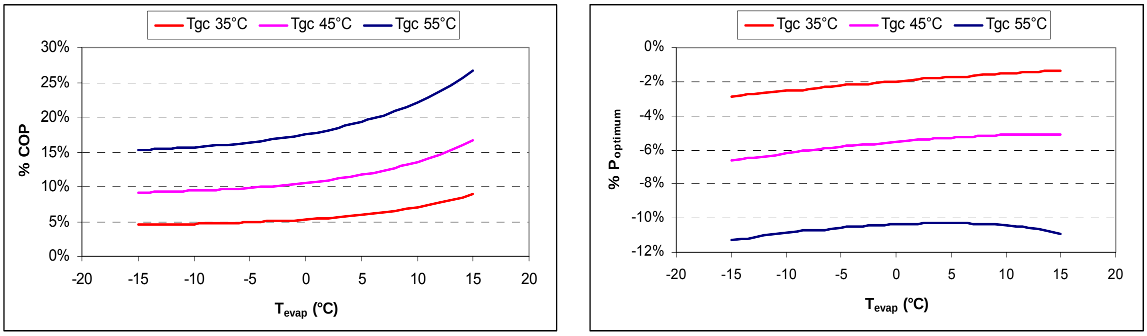

c. η_{comp} = 1, η_{IHX} = 0.75, SC = 0 K, SH = 5 K, d. η_{comp} = 1, η_{IHX} = 0.75, SC = 0 K, SH = 5 K,

Figure 1.27: Performance improvement of the conventional refrigeration cycle with IHX.

For an evaporation temperature of 0°C, Figure 1.27.a shows that for T_{gc} below 25°C, the IHX decreases the performance of the cycle. Therefore for T_{gc} higher than 25°C, the energy performance improvement increases with T_{gc} and IHX efficiency, it reaches more than 25% for T_{gc} higher than 60°C and IHX efficiency higher than 0.75.

Figure 1.27.b shows that the energy efficiency improvement is due to the decrease of the optimum high pressure that decreases with the increase of T_{gc} and IHX efficiency.

Around the critical point 31°C, there is a high variation of performances due to the change of CO_2 thermo-physical properties.

1.4.2 Work generating expansion

Another approach to enhanced refrigeration cycle efficiency, is to extract and make use of the expansion work potentially available from the process. There is a considerable potential for COP improvement by the introduction of an expander due to the high throttling loss of CO_2 cycle.

Positive-displacement devices, specifically internal and external gear pumps, scroll and screw machines are theoretically more desirable because of the edge losses inherent in small axial turbines and pistons. Research has focused on finding an instantaneous use for the highly variable work output, because of the losses associated with electric generators and motors.

Most available isentropic expanders use the generated work as a secondary compression stage, but the key of the enhancement is the control of the optimum COP of the cycle that will depend of the high-side pressure.

In this section, the expander is assumed to be mounted on the same axis as the compressor, so as the expander assists the compressor.

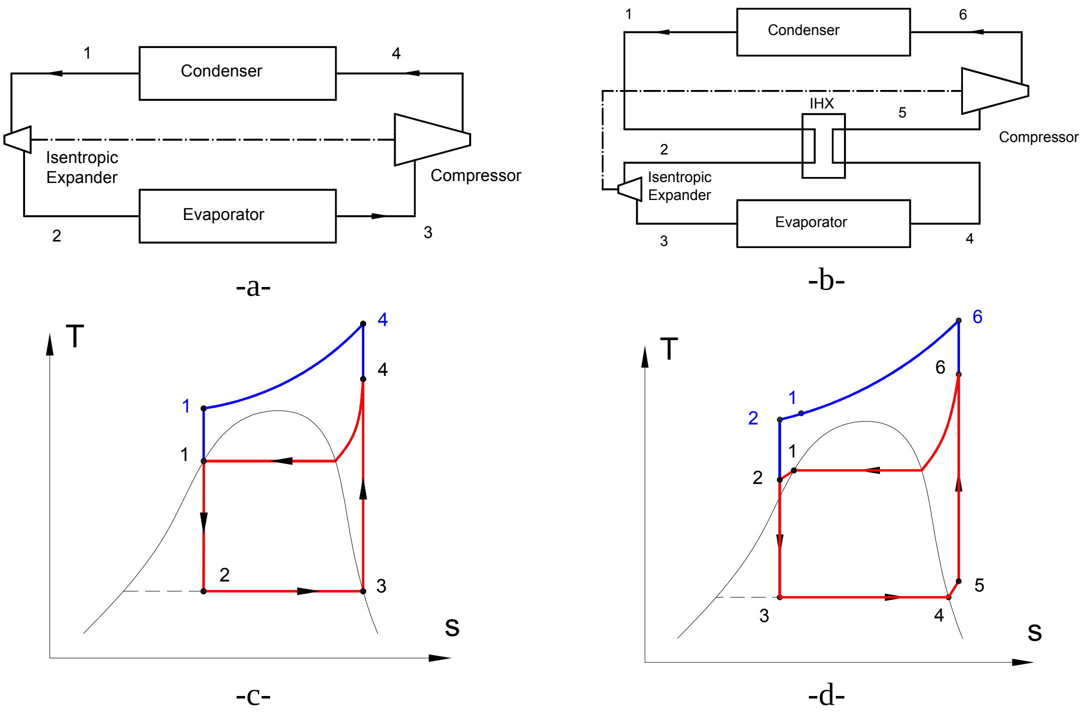

Figure 1.28: Isentropic expansion refrigeration cycle with and without IHX.

Referring to Figure 1.28.a, the efficiency of the expander is:

$$\eta_{expander}=\frac{h_1-h_2}{h_1-h_{2,is}}$$ Eq. 1.37

Using Eq. 1.37, Figure 1.29 is drawn.

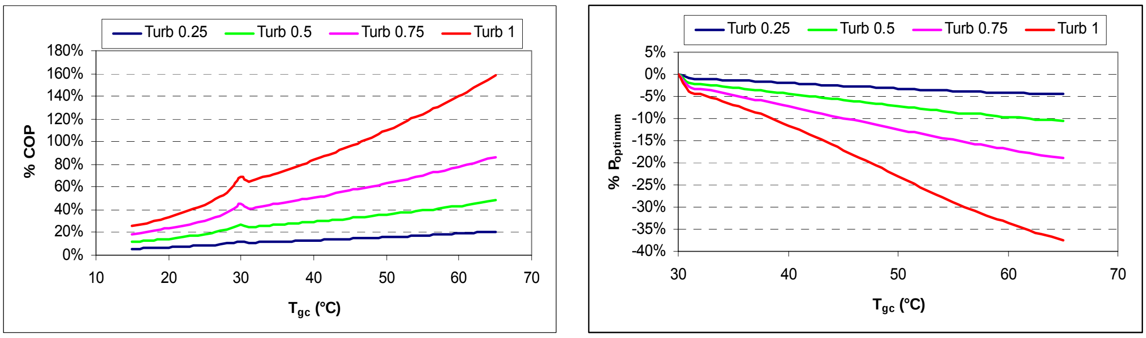

a. T_{evap} = 0°C, η_{comp} = 1, SH = 5 K, SC = 0 K b. T_{evap} = 0°C, η_{comp} = 1, SH = 5 K, SC = 0 K

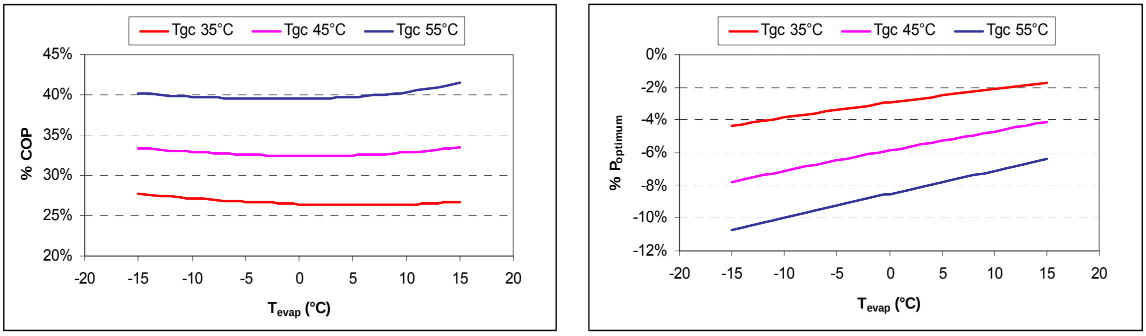

c.η_{turb} = 0.5, η_{comp} = 1, SH = 5 K, SC = 0 K d.η_{turb} = 0.5, η_{comp} = 1, SH = 5 K, SC = 0 K

Figure 1.29: Isentropic expansion with work recovery.

Considering an isentropic expansion with work recovery, for an evaporation temperature of 0°C, Figure 1.29.a shows that the isentropic expansion improves significantly the cycle performance, specially for transcritical cycles, the COP may reach more than 60% enhancement (for T_{gc} = 50°C and $\eta_{expander}$= 0.75) , compared to the conventional refrigeration cycle. Around the critical point (31°C), there is a strong increase of performances due to the change of the CO_2 thermodynamic properties. The increase of expansion efficiency increases also highly the COP.

Compared to the optimal high pressure of the conventional cycle, Figure 1.29.b shows that the improvement is due to the decrease of the optimum high pressure that decreases with the increase of T_{gc} and of the expander efficiency.

By fixing the gas cooler outlet temperature T_{gc} and the expansion efficiency $\eta_{expander}$, the variation of evaporation temperature T_{evap} shows that the improvement due the isentropic expander is quasi-constant as T_{evap} increases, thereby the optimum pressure increases as T_{evap} increases. Thus, the added compression work due to the decrease of evaporation temperature is recovered by the added generated work by the expander due to lower pressure.

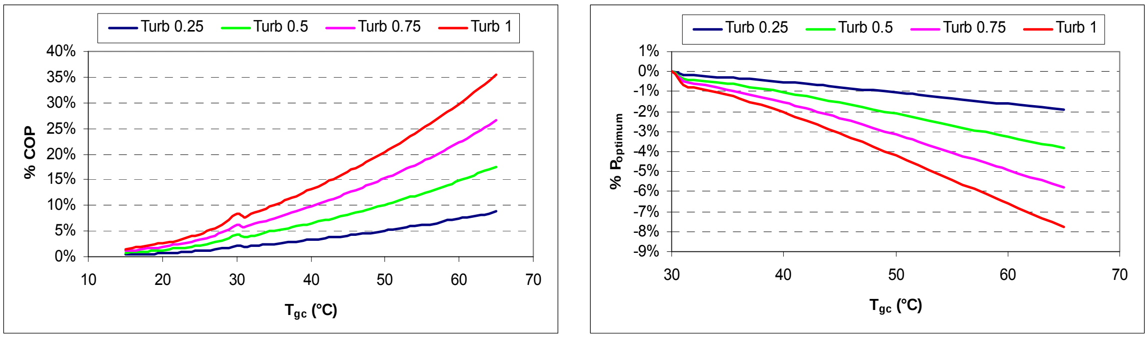

a. T_{evap} = 0°C, η_{comp} = 1, SH = 5 K, SC = 0 K b. T_{evap} = 0°C, η_{comp} = 1, SH = 5 K, SC = 0 K

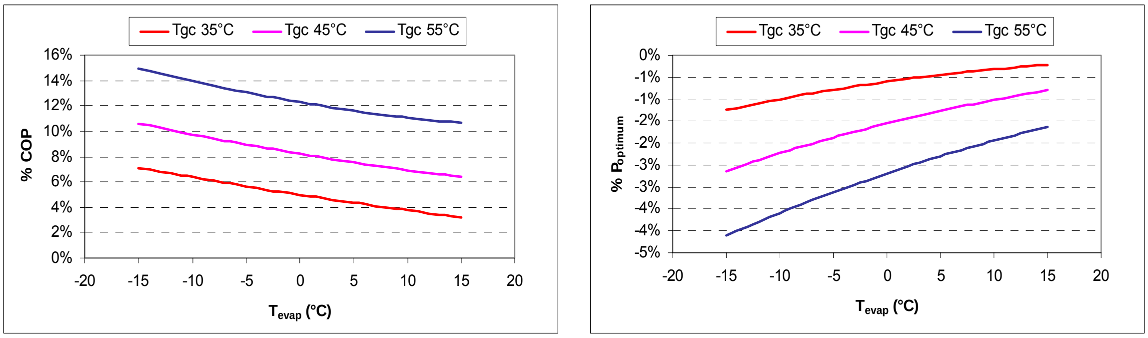

ç.η_{turb} = 0.5, η_{comp} = 1, SH = 5 K, SC = 0 K ḍ.η_{turb} = 0.5, η_{comp} = 1, SH = 5 K, SC = 0 K

Figure 1.30: Isentropic expansion without work recovery.

Considering an isentropic expansion without work recovery, for 0°C evaporation temperature, Figure 1.30.a shows that the isentropic expansion improves the cycle performance, but this improvement is lower than the one of isentropic expansion with work recovery. The improvement is higher for transcritical cycle, than for sub-critical cycle; the cycle COP reaches more than 15% improvement for T_{gc} = 50°C and $\eta_{expander}$ = 0.75, compared to the conventional refrigeration cycle. The COP improvement increases continuously with T_{gc} and $\eta_{expander}$, and shows small irregularity around the critical point 31°C.

Figure 1.30.b shows that the improvement is due to the decrease of the optimum high pressure that decreases with the increase of T_{gc} and of the expander efficiency.

By fixing the gas cooler outlet temperature T_{gc} and the expansion efficiency $\eta_{expander}$, the variation of evaporation temperature T_{evap} shows that the enhancement due the isentropic expander, without work recovery, decreases as T_{evap} increases, thereby the optimum pressure percentage increases as T_{evap} increases.

Thus, the added evaporator capacity by the expander, improves the COP of the cycle.

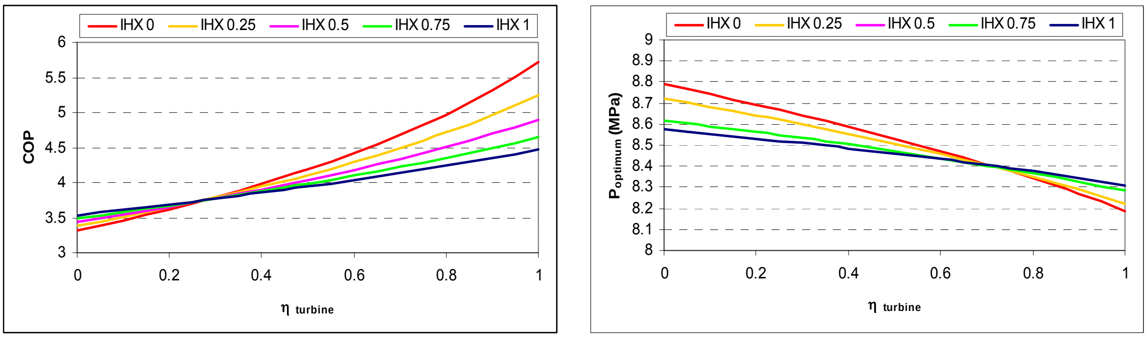

a. T_{evap} = 0°C, T_{gc} = 35°C, η_{comp} = 1, SH = 5 K, SC = 0 K. The inflection point of COP is between 0.27 and 0.28 as $\eta_{expander}$.

b. T_{evap} = 0°C, T_{gc} = 35°C, η_{comp} = 1, SH = 5 K, SC = 0 K. The inflection point of the optimum pressure is between 0.65 and 0.75 as $\eta_{expander}$.

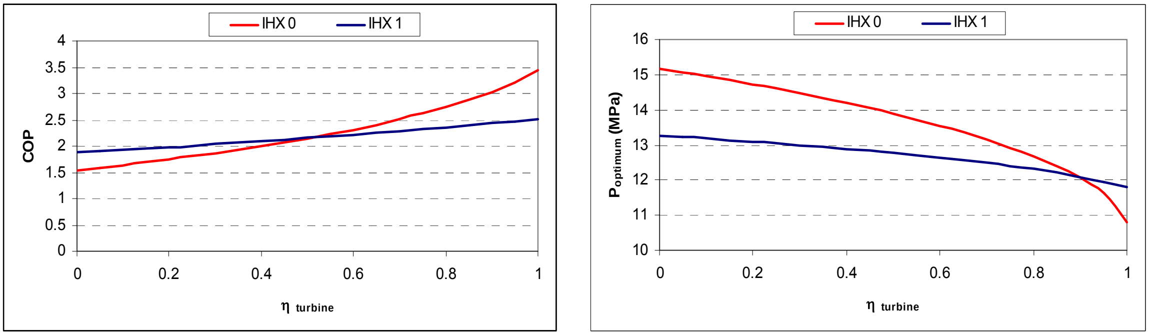

c. T_{evap} = 0°C, T_{gc}°C = 55°C, η_{comp} = 1, SH = 5 K, SC = 0 K. The inflection point of COP is between 0.5 and 0.52 as $\eta_{expander}$.

d. T_{evap} = 0°C, T_{gc}°C = 55°C, η_{comp} = 1, SH = 5 K, SC = 0 K. The inflection point of the optimum pressure is between 0.87 and 0.93 as $\eta_{expander}$.

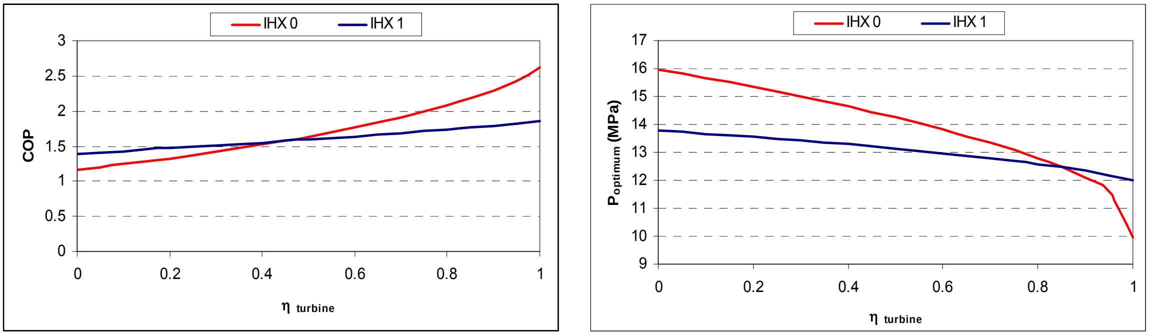

e. T_{evap} = -15°C, T_{gc}°C = 55°C,η_{comp} = 1, SH = 5 K, SC = 0 K. The inflection point of COP is between 0.44 and 0.45 as $\eta_{expander}$.

f. T_{evap} = -15°C, T_{gc}°C = 55°C, η_{comp} = 1, SH = 5 K, SC = 0 K. The inflection point of the optimum pressure is between 0.82 and 0.88 as $\eta_{expander}$.

Figure 1.31: Combining effect of IHX and isentropic expansion with work recovery.

The recovery of expansion work involves thermodynamic tradeoffs with internal heat exchanger. In fact the expansion improvements have to be studied including the internal heat exchanger. Those two options are competing for COP improvements.

A detailed parametric analysis shows that internal heat exchange could increase the cycle COP if the expander efficiency is lower than 30%, but would substantially decrease COP if the expander isentropic efficiency is higher as shown in Figure 1.31.

Considering an isentropic expansion with work recovery and an internal heat exchanger IHX, evaporation temperature at 0°C and gas cooler outlet temperature T_{gc} at 35°C, Figure 1.31.a shows that the IHX with isentropic expansion, with work recovery, improves the cycle performance only if the expansion efficiency is lower than 0.28, whatever the IHX efficiency the improvement is small.

On the other side, the optimum pressure presents an inflection point between 0.65 and 0.75 expansion efficiency. For expansion efficiency lower than 0.65, the IHX decreases the optimum pressure, and for expansion efficiency higher than 0.75, the IHX increases the optimum pressure.

For other operating parameters, T_{ev} = 0°C and T_{gc} = 55°C, the inflection point for COP and $P_{optimum}$ is around 0.5 and 0.9 expansion efficiency, as shown in Figures 131.c and d.

By decreasing the evaporation temperature, the inflection point for COP and $P_{optimum}$ is around 0.45 and 0.85 expansion efficiency, as shown in Figures 131.e and f. So the inflection points of COP and $P_{optimum}$ depend on the temperature operating temperature.

Therefore, the isentropic expansion brings improvement to the conventional refrigeration cycle. The expansion with work recovery shows higher improvements than the expansion without work recovery, while an IHX penalizes the performance of the cycle with isentropic expansion as shown in Figure 1.32. The performance loss due to the IHX can reach more than 20% as shown in Figure 1.32.c.

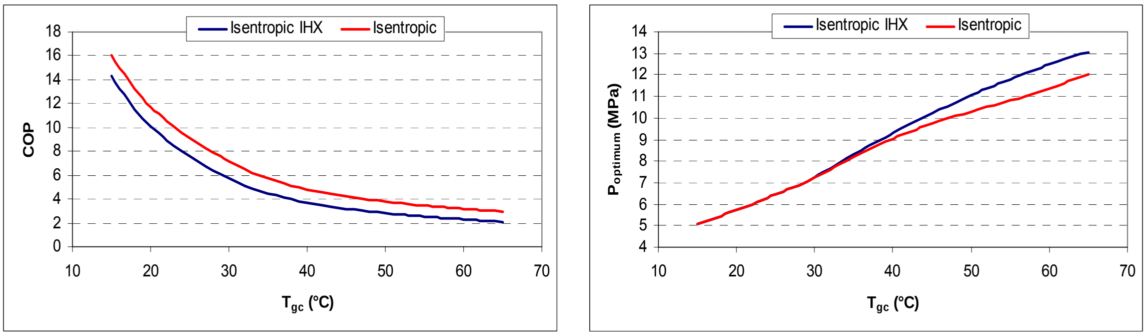

a. COP variation with T_{gc}

b. Optimum pressure variation with T_{gc}

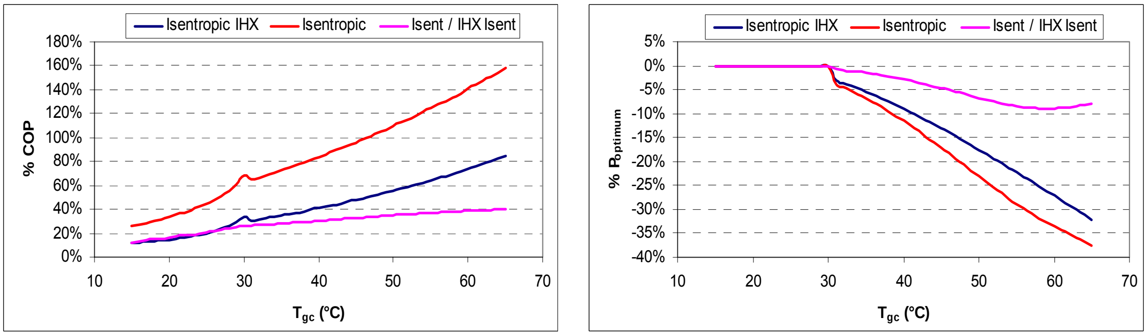

c. COP enhancement variation with T_{gc}

b. Optimum pressure enhancement variation with T_{gc}

Figure 1.32: Comparison of refrigeration conventional cycle performance improvement with isentropic expansion (IHX. $\eta_{IHX} = 1$, $\eta_{expander} = 1$, T_{ev} = 0°C,$\eta_{comp} = 1$, SC = 0 K, SH = 5 K).

1.4.3 Staging of compression phase

The performance deterioration of the basic single-stage cycle can be largely mitigated by using multi-stage compression and with inter-cooling of liquid and vapor refrigerant. Installing intermediate heat exchangers may enhance the two-stage cycle by decreasing the gas cooler inlet temperature that decreases the irreversibility of the gas cooler. Many configurations of two-stage compression refrigeration cycles exist:

- Two-stage compression in series with intercooler between the stages TSCSI.
- Two-stage compression with injection between the stages as integrated cascade TSCI.
- Two-stage compression with economizer TSCE.

a. Two-stage compression in series with intercooler between the stages TSCSI

The TSCSI, shown in Figures 1.33 (a and b), is composed of: an evaporator, a low-pressure compressor, an intercooler, a high-pressure compressor, a gas cooler, and a throttling device (valve or turbine). An internal heat exchanger could be installed as shown in Figures 1.33 (c and d) between the suction line of the low-pressure compressor and the gas cooler outlet line.

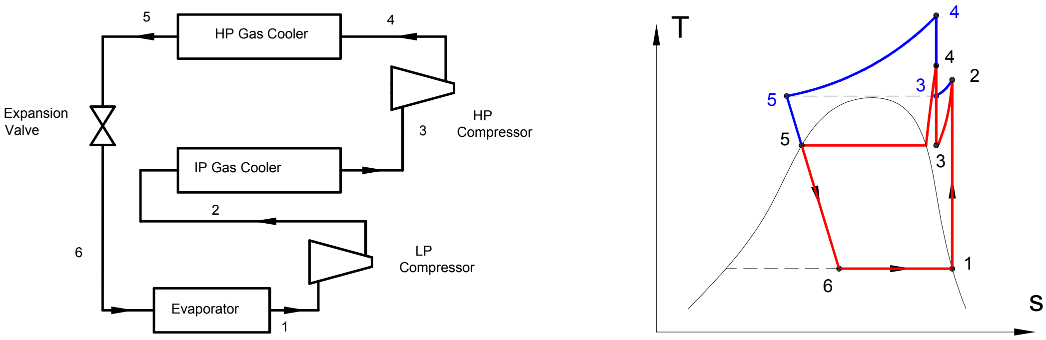

a. Two stage compression in series with isenthalpic expansion

b. T-S diagram of TSCSI with isenthalpic expansion

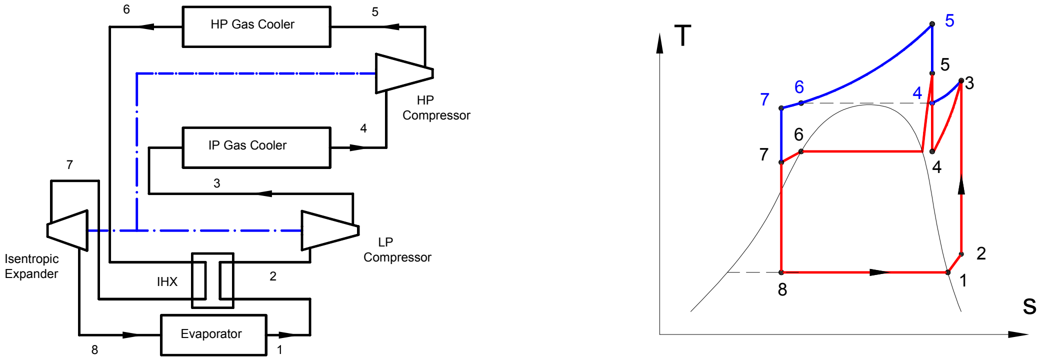

c. TSCSI with IHX and isentropic expansion

d. T-S diagram of TSCSI with IHX and isentropic expansion

Figure 1.33: Two-stage compression cycle in series with intercooler.

b. Two-stage compression with injection between the stages as integrated cascade TSCI.

The two-stage compression cycle with indirect injection TSCII, shown in Figures 1.34 (a and b),or direct injection TSCDI shown in Figures 1.34 (c and d), is composed of: an evaporator, a low-pressure compressor, a diphase separator, a high-pressure compressor, a gas cooler, and a throttling device (valve or turbine). An internal heat exchanger could be installed between the suction line of the high-pressure compressor and the gas cooler outlet line, and between the suction line of the low-pressure compressor and the separator liquid outlet line. The inlet of the high-pressure compressor is saturated vapor for TSCII and superheated vapor for TSCDI.

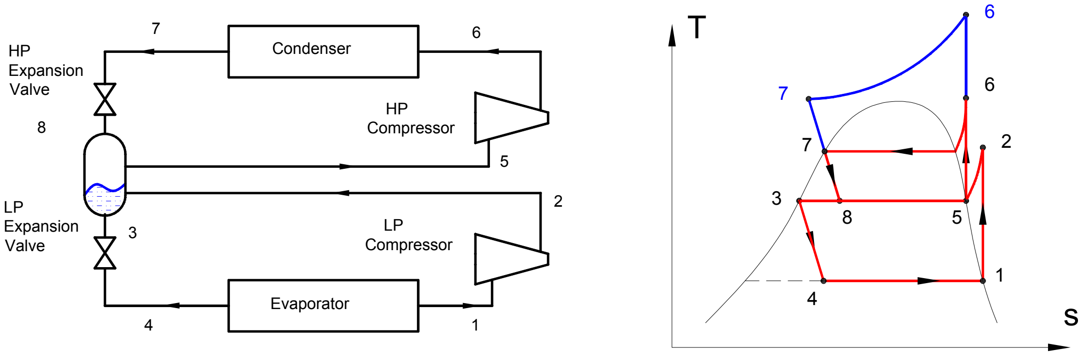

a. TSCII b. T-S diagram of TSCII

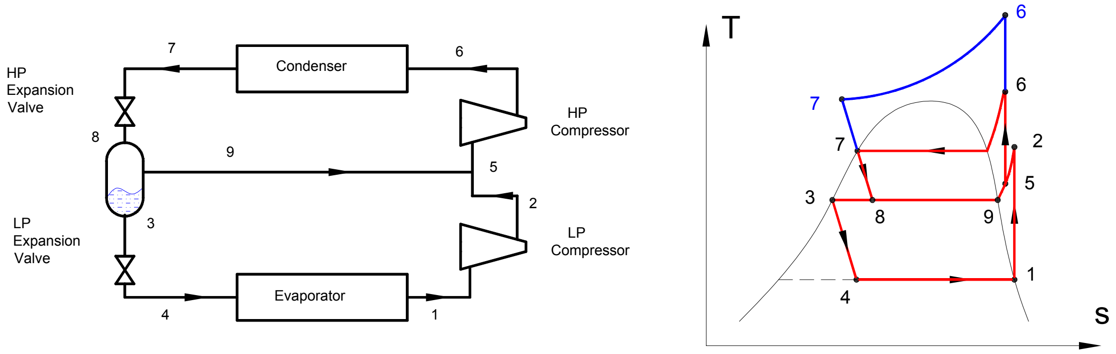

c. TSCDI d. T-S diagram of TSCDI

Figure 1.34: Two-stage compression cycle with injection.

c. Two-stage compression with economizer TSCE

The two-stage compression cycle with economizer, shown in Figure 1.35, is composed of: an evaporator, a low-pressure compressor, a two-phase separator, a high-pressure compressor, two gas coolers, and a throttling device (valve or turbine). An internal heat exchanger could be installed between the suction line of the high-pressure compressor and the gas cooler outlet line, and between the suction line of the low-pressure compressor and the separator liquid outlet line or the gas cooler outlet line. The inlet of the compressor is saturated vapor coming from the separator or the evaporator. The separator outlets are saturated liquid and saturated vapor.

Since there are two gas coolers, in transcritical refrigeration cycle, there are two possibilities to connect them to the separator: even considering a common high-pressure side for the two compressors, or considering each gas cooler separated from the other and then each gas cooler has its high pressure. Calculations show that for the two options, the same refrigeration performances are achieved but at different high pressures. In this study, the outlet of the gas coolers is connected to the two compressors under the same high pressure.

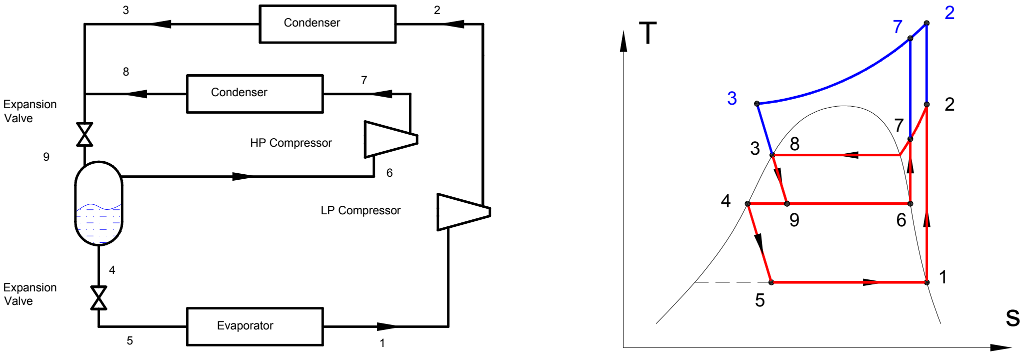

a. TSCE cycle b. T-S diagram of TSCE

Figure 1.35: Two-stage refrigeration compression cycle with economizer TSCE.

Another refrigeration cycle with economizer could be used to improve the performance of the conventional cycle. Two compressors, a gas cooler, an evaporator, an internal heat exchanger, and a throttling device compose this system, shown in Figure 1.56. The IHX efficiency is considered as the ratio between the temperature difference of the high-side pressure and its maximal value.

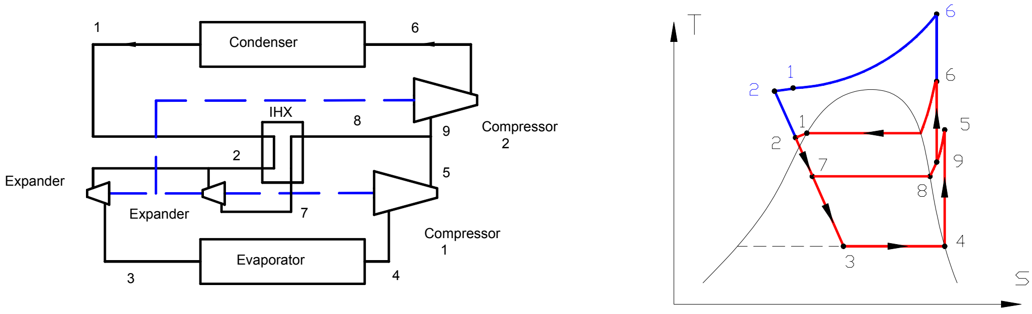

a. Second TSCE with isentropic expansion

b. T-S diagram of the second TSCE with isentropic expansion

Figure 1.36: Second economizer refrigeration cycle.

d. Cooling of the compressor

Since the high discharge compressor temperature increases the exergy numbers of the gas cooler and of the compressor, by limiting this temperature, the performance of the cycle is improved. To limit the discharge temperature of the compressor, an external cold source could be used to absorb the energy generated by the compression work. Therefore, the compression is made in two stages: the poly-tropic compression from the evaporator pressure to an intermediate pressure, and the “isothermal” compression from the intermediate pressure to the high pressure. The intermediate temperature varies between the gas cooler outlet temperature and the conventional compressor discharge temperature with poly-tropic compression. In this study, two intermediate temperatures are considered: the gas cooler outlet temperature and the gas cooler outlet temperature plus 15 K.

In the poly-tropic compression stage, the work is calculated similarly to the conventional cycle; or in the isothermal compression, the work is calculated by:

$$w_{isothermal} = \int_{P_{\text{int}}}^{P_{gc}} v dP = \sum_{i=1}^{100} \frac{2}{\frac{1}{v_i} + \frac{1}{v_{i-1}}} \Delta P$$

$$\Delta P = \frac{(P_{gc} - P_{\text{int}})}{100}$$

$$v_i = f(T_{\text{int}}, P_{\text{int}} + i\,\Delta P)$$

The compression cycle with compressor cooling CC, shown in Figure 1.37, is composed of: an evaporator, a cooled-compressor, a gas cooler, and a throttling device (valve or turbine). An internal heat exchanger could be installed between the suction line of the compressor and the gas cooler outlet line.

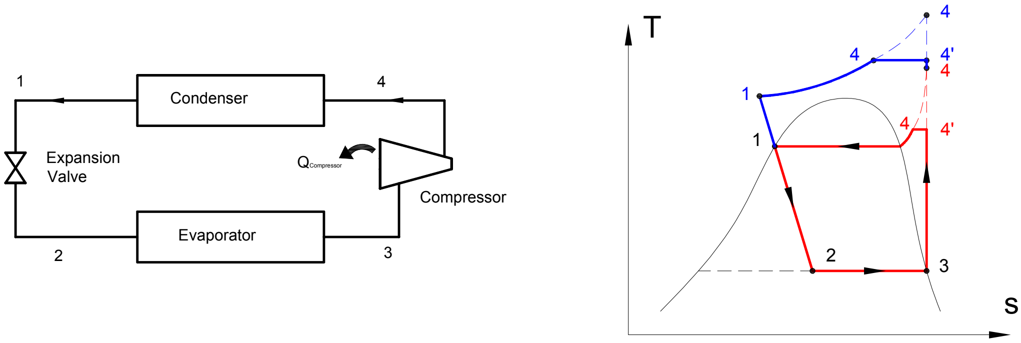

a. RCC scheme b. T-S diagram of RCC

Figure 1.37: Refrigeration compression cycle with compressor cooling CC.

The operating performances at different T_{gc} and T_{ev} of each two-stage compression cycles are presented in Annex 1.

1.5 Comparison of cycles

For air-conditioning systems, the heat source temperature (evaporation temperature) is around 0°C and the heat sink temperature (condensation temperature) varies between 15°C in winter and more than 50°C in summer. Using these operating conditions, the refrigeration cycles are compared.

The simulation conditions are as follows:
isenthalpic expansion, η_{comp} = 1, $\eta_{turbine}$ = 1, T_{SH} = 5 K, and η_{IHX} = 1, the COP improvement is calculated with an evaporating temperature of 0°C in Figures 1.38.a, 1.38.b and 1.38.c. In sub-critical operating conditions, the cycles are classified as follows with increasing COPs:

1- Simple cycle with IHX
2- Two-stage compression cycle with intercooler
3- Compression cycle with compressor cooling
4- Economizer cycle
5- Direct injection cycle
6- Indirect injection cycle.

In supercritical operating conditions, the COP improvements vary with Tgc and cannot be clearly classified, but the compression cycle with compressor cooling (CC) has the higher COP improvement, followed by the direct injection cycle. However the simple cycle with IHX becomes the most efficient at T_{gc} higher than 60°C.

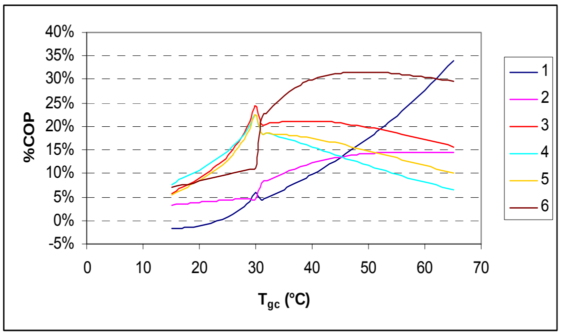

- a – Isenthalpic expansion

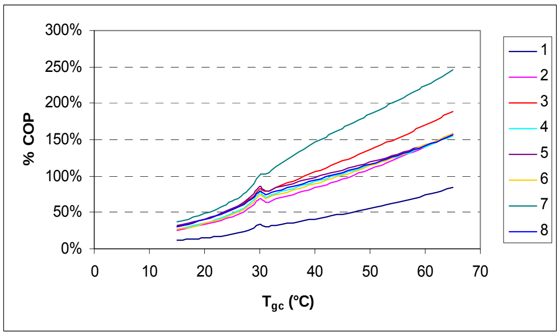

- d - Isentropic expansion

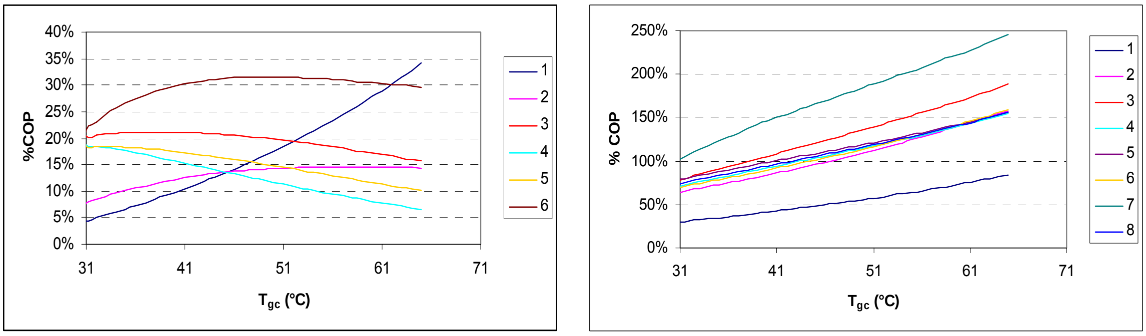

- b – Transcritical operating cycle with isenthalpic expansion

- e - Transcritical operating cycle with isentropic expansion

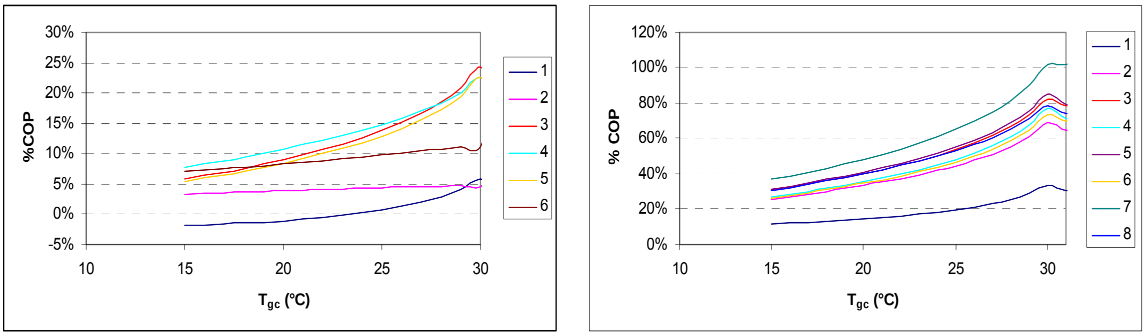

- c – Sub-critical operating cycle with isenthalpic expansion

- f – Sub-critical operating cycle with isentropic expansion

Figure 1.38: Comparison of COP enhancement for different modified refrigeration cycles.

Captions for isenthalpic expansion: Figure 1.38.a,b,c.	
1	Simple cycle with IHX
2	Two stage compression cycle with intercooler
3	Direct injection cycle
4	Indirect injection cycle
5	Economizer cycle
6	compression cycle with compressor cooling

Captions for isentropic expansion: Figures 1.38.d,e,f.	
1	Simple cycle with IHX and isentropic expansion
2	Simple cycle with isentropic expansion
3	Two stage compression cycle with intercooler and isentropic expansion
4	Direct injection cycle with isentropic expansion
5	Indirect injection cycle with isentropic expansion
6	Economizer cycle with isentropic expansion
7	compression cycle with compressor cooling and isentropic expansion
8	Two stage compression cycle with intercooler and isentropic expansion $W_{turb} = W_2$

For the modified refrigeration cycles with isentropic expansion, the COP improvement is drawn as a function of T_{gc}(at 0°C as evaporating temperature) in Figures 1.38.d, 1.38.e and 1.38.f. In sub-critical and transcritical operating conditions, the cycles are ranked based on improved COP:

1- Simple cycle with IHX and isentropic expansion
2- Simple cycle with isentropic expansion
3- Economizer cycle with isentropic expansion
4- Direct injection cycle with isentropic expansion

5- Two-stage compression cycle with intercooler and isentropic expansion $W_{turb} = W_2$
6- Indirect injection with isentropic expansion
7- Two-stage compression cycle with intercooler and isentropic expansion
8- Compression cycle with compressor cooling and isentropic expansion (ΔT = 0 K).

The COP increases from 10% at 15°C up to 250% at 65°C.

Table 1.4: Cycle classification based on COP improvement.

CO_2 Refrigeration Cycle	Average COP (15 - 65°C)	% Average COP
Conventional Cycle	3.943	0.00
Simple Cycle with IHX	4.143	5.08
Two-stage compression cycle with Intercooler	4.221	7.04
Economizer Cycle	4.428	12.30
Indirect Injection Cycle	4.448	12.81
Direct Injection Cycle	4.505	14.25
Refrigeration compression cycle with compressor cooling	4.583	16.24
Simple Cycle with IHX and isentropic expansion	5.073	28.66
Simple Cycle with isentropic expansion	6.294	59.63
Economizer Cycle with isentropic expansion	6.403	62.40
Direct Injection Cycle with isentropic expansion	6.450	63.58
Two-stage compression cycle with Intercooler with isentropic expansion Wt = W2	6.587	67.06
Indirect Injection Cycle with isentropic expansion	6.672	69.23
Two-stage compression cycle with Intercooler with isentropic expansion	6.820	72.96
Compression cycle with compressor cooling and isentropic expansion	7.666	94.42

The average is calculated on COP and %COP for a T_{gc} step ΔT_{gc} = 1 K, from 15°C to 65°C for total average, from 15 to 30°C for sub-critical average and from 31 to 65°C for transcritical one: $COP_{average} = \frac{1}{m-n+1}\sum_{i=n}^{m} COP_i$; $\%COP_{average} = \frac{1}{m-n+1}\sum_{i=n}^{m} \%COP_i$

With, for total average: n = 15 and m = 65; for sub-critical average: n = 15 and m =30; and for transcritical average: n= 31 and m = 65.

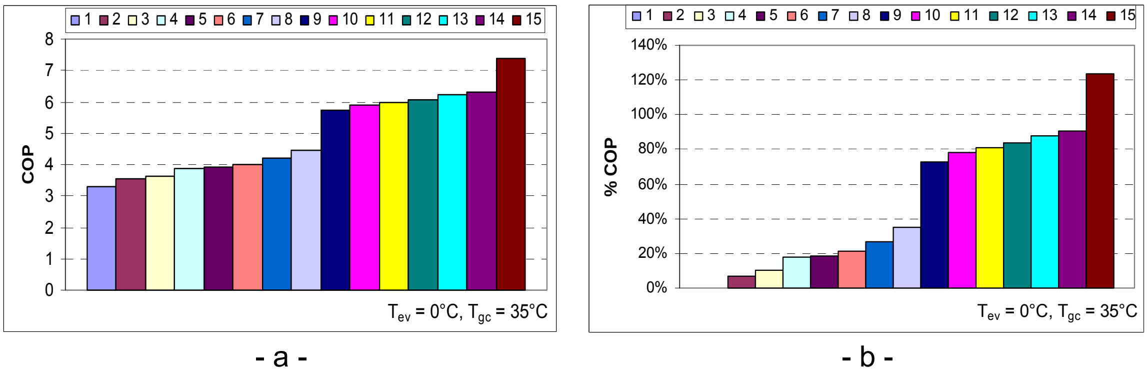

- a - - b -

Figure 1.39: Comparison of the 15 different refrigeration cycles with T_{ev} at 0°C and T_{gc} at 35°C in transcritical operation.

Table 1.5: Cycle classification based on COP improvement.

CO_2 Refrigeration Cycle in Sub-critical operation	Average Sub-critical COP (15-30°C)	% Average Sub-critical COP
Simple Cycle with IHX	7.829	-0.21
Conventional Cycle	7.846	0.00
Two-stage compression cycle with Intercooler	8.153	3.91
Refrigeration compression cycle with compressor cooling	8.525	8.65
Economizer Cycle	8.636	10.07
Direct Injection Cycle	8.694	10.80
Indirect Injection Cycle	8.795	12.10
Simple Cycle with IHX and isentropic expansion	9.170	16.88
Simple Cycle with isentropic expansion	10.788	37.49
Economizer Cycle with isentropic expansion	10.918	39.15
Direct Injection Cycle with isentropic expansion	11.007	40.29
Two-stage compression cycle with Intercooler with isentropic expansion Wt = W2	11.350	44.66
Two-stage compression cycle with Intercooler with isentropic expansion	11.386	45.12
Indirect Injection Cycle with isentropic expansion	11.465	46.13
Compression cycle with compressor cooling and isentropic expansion	12.122	54.49

Table 1.6: Transcritical Cycle Classification based on COP improvement.

CO_2 Refrigeration Cycle in Transcritical operation	Average supercritical COP (31-65°C)	% Average supercritical COP
Conventional Cycle	2.159	0.00
Two-stage compression cycle with Intercooler	2.423	12.25
Simple Cycle with IHX	2.458	13.88
Indirect Injection Cycle	2.461	14.00
Economizer Cycle	2.504	16.01
Direct Injection Cycle	2.590	19.97
Refrigeration compression cycle with compressor cooling	2.781	28.85
Simple Cycle with IHX and isentropic expansion	3.200	48.25
Simple Cycle with isentropic expansion	4.240	96.40
Economizer Cycle with isentropic expansion	4.339	101.02
Direct Injection Cycle with isentropic expansion	4.367	102.29
Two-stage compression cycle with Intercooler with isentropic expansion Wt = W2	4.410	104.30
Indirect Injection Cycle with isentropic expansion	4.481	107.60
Two-stage compression cycle with Intercooler with isentropic expansion	4.732	119.23
Compression cycle with compressor cooling and isentropic expansion	5.629	160.77

Table 1.7: Refrigeration cycle comparison at T_{ev} = 0°C, T_{gc} = 35°C, $\eta_{comp} = 1$, $\eta_{turb} = 1$, $\eta_{IHX} = 1$.

Cycle type	Nb.	COP	%COP
Conventional cycle	1	3.313	0.00
Simple cycle with IHX	2	3.533	6.64
Two-stage compression cycle with intercooler	3	3.647	10.10
Indirect injection cycle	4	3.895	17.58
Economizer cycle	5	3.919	18.29
Direct injection cycle	6	4.009	21.00
Refrigeration compression cycle with compressor cooling	7	4.194	26.60
Simple cycle with IHX and isentropic expansion	8	4.465	34.78
Simple cycle with isentropic expansion	9	5.717	72.56
Economizer cycle with isentropic expansion	10	5.906	78.26
Direct injection cycle with isentropic expansion	11	5.985	80.66
Two-stage compression cycle with intercooler and isentropic expansion and $W_{turb} = W_{HP\ compressor}$	12	6.080	83.52
Indirect injection cycle with isentropic expansion	13	6.229	88.01
Two-stage compression cycle with intercooler and isentropic expansion	14	6.311	90.50
Compression cycle with compressor cooling and isentropic expansion	15	7.399	123.32

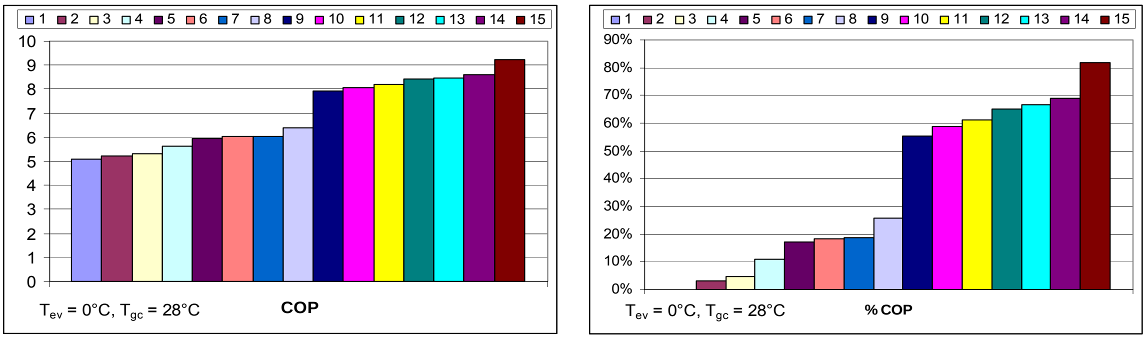

-a- -b-

Figure 1.40: Comparison of the 15 different refrigeration cycles T_{ev} at 0°C and T_{gc} at 28°C in sub-critical operation.

The caption of Figure 1.39, respectively 1.40, is the number column of Table 1.7, respectively 1.8.

Considering ideal compression efficiency, ideal expansion efficiency, and ideal internal heat exchanger efficiency, different refrigeration cycles have been compared at two different operating parameters: sub-critical operation at 28°C as T_{gc} and 0°C as T_{ev}, and transcritical operation at 35°C as T_{gc} and 0°C as T_{ev}.

In sub-critical operation, with isenthalpic expansion, the 2-stages indirect and direct injection cycles present the best performances, but with isentropic expansion, the compression cycle with compressor cooling is the best followed by the indirect injection cycle.

In transcritical operation, with isenthalpic expansion, the compression cycle with compressor cooling presents the best performance preceded by the direct injection cycle, but with isentropic expansion, the compression cycle with compressor cooling is the best preceded by the two-stage compression cycle with intercooler that is preceded by the indirect injection cycle.

Table 1.8: Refrigeration cycle comparison at T_{ev} = 0°C, T_{gc} = 28°C, η_{comp} = 1, η_{turb} = 1, η_{IHX} = 1.

Cycle type	Nb.	COP	%COP
Conventional cycle	1	5.086	0.00
Simple cycle with IHX	2	5.236	2.95
Two-stage compression cycle with intercooler	3	5.322	4.62
Refrigeration compression cycle with compressor cooling	4	5.633	10.74
Economizer cycle	5	5.960	17.18
Indirect injection cycle	6	6.023	18.40
Direct injection cycle	7	6.029	18.53
Simple cycle with IHX and isentropic expansion	8	6.399	25.81
Simple cycle with isentropic expansion	9	7.910	55.51
Economizer cycle with isentropic expansion	10	8.077	58.79
Direct injection cycle with isentropic expansion	11	8.191	61.04
Two-stage compression cycle with intercooler and isentropic expansion $W_{turb} = W_2$	12	8.405	65.24
Two-stage compression cycle with intercooler and isentropic expansion	13	8.481	66.74
Indirect injection cycle with isentropic expansion	14	8.585	68.79
Compression cycle with compressor cooling and isentropic expansion	15	9.242	81.69

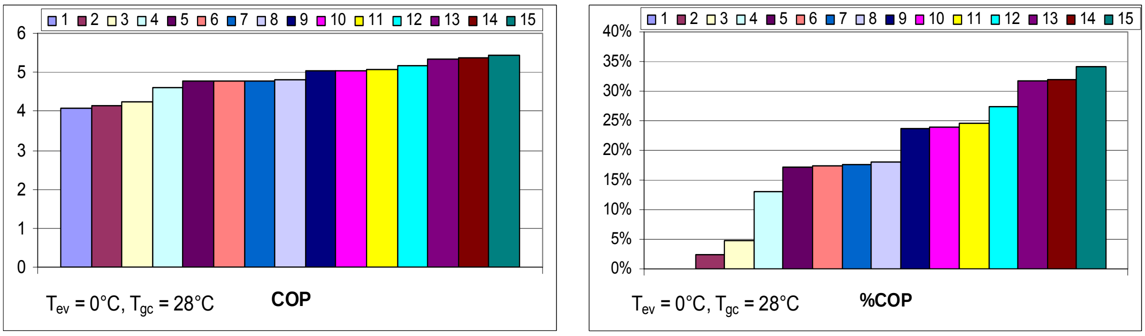

-a- -b-

Figure 1.41: Comparison of the 15 different refrigeration cycles in sub-critical operation: T_{ev} = 0°C, T_{gc} = 28°C, η_{comp} = 0.8, η_{turb} = 0.5, η_{IHX} = 0.7.

The caption of Figure 1.41, respectively 1.42, is the number column of Table 1.9, respectively 1.10.

By considering typical component efficiencies: $\eta_{compressor}$ = 0.8; $\eta_{expander}$ = 0.5; η_{IHX} = 0.7; CO_2 cycles have been compared at 28°C and 35°C for T_{gc} and 0°Cfor T_{ev}.

In sub-critical operation, with isenthalpic expansion, the compression cycle with compressor cooling presents the best performance preceded by the indirect and direct injection cycles, but with isentropic expansion, the indirect injection cycle is the best preceded by the direct injection cycle.

In transcritical operation, with isenthalpic expansion, the compression cycle with compressor cooling presents the best performance preceded by the direct injection cycle, also with isentropic expansion, the compression cycle with compressor cooling and isentropic expansion is the best preceded by the direct injection cycle with isentropic expansion.

Table 1.9: Refrigeration cycle comparison at $T_{ev} = 0°C$, $T_{gc} = 28°C$, $\eta_{comp} = 0.8$, $\eta_{turb} = 0.5$, $\eta_{IHX} = 0.7$.

Cycle type	Nb.	COP	%COP
Conventional cycle	1	4.066	0.00
Simple cycle with IHX	2	4.160	2.31
Two-stage compression cycle with intercooler	3	4.257	4.71
Simple cycle with IHX and isentropic expansion	4	4.595	13.02
Economizer cycle	5	4.768	17.28
Indirect injection cycle	6	4.775	17.43
Direct injection cycle	7	4.780	17.56
Simple cycle with isentropic expansion	8	4.802	18.11
Isothermal compression cycle	9	5.034	23.80
Two-stage compression cycle with intercooler and isentropic expansion $W_{turb} = W_2$	10	5.039	23.93
Two-stage compression cycle with intercooler and isentropic expansion	11	5.066	24.59
Isothermal compression cycle with isentropic expansion	12	5.177	27.33
Economizer cycle with isentropic expansion	13	5.353	31.66
Direct injection cycle with isentropic expansion	14	5.362	31.88
Indirect injection cycle with isentropic expansion	15	5.452	34.10

On the other hand, the compression cycle with compressor cooling is not used yet, so the indirect injection cycle with isentropic expansion presents the best performance for CO_2 refrigeration cycle.

The available isentropic expanders are formed by moving parts: reciprocating machine (pistons) or rotating machines (scroll, screw, impulse turbine, axial turbine). Since the CO_2 transcritical cycle requires high control of the high-pressure side to reach the best COP, the ejector refrigeration cycle, which is similar to the indirect injection refrigeration cycle and will be studied in ***Chapter 2***, seems to be a promising CO_2 refrigeration cycle.

Table 1.10: Refrigeration Cycles comparison at
$T_{ev} = 0°C$, $T_{gc} = 35°C$, $\eta_{comp} = 0.8$, $\eta_{turb} = 0.5$, $\eta_{IHX} = 0.7$.

Cycle type	Nb.	COP	%COP
Conventional cycle	1	2.649	0.00
Simple cycle with IHX	2	2.781	4.99
Two-stage compression cycle with intercooler	3	2.918	10.16
Indirect injection cycle	4	3.076	16.10
Simple cycle with IHX and isentropic expansion	5	3.119	17.76
Economizer cycle	6	3.135	18.35
Direct injection cycle	7	3.172	19.73
Simple cycle with isentropic expansion	8	3.215	21.37
Two-stage compression cycle with intercooler and isentropic expansion $W_{turb} = W_2$	9	3.494	31.91
Two-stage compression cycle with intercooler and isentropic expansion	10	3.519	32.83
Compression cycle with compressor cooling	11	3.594	35.67
Economizer cycle with isentropic expansion	12	3.642	37.48
Indirect injection cycle with isentropic expansion	13	3.670	38.53
Direct injection cycle with isentropic expansion	14	3.685	39.11
Compression cycle with compressor cooling and isentropic expansion	15	3.758	41.86

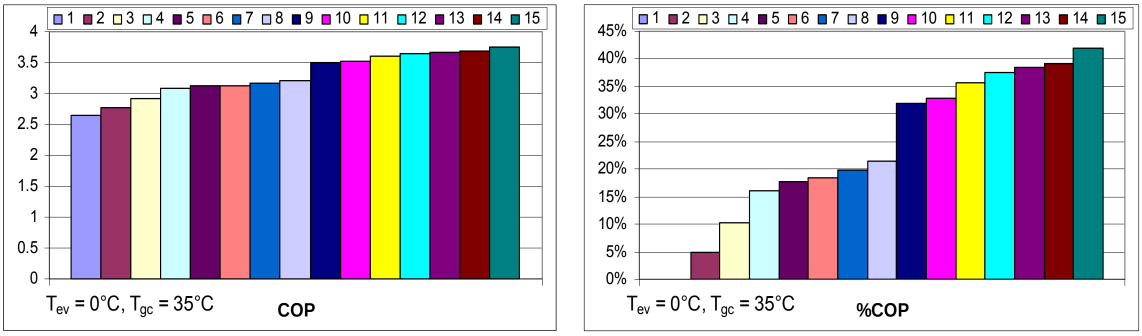

-a- -b-

Figure 1.42: Comparison of the 15 different refrigeration cycles in transcritical operation: T_{ev} = 0°C, T_{gc} = 35°C, η_{comp} = 0.8, η_{turb} = 0.5, η_{IHX} = 0.7.

1.6 Conclusions

In this chapter, the thermo-physical and thermodynamic properties of R-744 have been presented and compared to other refrigerants. The CO_2 transcritical refrigeration cycle was presented and, as already known, optimum COPs exist depending on high pressures and outdoor temperatures. A detailed exergy analysis of the CO_2 cycle has shown that the main energy losses in the conventional CO_2 refrigeration cycle are in the throttling operation and the high discharge temperature of the compressor.

Then, modified refrigeration cycles were presented and studied at different heat source and heat sink temperatures. When taking into account the constraints of mobile-air conditioning systems, the comparison between those cycles showed that the indirect injection cycle with isentropic expansion presents the best performance at 0°C as evaporation temperature and at 28°C as condenser outlet temperature in sub-critical operation, and at 35°C as gas cooler outlet temperature in transcritical operation.

In Chapter 2, the ejector refrigeration cycle that will be presented and its performances are close to the ones of the indirect injection cycle with isentropic expansion.

References

[PEU 06] Steffen PEUKER, Predrag HRNJAK: "R744 TWO EVAPORATOR SYSTEM FOR US ARMY HMMWV"; R166, International Refrigeration and Air Conditioning Conference at Purdue, July 17-20, 2006.

[VAI 02] Igor B. Vaisman, Ph.D., Menber of ASHRAE: "COP analysis of carbon dioxide cycles"; 2002.

[SAR 05] J. Sarkar, Souvik Bhattacharyya, M. Ram Gopal, Department of Mechanical Engineering, Indian institute of technology , Kharagpur, Indiaa : "Transcritical CO_2 heat pump systems: exergy analysis including heat transfer and fluid flow effects"; December 2004.; energy conversion and management 46(2005) 2053-2067.

[YAN 05] JunLan Yang, Yi Tai Ma, Min Xia Li, Hai Qing Guan: "Exergy analysis of transcritical carbon dioxide refrigeration cycle with an expander". Energy 30 (2005) 1162-1175.

[HAF 04] A. Hafner; SINTEFF/NTNU, Trondheim; NORWAY: „Major design issues for compact interior heat exchangers". 2004.

[FAR 04] Amir Fartaj, David S.-K. Ting, Wendy W. Yang: "Second law analysis of the transcritical CO_2 refrigeration cycle". Energy conversion and management 45 (2004) 2269-2281.

[CHE 05] Jiangping Chen, Hongsheng Liu, Zhijiu Chen:" Experimental analysis of a CO_2 automotive air conditioning system". , Institute of refrigeration and Cryogenics Engineering, Shanghai, China. 2005.

[TAK 00] Torahide Takahashi: "Development of Carbon dioxide applied refrigeration system". Calsonickansei Corporation; SAE automotive alternate refrigerant system, 11-13 July 2000 Arizona USA.

[HAM 00] Hans Hammer, Juergen Wertenbach: "Carbon dioxide R-744 as supplementary heating device". Engineering conference, Pheonix USA July 11 – 13 2000.

[FRO 00] Jorn Frohling :" CO_2 as refrigerant for A/C and heat pump operation". Phoenix 11.07.2000, SAE 2000 Automotive Alternate refrigerant systems symposium.

[BEL 05] Iann Bell: "Performance increase of carbon dioxide refrigeration cycle with the addition of parallel compression economization". Cornell University (Ithaca, NY USA), Cornell University, Ithaca, NY. 2005.

[NEK 02] Petter Neksa: "CO2 heat pump systems". International Journal of Refrigeration 25 (2002) 421–427.

[TEG 04] Wilhelm Tegethoff, Jürgen Köhler,TU-Braunschweig; Sven Försterling, Nicholas Lemke,TLK-Thermo GmbH; VDA: "Expansion device specification using steady state and transient simulation".VDA-Wintermeeting 2004 / Saalfelden.

[PEA 05] Andy Pearson: "Carbon dioxide—new uses for an old refrigerant". International Journal of Refrigeration 28 (2005) 1140–1148.

[WHI 02] S.D. White, M.G. Yarrall, D.J. Cleland, R.A. Hedley : "Modelling the performance of a transcritical CO2 heat pump for high temperature heating". International Journal of Refrigeration 25 (2002) 479–486.

[ROB 98] Douglas M. Robinson, Eckhard A. Groll: "Efficiencies of transcritical CO_2 cycles with and without an expansion turbine". International Journal of Refrigeration, volume 21 No. 7, pp; 577-589, 1998.

[KIM 04] Man-Hoe Kim, Jostein Pettersen, Clark W. Bullard: "Fundamental process and system design issues in CO_2 vapor compression systems".Progress in Energy and Combustion Science 30 (2004) 119–174.

[SRI 03] K. Srinivasan, Y.K. Lim, J.C. Ho, N.E. Wijeysundera: "Exergetic analysis of carbon dioxide vapour compression refrigeration cycle using the new fundamental equation of state". Energy Conversion and Management 44 (2003) 3267–3278.

[YUM 02] Recep Yumrutas, Mehmet Kunduz, Mehmet Kanoglu: "Exergy analysis of vapor compression refrigeration systems". Exergy, an International Journal 2 (2002) 266–272.

[SAR 04] J. Sarkar, Souvik Bhattacharyya, M. Ram Gopal : "Optimization of a transcritical CO2 heat pump cycle for simultaneous cooling and heating applications". International Journal of Refrigeration 27 (2004) 830–838.

[RIG 05] J. Rigola, G. Raush, C.D. Perez-Segarra, A. Oliva: "Numerical simulation and experimental validation of vapour compression refrigeration systems. Special emphasis on CO_2 trans-critical cycles". International Journal of Refrigeration 28 (2005) 1225–1237.

[LIA 00] S.M. Liao, T.S. Zhao, A. Jakobsen: "A correlation of optimal heat rejection pressures in transcritical carbon dioxide cycles". Applied Thermal Engineering 20 (2000) 831-841.

[NAV 05] J. Navarro-Esbrı, R. Cabello, E. Torrella: "Experimental evaluation of the internal heat exchanger influence on a vapour compression plant energy efficiency working with R22, R134a and R407C". Energy 30 (2005) 621–636.

[HAF 98] A. Hafner, J. Pettersen, G. Skaugen, P. Neksa: "An automobile HVAC system with CO_2 as the refrigerant". IIF-IIR,Section B and E, Oslo,Norway,1998.

[KOH 98] Jurgen Kohler, Michael Sonnekalb, Harald Kaiser: "A transcritical refrigeration cycle with carbon dioxide for bus air conditioning and transport refrigeration", Germany, 1998.

[KAM 03] H. Kampf, M. Sickelmann, B. Taxix-Reischl, W. Baruschke, G. Feuerecker, and H. Raiser: "Control technologies to optimize operating performance of R-744 climate control systems", Behr Gmbh and Compagny KG, Stuttgart, Germany, C599/052/2003, IMechE 2003.

[BER 03] A. Bergami and T. Cowell: "Control of a transcritical cycle for optimum efficiency", Delphi thermal system, Luxembourg, , C599/063/2003, IMechE 2003.

[GEN 98] H. Gentner, BMW AG, Munchen: “Passenger car air conditioning using carbon dioxide as refrigerant”, IIF-IIR-Commission B2, with B1,E1 & E2- Oslo, Norway – 4 / 1998.

[APP 00] Roger Appelo, Arjan Kolling, Harry Nijenhuis: “Pressure controls for R-744 climate control systems”, Texas instruments Holland BV, 2000.

[LEP 03] L. Lepetit, M.B. Yahia, P. Meurillon, Y. Bernard : "Optimisation de la haute pression pour un cycle CO2", Revue generale du Froid, Janvier-Fevrier 2003- n. 1031.

[BEN 98] M. Ben Yahia, C. Mann, P. Meurillon: “Optimisation of the CO2 A/C system: The gas cooler effect”, Valeo Climate Control, France, 1998.

[HAM 02] Hans Hammer (AUDI), Jurgen Wertenbach (Daimler-Chrysler): “Performance and efficiency of R-744 heat pump systems for vehicles”, The conference on climate change and Ozone protection ,2002.

[FOR 02] Sven Forsterling, Wihelm Tegethoff, Jurgen Kohler: “Theoretical and experimental investigations on carbon dioxide compressors for mobile air conditioning systems and transport refrigeration”, TU Braunschweig, Purdue, 2002.

Chapter 2. Improved expansion cycle and simulation of a refrigeration ejector cycle

2.1 Introduction

Throttling losses in an expansion valve, through which the refrigerant is expanded from the condenser / gas cooler pressure to the evaporator pressure, are one of the highest thermodynamic losses in a conventional vapor compression refrigeration cycle. This expansion results during the isenthalpic process in which the kinetic energy, developed as the refrigerant pressure decreases, is dissipated as friction heat. The isenthalpic process increases the vapor quality at the evaporator inlet compared to the isentropic process. As a result, the refrigerating capacity of the cycle is reduced. Due to the low cost, no moving parts and ability to handle two-phase flow without damage, an ejector is an attractive alternative to the expansion valve (in term of efficiency) and to turbine (in term of costs).

Ejector systems have been modeled, designed, and built since the early 20th century. Maurice Leblanc and Charles Parsons first developed a steam ejector refrigerator around 1901. It experienced a wave of popularity during the early 1930s for air-conditioning systems of large buildings using water as refrigerant. However, it was supplanted by CFC vapor compression system.

Since its invention in the early twentieth century, the gas-to-gas or vapor-to-vapor ejector has found in a number of industrial applications for evacuation and refrigeration, or in modern jet planes for thrust augmentation. Air and steam were the common working fluids of ejectors.

The first significant effort to set guidelines and recommendations for ejector design was made by Flugel (1939): the analysis was based on writing and solving the energy equation and adding many experimentally constants.

Keenan and Neumann(1942) made one of the earliest efforts to model ejectors in a completely analytical way: they developed a one-dimensional model of an air ejector that had no diffuser.

Elrod (1945) obtained a single equation by combining the equations for the flow through the nozzle and the diffuser as well as the conservation equations for the flow in the mixing section. The optimum area of the mixing section was determined by maximizing the mass flow rate of the secondary flow in the final single equation. He compared his theoretical results with the experimental results of Flugel (1939) and Keenan & Neumann (1942), and concluded that his method is in satisfactory quantitative agreement and in an excellent qualitative agreement with others works.

The study of refrigerant (CFCs, HCFCs and HFCs) ejectors for air-conditioning or refrigeration applications started in the mid 1950s for utilizing low-grade energy such as solar or waste heat energy as heat source.

Relatively, little information is currently available on the application of the ejector as an expansion device in a refrigeration cycle. Most of the available information and experimentation are on the steam ejector using water as refrigerant in a superheat vapor expansion ejector cycle. The ejector studies on different refrigerants like R-11, R-12, R-22, R-141b, and R-134a are done on vapor expansion ejector cycle as reported by Chunnanond and Aphornratana [CHU 04a].

Also Chunnanond and Aphornratana [CHU 04b] studied the variation of static pressure through a steam ejector refrigerator. The throat diameters of the primary tested nozzle are 2, 1.75, and 0.5 mm; the cooling capacity is 3 kW. The operating parameters: the boiler pressure, the superheat level, the geometry, and the position of the primary nozzle, are examined on the system performance. It was found that the expansion angle, the effective position of the primary nozzle and the choking position explain the flowing and mixing characteristics through the steam ejector. Retracing the primary nozzle out of the mixing chamber, decreasing the boiler pressure, and using a smaller nozzle reduce the expansion angle of the expanded wave, and thereby larger amount of the secondary fluid is entrained and higher COP and cooling capacity are achieved.

Huang and Chang [HUA 99a,b] tested 15 ejectors using R-141b as working fluid, and they correlate the performance of the ejector as functions of the area ratio of the nozzle critical throat, the constant area and the diffuser exit area, the effective area of the secondary fluid, the pressure ratio of the ejector, the condenser, and the critical pressure at the nozzle throat area. They found that R-141b is a good working fluid for an ejector.

Few researchers study the two-phase ejector as expansion device. Disawas and Wongwises [DIS 04] investigate the performances of a refrigeration cycle using a two-phase ejector as an expansion device with R-134a refrigerant. The experiment shows that the COP of the two-phase ejector refrigerant cycle is higher than that of the conventional refrigeration cycle. Also, they report that the motive mass flow rate of the ejector is highly dependent on the heat sink temperature, so of the condensation pressure, and is independent of the heat source temperature, the evaporating temperature. The experiment shows an improvement of the COP for low heat sink temperature that relatively decreases as the heat sink temperature increases.

Li and Groll [LI 05] describe the transcritical CO_2 refrigeration cycle with ejector-expansion device as a performance enhancement option. They present a constant pressure mixing model for the ejector and found that the COP of a transcritical CO_2 cycle is improved of more than 16% due to an ejector expansion compared to the conventional transcritical CO_2 for typical air-conditioning operating conditions.

Simulation of ejector begins with 1D model then it was extended to 2D and 3D models with computational calculations progress. Hedges and hill (1974) developed the first CFD code for analysis of ejectors and they showed that this method was superior to the integral method where velocity profiles are assumed. By the beginning of the 1990s, many commercial CFD software programs appear that enable researchers to look in details at the mixing process even for the complicated supersonic flow.

CFD simulation of two-phase flow in ejector is not available yet. Currently, there are two main models for two-phase, gas-droplet flows. The two-fluid Eulerian modeling technique models the gas and the liquid droplets as a continuum field and the two fields are each represented by a separate set of conservation equations, all in the Eulerian frame. The other model is the Monte-Carlo, or particle-tracking model, where the conservation equations representing the gas are first solved numerically in Eulerian frame and subsequently the conservation equations representing a significant sample population of droplets are solved in a Lagrangian frame assuming known gas-side parameters.

Rusly et al. [RUS 05] analyze an ejector operating with R-141b in a superheat vapor expansion ejector refrigeration cycle. CFD simulations of ejectors were made and validated by experimental data given by Huang and Chang [HUA 99]. It is found that the maximum entrainment ratio happens in the ejector just before a shock occurs and that the position of the nozzle is an important ejector design parameter. The ejector geometry design depends on the operating parameters. According to the operating parameters of pressure and temperature, changing the constant area duct diameter with the same nozzle throat affects ejector performance dramatically.

So the available scientific literature shows that a transcritical CO_2 refrigeration cycle using an ejector is a promising enhanced cycle that will be modeled and characterized in the following sections.

The bibliography study of the use of a turbine as an expansion device, presented here below, is focused on the energy gains compared to an expansion valve of a usual simple refrigeration cycle. Then, the ejector refrigeration cycle will be discussed in details, and 1D model is elaborated to characterize the ejector cycle operation.

2.2 CO_2 transcritical cycle with expander turbines

Since the CO_2 critical temperature is 31°C, the heat transfer above 31°C as ambient temperature is gas cooling. The high-side pressure of a transcritical cycle is supercritical and the low side is an evaporation.

The COP of a CO_2 transcritical refrigeration cycle is relatively low. The exergy analysis of the cycle shows that the irreversibility losses are mostly due to the isenthalpic Joule-Thomson expansion and the compression phases. Therefore there are many methods to increase the performance of the cycle described in Chapter 1.

The cycle calculations show that the two-stage compression in series with inter-cooling with isentropic expansion and the two stage compression cycle with indirect injection offer the highest energy performances while reducing irreversibilities.

The high efficiency system could use a turbo-compressor, or other expander-compressor machine like scroll expander or piston expander to expand the high-pressure CO_2 and generates work that will be used as a compression stage. Several researchers have studied expansion by turbine for refrigeration cycles. The results are presented now.

FUKUTA et al. [FUK 06] investigated the performance of the carbon dioxide scroll expander, Figures 2.1 and 2.2, both theoretically and experimentally.

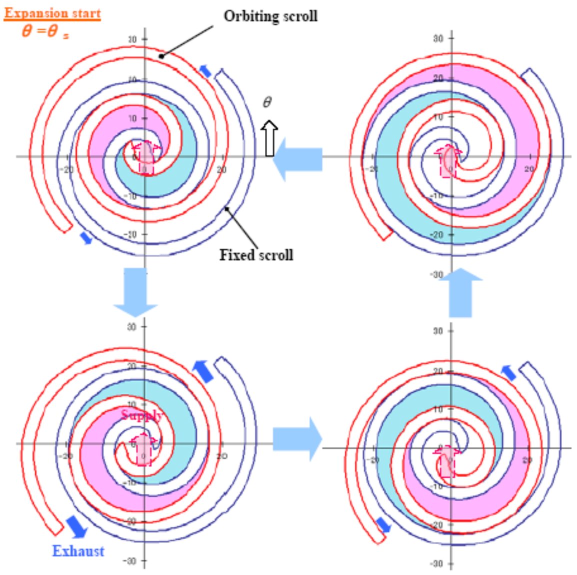

Figure 2.1: Operating principle of scroll expander [FUK 06]

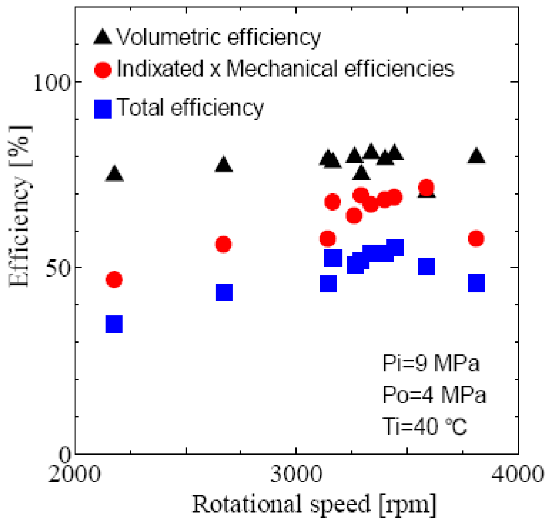

Figure 2.2: Scroll expander efficiency [FUK 06]

The internal leakage between the scroll in the expander influences greatly its performance, and for the trans-critical the flow in expander passes from a supercritical to the two-phase region. The calculation results show that the global efficiency of the scroll expander is about 60% when the leakage gap size is 10 μm and the rotational speed is 3600 RPM. The prototype of scroll expander was made using a mechanical element of a

CO_2 scroll compressor for a water heater. The measured prototype volumetric efficiency is about 80 % and the total efficiency experimentally reached is about 55%, although the scroll element of the compressor is used without any major modifications.

RIHA et al. [RIH 06], [NIK 05] used a vapor steam machine with slider piston as three-stage expander coupled to a piston compressor.

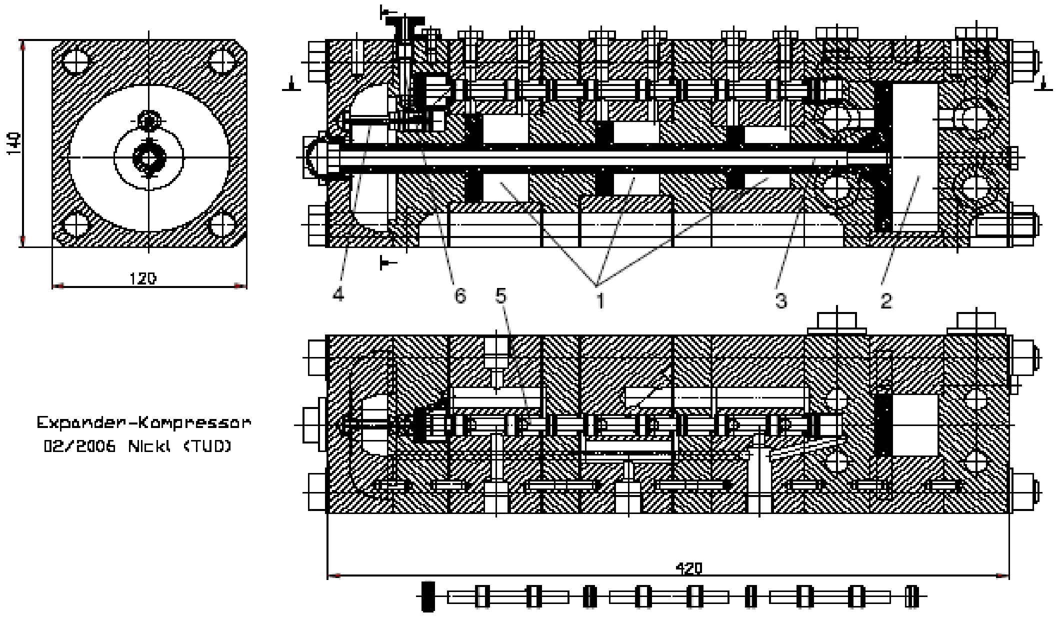

Figure 2.3: Expander/compressor with three-stage expansion coupled with a one-stage compression [RIH 06].

In Figure 2.3, the newest generation (fourth)of the expander/compressor with three expansion stages coupled with a one-stage compression is shown. All pistons are double acting. The expander (1) and the compressor (2) cylinders are arranged in order to obtain minimum internal temperature differences. The warm side of the machine is on the right, the cold side on the left. To control the charging and discharging, an auxiliary (4) and a main (5) sleeve valves are being used with a throttling valve (6) in between.

Kruse et al. [KRU 06] studied a simple reciprocating CO_2 expansion machine, Figures 2.4 and 2.5, without special valve- or slot-control previously designed by Doll and Eder for cryogenic helium expansion. This simple kind of charge and discharge control works without any additional control components except the piston, and allows also dead volume capacity control.

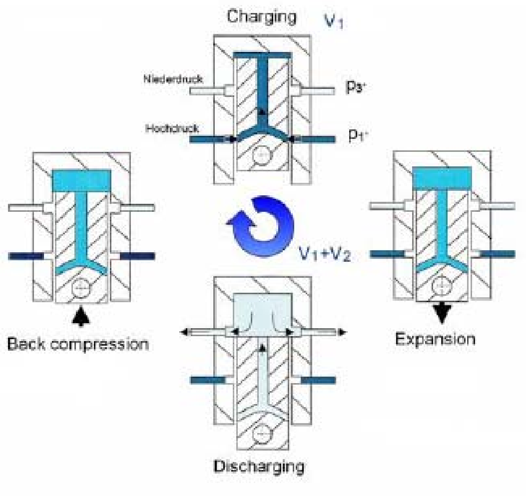

Figure 2.4: Functional principle for Doll and Eder [KRU 06].

Figure 2.5:Reciprocating compressor-expander unit [KRU 06].

Westphalen and Dieckmann [WES 06] developed a design for a scroll energy recovery expander for use in a CO_2 air conditioning circuit for a 5.28 kW (18,000 Btu/hr) military environmental control unit (ECU). The design is based on integration of the expander with an established-design two-stage rotary CO_2 compressor. Key technical issues have been addressed through analysis, including bearing loads, friction, leakage, and material stresses and deflections.

Kim et al. [KIM 06] studied a combined scroll expander-compressor unit, Figure 2.6, in order to improve the cycle COP in a two-stage trans-critical cycle. For the combined scroll expander-compressor unit, power was recovered from a scroll expander, which replaced the expansion valve and transmitted to the first stage compressor (from low pressure to intermediate pressure), which was directly coupled to the expander through a common crankshaft. Numerical simulation on its performance showed that for a suction pressure of 3.5 MPa, and a discharge pressure of 10 MPa with expander inlet temperature of 35°C, the main compressor input could be reduced by 12.1%, the increase in the cooling capacity by the expander was 8.6%. As a consequence, COP improvement of the cycle was estimated to be 23.5% by the application of this expander-compressor unit. Performance of the scroll expander was relatively insensitive to changes of operating pressure ratio, whereas that of the scroll compressor decreased rapidly as the operating pressure ratio became far from the design pressure ratio.

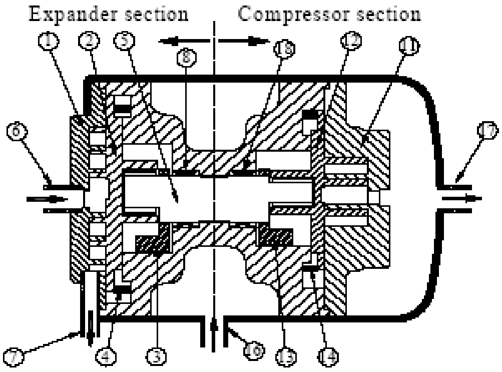

Expander		Compressor	
1	Fixed scroll	11	Fixed scroll
2	Orbiting scroll	12	Orbiting scroll
3	Balance weight	13	Balance weight
4	Oldham-ring	14	Oldham-ring
5	Crank shaft	15	Crank shaft
6	Suction pipe	16	Suction pipe
7	Discharge pipe	17	Discharge pipe
8	Journal bearing	18	Journal bearing

Figure 2.6: Scroll expander-compressor unit [KIM 06].

In order to improve the efficiency of the transcritical CO_2 cycle, Yang et al. [YAN 06] propose a new two-cylinder rolling piston expander, Figure 2.7. Compared with the traditional rolling piston expander, the suction valve of this expander could be removed, and therefore the expansion process becomes continuous.

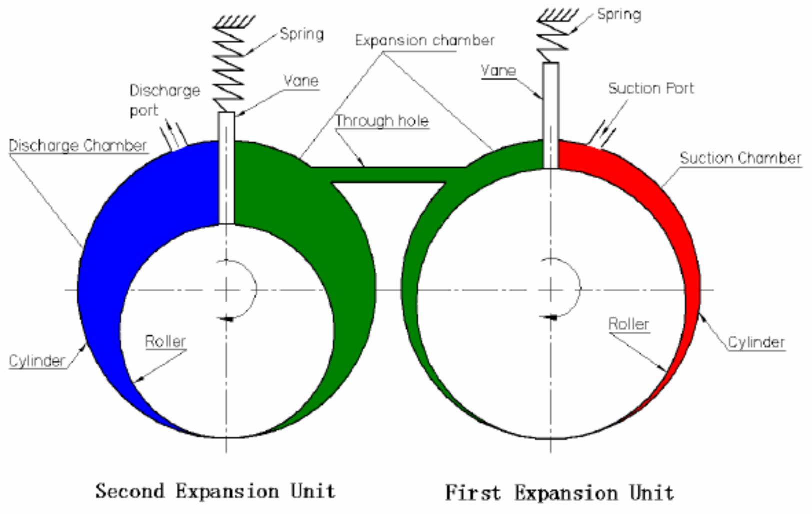

Figure 2.7: Schematic view of the two cylinder rolling piston expander [YAN 06].

Kohsokabe et al. [KOH 06] studied a transcritical CO_2 refrigeration cycle with a scroll expander to improve the coefficient of performance (COP) of the cycle of a simple expansion valve by recovering the throttling loss. An expander-compressor unit was developed. A scroll type expander and a rolling-piston type rotary sub-compressor were adopted and connected them with a shaft, Figure 2.8. In experiments, the expander-compressor unit was shown to be stable and to improve the COP of the CO_2 refrigeration cycle. The test results indicated that the COP improvement of the cycle was more than 30%, while the total efficiency of the expander-compressor unit was 57%.

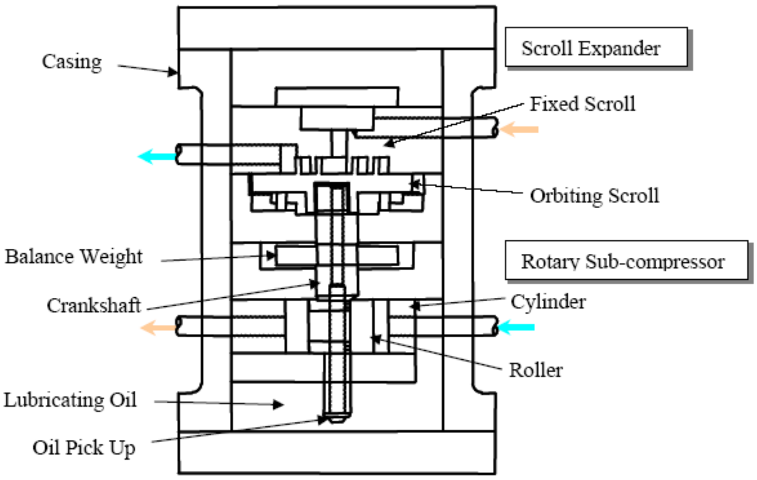

Figure 2.8: Cross-sectional view of expander-compressor unit [KOH 06].

Many different expanding machines exist that can be used to improve the transcritical CO_2 refrigeration cycle. The efficiency of the CO_2 expander varies between 30 and 60% depending on operating conditions. The experimental COP improvement measured with two-phase expander varies between 10% and 30%.

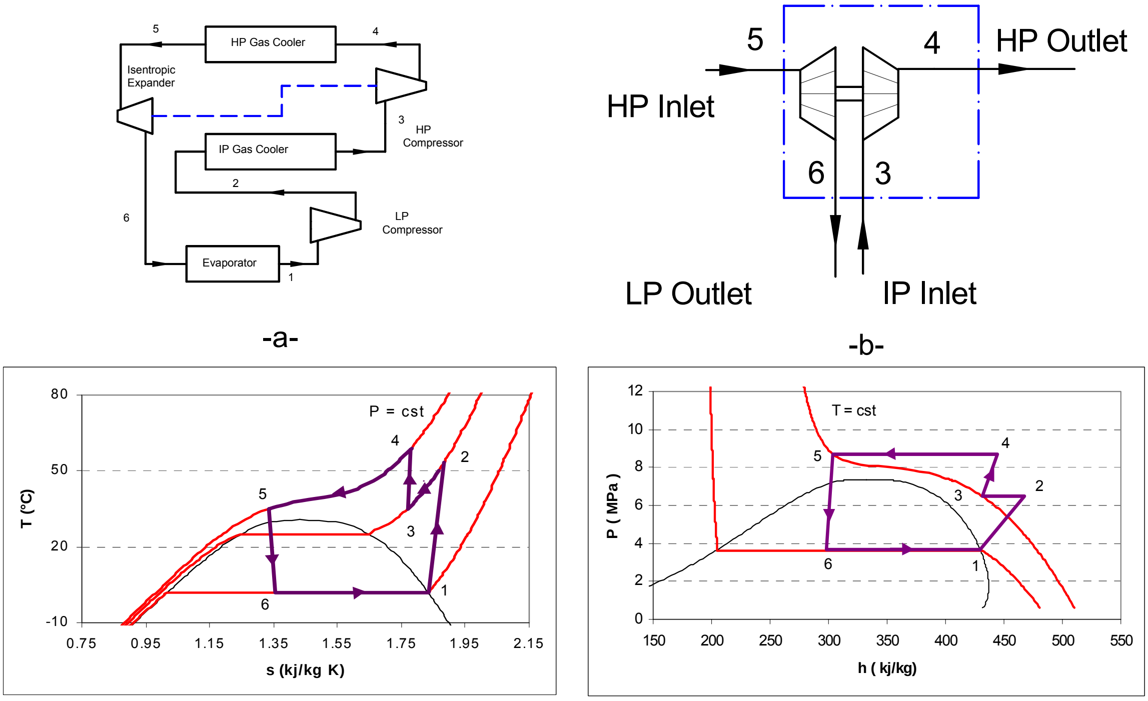

-a-

-b-

-c-

-d-

Figure 2.9: Two-stage compression cycle in series with inter-cooling:
a- physical schema, b- Turbo-compressor, c- T-s diagram, d- P-h diagram.

In Figure 2.9 (a, b, c, d), CO_2 expands in a turbine, and the generated work is used to drive the high-pressure CO_2 compressor. An isentropic efficiency of 0.8 is considered for the expansion and compression calculations. The performance of a two-stage transcritical cycle depends on the high-side and the intermediate pressures. Coupling the high and the intermediate pressures through the generated work of the turbine leads to a complex control of optimum pressures.

As shown in Figure 2.10, the high pressure CO_2 expands in the first stage of the turbine reaching the separator pressure, which is the discharge pressure of the low-stage compressor, then the saturated liquid exiting the separator expands in the second stage of the turbine to the evaporator pressure. The generated work is used to drive the high pressure CO_2 compressor. The same issue of pressure control is met if the shaft of the low-pressure turbine is coupled to one of the compressors.

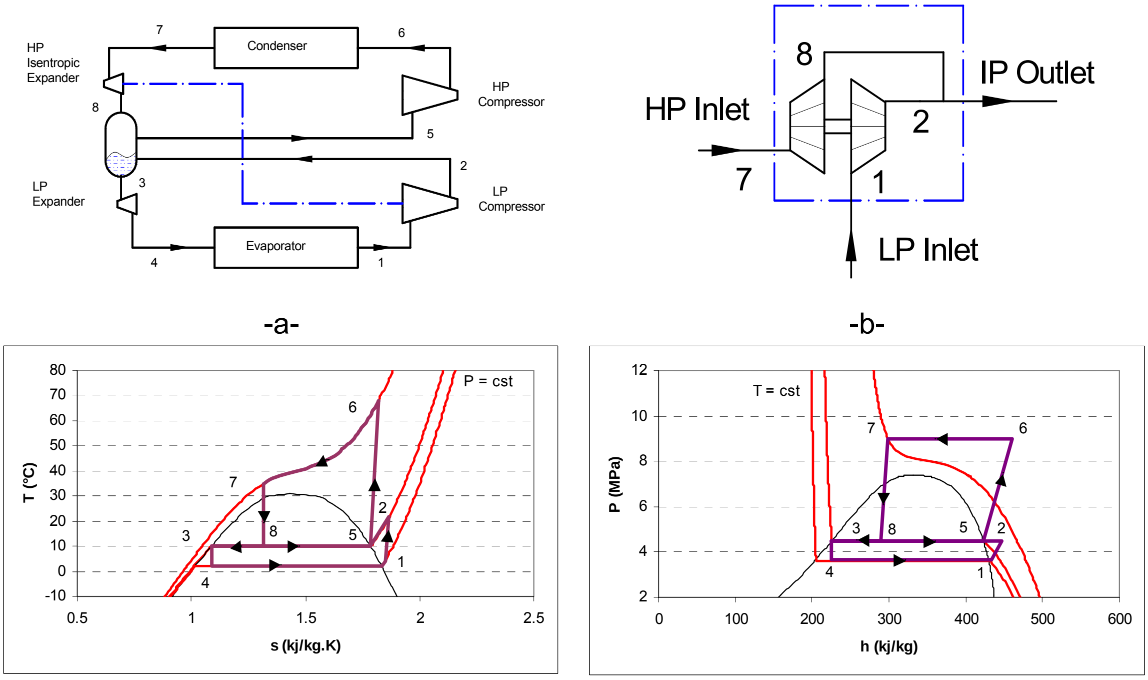

-a-

-b-

-c-

-d-

Figure 2.10: Two-stage compression cycle with indirect injection:
a- physical schema, b- Two- stage turbo-compressor, c- T-s diagram, d- P-h diagram.

The complexity of expansion by turbines plays in favor of the ejector refrigeration cycle, which is similar to a two-stage compression refrigeration cycle, gives increased performances without moving parts, so it can be used with CO_2 refrigerant as an enhancement cycle option.

2.3 Ejector cycles

The ejector is a component that expands a high-pressure primary substance to absorb a secondary substance at a pressure slightly above the low pressure reached by the primary substance. In refrigeration cycles, the two substances are identical, so both flows mix together leading to a pressure raise of the low-pressure flow due to the flow momentum generated by the high pressure flow.

An ejector is composed of a nozzle and a body, Figure 2.11. The nozzle is a convergent-divergent pipe with a throat that defines the primary mass flow rate. The role of the nozzle is to create a low-pressure flow with high momentum, so it transforms the pressure potential energy into kinetic energy.

A constant section tube and a diffuser form the body of the ejector shape that defines the ejector operation modes:

- either "constant area mixing" ejector (Figure 2-11 a)
- or "constant pressure mixing" ejector (Figure 2-11 b)

The constant pressure ejector body is composed of a convergent to insure a constant pressure for the two flows before entering a constant area throat where the flows mixture occurs at constant pressure.

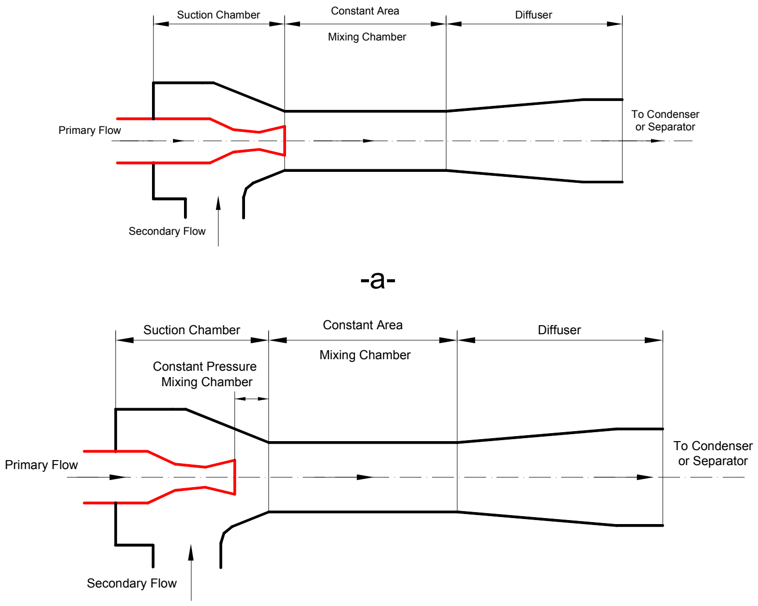

-a-

-b-

Figure 2.11: Schematic view of an ejector: a- constant area mixing ejector; b- constant pressure mixing ejector.

In the constant area-mixing ejector, the two flows enter directly in a constant area region and the flow mixing does not occur at constant pressure. After the constant area, a diffuser is installed for both types to decelerate the mixture flow and increase the ejector outlet pressure. The role of the body is to define the secondary inlet area, to insure the mixture between the flows and to transform the kinetic energy into pressure potential energy.

The high-pressure fluid, known as "primary fluid", expands, accelerates through the nozzle, and exits with high speed (almost supersonic) to create a very low-pressure region at the nozzle exit plane and hence in the mixing chamber. Having a pressure difference between the expanded flow and the low-pressure side (known as "secondary fluid"), the low-pressure fluid is sucked into the mixing chamber. The primary fluid expansion continues (in a fictive cone) without mixing with the secondary fluid in the constant pressure chamber. At a given cross-section along this duct, the speed of the secondary fluid may reach sonic velocity and chokes, Figure 2.14.

Experiences show that the constant pressure-mixing ejector offers higher energy performances compared to the constant-area ejector.

The ejector cycle has two operation modes:

- sub-cooled (or supercritical) expansion (Figure 2.12-a), which is vapor compression cycle for the low-side fluid, and
- superheated vapor expansion (Figure 2.12-b), which is a liquid compression cycle also for the low-side fluid.

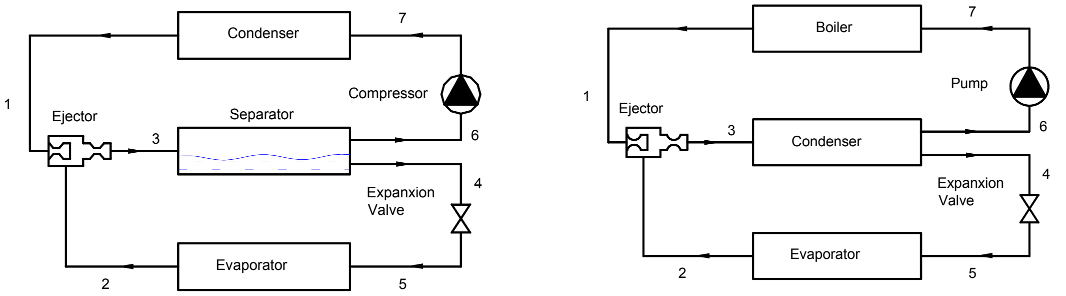

a- Sub-cooled expansion ejector refrigeration cycle

b- Superheated vapor expansion ejector refrigeration cycle

Figure 2.12: Schematic of ejector refrigeration cycle.

The sub-cooled expansion ejector cycle, Figures 2.13.a and c, is a two-phase expanding process; it can be used with all fluids. It is a promising cycle to enhance the energy performances. The compressor sucks the saturated vapor from the separator. The superheat vapor from the compressor discharge port enters a condenser/gas cooler to cool or condense. The refrigerant getting out of the condenser / gas cooler outlet enters the ejector nozzle, expands in the nozzle to a two-phase flow at a low pressure, and sucks the vapor from the evaporator (which is at a slightly higher pressure). Then the two flows are mixed in the mixture chamber before entering the diffuser that will decelerate the mixture velocity. The ejector outlet two-phase flow enters the separator where it will be divided in two flows: saturated liquid is expanded and evaporated in the evaporator, and the saturated vapor is sucked by the compressor.

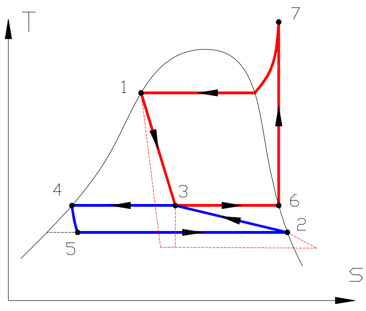

a. Sub-critical sub-cooled expansion ejector refrigeration cycle

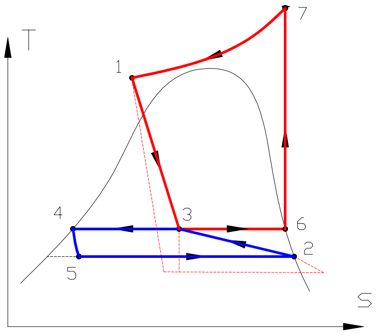

c. Transcritical sub-cooled expansion ejector refrigeration cycle

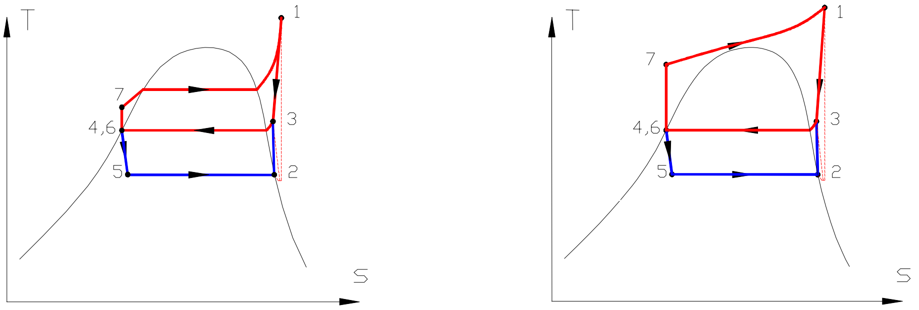

b. Sub-critical superheated vapor expansion ejector refrigeration cycle

d. Transcritical superheated vapor expansion ejector refrigeration cycle

Figure 2.13: T-s diagram of ejector refrigeration cycle.

The superheated vapor expansion ejector cycle, Figures 2.13.b and d, is a one-phase expanding process. It presents low performance. The COP of the cycle is below 1 due to the required energy to vaporize the refrigerant in the boiler, so the cycle is generally used with waste heat or solar energy as boiler heat source to enhance the performances. The liquid flow exiting the condenser is divided in two parts: one flow is expanded into the evaporator, and the other is compressed by a liquid pump to a high pressure. The high-pressure flow enters the boiler where it will be vaporized and heated. The superheated high-pressure vapor enters the ejector nozzle, and expands in the nozzle to vapor flow at a low pressure able to absorb vapor from the evaporator, then the two vapor flows are mixed in the mixture chamber before entering the diffuser that will decelerate the mixture velocity. After, the vapor ejector outlet flow enters the condenser.

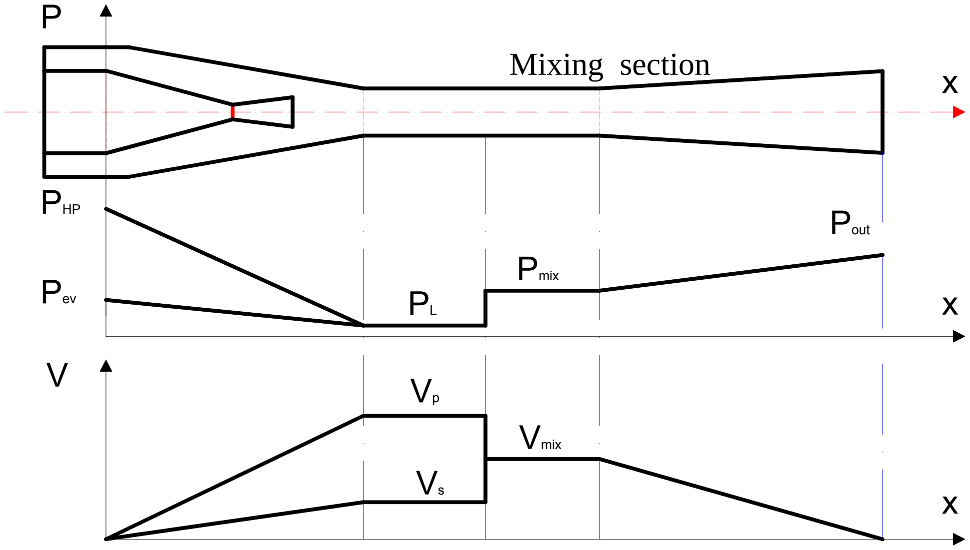

Figure 2.14: Velocity and pressure profile through an ejector

An ejector is analog to a turbo-machinery system, whereby a turbine mechanically drives a compressor through a common shaft. In the analog turbo-machinery, Figure 2.15, the high pressure fluid, the primary fluid, expands through the turbine to a pressure lower than the evaporator pressure, then the generated work is used to compress both fluids, primary and secondary, to an intermediate pressure.

In the ideal analog turbo-machinery of an ejector, Figure 2.16, the primary fluid expands to the intermediate pressure through the turbine while the compressor compresses the secondary fluid to the intermediate pressure. The discharge from the compressor and the discharge from the turbine combine to form the discharge mixture (equivalent to the discharge from an equivalent ejector).

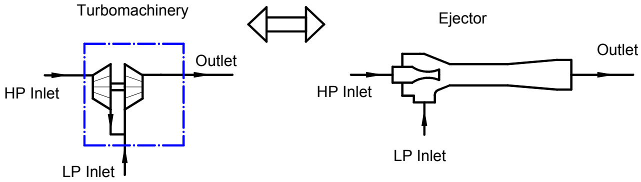

Figure 2.15: Ejector analog turbo compressor.

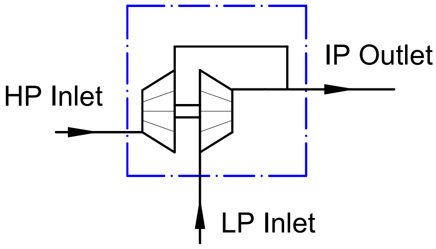

Figure 2.16:Ideal analog turbo-compressor.

2.4 1D simulation of an ejector cycle

Since the ejector cycle presents two operation modes: liquid compression cycle and vapor compression cycle, two different 1D models are elaborated to characterize each operation mode. Since the sub-cooled ejector cycle is not yet experimented and that no experimental results are published, the vapor ejector cycle will be studied to elaborate assumptions to be used for describing the two-phase flow ejector.

2.4.1 1D simulation of an ejector cycle with superheated vapor inlet as primary fluid

A theoretical model is elaborated to study the behavior of a superheated expansion ejector refrigeration cycle, using mass, momentum, and energy conservation equations. To simplify the theoretical model of the vapor ejector expansion refrigeration cycle, the following assumptions are made:

1- Flow is one dimensional and steady throughout the ejector
2- Friction at the walls is negligible
3- The inlet velocities of the primary and secondary flows are negligible
4- The flow is supersonic at the exit of the primary nozzle, so a shock occurs in the mixing chamber and ensures the mixing with the second flow. The second flow should always have a Mach number inferior or equal to 1 to prevent a shock wave that disturbs the primary flow.
5- The ejector is adiabatic, rigid and impermeable.
6- No chemical reactions are involved.
7- All fluid properties are uniform across their respective cross-sectional areas.

In this model, the inputs are the inlet pressure and temperature, and the nozzle geometry. The corresponding choked flow conditions will be part of the outputs.

The detailed input parameters of the model are:

- Primary stream stagnation conditions: pressure and temperature (and velocity): P_0, T_0, V_0.
- Secondary stream stagnation conditions: pressure, temperature (and velocity): P_2, T_2, V_2.
- Ejector geometry efficiencies.
- The output pressure that corresponds to the condensing pressure.

The outputs of the model are:

- Flow conditions at the exit of the mixing section: pressure, temperature, velocity: P_3, T_3, V_3.
- Flow conditions at the exit of the ejector: temperature: T_4, $V_4 \sim 0$.
- The optimum entrainment ratio w and the optimum pressure drop ΔP for which the optimum COP is reached.

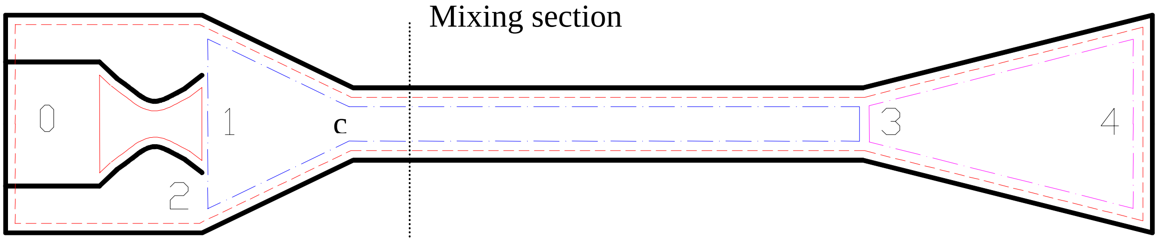

Figure 2.17: Specification of control volume of ejector model

The optimum output pressure is the condenser pressure. If the output pressure is higher than the condenser pressure, the ejector operates but the entrainment ratio w will be lower than the optimum value that decreases the performance since the pump work is negligible. Whereas, if the output total pressure is lower than the condenser pressure, the ejector will not operates and a back flow towards the evaporator occurs. Since the ejector output velocity is negligible, the total output pressure is the static pressure.

Considering the above assumptions and applying the conservation equations on the different control volumes of the ejector shown in Figure 2.17, the ejector refrigeration cycle equations are established.

- **Control volume 0-2 to 4**

- Continuity equation

$m_0 + m_2 = m_4$ so $m_4 = (1+w)m_0$ (2.1)

- Energy balance equation

$m_0 (h_0 + ½ V_0^2) + m_2 (h_2 + ½ V_2^2) = m_4 (h_4 + ½ V_4^2)$ (2.2)

so by neglecting $V_0 = V_2 = V_4 \approx 0$, the equation is reduced to : $h_4 = \frac{h_0 + w h_2}{1+w}$ (2.3)

- Second law equation (Entropy formation)

$\Delta s = m_0 (s_4 - s_0) + m_2 (s_4 - s_2)$ (2.4)

- **Control volume 0 to 1**

- Continuity equation

$m_0 = m_1$ (2.5)

- Energy balance equation

$m_0 (h_0 + ½ V_0^2) = m_1 (h_{1,p} + ½ V_{1,P}^2)$ (2.6)

so $V_{1s,P} = \sqrt{2(h_0 - h_{1s,P}) + V_0^2}$ then $V_{1,P} = \sqrt{2\eta_n (h_0 - h_{1s,P}) + V_0^2}$ (2.7)

so by neglecting $V_0 \approx 0$, the equation is reduced to : $V_{1,P} = \sqrt{2\eta_n (h_0 - h_{1s,P})}$ (2.8)

and : $h_{1,p} = h_0 (1 - \eta_n) + \eta_n h_{1s,p}$, so $T_1 = f(h_{1,p},P_1)$ (2.9)

The pressure P_1 is : $P_1 = P_2 - \Delta P$. (2.10)

- **Control volume 2 to 1**

- Continuity equation: $m_{1,s} = m_2$ (2.11)

- Energy balance equation

$m_2 (h_2 + ½ V_2^2) = m_{1,s} (h_{1,s} + ½ V_{1,s}^2)$ (2.12)

so: $V_{1s,s} = \sqrt{2(h_2 - h_{1s,s}) + V_2^2}$ then $V_{1,s} = \sqrt{2\eta_s (h_2 - h_{1s,s}) + V_2^2}$ (2.13)

so by neglecting $V_2 \approx 0$, the equation is reduced to : $V_{1,s} = \sqrt{2\eta_n (h_2 - h_{1s,s})}$ (2.14)

and : $h_{1,s} = h_2 (1 - \eta_s) + \eta_s h_{1s,s}$, so: $T_{1,s} = f(h_{1,s},P_1)$ (2.15)

➢ Control volume 1-2 to 3

Assuming that the properties at Section c are the same as at Section 1:

- Continuity equation: $m_1 + m_2 = m_3$ so $\mathbf{m_3} = (1 + w)m_0$ (2.16)

- Momentum balance equation

$m_0 V_{1,p} + P_1 A_1 + m_2 V_{1,s} + P_1 (A_3 - A_1) = m_3 \mathbf{V_3} + \mathbf{P_3} A_3$ (2.17)
$m_0 = \rho_{1,p} V_{1,p} A_1$. (2.18)
$m_2 = \rho_{1,s} V_{1,s} (A_3 - A_1)$. (2.19)
$m_3 = \rho_3 V_3 A_3$. (2.20)
By dividing by m_3:
$a_1 = A_1/m_3$; $a_3 = A_3/m_3$. (2.21)

$$(P_1\ a_1 + \frac{1}{1+w} V_{1,p}) + (P_1\ (a_3\text{-}a_1) + \frac{w}{1+w}\ V_{1,s}) = P_3\ a_3 + V_3 \quad (2.22)$$

➢ Control volume 0-2 to 3

- Energy balance equation

$m_0 (h_0 + ½ V_0^2) + m_2 (h_2 + ½ V_2^2) = m_3 (h_3 + ½ V_3^2)$ (2.23)

An iteration loop has to be done to calculate the pressure, the temperature, and the density of the mixture.

The unknowns are P_3 and V_3. To solve the equations for a given w, the mixture pressure P_3 is guessed, then V_3 is calculated from the momentum balance equation that gives the mixture enthalpy h_3 from the energy balance equation. Knowing the pressure and the enthalpy of the mixture, the mixture density is then calculated:

$$\rho_3 = f (h_3, P_3) \quad (2.24)$$

The loop condition is the mass conservation in the constant area:

$$m_3 = \rho_3 V_3 A_3 \quad (2.25)$$

In the mixture, a shock wave occurs and so two V_3 will be calculated: one with shock wave, the flow becomes subsonic, and another one without shockwave to reject where the flow stays supersonic.

➢ Control volume 3 to 4

- Continuity equation : $m_3 = m_4$ (2.26)

- Energy balance equation
-

$m_3 (h_3 + ½ V_3^2) = m_4 (h_{4s} + ½ V_{4s}^2)$ (2.27)

The flow properties at Section 3 are the mixture properties and $V_{4s} \approx 0$. Knowing the pressure and the enthalpy of the mixture, the entropy is then calculated:

$$s_3 = f (h_3, P_3) \quad (2.28)$$

The ejector outlet pressure is calculated as a function of the enthalpy and the entropy with the assumption of isentropic expansion. The enthalpy at the outlet is given from the diffuser expansion efficiency η_d.

$$\eta_d = \frac{h_{4,is} - h_3}{h_4 - h_3} \Rightarrow \mathrm{h}_{4,\mathrm{is}} = h_3 + \eta_d (h_4 - h_3) \tag{2.29}$$

$$\mathrm{P}_4 = \mathrm{f}(\mathrm{h}_{4,\mathrm{is}}, \mathrm{s}_3) \tag{2.30}$$

An iteration loop is used with a guessed entrainment ratio w to fulfill the criterion that the ejector outlet pressure is equal to the condenser pressure.

The cycle coefficient of performance is defined as:

$$COP = \frac{Q_{ev}}{Q_{boiler} + w_{pump}} = \frac{w(h_{o,ev} - h_{i,ev})}{h_{o,boiler} - h_{i,pump}} \tag{2.31}$$

For air or ideal gas, assuming isentropic expansion, the maximum flow rate through a nozzle is given by:

$$m_{\max} = A^* P_0 \sqrt{\frac{\gamma}{RT_0}} \left(\frac{2}{\gamma + 1} \right)^{(\gamma+1)/[2(\gamma-1)]} \sqrt{\eta_n} \tag{2.32}$$

$$\left(\frac{A_1}{A^*} \right)^2 = \frac{1}{M_1^2} \left[\frac{2}{\gamma + 1} \left(\frac{1 + \frac{\gamma - 1}{2} M_1^2}{1 + \frac{\gamma - 1}{2} M_0^2} \right) \right]^{(\gamma+1)/(\gamma-1)} \tag{2.33}$$

$$\frac{P_1}{P_0} = \left[1 + \frac{\gamma - 1}{2} M_1^2 \right]^{\gamma/(\gamma-1)} \tag{2.34}$$

These equations are used for the nozzle sizing . For vapor phase, the velocity at the nozzle throat is sonic, M = 1, so the mass flow rate is calculated to ensure sonic velocity at the nozzle throat.

The equations of shock wave, for air or ideal gas flow, are:

$$M_{down}^2 = \frac{1 + [(\gamma - 1)/2] M_{up}^2}{\gamma M_{up}^2 - (\gamma - 1)/2} \tag{2.35}$$

$$\frac{T_{down}}{T_{up}} = \left[1 + \frac{2\gamma}{\gamma + 1} (M_{up}^2 - 1) \right] \left[\frac{2 + (\gamma - 1) M_{up}^2}{(\gamma + 1) M_{up}^2} \right] \tag{2.36}$$

$$\frac{P_{down}}{P_{up}} = 1 + \frac{2\gamma}{\gamma + 1} (M_{up}^2 - 1) \tag{2.37}$$

Another iteration loop has to be done on the pressure drop ΔP to optimize the system COP.

2.4.2 Results of the superheated vapor inlet model

The superheat vapor inlet 1D model assumes that the primary and the secondary flows are in vapor state in the ejector components. So, the completion of assumptions requires either the use of a “dry” fluid like R-141b, either assuring a high superheat level at the boiler outlet.

Note: A fluid is called “dry” when the isentropic expansion transforms a saturated vapor at high pressure to a superheat vapor at lower pressure.

Considering R-141b as working fluid, the 1D model of superheat vapor inlet is used to analyze the effect of the entrainment ratio w, the pressure drop DP, the boiler pressure P_{boiler}, the boiler temperature T_{boiler} and the condensing temperature with isentropic efficiency equal to 1: $\eta_n = \eta_s = \eta_d = 1$. For all calculations, the Mach number of the second flow should be lower than 1 before the mixing surface.

- **Variation of the entrainment ratio**

The input parameters are:
P_{boiler} = 604 kPa that correspond to a saturation temperature of 95°C,
T_{boiler} = 100°C so a 5 K superheat ensures vapor flow,
a pressure drop ΔP = 11 kPa,
the evaporating temperature T_{ev} = 8°C so P_{ev} = 40 kPa, $T_{o,ev}$ = 13°C with a 5 K useful superheat, and
the condensing temperature T_{cond} = 30°C, so the minimum operating condensing pressure P_c = 94.2 kPa,
the entrainment ratio w is varied.

Figure 2.18 shows that the COP increases with w since the pump work is negligible compared to the boiler heat capacity, and so the sub-cooling does not increases the COP.

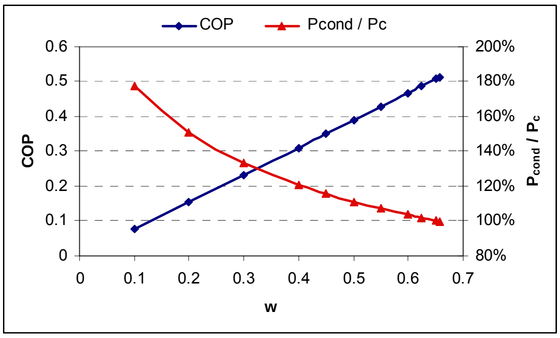

Figure 2.18: Variation of COP and condenser pressure ratio with the entrainment ratio w.

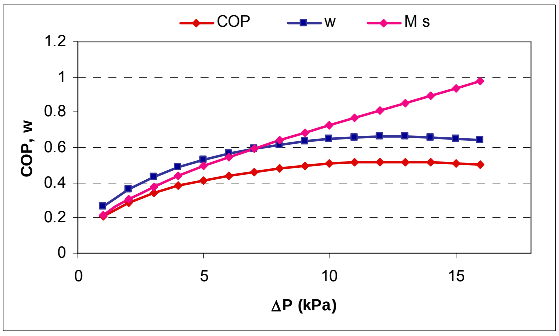

Figure 2.19: Variation of COP, optimal w and the secondary low pressure Mach number with the pressure drop ΔP.

Figure 2.18 shows also that the ratio between the condenser pressure and the minimum operating condensing pressure P_c decreases with w. Thus, the ejector should operate with the optimal entrainment ratio for which the maximal COP is reached at the critical back pressure P_c, the minimum operating condensing pressure. For ejector outlet pressure lower than P_c, a reverse flow occurs and the ejector cannot operate.

- **Variation of pressure drop**

The input parameters are : P_{boiler} = 604 kPa, T_{boiler} = 100°C, T_{ev} = 8°C (P_{ev} = 40 kPa), $T_{o,ev}$ = 13°C, and T_{cond} = 30°C, the pressure drop is varied.
Figure 2.19 shows that the COP and the entrainment ratio w present optimal values at the same ΔP, since the COP is directly proportional to w. However, the Mach number of the secondary flow is lower than 1 over the variation range of ΔP. Thus, the ejector should operates with the optimal pressure drop at which the maximal COP is reached at the optimal w.

Variation the outlet boiler temperature

The input parameters are:
P_{boiler} = 604 kPa, T_{ev} = 8°C (P_{ev} = 40 kPa), $T_{o,ev}$ = 13°C, and T_{cond} = 30°C, the outlet boiler temperature is varied.
Figure 2.20 shows that the optimal entrainment ratio w increases slightly with T_{boiler}, but the optimal COP slightly decreases with T_{boiler} since the added heat to the boiler is higher than the added absorbed heat at the evaporator. However, the Mach number of the secondary flow is nearly constant around 0.84 and the optimal pressure drop is nearly

constant around 12.6 kPa. Thus, the ejector should operate with the optimal boiler outlet temperature that corresponds to the saturation temperature.

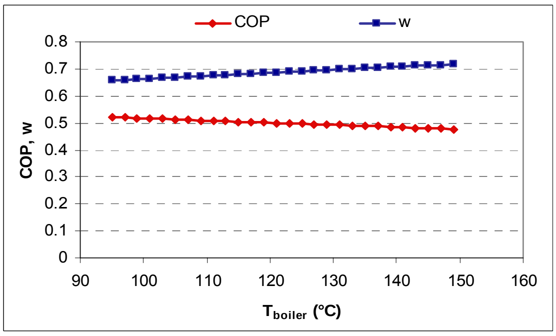

Figure 2.20: Variation of optimal COP and optimal w with the boiler outlet temperature T_{boiler}.

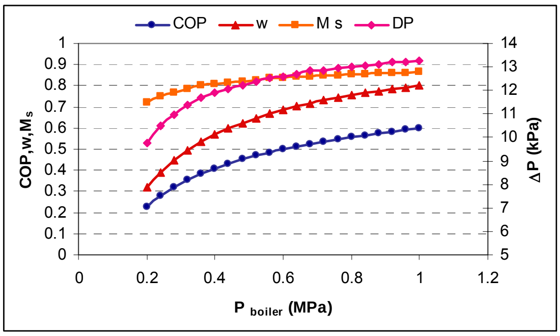

Figure 2.21: Variation of optimal COP, optimal w and optimal pressure drop ΔP with the boiler pressure P_{boiler} at 120°C as T_{boiler}.

➢ Variation of the boiler pressure

The input parameters are :
T_{boiler} = 120 °C that correspond to a saturation pressure of 103.4 kPa
T_{ev} = 8°C (P_{ev} = 40 kPa),
$T_{o,ev}$ = 13°C, and
T_{cond} = 30°C,
the boiler pressure is varied.

Figure 2.21 shows that the optimal entrainment ratio w, the optimal pressure drop, and the optimal COP increase with P_{boiler}. However the Mach number of the secondary flow increases slightly with P_{boiler} because ΔP increases. Thus, the ejector should operate with the optimal boiler pressure that corresponds to the saturation pressure (same conclusion as before), but a small superheat at the boiler outlet is required to insure vapor flow through the nozzle.

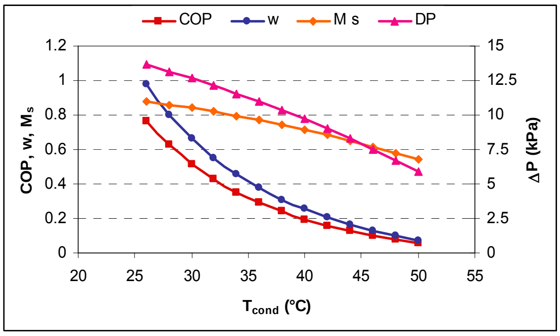

Figure 2.22: Variation of optimal COP, optimal w and optimal pressure drop ΔP with the condensing temperature T_{cond}.

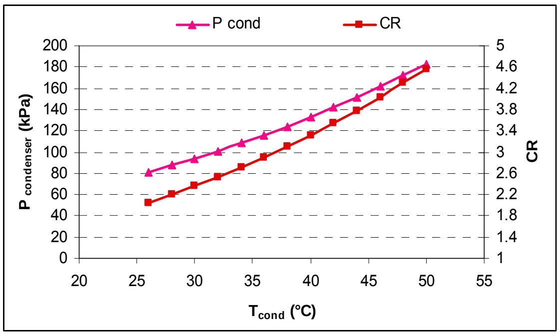

Figure 2.23: Variation of the condenser pressure and the compression ratio with the condensing temperature T_{cond}.

➢ Variation of condensing pressure

The input parameters are:
P_{boiler} = 604 kPa,
T_{boiler} = 100°C,
T_{ev} = 8°C (P_{ev} = 40 kPa),
$T_{o,ev}$ = 13°C, and
the condensing temperature is varied.

Figure 2.22 shows that the optimal COP, the optimal pressure drop and the optimal entrainment ratio w decrease with T_{cond} since the minimum operating condensing pressure increases as shown in Figure 2.23, which increases the compression ratio of the ejector that is not significant because the pump work is negligible before the boiler heat capacity. However, the secondary Mach number decreases with T_{cond} because ΔP decreases. Thus, the ejector vapor cycle is loosing performance as the ambient temperature that defines the condensing temperature increases, similarly to the conventional refrigeration cycle.

In conclusion, for the superheated vapor ejector cycle with R-141b, the minimum operating condensing pressure, which is the condensing pressure fixed by the ambient temperature, defines an optimal operating entrainment ratio w and an optimal operating pressure drop for a given boiler pressure and temperature outlet that should be close to the saturated vapor line to reach the maximal cycle COP.

Huang et al. [HUA 99] tested different ejectors sizes with R-141b and analyze it with 1D model based on ideal gas assumptions. Huang assumes that:

- The pressure of the mixing chamber is fixed by the expansion of the secondary flow up to the sonic velocity: Mach number = 1;
- The expansion through the nozzle of the primary flow continues after leaving the nozzle with an isentropic coefficient equal to 0.88 to reach the low chamber pressure.
- The mixture before the shock wave is at constant pressure, a coefficient of mixing is introduced to insure the continuity equation.

By comparing the model presented above with Huang 1D model, the pressure of the mixing chamber is higher because the second flow sonic velocity is not reached. By assuming that primary flow continues to expand outside the nozzle with a isentropic η_p, and by adding a mixing coefficient η_m to the momentum balance equation:

$$m_0 \, \eta_m \, V_{1,p} + P_1 \, A_1 + m_2 \, \eta_m \, V_{1,s} + P_1 \, (A_3 - A_1) = m_3 \, V_3 + P_3 \, A_3. \quad (2.38)$$

$$h_{c,p} = h_{1,p} \, (1 - \eta_p) + \eta_p \, h_{cs,p} \quad (2.39)$$

$$V_{c,P} = \sqrt{2(h_{1,p} - h_{c,P}) + \frac{1}{2} V_{1,p}^2} \, . \quad (2.40)$$

The 1D model is used to analyze the ejector tested by Huang, and results are compared. To calculate the primary mass flow rate, a sonic velocity is assumed at the nozzle throat calculated by an iteration loop.

By fixing the nozzle efficiency η_n at 0.95, the outside primary expansion η_p at 0.95, the secondary expansion efficiency η_s at 1, the diffuser expansion efficiency η_d at 1, the evaporator superheat SH at 5 K, **the entrainment ratio w is optimized to a maximum value by evaluating the optimum pressure drop to calculate the mixing pressure**.

The mixing coefficient η_m is calculated to obtain the experimental condensing temperature (minimum operating condensing pressure). The error is calculated by:
Error = $(w_{theory} - w_{experiment}) / w_{experiment}$.

For the experimental tests, the evaporator superheat is set between 5 and 20 K, however the evaporator superheat has small effect on the ejector operation.

Table 2.1: Comparison of models results and experiments for T_{ev} = 8°C (40 kPa).

T °C	Ejector	T_c °C	Huang	Exp.	Study	M s	η mixture	Er. Huang	Er.
95 (604 kPa)	EH	31.3	0.4627	0.4377	0.4354	0.7838	0.9274	5.71%	-0.53%
	EF	33	0.3774	0.3937	0.3773	0.7652	0.9366	-4.14%	-4.16%
	AD	33.6	0.3476	0.3457	0.3483	0.7542	0.9302	0.55%	0.76%
	EE	34.2	0.3253	0.3505	0.3312	0.7484	0.9341	-7.19%	-5.52%
	AC	36.3	0.2983	0.2814	0.2699	0.7188	0.9384	6.01%	-4.09%
	ED	37.1	0.2658	0.2902	0.2672	0.7183	0.9615	-8.41%	-7.92%
	EC	38.8	0.2078	0.2273	0.2003	0.6763	0.9325	-8.58%	-11.90%
	AG	38.6	0.2144	0.2552	0.2318	0.6977	0.9668	-15.99%	-9.17%
	EG	41	0.1919	0.2043	0.1680	0.6508	0.9541	-6.07%	-17.77%
	AA	42.1	0.1554	0.1859	0.1465	0.6304	0.9532	-16.41%	-21.20%
90 (538 kPa)	AD	31.5	0.4178	0.4446	0.4209	0.7782	0.9445	-6.03%	-5.33%
	AC	33.8	0.3552	0.3488	0.3319	0.7468	0.9450	1.83%	-4.84%
	AG	36.7	0.2395	0.304	0.2885	0.7277	0.9980	-21.22%	-5.09%
	AB	37.5	0.2093	0.2718	0.2319	0.6954	0.9580	-22.99%	-14.69%
	AA	38.9	0.2156	0.2246	0.1907	0.6683	0.9488	-4.01%	-15.11%
84 (465 kPa)	AD	28	0.5215	0.5387	0.5263	0.8054	0.9267	-3.19%	-2.31%
	AC	30.5	0.4605	0.4241	0.4224	0.7765	0.9411	8.58%	-0.40%
	AG	32.3	0.3704	0.3883	0.3715	0.7595	0.9614	-4.61%	-4.31%
	AB	33.6	0.3042	0.3117	0.3049	0.7334	0.9442	-2.41%	-2.19%
	AA	35.5	0.288	0.288	0.2561	0.7089	0.9558	0.00%	-11.07%
78 (400 kPa)	AD	24.4	0.6944	0.6227	0.6534	0.8290	0.8998	11.51%	4.93%
	AC	26.9	0.5966	0.4889	0.5320	0.8038	0.9214	22.03%	8.81%
	AG	29.1	0.4609	0.4393	0.4724	0.7891	0.9600	4.92%	7.53%
	AB	29.5	0.4422	0.3922	0.3940	0.7669	0.9181	12.75%	0.46%
	AA	32.5	0.3525	0.3257	0.3364	0.7449	0.9717	8.23%	3.30%

Table 2.2: Ejector geometrical parameters.

Core	D const area mm
A	6.7
B	6.98
G	7.34
C	7.6
D	8.1
E	8.54
F	8.84
H	9.2

Nozzle	D throat mm	D out mm
A	2.64	4.5
E	2.82	5.1

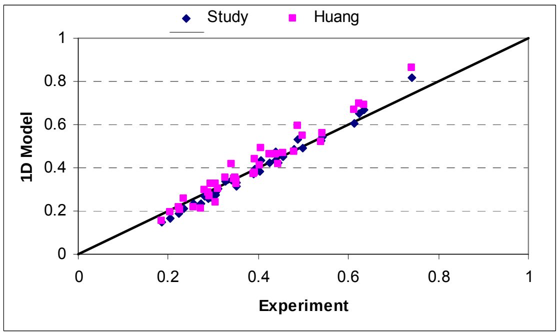

Figure 2.24: Comparison between experimental results and 1D model results: study and Huang.

The results of the elaborated 1D model show a better prediction when comparing the experimental results and the simulation ones compared to the Huang 1D model (see Figure 2.24 and Tables 2.1 and 2.3), especially that the error on the mass flow meter is ±5%. The entrainment ratio w decreases if the nozzle efficiency η_n is decreased.. The Mach number of the second flow, upstream the mixture point, is lower than 1; so the mixture is between a supersonic motive flow and a subsonic entrained flow. The mixing efficiency η_m varies between 0.9 and 0.98, the ideal mixture gives a higher outlet pressure and so a larger sub-cooling of liquid. Assuming that η_m varies with area ratio of constant area chamber and the nozzle throat, a correlation of η_m is elaborated:

$$\eta_m = -0.0113\ (D_{\text{const area}} / D_{\text{throat}})^2 + 1.0501 \qquad (2.41)$$

Table 2.3: Comparison of models results and experiments for T_{ev} = 12°C (47.3 kPa).

T °C	Ejector	T_c °C	Huang	Exp.	Study	M s	η_{mixture}	Er. Huang	Er.
95 (604 kPa)	EF	33.1	0.5482	0.4989	0.4888	0.7961	0.9005	9.88%	-2.02%
	EE	34.2	0.4894	0.4048	0.4337	0.7806	0.8981	20.90%	7.14%
	AD	34.5	0.4708	0.4541	0.4542	0.7866	0.9212	3.68%	0.02%
	AG	38.7	0.3434	0.3503	0.3144	0.7383	0.9402	-1.97%	-10.24%
	EC	39.3	0.3235	0.304	0.2763	0.7195	0.9215	6.41%	-9.11%
	AA	42.5	0.2573	0.235	0.2108	0.6813	0.9437	9.49%	-10.31%
90 (538 kPa)	AD	32	0.5573	0.5422	0.5412	0.8070	0.9175	2.78%	-0.19%
	AG	36	0.4142	0.4034	0.3830	0.7632	0.9390	2.68%	-5.04%
	AA	39.5	0.3257	0.2946	0.2650	0.7120	0.9412	10.56%	-10.04%
84 (465 kPa)	AD	28.9	0.6906	0.635	0.6669	0.8301	0.9071	8.76%	5.03%
	AG	32.4	0.4769	0.479	0.4829	0.7912	0.9233	-0.44%	0.81%
	AA	36	0.4147	0.3398	0.3446	0.7472	0.9392	22.04%	1.41%
78 (400 kPa)	AD	25.7	0.8626	0.7412	0.8182	0.8504	0.8879	16.38%	10.39%
	AG	29.2	0.6659	0.6132	0.6035	0.8167	0.9148	8.59%	-1.58%

Note: the first letter of the ejector name is the nozzle type, and the second letter is the constant area chamber type.

In conclusion, the 1D model results are validated by the experimental results presented by Huang et al. [HUA 99]. Therefore, the assumptions made for the analysis of the vapor ejector are validated:

- The mixing efficiency is variable and depends on the diameter ratio of the nozzle throat and the constant area diameters.
- The mixing pressure is evaluated to entrain the maximum secondary flow, when the geometry is fixed.
- When the geometry is not defined, the calculation of w is related to the ejector outlet.

These assumptions will be taken into account for the analysis of the two-phase flow ejector.

2.4.3 CFD comparison with R-141b

Ansary [ANS 04] studied a CFD model of an **air** ejector and gave the following results:

- The RNG ķ-ε model with fine meshes gives the more accurate values compared to the experimental results.
- The primary stream can be injected upstream of the nozzle exit as a result of boundary layer separation and low momentum. In this case, the velocity profile at the nozzle exit will be far from uniform, as both reverse flow near the nozzle wall and the supersonic jet flow at the nozzle core will exit at that section. Therefore, any 1D model that assumes uniform properties at the nozzle exit will not be accurate at such operating conditions.
- The mixture of the primary and secondary streams is compressed in the diffuser through a series of oblique shocks induced by boundary layer separation. These oblique shocks vary in strength with the primary stream inlet pressure. Therefore,

diffuser efficiency will also vary greatly depending on the primary stream inlet pressure. For this reason, it is impossible to define a universal value for ejector efficiency.

- The variation in static wall pressure was found to be strong enough to make the constant pressure assumption inaccurate. These variations can seriously cause a 1D ejector model to make inaccurate computations of pressure terms in the axial momentum equation for certain control volumes.

Since the 1D model does not take into account the shape of the secondary flow nozzle, the length of the diffuser, and the length of the constant area mixing chamber, a 3D simulation is essential to analyze the flow lines through an ejector. The CFD tool, Fluent, simulates the one-phase flow, vapor flow, assumed as ideal gas. By choosing R-141b as a working fluid, the boiler outlet temperature has been chosen at more than 200°C to ensure that the nozzle outlet is superheat vapor and not two-phase flow. Then the results obtained with Fluent will be compared to those of the 1D model.

Assuming isentropic expansion: $\eta_n = \eta_p = \eta_s = \eta_d = 1$; an ejector is sized for an evaporator cooling capacity of 1000 W at 8°C evaporating temperature. For the operating parameters listed in Table 2.5, the primary flow rate is 9.624 g/s, and the critical temperature is 35.2°C.

Table 2.4: Specific diameter of the simulated ejector.

d_{th} mm	d_{out} mm	$D_{const\ area}$ mm
2.5	5	8

Table 2.5: Results of 1D model for R-141b fluid.

P_b kPa	600	P_{mix} kPa	99.24
T_b °C	250	T_{mix} °C	176.60
P_{ev} kPa	40	P_{out} kPa	112.91
T_{ev} °C	26	T_{out} °C	181.06
P_{th} kPa	355.90	$P_{out\ nozzle}$ kPa	33.46
T_{th} °C	229.94	$T_{out\ nozzle}$ °C	147.20
DP kPa	11.12	w	0.4829

By referring to Rusly et al. [RUS 05], the constant area chamber length is taken equal to 5 $D_{const\ area}$; the diffuser length equal to 6 $D_{const\ area}$, and the distance between the nozzle outlet and the constant area chamber equal to 1.5 $D_{const\ area}$. The total angle of the diffuser is 7°; the total convergent angle of the constant pressure chamber is 20°, the total angle of the nozzle divergent is 14°; and the total nozzle convergent angle is 30°, Figure 2.25. Annex 2 presents the detail of the CFD model.

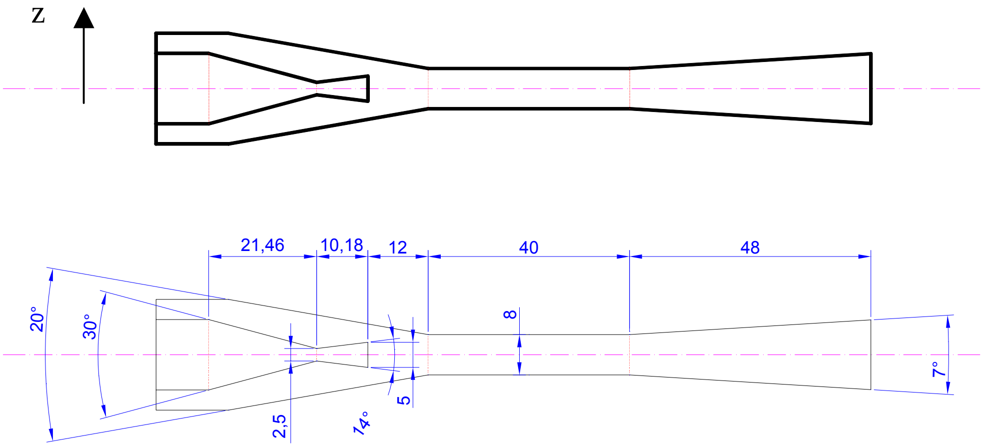

Figure 2.25: Ejector geometry modeled in CFD.

The nozzle inlet pressure and temperature are chosen for the 1D model to obtain a compressibility factor Z higher than 0.98 so that the CFD fluid properties will be close to the 1D model fluid properties. The R-141b heat capacity Cp depends on pressure more than temperature, but in Fluent, the heat capacity Cp can be expressed only as a function of the temperature, so to be at maximum accuracy, the fluid properties are calculated by taking an isentropic expansion (at constant entropy), and by varying the pressure, the temperature is calculated. Then the heat capacity Cp, the conductivity k, and the viscosity μ are correlated as functions of the temperature.

- High pressure nozzle inlet: s = 2.2104967 kj/kg.K ; 20 < P < 600 kPa
  - 403.15 < T < 573.15

* C_p (j/kg.K) = $0.00001549\ T^3 - 0.0218\ T^2 + 11.3153\ T - 1140.16$ (2.42)

* k (W/m.K) = $0.00000019566\ T^2 - 0.0000666\ T + 0.013853$ (2.43)

* μ (Pa.s) = $0.000000000034111\ T^2 - 0.000000000573\ T + 0.000007361$ (2.44)

- Low pressure body inlet: s = 1.912278 kj/kg.K ; 20 < P < 40 kPa
  - 283.15 < T < 303.15

* C_P (j/kg.K) = $1.719316\ T + 254.689$ (2.45)

* k (W/m.K) = $0.00006752\ T - 0.01025$ (2.46)

* μ (Pa.s) = $0.00000003147\ T - 0.00000016268$ (2.47)

- Ejector outlet : s = 2.195053 kj/kg.K ; 10 < P < 112.9 kPa
  - 303.15 < T < 403.15

* C_p (j/kg.K) = $1.311075\ T + 367.420$ (2.48)

* k (W/m.K) = $0.000086774\ T - 0.01646$ (2.49)

* μ (Pa.s) = y = $0.000000031732\ T - 0.0000001973$ (2.50)

The CFD simulations give that the entrainment ration w decreases by increasing the outlet pressure. For 80 kPa as pressure outlet, the primary mass flow rate is 9.849 g/s ($m_{p\ 1D}$ = 9.624 g/s) and the secondary mass flow rate is 4.614 g/s ($m_{s\ 1D}$ = 4.647 g/s), which give an entrainment ratio of 0.4685 (w_{1D} = 0.4829). For outlet pressure higher than 80 kPa, the primary mass flow rate remains constant but the entrainment ratio w decreases to 0.22 at P_{out} = 112.9 kPa. The CFD nozzle flow is similar to the 1D model due to the same fluid properties, but the mixture properties in the constant area zone of the CFD model are different from the 1D model since the pressure is not introduced in the polynomial function of the fluid properties. Thus the comparison of the ejector outlet is not accurate, so the internal flow of the CFD simulation will be used to compare the properties of the fluid at different ejector sections with the 1D model assumptions.

The velocity profile of the ejector, Figure 2.26, shows that the primary flow velocity of R-141b increases from negligible values, less than 5 m/s, to sonic velocity near the throat, and continues to increase to around 450 m/s until the diffuser inlet where the flow is chocked. Similarly to the primary flow, the secondary flow velocity increases from negligible values to high values exceeding the sonic velocity in the constant area chamber, and then in the diffuser inlet where the two flows are choked, which decreases the velocity, then the mixture velocity decreases through the diffuser.

The Mach number profile of the ejector, Figure 2.27, shows the passage from sonic to supersonic flow, and also the location of the chock wave that occurs in the diffuser.

The analysis of the contact surface between the primary flow and the secondary flow in the constant pressure mixing chamber, Figures 2.28 and 2.29, shows that the entrained fluid flow in streamline nearly parallel to the primary current line with a small number of secondary streamlines that mix with the primary flow.

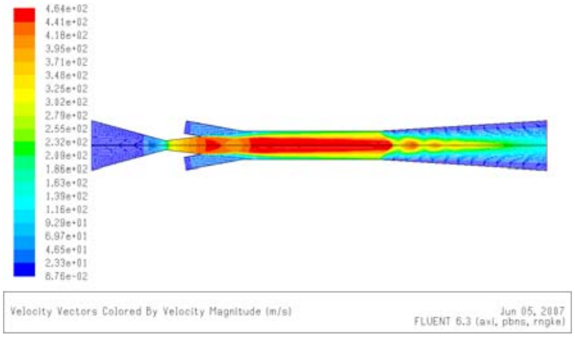

Figure 2.26: Velocity of the internal flow in the ejector.

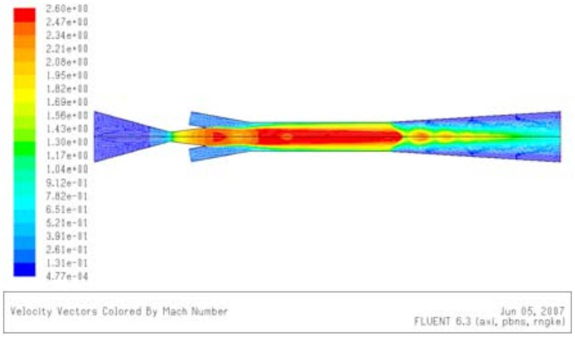

Figure 2.27: Mach number of the internal flow in the ejector.

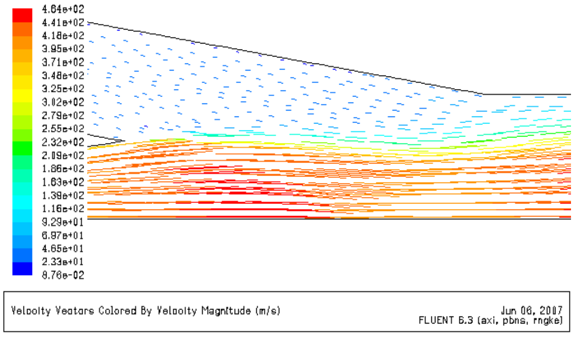

Figure 2.28: Constant pressure chamber flow velocity.

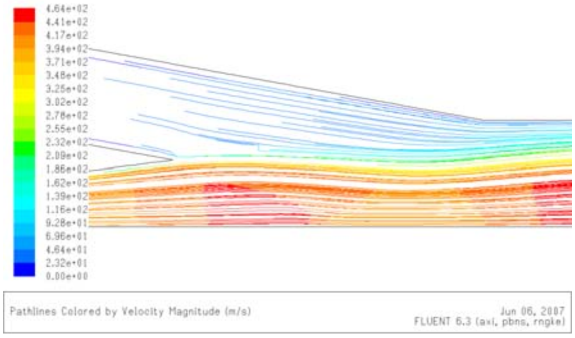

Figure 2.29: Constant pressure chamber flow line.

The pressure profile of the flow in the ejector, Figure 2.30, shows the existence of nearly constant pressure zones that begin from the nozzle outlet to the constant area inlet, and from the constant area inlet to the diffuser inlet.

The temperature profile of the flow in the ejector, Figure 2.31, shows that the temperature decreases through the nozzle, and it is nearly constant in the constant area chamber, and then it increases through the diffuser.

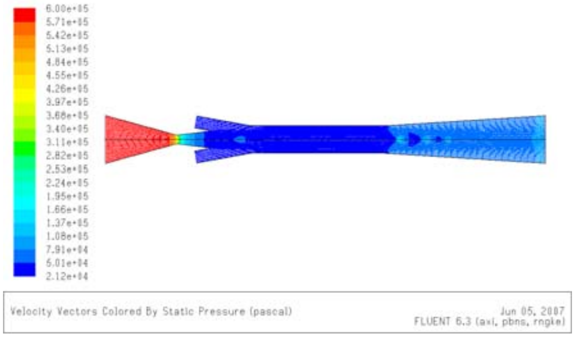

Figure 2.30: Pressure of the internal flow in the ejector.

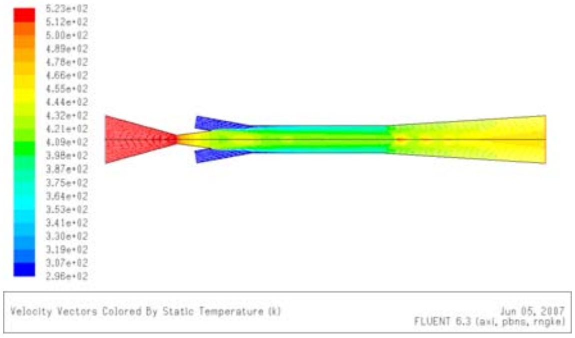

Figure 2.31: Temperature of the internal flow in the ejector.

The property profiles of the primary flow at the nozzle throat area, Figures 2.32 and 2.33, show a nearly constant velocity around 170 m/s, and a nearly temperature between 230 and 236°C. The pressure at the throat varies from 415 kPa at the center to around

340 kPa at the borders. The Mach number is equal to 1 at the border and around 0.8 at the flow center.

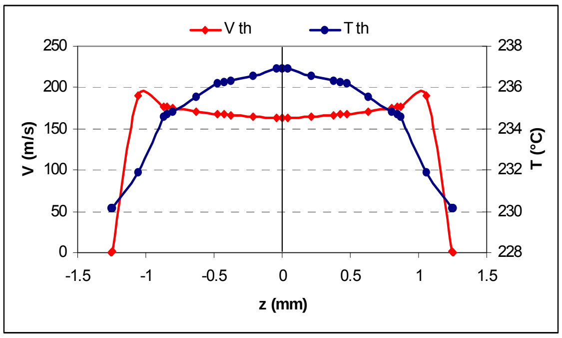

Figure 2.32: Velocity and temperature profile at the nozzle throat.

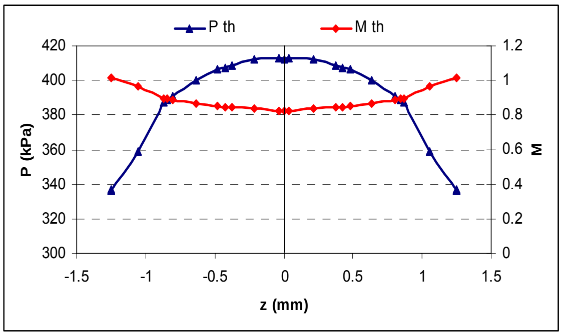

Figure 2.33: Mach number and pressure profile at the nozzle throat.

The property profiles of the flow at the nozzle outlet section, Figures 2.34 and 2.35, show nearly constant velocities around 430 m/s for the primary flow and 25 m/s for the secondary flow, and a nearly constant temperature around 155°C for primary flow and around 25.5°C for the secondary flow. The pressure of the secondary flow is nearly constant around 39.4 kPa, but the pressure of the primary flow varies from 37.4 kPa at the center to 36 Kpa at the border. The Mach number is around 2.35 for the primary flow, and around 0.175 for the secondary flow. So, the properties profiles at the nozzle outlet section are close to uniform properties, which is an assumption for the 1D model.

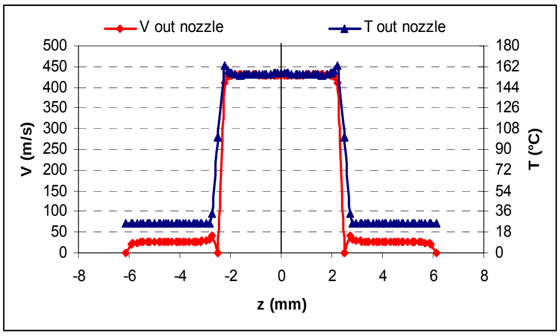

Figure 2.34: Velocity and temperature profile at the nozzle outlet section.

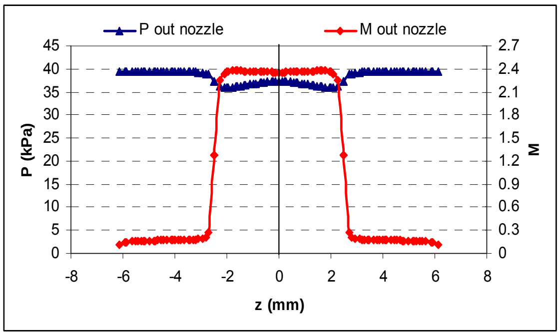

Figure 2.35: Mach number and pressure profile at the nozzle outlet section.

The property profiles of the flow at the constant area inlet section, Figures 2.36 and 2.37, show that the secondary flow is entrained. The velocity at the center, which is mainly the primary flow, is nearly constant around 415 m/s, smaller by 15 m/s from the nozzle outlet; also the center temperature is around 160°C, and the Mach number at the center varies around 2.28. The primary and the secondary flows mix a little between the nozzle outlet and the constant area chamber. This mixing decreases slightly the velocity at the center, increases slightly the temperature, and creates a pressure variation from 42 kPa at the center to 35 kPa at the exchange surface between the primary and the secondary flows. For the flow near the border (mainly the secondary flow), gradients of velocity, Mach number and temperature occur at constant pressure around 35 kPa.

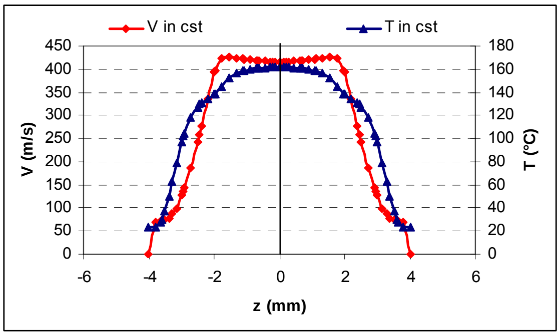

Figure 2.36: Velocity and temperature profile at the constant area chamber inlet section.

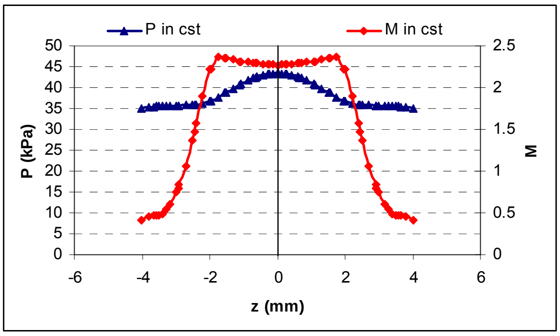

Figure 2.37: Mach number and pressure profile at the constant area chamber inlet section.

The profiles of the flow at the diffuser inlet section, Figures 2.38 and 2.39, show a nearly constant velocity at the center around 450 m/s and a Mach number around 2.5. These values are close to the ones given by the 1D model 446 m/s and 2.498.

Gradients of velocity and Mach number occur between the border from 180 m/s and 0.8 to 450 m/s and respectively 2.5. The temperature varies from 144°C at the center to 112°C at the border. The pressure at the center is nearly constant around 25 kPa. A small increase of pressure occurs at the border from 25 to 33 kPa. By comparing the diffuser inlet section to the constant inlet section, an expansion occurs through the constant area section. In addition, the velocity profile through the constant area chamber shows that 3 $D_{\text{cst area}}$ is a sufficient length to ensure the inlet nozzle section properties.

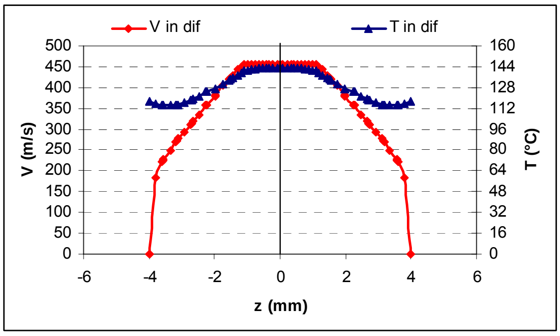

Figure 2.38: Velocity and temperature profile at the diffuser inlet section.

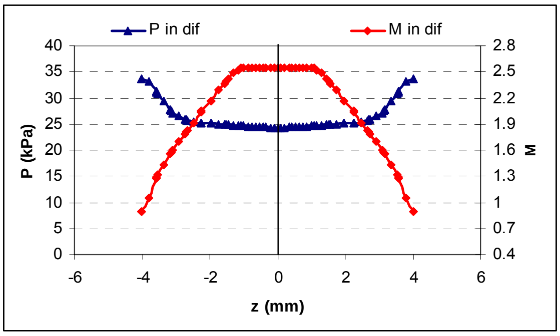

Figure 2.39: Mach number and pressure profile at the diffuser inlet section.

The pressure at the ejector outlet is fixed to 80 kPa to match the entrainment ratio w of the 1D model. The velocity profile at the ejector outlet section, Figure 2.40, shows that a large part of the dynamic pressure is not converted into static pressure, so the length of the diffuser is not sufficient, so the diffuser should have a larger length about 9 $D_{\text{cst area}}$ with the same outlet diameter.

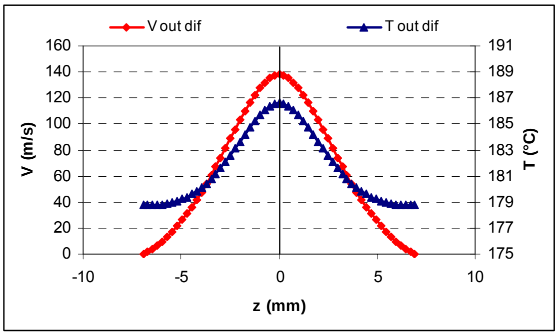

Figure 2.40: Velocity and temperature profile at the outlet section.

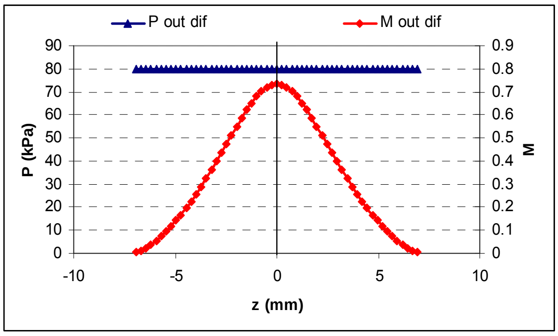

Figure 2.41: Mach number and pressure profile at the outlet section.

The velocity and pressure profiles through the ejector with the larger diffuser show the same flows as the previous ejector up to the diffuser inlet. The new diffuser converts more efficiently velocity to pressure than the previous one.

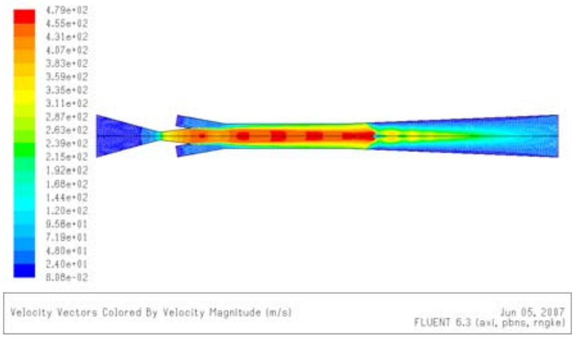

Figure 2.42: Velocity of the internal flow in the ejector with larger diffuser.

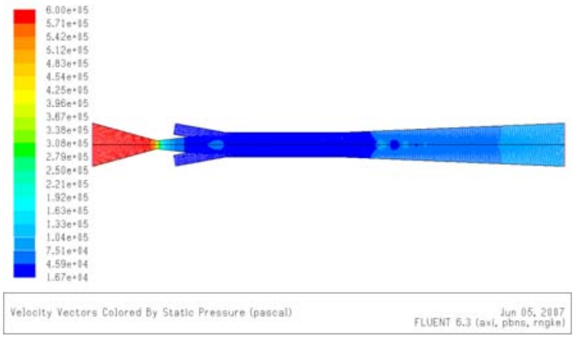

Figure 2.43: Pressure of the internal flow in the ejector with larger diffuser.

The flows through the two diffusers show that chock waves occur when a change of diameters occurs, as shown in Figures 2.44 and 2.45. For the small diffuser, a big oblique chock wave occurs at the diffuser inlet followed by many other small oblique chock waves to compress the flow; but in the larger diffuser, a big chock wave occurs at the diffuser inlet followed by smaller oblique choke waves. Thus by increasing the length of the diffuser, less oblique chock waves occur and the flow will reach a higher outlet pressure due to the decrease of entropy generation by the chock waves.

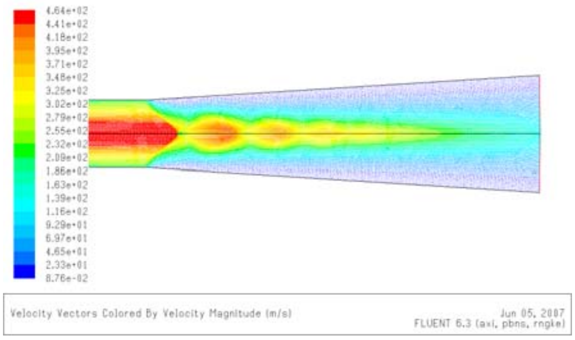

Figure 2.44: Shock wave in the diffuser of the ejector.

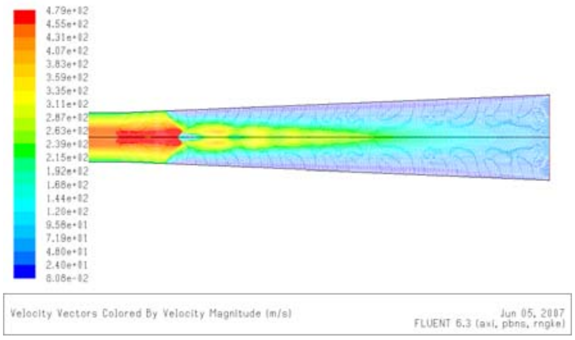

Figure 2.45: Shock wave in the diffuser of the ejector with taller diffuser.

By increasing the diffuser length, the velocity profile at the diffuser inlet section, Figure 2.46, is the same for the two diffusers, but the pressure is uniform, around 25 kPa, for the largest diffuser, see Figure 2.47. In addition, the variation of the velocity profile at the diffuser outlet section is reduced, as shown in Figures 2.48 and 2.49. Thus, the increase in the diffuser length improves the converting process of the velocity to pressure.

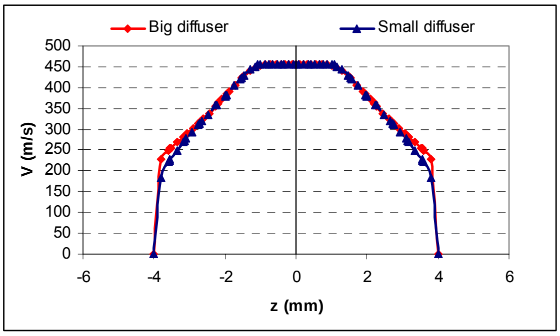

Figure 2.46: Velocity profile at the diffuser inlet section.

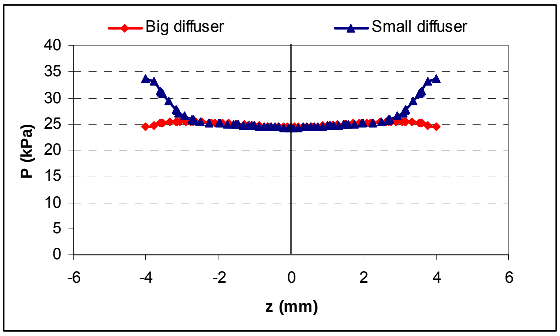

Figure 2.47: Pressure profile at the diffuser inlet section.

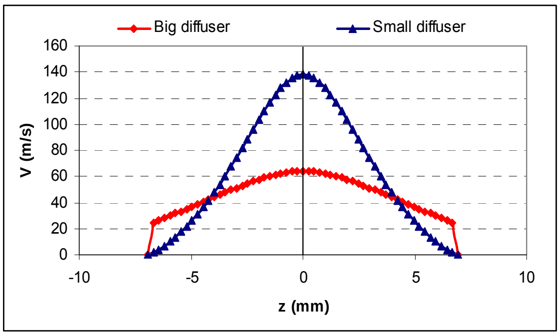

Figure 2.48: Velocity profile at the ejector outlet section.

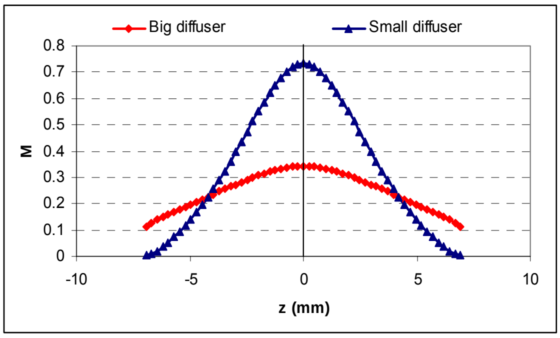

Figure 2.49: Mach number profile at the ejector outlet section.

The diffuser flow comparison between the ejector with the small diffuser: 8 D $_{\text{cst area}}$ (48 mm) and the ejector with the larger diffuser: 9 D $_{\text{cst area}}$ (72 mm) by conserving the same outlet diameter is shown in Figures 2.46, 2.47, 2.48, and 2.49.

An ejector with the same nozzle and the same secondary inlet geometry as the previous one, with the larger diffuser: 9 D $_{\text{cst area}}$, and with a constant area chamber length of 3 D $_{\text{cst area}}$ is simulated, Figure 2.50. Similar results to the ejector with the larger diffuser are obtained.

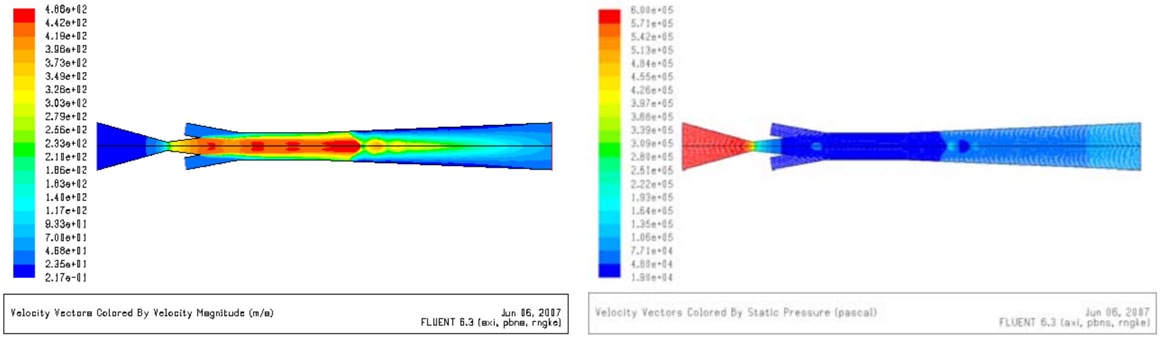

Figure 2.50: Velocity and pressure of the ejector flow with 3 D$_{\text{cst area}}$ as constant area chamber and 9 D $_{\text{cst area}}$ as diffuser length.

In conclusion, the nozzle distance from constant area chamber is equal to 1.5 D $_{\text{cst area}}$, a length of the constant area chamber longer than 3 D $_{\text{cst area}}$, and a diffuser length longer than 9 D $_{\text{cst area}}$ are optimal geometrical parameters for ejector optimal operation.

2.4.4 1D simulation of an ejector cycle with liquid / supercritical inlet as primary fluid

A theoretical model is elaborated to study the behavior of a sub-cooled expansion ejector refrigeration cycle, using mass, momentum, and energy conservation equations. To simplify the theoretical model of the ejector expansion refrigeration cycle, the following assumptions are made:

1. Friction at the walls is neglected, as well as the pressure drop in the gas cooler, the evaporator and the connection tubes.
2. All the components are thermally insulated, so there are no heat losses to the environment from the system except the heat rejection in the gas cooler. The ejector is adiabatic, rigid, and impermeable.
3. The vapor stream from the separator is in saturated state and the liquid stream from the separator is also saturated.
4. The flow across the expansion valve is isenthalpic.
5. The compressor has a constant isentropic efficiency independent of the compression ratio or the compressor speed.

6. The evaporator outlet is either saturated vapor or superheated vapor, the gas cooler outlet temperature is determined by the ambient temperature.
7. The flow in the ejector is a 1D homogeneous equilibrium flow and steady throughout the ejector. All fluid properties are uniform across their respective cross-sectional area.
8. The primary stream and the secondary stream reach the same pressure at the inlet of the constant area mixing section of the ejector. There is no mixing between the two streams before the inlet of the constant area mixing section. The inlet velocities of the primary and secondary flows are negligible. Homogeneous equilibrium flow conditions are considered at the nozzle outlet in the primary flow.
9. The isentropic expansion efficiencies of the primary stream and secondary stream are constant. The isentropic compression efficiency of the ejector diffuser is also constant.

Considering the above assumptions and applying the conservation equations on the different control volumes of the ejector shown in Figure 2.51, the ejector refrigeration cycle equations have been established.

The pressure in the control volume CV a-a'-b is considered constant and equal to P_L. The pressure P_L is lower than the evaporator pressure P_2, the pressure drop ΔP is the driving potential of the secondary stream flow. The entrainment ratio w is given as the mass ratio between the primary and secondary streams.

The inputs of the sub-cooled ejector refrigeration cycle 1D model are:

- The pressure drop ΔP.
- The gas cooler exit temperature T_1 (T_{gc}) and pressure P_1 (P_{gc}).
- The evaporation temperature T_5.
- The superheat at the evaporator outlet TS.
- The nozzle efficiency η_n and the mixture efficiency η_m..
- The secondary stream expansion efficiency η_s.
- The diffuser efficiency η_d .
- The compression isentropic efficiency η_{comp}.

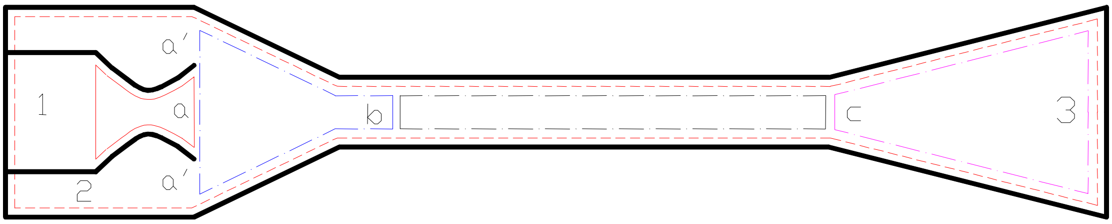

Figure 2.51: Specification of control volume for the one dimensional flow model.

Considering the control volume 1-a, the primary stream is accelerated as its pressure drops from P_1 to P_L. An isentropic expansion process is used to determine the actual state parameters.

$$m_1 = m_a = m_p \tag{2.51}$$

$$h_1 = f\,(P_1, T_1) \tag{2.52}$$

$$s_1 = f\,(P_1, T_1) \tag{2.53}$$

$$h_{a,p,is} = f\,(s_{1,p}, P_L) \tag{2.54}$$

Using the definition of expansion efficiency, the real enthalpy $h_{a,p}$ is calculated by:

$$\eta_n = \frac{h_{1,p} - h_{a,p}}{h_{1,p} - h_{a,p,is}} \Rightarrow h_{a,p} = h_{1,p} - \eta_n (h_{1,p} - h_{a,p,is}) \tag{2.55}$$

By applying the conservation of energy on CV 1-a considering assumption 8, the velocity of the primary stream at section 2 is:

$$h_{1,p}+\frac{1}{2}v_{1,p}^{2}=h_{a,p}+\frac{1}{2}v_{a,p}^{2} \Rightarrow \mathrm{v_{a,p}}=\sqrt{2(h_{1,p}-h_{a,p})+v_{1,p}^{2}}=\sqrt{2\,\eta_{n}(h_{1,p}-h_{a,p,is})} \qquad (2.56)$$

Section b is located in the constant area part of the ejector. Section b is considered as the mixing section between the primary and the secondary streams. The secondary stream expands, with expansion efficiency η_s, from P_3 to P_L in CV a-a'-b. The calculation sequence for the secondary stream is identical to the one for the primary stream.

$$m_2 = m_{a'} = m_s \qquad (2.57)$$

$$h_{b,s,is} = f\,(\,s_{2,s}\,,\,P_L) \qquad (2.58)$$

$$\eta_s=\frac{h_{2,s}-h_{b,s}}{h_{2,s}-h_{b,s,is}} \Rightarrow \mathrm{h_{b,s}}=h_{2,s}-\eta_s(h_{2,s}-h_{b,s,is}) \qquad (2.59)$$

$$h_{2,s}+\frac{1}{2}v_{2,s}^{2}=h_{b,s}+\frac{1}{2}v_{b,s}^{2} \Rightarrow \mathrm{v_{b,s}}=\sqrt{2(h_{2,s}-h_{b,s})+v_{2,s}^{2}}=\sqrt{2\,\eta_{s}(h_{2,s}-h_{b,s,is})} \qquad (2.60)$$

The properties of the primary stream are the same at section b of CV a-a'-b. Applying the mass conservation on section b gives:

$$m_{b,m} = m_{b,p} + m_{b,s}\ ;\ v_{b,p} = v_{a,p}\ ;\ w=\frac{m_s}{m_p} \qquad (2.61)$$

The density of primary and secondary streams can be calculated at section b as a function of enthalpy and pressure:

$$\rho_{\,b,p} = f\,(\,h_{b,p},\,P_L\,) \qquad (2.62)$$

$$\rho_{\,b,s} = f\,(\,h_{b,s},\,P_L\,) \qquad (2.63)$$

The area portion of section b occupied by the primary and secondary streams are given by:

$$m_{b,p} = \rho_{b,p}\,v_{b,p}\,A_{b,p} \qquad (2.64)$$

$$m_{b,s} = \rho_{b,s}\,v_{b,s}\,A_{b,s} \qquad (2.65)$$

Dividing by $m_{b,m}$, generalized equations become:

$$a_{b,p}=\frac{1}{(1+w)\rho_{b,p}v_{b,p}} \qquad (2.64')$$

$$a_{b,s}=\frac{w}{(1+w)\rho_{b,s}v_{b,s}} \qquad (2.65')$$

To calculate the properties of the mixture of the two streams, an iteration loop is applied. Applying the conservation of momentum at section b gives:

$$(P_L\;\mathrm{A_{b,p}}+\eta_{\mathrm{m}}\mathrm{m_{b,p}}\;\mathrm{v_{b,p}}\,)+(P_L\;\mathrm{A_{b,s}}+\eta_{\mathrm{m}}\mathrm{m_{b,s}}\;\mathrm{v_{b,s}}\,)=\mathrm{P}_m\,(\mathrm{A_{b,p}}+\mathrm{A_{b,s}})+m_{b,m}v_{b,m}. \qquad (2.66)$$

The unknowns are P_m and $v_{b,m}$. Applying the conservation of energy and assumption 8 on the CV 1-2-b give:

$$\mathrm{m}_{1,p}\,\mathrm{h}_{1,p}+\mathrm{m}_{2,s}\,\mathrm{h}_{2,s}=\mathrm{m}_{b,m}\left(h_{b,m}+\frac{1}{2}v_{b,m}^2\right) \tag{2.67}$$

Dividing by $m_{b,m}$ gives:

$$(P_L\ \mathrm{a}_{b,p}+\frac{1}{1+\mathrm{w}}\eta_{\mathrm{m}}\ \mathrm{v}_{b,p})+(P_L\ \mathrm{a}_{b,s}+\frac{\mathrm{w}}{1+\mathrm{w}}\ \eta_{\mathrm{m}}\mathrm{v}_{b,s})=\mathrm{P}_m\ (\mathrm{a}_{b,p}+\mathrm{a}_{b,s})+v_{b,m} \tag{2.68}$$

$$\frac{1}{1+\mathrm{w}}\,\mathrm{h}_{1,p}+\frac{\mathrm{w}}{1+\mathrm{w}}\,\mathrm{h}_{2,s}=h_{b,m}+\frac{1}{2}v_{b,m}^2 \tag{2.69}$$

To solve the equations for a given w, the mixture pressure P_m is guessed, then Equation (2.68) gives $v_{b,\,m}$ that gives the mixture enthalpy $h_{b,m}$ from Equation (2.69). Knowing the pressure and the enthalpy of the mixture, the mixture density is then calculated:

$$\rho_{b,m} = f\ (h_{b,m},P_m\ ) \tag{2.70}$$

The loop condition is the mass conservation in the constant area:

$$m_{b,m}=\rho_{b,m}v_{b,m}(A_{b,p}+A_{b,s})\ \Leftrightarrow\ \rho_{b,m}v_{b,m}(a_{b,p}+a_{b,s})=1 \tag{2.71}$$

The flow properties at section c are the mixture properties. Knowing the pressure and the enthalpy of the mixture, the entropy is then calculated:

$$s_{b,m} = f\ (h_{b,m},P_m) \tag{2.72}$$

Considering CV 1-2-3, the flow enthalpy at the ejector outlet at section 3 is given by applying the conservation of energy:

$$m_{1,p}\ h_{1,p} + m_{2,s}\ h_{2,s} = m_3\ h_3 \ \leftrightarrow\ h_{1,p} + w\ h_{2,s} = (1 + w\ )\ h_3 \tag{2.73}$$

The ejector outlet pressure is calculated as a function of the “isentropic” enthalpy and the entropy. The isentropic enthalpy is given from the diffuser expansion efficiency η_d.

$$\eta_d=\frac{h_{3,is}-h_c}{h_3-h_c}\Rightarrow \mathrm{h}_{3,is}=h_c\ +\eta_d(h_3-h_c) \tag{2.74}$$

$$P_3 = f(h_{3,is},s_{b,m}) \tag{2.75}$$

$$x_3 = f(h_3,\ P_3) \tag{2.76}$$

Assumption 3 and applying the continuity equation on the separator give the following condition to realize the cycle:

Liquid flow: $m_s = m_4 = m_3\ (1 - x_3) \leftrightarrow w = (1 + w)(1 - x_3)$ (2.77)

Vapor flow: $m_p = m_6 = m_3\ x_3 \leftrightarrow 1 = (1 + w)\ x_3$ (2.77')

To fulfill this condition, an iteration loop is used with a guessed value of entrainment ratio w_0. The iteration loop begins from Equation (2.64') to Equation (2.77).

For an entrainment ratio lower than the equilibrium value, an accumulation of liquid in the separator occurs, and for an entrainment ratio higher than the equilibrium value, the excess vapor is expanded at the ejector low pressure inlet to fulfill the continuity of the separator.

The cycle performances are given as follows:

$$h_4 = f(P_3, x_4 = 0) \tag{2.78}$$
$$h_6 = f(P_3, x_6 = 1) \tag{2.79}$$
$$h_{2,sat} = f(T_5\ , x_2 = 1) \tag{2.80}$$
$$T_2 = T_5 + TS \tag{2.81}$$
$$h_2 = f(T_2, P_2) \tag{2.82}$$
$$s_6 = f(P_3, x_6 = 1) \tag{2.83}$$
$$h_{7,is} = f(P_1, s_6) \tag{2.84}$$
$$h_7 = h_6 + (h_{7,is} - h_6)/\ \eta_{comp} \tag{2.85}$$

The evaporator cooling capacity is given by:

$$Q_{ev} = m_4\ (\ h_4 - h_{2,sat}) \ \leftrightarrow q_{ev} = (m_4 / m_6\ )\ (\ h_{2,sat} - h_4) \leftrightarrow q_{ev} = w\ (h_{2,sat} - h_4) \tag{2.86}$$

The compression work is:

$$W_{comp} = m_6\ (\ h_7 - h_6) \leftrightarrow w_{comp} = (m_6\ /\ m_6\ )\ (\ h_7 - h_6) \leftrightarrow w_{comp} = (\ h_7 - h_6) \tag{2.87}$$

Then, the COP of the ejector expansion cycle can be determined by:

$$COP_{ejector} = \frac{w\ \left(h_{2,sat} - h_4\right)}{h_7 - h_6} \tag{2.88}$$

For given parameters: the isentropic efficiencies of nozzle, secondary stream, diffuser, and compressor; the gas cooler exit temperature; the evaporation temperature; the superheat at the evaporator outlet, the COP of the ejector expansion cycle depends of the gas cooler pressure P_{gc} and the pressure drop ΔP between P_{ev} and P_L.

The compression ratio of the ejector is defined as:

$$CR = P_3/P_2 \tag{2.89}$$

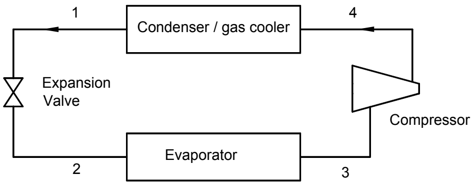

Figure 2.52 : Scheme of a conventional refrigeration cycle.

For the conventional transcritical CO_2 cycle, Figure 2.52, the COP is calculated as follows:

$$h_1 = f\ (\ P_1,\ T_1) \tag{2.90}$$
$$h_2 = h_1 \tag{2.91}$$
$$h_{3,sat} = f\ (\ T_2,\ x_3 = 1) \tag{2.92}$$
$$T_3 = T_2 + TS \tag{2.93}$$
$$h_3 = f\ (\ P_3,\ T_3) \tag{2.94}$$
$$s_3 = f\ (\ P_3,\ T_3) \tag{2.95}$$
$$h_{4,is} = f\ (\ P_4,\ s_3) \tag{2.96}$$
$$h_4 = h_3 + (h_{4,is} - h_3)/\eta_{comp} \tag{2.97}$$

The specific evaporator capacity and compression work are:

$$q_{ev} = h_{3,sat} - h_2 \qquad (2.98)$$

$$w_{comp} = h_4 - h_3 \qquad (2.99)$$

So, the COP of the conventional transcritical cycle will be:

$$\mathrm{COP}_{\mathrm{conventional}} = \frac{\left(h_{3,sat} - h_2\right)}{h_4 - h_3} \qquad (2.100)$$

The conventional COP depends on the gas cooler pressure. An optimum pressure exists allowing maximum COP for a specified evaporation temperature and a gas cooler exit temperature. So, the comparison factor F, between the conventional transcritical cycle and the ejector one, is considered in the case of optimum pressure.

$$F = \frac{COP_{ejector}}{COP_{conventional}} \qquad (2.101)$$

The outputs of the sub-cooled ejector refrigeration cycle 1D model are:

- The cycle thermodynamic properties: T, P, h, s, ρ.
- The optimal entrainment ratio w.
- The ejector outlet pressure and temperature.
- The mixing velocity, density and pressure.
- The ejector compression ratio.
- The comparison factor.

Considering the above theoretical model, the influence of pressure drop ΔP and gas cooler pressure P_{gc} on the comparison factor is investigated using REFPROP7 to calculate the refrigerant thermodynamic properties. The study is extended to evaluate the influence of different operating conditions for a given pressure drop ΔP on the comparison factor F.

2.4.5 Theoretical results of liquid / supercritical inlet ejector model

The following standard operating conditions are assumed for calculations:
$T_{gc,out} = T_1 = 35°C$, $T_{ev} = T_5 = 2°C$, TS = 5 K.
The ejector efficiencies are: $\eta_n = \eta_s = 0.85$, $\eta_d = 0.75$. These values are chosen smaller than the values of the vapor ejector model because there is a phase change, and because the mixture efficiency η_m is taken equal to 1. The isentropic compression efficiency is assumed equal to 0.8.

For these operating conditions, Table 2.6 for different refrigeration cycles is built to compare the performances and the optimum operating pressure of gas cooler. The isentropic expansion efficiency of expander is taken equal to 0.5.

The comparison between different CO_2 refrigeration cycles show that the CO_2 transcritical ejector cycle presents a coefficient of performance close the COP of the cycle with isentropic expander. Thus, the CO_2 transcritical ejector improves the cycle performance without using movable parts, and possibly with an easier control.

Table 2.6: Comparison of different CO_2 transcritical cycle performances.

Refrigeration cycle configuration	COP	COP with isentropic expansion without work recovery	$P_{optimum}$ MPa	$P_{intermediate}$ MPa
Conventional	2.820		8.758	
Conventional with isentropic expansion	3.418	2.944	8.559	
Two stages of compression in series with inter-cooling	3.102		9.934	8.123
Two stages of compression in series with isentropic expansion and inter-cooling	3.739	3.2365	9.8123	8.116
Two stages of compression with indirect injection	3.25		8.488	5.552
Two stages of compression with indirect injection and isentropic expansion	3.878	3.341	8.478	5.518
Ejector transcritical refrigeration cycle DP = 3.467 bar, w = 0.5353, P_{mix} = 39.17 bar.	3.696		8.513	4.4

The consequence of the pressure drop ΔP in the constant pressure chamber of the ejector P_{ev} - P_L on the F factor is shown on Figure 2.53. It can be seen that for the given conditions, the ejector expansion transcritical CO_2 cycle can achieve more than 30% COP improvements over the conventional transcritical CO_2 cycle for an optimum pressure drop of 347 kPa, which depends on the nozzle geometric properties and on the operating conditions of the ejector. Increasing the pressure drop increases the ejector compression ratio, decreases the compressor compression ratio, and improves the cycle performances, but shows an optimum CR value at 1.198. The compression ratio (CR) achieves the optimum value at the optimum COP, then, the performances tend to decrease while the pressure drop increases. The optimum gas cooler pressure varies from 8.65 to 8.51 MPa (delta lower than 0.14 MPa) and the entrainment ratio w varies from 0.54 to 0.532, (delta less than 0.008) for the studied variation. The ejector outlet quality is around 0.65 ± 0.0025.

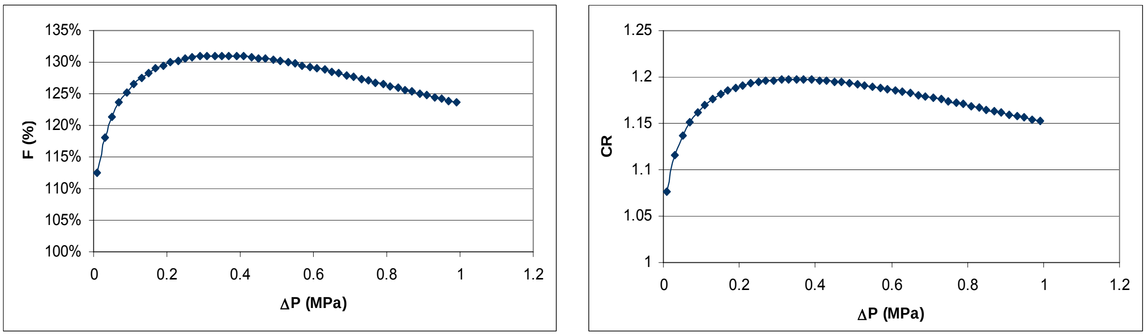

Figure 2.53: Comparison factor and compression ratio versus pressure drop.
TS = 5K, T_{ev}= 2°C, T_{gc} = 35°C.

The influence of the gas cooler pressure on the comparison factor F and the compression ratio CR of the ejector transcritical CO_2 cycle is shown in Figure 2.54. The two cycles are very dependent on the gas cooler pressure, and show an optimum gas cooler pressure for optimum energy performances. It can be seen that the comparison factor F of the ejector expansion transcritical CO_2 cycle decreases with the increase in the gas cooler pressure. At the optimum pressure, factor F is not at its maximum value; the optimum enhancement varies from –4% to 50% according to the pressure drop. As the gas cooler pressure increases, CR decreases to a minimum value that corresponds to the optimum gas cooler pressure, and then continues to slightly increase with pressure for different pressure drops. Factor F and CR increase with the pressure drop to reach the optimum pressure drop (that is above 0.1 MPa).

The optimum pressure and the COP of the ejector cycle are respectively:

- 8.643 MPa and 3.171 for ΔP = 0.01 MPa,
- 8.570 MPa and 3.422 for ΔP = 0.05 MPa, and
- 8.542 MPa and 3.55 for ΔP = 0.1 MPa

whereas the conventional cycle gives an optimum pressure of 8.755 MPa and a COP of 2.82. The entrainment ratio w increases strongly with the gas cooler pressure until it reaches the optimum pressure, after which it increases slightly. However, the entrainment ratio w is basically independent of the pressure drop.

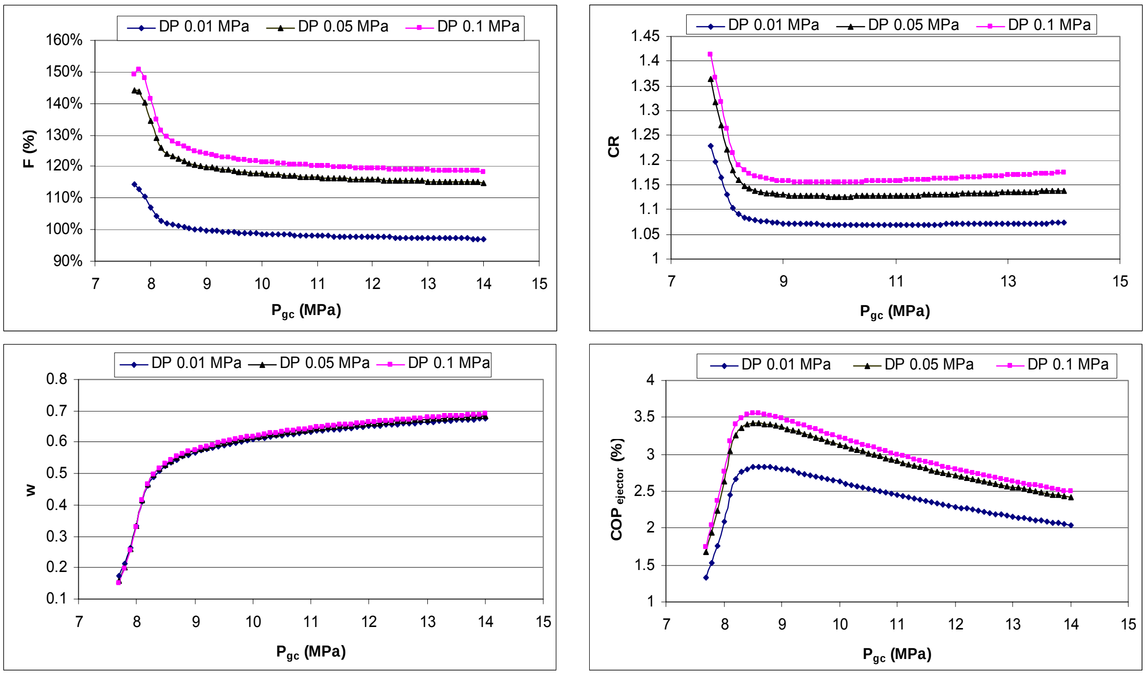

Figure 2.54: COP, w, Comparison factor and compression ratio versus gas cooler pressure. TS = 5K, T_{ev}= 2°C, T_{gc} = 35°C

The effect of the gas cooler outlet temperature on F and CR of the ejector transcritical CO_2 cycle are shown in Figure 2.55. It can be seen that F is almost constant while increasing the gas cooler outlet temperature, so the ejector cycle and the conventional cycle performances decrease proportionally to the increase of the gas cooler outlet temperature. CR increases due to the increase of the optimum gas cooler pressure with T_{gc}. The pressure drop enhances F and increases CR because the optimum pressure drop is above 0.1 MPa. The entrainment ratio w decreases linearly with T_{gc} from 0.56 at 33°C to 0.39 at 60°C.

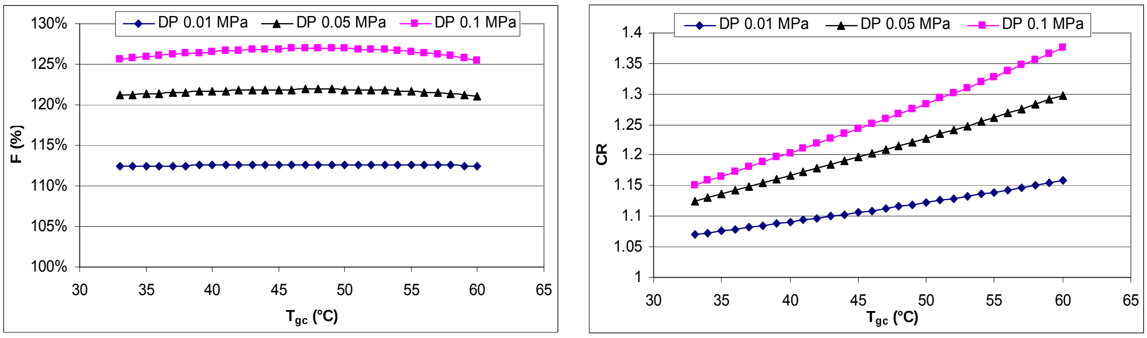

Figure 2.55: Comparison factor and compression ratio versus gas cooler outlet temperature. TS = 5K, T_{ev} = 2°C.

The effect of the evaporation temperature on F and CR of the ejector transcritical CO_2 cycle are shown in Figure 2.56. It can be seen that F is almost constant while decreasing the evaporation temperature, so the ejector cycle and the conventional cycle performances decrease proportionally with the evaporation temperature reduction. The optimum gas cooler pressure and the entrainment ratio vary slightly, respectively, around 8.6 ± 0.2 MPa and 0.54 ± 0.02 for pressure drops between 0.01 and 0.1 MPa and evaporation temperature between –5 and 15°C. CR decreases with the increase of the evaporation temperature. With lower evaporation temperatures, the evaporating pressure decreases, so the ejector expansion process increases because the gas cooler optimum pressure is almost constant, yielding to a compression ratio increase. F and CR increase with pressure drop because the optimum pressure drop is above 0.1 MPa.

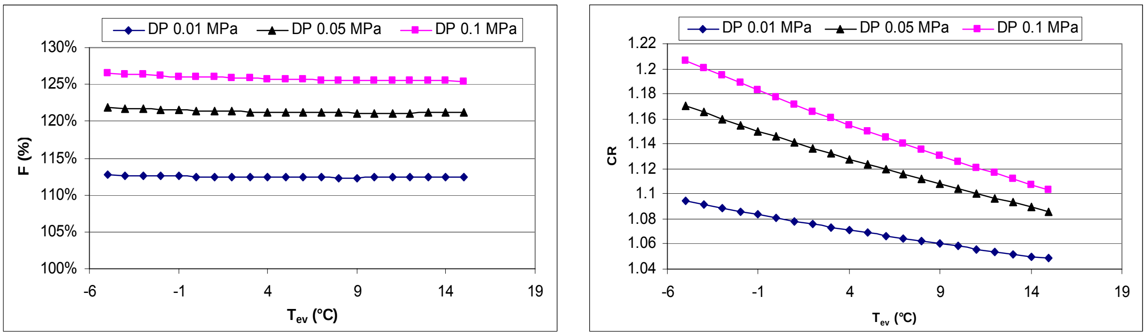

Figure 2.56: Comparison factor and compression ratio versus evaporator temperature. TS = 5 K, T_{gc}= 35°C.

The effect of the evaporator outlet superheat on F and the pressure ratio of ejector transcritical cycle are shown in Figure 2.57. It can be seen that an increase of the superheat increases F because the superheat penalizes the performance of the conventional cycle more than the ejector one. In the conventional cycle, the compressor suction is superheated, which increases the entropy at the compressor inlet and so the compression work, while in the ejector cycle, the compressor inlet state is saturated vapor and the secondary stream is superheated, which penalizes the entrainment ratio because of the mixture vapor quality increase. Increasing the evaporator superheat will decrease the evaporator capacity for both the conventional cycle and the ejector cycle b. CR is almost constant, increasing slightly with the superheat. The optimum gas cooler pressure is almost constant around 8.6 MPa for different pressure drops. F and CR increase with pressure drop because the optimum pressure drop is above 0.1 MPa.

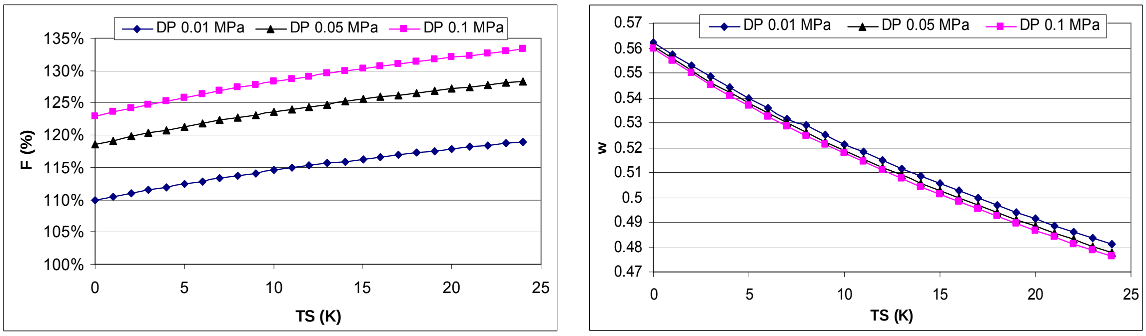

Figure 2.57: Comparison factor and compression ratio versus evaporator outlet superheat. T_{gc} = 35°C, T_{ev}= 2°C.

2.5 Performance comparison of fluids: CO_2 and R-134a

When the ejector expansion cycle works in sub-critical conditions (condenser outlet in liquid phase), the cycle performances are degraded in the CO_2 case. Tables 2.7 and 2.8 show the performance of CO_2 and R-134a in conventional cycles and ejector expansion cycles.

The following standard operating conditions are assumed: T_{ev} = 2 and -10 °C, TS = 5 K. The ejector efficiencies are: $\eta_n = \eta_s = 0.85$, $\eta_d = 0.75$. The isentropic compression efficiency is 0.8 for CO_2 and 0.7 for R134a.

Table 2.7: Optimum operation of CO_2 ejector cycle.

CO_2 η_{comp} = 0.8										
T_{evap} °C / P_{ev} MPa	T_{gc} / condenser °C	COP ejector	COP_{conv}	$P_{gc\ ejector}$ MPa	DP MPa	$P_{mixture}$ MPa	P_{out} ejector MPa	W	$P_{gc\ conv}$ MPa	F (%)
2 / 3.67	22	8.182	6.856	6.0	0.1440	3.728	3.922	0.7251	6.0	119.3%
	28	5.611	4.430	6.892	0.2290	3.7954	4.1171	0.6142	6.892	126.7%
	30	4.833	3.684	7.214	0.2708	3.8484	4.2405	0.55	7.214	131.2%
	35	3.696	2.820	8.513	0.3467	3.917	4.399	0.5352	8.755	131.0%
-10 / 2.65	35	2.653	1.995	8.608	0.3763	2.9476	3.4182	0.5133	8.968	133.0%
2 / 3.67	45	2.451	1.807	11.136	0.5477	4.1732	4.8502	0.4682	11.682	135.7%

For CO_2 at 2°C, the optimum ejector cycle performances decrease when the gas cooler temperature increases; the F factor, the optimum pressure drop, the mixture pressure and the ejector outlet pressure increase but the entrainment ratio w decreases with the increase of the gas cooler pressure, because the nozzle outlet vapor quality increases; that is why the ejector cycle COP decreases.

Table 2.8: Optimum operation of R134a ejector cycle.

R-134a η_{comp} = 0.7										
T_{evap} °C / P_{ev} KPa	T_{gc} / condenser °C	COP ejector	COP_{conv}	$P_{gc\ ejector}$ KPa	DP KPa	$P_{mixture}$ KPa	$P_{out\ ejector}$ KPa	w	$P_{gc\ conv}$ KPa	F (%)
2 / 314.6	22	8.949	8.492	608	6	316	324	0.8478	608	105.4%
	28	6.771	6.322	727	9.6	317.5	330.2	0.8096	727	107.1%
	35	5.220	4.773	887	14.9	320	340	0.7651	887	109.4%
-10 / 200.6	35	3.568	3.169	887	17.9	208	230.6	0.7095	887	112.6%
2 / 314.6	45	3.862	3.409	1160	24.7	325.9	357.7	0.7014	1160	113.3%

For R-134a at 2°C, the same behavior is noticed, but the performance improvements are lower than that of CO_2 ejector cycle, also the pressure drop is smaller. The R-134a ejector cycle is very sensible to the pressure drop in the heat exchangers: condenser, evaporator, IHX and in the connecting tubes.

For comparison, it can be seen in Figure 2.58 that the CO_2 ejector cycle performances approach the R-134a conventional performances at low gas cooler temperature and are higher than the CO_2 conventional cycle performance.

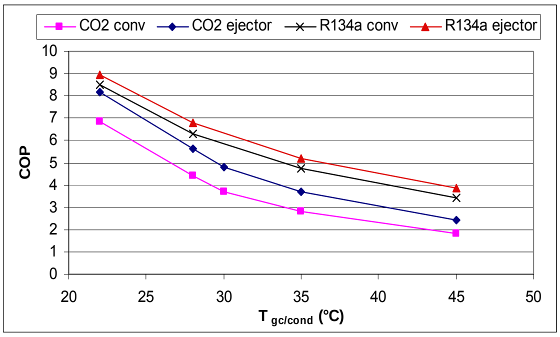

Figure 2.58: Comparison of optimum performance of CO_2 refrigerant with R-134a refrigerant.

2.6 Conclusions

In this chapter, the refrigeration cycle with ejector was presented. The two types of ejector refrigeration cycle: superheated vapor ejector cycle and sub-cooled/ supercritical ejector cycle have been studied.

For the superheated vapor ejector cycle, a 1D vapor model has been elaborated, and the results for dry refrigerant R-141b have been compared to experimental results from bibliography. A CFD analysis of an ejector with R-141b vapor flow has been done, and the internal flow properties have been compared to the 1D vapor model.

For the sub-cooled / supercritical ejector cycle, a 1D two-phase model has been elaborated. Using the 1D model, the ejector with two-phase flows has been characterized, and the effects of different cycle parameters have been described for CO_2 as refrigerant.

A comparison between CO_2 and R-134a for the conventional refrigeration cycle and sub-cooled/supercritical ejector refrigeration cycle has shown that the ejector cycle improves more the CO_2 system energy performances than to R-134a system.

The 1D two-phase model will be used to design different ejectors. When realized, they will be tested on a test bench to validate the model and to verify the energy gains. In addition, the 1D two-phase model will also be used to analyze different ejectors with different geometries.

References

[AID 04] Z. Aidoun, M. Ouzzane: “The effect of operating conditions on the performance of a supersonic ejector for refrigeration”, International journal of refrigeration 27,974-984, 2004.

[ALE 03] G.K. Alexis, E.D. Rogdakis: “ A verification study of steam-ejector refrigeration model”, Applied Thermal Engineering 23 (2003) 29–36.

[ALE 04] G.K. Alexis: “Estimation of ejector’s main cross sections in steam-ejector refrigeration system”, Applied Thermal Engineering 24 (2004) 2657–2663.

[ALE 05] G.K. Alexis, E.K. Karayiannis: “A solar ejector cooling system using refrigerant R134a in the Athens area”, Renewable Energy 30 (2005) 1457–1469.

[ANS 04] H. A. M. Al-Ansary, “INVESTIGATION AND IMPROVEMENT OF EJECTOR DRIVEN HEATING AND REFRIGERATING SYSYEMS”; thesis at Georgia Institute of technology, April 2004.

[ANS 04] Hany A.M Al-Ansary, Sheldon M. Jeter: “Numerical and experimental analysis of single-phase and two-phase flow in ejectors”, Volume 10, Number 4, October 2004.

[BAR 05] Y. Bartosiewicz , Zine Aidoun , P. Desevaux, Yves Mercadier : "Numerical and experimental investigations on supersonic ejectors (CFD modelisation)”, International Journal of Heat and Fluid Flow 26 (2005) 56–70.

[CHA 99] J.M. Chang, B.J. Huang : "Empirical correlation for ejector design”, International Journal of Refrigeration 22 (1999) 379–388.

[CHU 04a] Kanjanapon Chunnanond, Satha Aphornratana."Ejectors: applications in refrigeration technology”. Renewable and Sustainable Energy Reviews 8 (2004) 129–155.

[CHU 04b] Kanjanapon Chunnanond, Satha Aphornratana : “An experimental investigation of a steam ejector refrigerator: the analysis of the pressure profile along the ejector”, Applied Thermal Engineering 24 (2004) 311–322.

[CIZ 05] K. Cizungu, M. Groll, Z.G. Ling: “Modelling and optimisation of two-phase ejectors for cooling systems”, Applied Thermal Engineering 25 (2005) 1979–1994.

[DIS 04] Somjin Disawas, Somchai Wongwises. "Experimental investigation on the performance of the refrigeration cycle using a two-phase ejector as an expansion device". International Journal of Refrigeration 27 (2004) 587–594.

[DOR 95] R. Dorants et A. Lallemand : "Prediction of performance of a jet cooling system operating with pure refrigerants or non-azeotropic mixtures”, Revue International du Froid 1995 Volume 18 Numéro 1, p. 21-30.

[EAM 02] Ian W. Eames: “A new prescription for the design of supersonic jet-pumps: the constant rate of momentum change method”, Applied Thermal Engineering 22 (2002) p. 121-131.

[EAM 95] I.W. Eames, S. Aphornratana and H.Haider: “A theoretical and experimental study of a small-scale steam jet refrigerator”, International Journal of refrigeration Volume 18 Number 6; 378 – 386, 1995.

[ELB 06] Stefan ELBEL, Predrag HRNJAK: “A THERMODYNAMIC PROPERTY CHART AS A VISUAL AID TO ILLUSTRATE THE INTERFERENCE BETWEEN EXPANSION WORK RECOVERY AND INTERNAL HEAT EXCHANGE”, R165, International Refrigeration and Air Conditioning Conference at Purdue, July 17-20, 2006.

[FUK 06] Mitsuhiro FUKUTA, Tadashi YANAGISAWA, Osamu KOSUDA and Yasuhiro OGI; 2006; “Performance of Scroll expander for CO2 Refrigeration Cycle”,*C109; Eighteenth international compressor engineering conference* at Purdue, 17-20 July 2006.

[GIU 02] Giuseppe Grazzini, Andrea Rocchetti: “Numerical optimisation of a two-stage ejector refrigeration plant”, International Journal of Refrigeration 25 (2002) 621–633.

[GRA 98] Giuseppe Grazzini and Alessio Mariani: “A simple program to design a multistage jet-pump for refrigeration cycles”, Energy Conservion and management Volume 39, No. 16-18, p. 1827-1834, 1998.

[HER 04] Jorge I. Hernandez, Ruben J. Dorantes, Roberto Best, Claudio A. Estrada: “The behaviour of a hybrid compressor and ejector refrigeration system with refrigerants 134a and 142b”, Applied Thermal Engineering 24 (2004) 1765–1783.

[HUA 01] B.J. Huang, V.A. Petrenko, J.M. Chang, C.P. Lin, S.S. Hu: “A combined cycle refrigeration system using ejector-cooling cycle as the bottom cycle”, International journal of refrigeration 24 (2001) 391-399.

[HUA 99a] B.J. Huang, J.M. Chang ."Empirical correlation for ejector design". International Journal of Refrigeration 22 (1999) 379–388.

[HUA 99b] B.J. Huang, J.M. Chang, C.P. Wang, V.A. Petrenko: “A 1-D analysis of ejector performance”, International Journal of Refrigeration 22 (1999) 354–364.

[INV 04] Costante Invernizzi , Paolo Iora: “Heat recovery from a micro-gas turbine by vapour jet refrigeration systems”, Applied Thermal Engineering (2004).

[JON] Woo Jong Hong, Khaled Alhussan, Hongfang Zhang, Charles A. Garris Jr.: “A novel thermally driven rotor-vane/pressure-exchange ejector refrigeration system with environmental benefits and energy efficiency”, Energy 29 (2004) 2331-2345.

[KIM 06] Hyun Jin Kim, Jong Min Ahn , Sung Ouk Cho, Kyung Rae Cho, “NUMERICAL SIMULATION ON SCROLL EXPANDER-COMPRESSOR UNIT FOR CO2 TRANS-CRITICAL CYCLES”, C104; *Eighteenth international compressor engineering conference* at Purdue, 17-20 July 2006.

[KOH 06] Hirokatsu Kohsokabe, Sunao Funakoshi, Kenji Tojo, Susumu Nakayama, Kyoji Kohno, Kazutaka Kurashige, “BASIC OPERATING CHARACTERISTICS OF CO2 REFRIGERATION CYCLES WITH EXPANDER-COMPRESSOR UNIT”, R159; *Eleventh international refrigeration engineering conference* at Purdue, 17-20 July 2006.

[KRU 06] Horst KRUSE, Hans RÜSSMANN, Eduardo MARTIN, Rainer JAKOBS, 2006, “Positive Displacement Carbon Dioxide Expansion Machines - Chances and Limitations”, C138; *Eighteenth international compressor engineering conference* at Purdue, 17-20 July 2006.

[LI 05] Daqing Li, Eckhard A. Groll. "Transcritical CO2 refrigeration cycle with ejector-expansion device". International Journal of Refrigeration 28 (2005) 766–773.

[NIC 05] J. Nickl, G. Will, H. Quack, W.E. Kraus. "Integration of a three-stage expander into a CO2 refrigeration system”; International Journal of Refrigeration 28 (2005) 1219–1224.

[OUZ 03] M. Ouzzane, Z. Aidoun : "Model development and numerical procedure for detailed ejector analysis and design”, Applied Thermal Engineering 23 (2003) 2337-2351.

[PRA 03] Thong Praew: “The performance of multistage condensing steam jet ejector”, I & Tantakitti, C. 2003.

[PRI 04] Wimolsiri Pridasawas, Per Lundqvist: “An exergy analysis of a solar-driven ejector refrigeration system”, Solar Energy 76 (2004) 369–379.

[RIH 06] Josef RIHA, Hans QUACK, Joerg NICKL , 2006, “SUB-CRITICAL OPERATION OF THE CO2-EXPANDER/COMPRESSOR”, *; C130; Eighteenth international compressor engineering conference* at Purdue, 17-20 July 2006.

[ROG 00] E.D. Rogdakis, G.K. Alexis: “Design and parametric investigation of an ejector in an air-conditioning system”, Applied Thermal Engineering 20 (2000) 213 – 226.

[RUS 05] E. Rusly, Lu Aye, W.W.S. Charters, A. Ooi ."CFD analysis of ejector in a combined ejector cooling system" . International Journal of Refrigeration. *Volume 28, Issue 7, November 2005, Pages 1092-1101.*

[SAN 06] T. Sankarlal, A. Mani: “Experimental studies on an ammonia ejector refrigeration system”, International Communications in Heat and Mass Transfer 33 (2006) 224–230.

[SEL 04] A. Selvaraju, A. Mani : "Analysis of a vapour ejector refrigeration system with environment friendly refrigerants”, International Journal of Thermal Sciences 43 (2004) 915–921.

[SUN 96] DA-WEN SUN: “Variable geometry ejectors and their applications in ejector refrigeration systems”, Energy volume 21, No. 10, pp. 919-929,1996.

[SUN 99] Da-Wen Sun: “Comparative study of the performance of an ejector refrigeration cycle operating with various refrigerants”, Energy Conversion & Management 40 (1999) 873 – 884.

[WES 06] Detlef Westphalen, John Dieckmann, “Scroll Expander for Carbon Dioxide Cycle”, R063; *Eleventh international refrigeration engineering conference* at Purdue, 17-20 July 2006.

[WON 05] Somchai Wongwises, Somjin Disawas: Performance of the two-phase ejector expansion refrigeration cycle", International Journal of Heat and Mass Transfer 48 (2005) 4282–4286.

[YAP 05] R. Yapıcı, H.K. Ersoy: "Performance characteristics of the ejector refrigeration system based on the constant area ejector flow model", Energy Conversion and Management 46 (2005) 3117–3135.

[YU 05] Jianlin Yu, Hua Chen, Yunfeng Ren, Yanzhong Li: "A new ejector refrigeration system with an additional jet pump", Applied Thermal Engineering (2005).

[YAN 06] J. Yang, L. Zhang, Y.J. Shi, "Development and Performance Analysis of a Two-Cylinder Rolling Piston Expander for Transcritical CO_2 System", C097; *Eighteenth international compressor engineering conference* at Purdue, 17-20 July 2006.

Chapter 3. Design of the CO_2 ejector system and test bench

Models are generally validated by referring to experiment results or for already validated models, then benchmarking on reference cases are made. Here, for the ejector 1D model a test bench has been designed to test ejectors that have been sized using the 1D model. The principal constraint that affects the test bench components is the CO_2 high pressure.

The main objectives of the test bench are:

- Control of the trans-critical parameters:
    - evaporation temperature
    - gas cooler pressure
- Validation of the 1D model of sub-cooled/ supercritical ejector cycle.

Currently, the components available for R-744 are either non-existent, or at the prototype stage. Only some companies that see an interest in the development of R-744 and having a Research and Development department propose CO_2 components.

3.1 Test Bench components

In order to reduce the costs of the test bench and to achieve high accuracy on the measured values, the heat exchangers will be cooled by water. Thus the test bench has a cooled water loop and a CO_2 refrigeration loop.

Since the triple point of water is around 0°C, and that CO_2 evaporating temperature can be controlled under 0°C, it is necessary to use an additive, like the calcium chloride $CaCl_2$, to decrease the freezing point to –40°C depending on the $CaCl_2$ concentration. The test bench is composed of three loops:

- A high temperature, water-cooling loop for CO_2 cooling at high pressure.
- A low temperature, heat transfer fluid (HTF) heating loop.
- A CO_2 refrigeration loop.

3.1.1 Water-cooling loop

The water and HTF circuits of the gas cooler and of the evaporator operate in closed loops. The additional heat coming from the compressor work and the pump work, is compensated by a plate heat exchanger cooled by city water (CWHE). The adjustments of the temperatures at the inlets of the gas cooler and of the evaporator are ensured by the control of water or HTF mass flow rates (MFRs) and the gate valves.

The water loop, Figure 3.1, is composed of two pumps, a volumetric flow meter, a city water heat exchanger (CWHE), and an internal heat exchanger (IHE), two air vents, a set of PT100 sensors to measure the temperatures, and several valves (gate and ball types) to control the required water MFR. The CWHE and the IHE are plate heat exchangers.

When the evaporating temperature is higher than 0°C, pump 2 and the internal heat exchanger are isolated by the valves, and only pump 1 ensures the water circulation through the condenser and the evaporator. The water volume flow rate is measured by a flow meter and the water temperature at the inlet and the outlet of heat exchangers are measured by PT100 sensors.

When the evaporating temperature and the evaporator HTF outlets are both at temperatures lower than 0°C, the water loops are divided in two:

- The high-temperature loop filled with water, in which the heat is absorbed from the gas cooler and released to city water and the internal heat exchangers.
- The low-temperature loop filled with HTF, in which the heat is absorbed from the internal heat exchanger and released to the evaporator.

The energy balance is always measured on the water loop because the evaluation of the HTF heat capacity leads to significant errors depending on the concentration of $CaCl_2$.

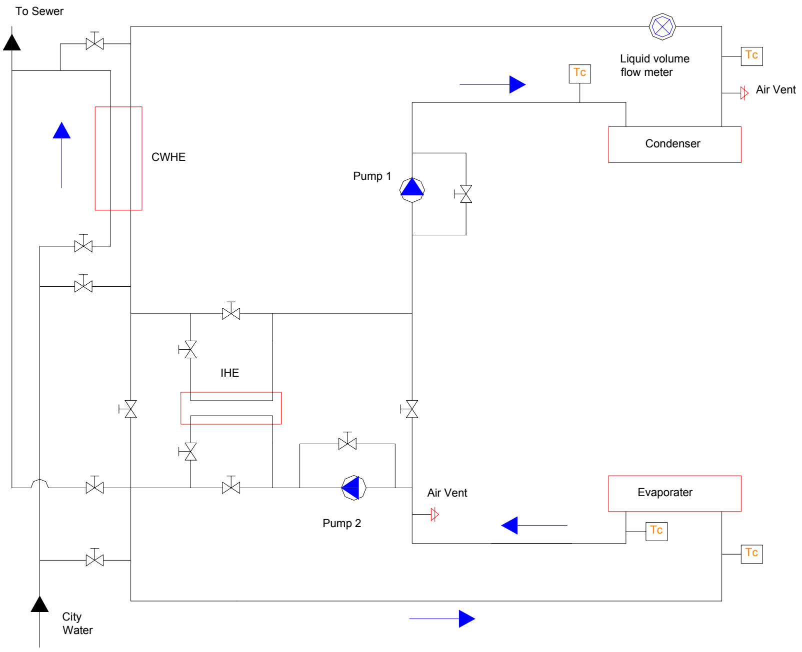

Figure 3.1: Lay-out of the test bench.

3.1.2 CO_2 refrigeration loop

The CO_2 refrigeration loop, Figure 3.2, is composed of:

- A CO_2 reciprocating compressor designed for mobile air-conditioning systems.
- An electric motor to drive the compressor.
- A water-cooled condenser/ gas cooler.
- A HTF heated evaporator.
- An ejector.
- A tow-phase separator.
- An electronic expansion valve.
- A set of ball valves.
- Pressure and temperature sensors.
- A filter, two safety valves, a mass flow meter and a torque meter.
- A data acquisition system.

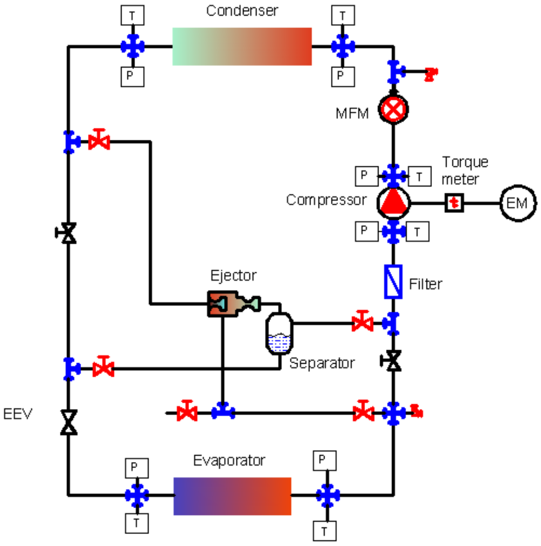

Figure 3.2: CO_2 refrigeration loop with ejector.

Components are connected by stainless tubes of 10 mm outer diameter and 1 mm thickness. These tubes withstand operating pressures higher than 25 MPa. The ball valves have a connection diameter of 10 mm and withstand pressures higher than 20 MPa. The ball valves are used to control the CO_2 MFR either for the conventional cycle operation or for the ejector refrigeration cycle operation. The safety valves are set at 14 MPa as maximal operating pressure.

3.1.3 CO_2 compressor and expansion valve

The performances of a transcritical CO_2 refrigeration cycle depends on the control the high pressure. Two components of the refrigeration system control the cycle parameters: the compressor, and the expansion valve.

Different compressor types are available for CO_2 application in mobile air conditioning systems: fixed swept volume, and variable swept volume. For the fixed swept volume, the variation of the rotation is used to control the cycle parameters. This option is convenient for electrically-driven compressors. For belt-driven compressor, where the compressor follows the engine rotation speed, the variable swept volume is the best option to control the cycle parameters.

Different types of expansion devices are also available: fixed orifice valve, thermostatic expansion valve, swiveling (reversible needle) expansion valve, and electronic expansion valve. The fixed orifice valve has no control effect; the expansion depends on the upstream and downstream pressures and temperatures. The thermostatic expansion valve controls the superheat at the evaporator outlet, and ensures a constant evaporator temperature according to its design parameters. The swiveling expansion valve controls the upstream pressure by varying the refrigerant mass flow rate. The electronic expansion valve is a variable orifice controlled by an electronic signal, it controls usually the evaporation temperature.

For the test bench, a larger flexibility of operating parameters is needed, a variable swept volume compressor with external control and an electronic expansion valve are chosen for the CO_2 refrigeration loop.

Since CO_2 equipment are not commercialized and not available in the market, a prototype compressor has been rented: a CO_2 OBRIST compressor. For the expansion device, the OBRIST electronic expansion valve has been chosen.

3.1.3.1 OBRIST compressor

The compressor represents the thermodynamic main component of the vapor compression cycle, and the overall energy performance of the system depends significantly on this component. The new developments for CO_2 compressors have started at the beginning of the 90’s and are extended today to many compressor technologies: open type, semi-hermetic and hermetic compressors, with rolling pistons, scroll, reciprocating pistons and screw.

The refrigerating capacities vary from few kW to more than 100 kW. The most advanced developments were dedicated to commercial refrigeration, heat pump water heaters (in Japan), and mobile air conditioning systems corresponding to the sectors where R-744 has the strongest potential of development. Technology is either semi-hermetic type with pistons and fixed speed for commercial refrigeration, or open type with pistons and oscillating plate: wobble or swash plate (variable displacement), for mobile air conditioning, and of all types for electric heat pump water heaters.

Many tests showed that CO_2 compressors have higher or equal performances compared to HFC compressors, due to the small swept volume and the low-pressure ratio. The CO_2 compressor performance reaches satisfactory values today but improvements are still possible. The problems are generally related to the internal leakage due to the important pressure difference between the suction and the discharge pressures; and to the vapor superheating during compression due to CO_2 properties.

The OBRIST compressor, Figure 3.3, is a swash plate axial piston compressor with external control and a pulley clutch, and a maximum swept volume of 33.5 cm^3. The external control vane is a solenoid winding that opens and closes according to the excitation signal that varies between 3 and 10 Volts. The excitation signal should be a Pulse Width Modulation PWM signal with a frequency between 10 and 40 Hz.

Figure 3.3: CO_2 OBRIST compressor.

The compressor of the vapor refrigeration cycle is characterized by three efficiency coefficients:

- Volumetric efficiency, η_v.
- Isentropic efficiency, η_{is}.
- Effective efficiency, η_{eff}.

The volumetric efficiency η_v determines the volumetric flow rate:

$$\eta_v = \frac{60\ \dot{V}}{N\ V_{swept}} \tag{3.1}$$

The compressor mass flow rate is evaluated by multiplying the volumetric flow rate by the suction density ρ_s, expressed in kg/m^3.

The isentropic efficiency η_{is} is the ratio between the isentropic compression work and the real work delivered to the refrigerant; it is used to calculate the discharge temperature:

$$\eta_{is} = \frac{h_{d,s} - h_s}{h_d - h_s} \tag{3.2}$$

The effective efficiency η_{eff} is the ratio between the isentropic compression work and the compressor shaft work; it is used to calculate the shaft power required by the compressor:

$$\eta_{eff} = \frac{60.(h_{d,s} - h_s).\rho_s.\dot{V}}{2\pi.M.N} \tag{3.3}$$

The manufacturer characterized the compressor at maximum volume (external vane control equal to 10 V) as presented in Table 3.1. According to these results, mathematical models of compressor efficiencies are elaborated.

The volumetric efficiency η_v, Figure 3.4, is given by:

$$\eta_v = a + b\,N + c\,N^2 + d\,N^3 + e\tau + f\,\tau^2 \tag{3.4}$$

a	b	c	d	e	f
0.96466	$-3.79\ 10^{-5}$	$5.52\ 10^{-8}$	$-1.55\ 10^{-11}$	-0.00022	-0.019957

The application range is between: $600 < N < 4500$, and $1.25 < \tau < 4$. The relative error varies between -2% and 3.24%.

Table 3.1: OBRIST compressor test results at maximum swept volume.

RPM	Compression ratio	Volumetric efficiency %	Mechanical Efficiency %	Isentropic Efficiency %	Overall efficiency %
598.03	2.546	82.22	87.18	85.10	74.19
598.94	1.976	88.52	87.87	88.83	78.06
796.59	3.343	72.26	90.26	78.90	71.22
796.77	2.944	78.39	90.28	82.57	74.54
995.9	3.402	73.30	94.38	77.96	73.58
996.26	2.917	80.26	91.85	83.48	76.68
997.32	2.521	85.24	92.81	84.28	78.22
998.62	2.041	89.31	92.08	84.84	78.12
1395.48	2.957	79.88	92.31	82.88	76.50
1396.2	3.397	74.75	96.59	77.79	75.14
1397.67	2.575	84.91	92.45	83.82	77.49
1397.86	2.046	89.44	91.85	82.30	75.60
1594.75	3.395	75.76	96.00	78.87	75.71
1596.59	2.555	84.81	92.40	82.51	76.24
1598.02	2.037	89.61	92.68	79.93	74.08
1992.4	3.373	75.36	95.84	77.90	74.66
1994.06	2.953	79.66	93.08	80.04	74.50
1994.12	2.428	85.75	93.38	79.27	74.02
1996.59	1.979	90.22	91.65	76.89	70.47
2390.23	3.382	75.50	95.81	76.56	73.35
2390.76	2.990	82.54	97.92	78.16	76.54
2392.95	2.440	84.96	93.71	75.60	70.85
2394.3	2.017	89.14	94.17	70.76	66.64
4595.57	2.935	27.74	31.97	82.26	26.30

The mechanical efficiency η_m, Figure 3.5, is given by:

$$\eta_m = a + b\,N + c\,N^2 + d\,N^3 + e\,\tau + f\,\tau^2 \tag{3.5}$$

a	b	c	d	e	f
0.94714	$-1.37\ 10^{-5}$	$5.92\ 10^{-8}$	$-1.81\ 10^{-11}$	-0.072241	0.017545

The application range is between: $600 < N < 4500$, and $1.25 < \tau < 4$. The relative error varies between -3.3% and 2.3%.

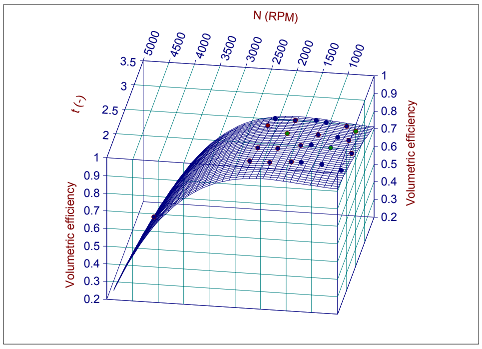

Figure 3.4: Volumetric efficiency.

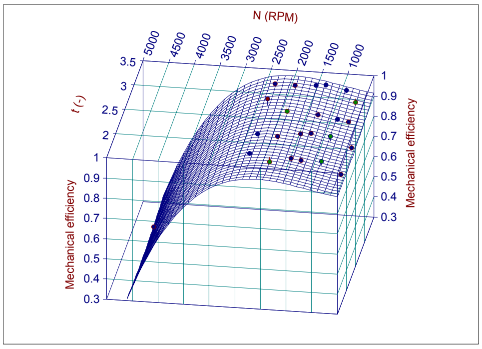

Figure 3.5: Mechanical efficiency.

The isentropic efficiency η_{is}, Figures 3.6 and 3.7, is given by:

$$\eta_{is} = a + b\,N + c\,\tau + d\,N\,\tau \qquad (3.6)$$

a	b	c	d
1.1459	-0.000196	-0.1036	0.0000568

The application range is between: $600 < N < 4500$, and $1.25 < \tau < 4$. The relative error varies between -3.5% and 5%.

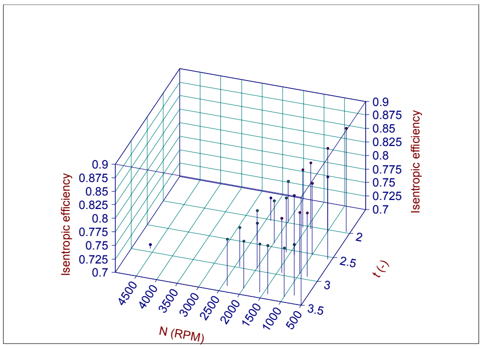

Figure 3.6: Results points of isentropic efficiency.

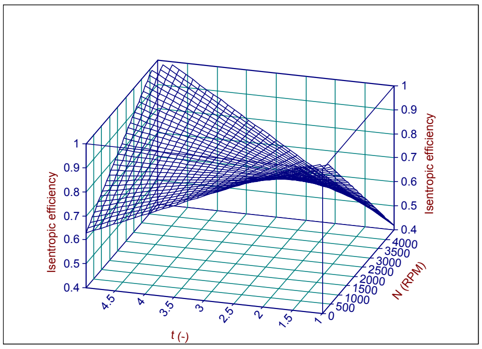

Figure 3.7: Isentropic efficiency.

To reduce the error by preventing the expression of the effective efficiency as η_{is} times η_{mec}, the effective efficiency τ_{eff}, Figure 3.8, is given by:

$$\eta_{eff} = a + b\,N + c\,N^2 + d\,N^3 + e\,\tau + f\,\tau^2 \qquad (3.7)$$

a	b	c	d	e	f
0.472478	$3.03\ 10^{-5}$	$-1.77\ 10^{-9}$	$-6\ 10^{-12}$	0.19931	-0.03645

The application range is between: $600 < N < 4500$, and $1.25 < \tau < 4$. The relative error varies between -5.55% and 6%.

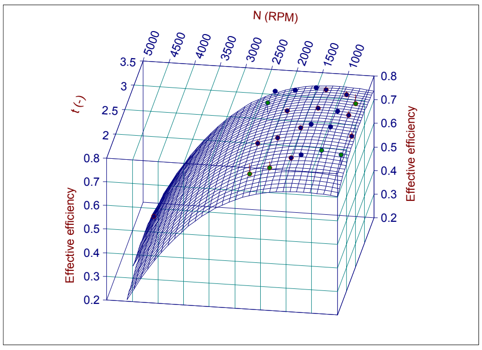

Figure 3.8: Effective efficiency.

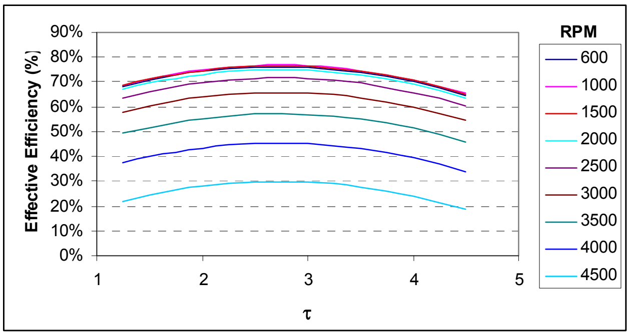

Figure 3.9: Variation of effective efficiency with τ.

The effective efficiency (Figure 3.9) presents optima around a compression ratio τ of 2.75 at different rotation speeds **N**. For a rotation speed lower than 2000 RPM, the compressor, at its maximum displacement, presents an effective efficiency quasi independent of the rotation speed N, but slightly variable with the compression ratio (Figure 3.10).

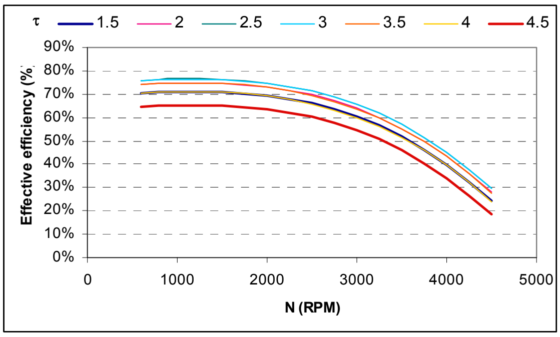

Figure 3.9: Variation of effective efficiency with N.

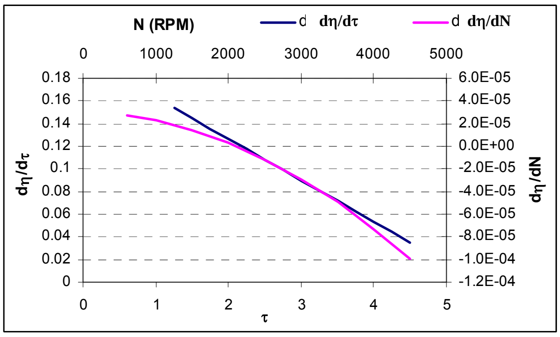

Figure 3.10: Variation of effective efficiency derivative with τ and N.

The derivative of the effective efficiency as a function of the compression ratio τ, Figure 3.11, decreases linearly with τ. Also, the derivative of the effective efficiency as a function of the rotation speed N, Figure 3.11, decreases with N, and it is equal to 0 around 2000 RPM.

In addition to rotation speed and compression ratio τ, the displacement of the compressor affects the efficiencies. The effect of the displacement on efficiencies has the shape of Figure 3.12.

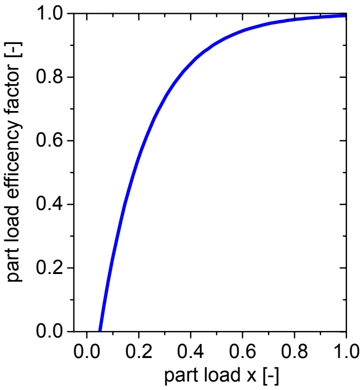

Figure 3.12: General variation of efficiencies with displacement.

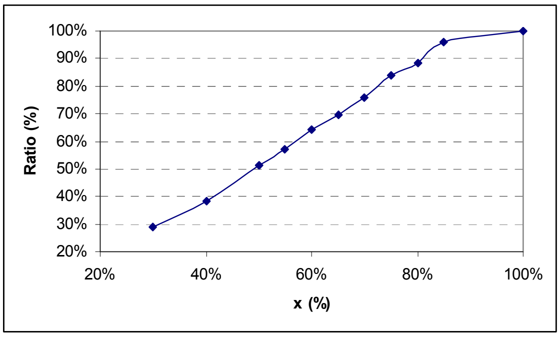

Figure 3.13: Effect of volume displacement x on the effective efficiency.

By varying the rotation speed, the compression ratio, and the volume displacement, the effect of the volume displacement of the compressor, Figure 3.13, is evaluated:

$$\text{Ratio} = \frac{\eta_{eff}}{\eta_{eff,\max}} = a + b\,x + c\,x^2 + d\,x^3 \qquad (3.8)$$

a	b	c	d
0.3823	- 1.517	4.897	-2.7574

Where Ratio and x are non dimensional values, the error on the polynomial function is lower than 2%.

The optimal operating high pressure of a conventional CO_2 refrigeration cycle depends mainly on the gas cooler outlet temperature and the evaporator temperature, also on the variable compressor efficiency, and the evaporator, and the gas cooler pressure drop.

The gas cooler pressure drop and the evaporator pressure drop affect the optimal high pressure by +0.2 MPa for a pressure drop of 0.1 MPa in the gas cooler and the evaporator (Figure 3.14), and by +0.3 MPa for a pressure drop of 0.15 MPa (Figure 3.15). For a constant compression efficiency, since the optimum pressure is independent of compression efficiency, if it is constant.

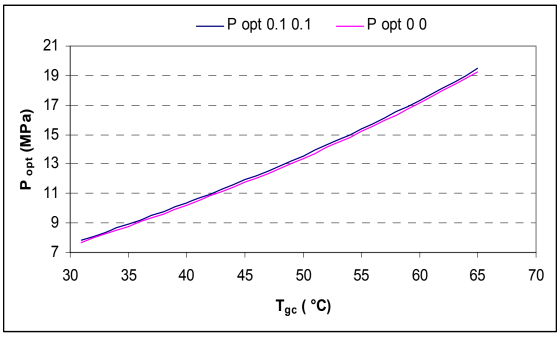

Figure 3.14: Variation of the optimal pressure with T_{gc} for a pressure drop of 0.1 MPa (for gas cooler and evaporator, T_{ev} = 0°c, η_{comp}= 1, SH = 0 K, SC = 0 K.)

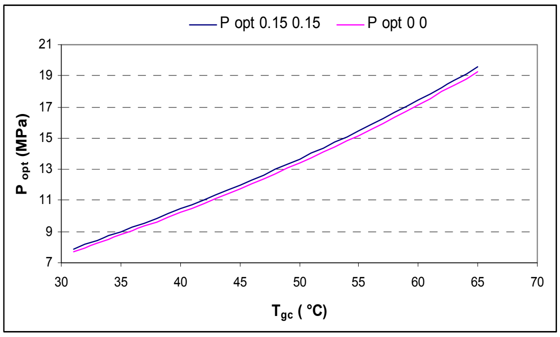

Figure 3.15: Variation of the optimal pressure with T_{gc} for a pressure drop of 0.15 MPa (for gas cooler and evaporator, T_{ev} = 0°c, η_{comp}= 1, SH = 0K, SC = 0 K).

Thus, for a constant RPM, the effective efficiency is quasi constant with τ, so the optimum gas cooler pressure, calculated assuming constant compressor isentropic efficiency, is applicable for this compressor since for a $\Delta \tau < 0.4$, the effective efficiency variation is lower than 0.05.

However, the CO_2 conventional refrigeration cycle presents a range of P_{gc} around the optimal value where the COP is quasi optimal. For T_{ev} = 0°C and T_{gc} = 35°C, the interval of ±0.3 MPa presents a COP loss lower than 1.3%, Figure 3.16. For T_{ev} = 0°C and T_{gc} = 55°C, the interval of ±0.3 MPa presents a negligible COP loss lower than 0.1%, Figure 3.17.

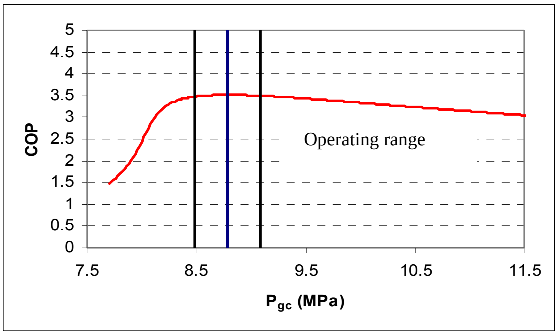

Figure 3.16: Variation of COP with P_{gc}, T_{ev} = 0°C, T_{gc} = 35°C, SH =0 K, SC = 0 K, η_{comp} = 1.

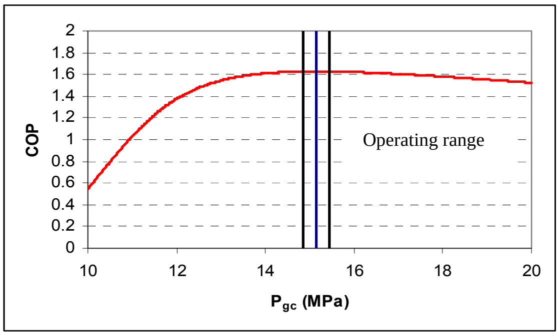

Figure 3.17: Variation of COP with P_{gc}, T_{ev} = 0°C, T_{gc} = 55°C, SH =0 K, SC = 0 K, η_{comp} = 1.

Table 3.2: Variation of COP with P_{gc} variation.

	P_{opt}	P_{opt} - 0.3 MPa	P_{opt} + 0.3 MPa
P_{gc} Mpa	8.788	8.488	9.088
COP_{opt}	3.516	3.472	3.496
% COP loss	0%	1.23%	0.56%
T_{gc} °C	35	T_{ev} °C	0
SH, SC K	0	η_{comp}	1

	P_{opt}	P_{opt} - 0.3 MPa	P_{opt} + 0.3 MPa
P_{gc} Mpa	15.152	14.852	15.452
COP_{opt}	1.629	1.628	1.628
% COP loss	0%	0.07%	0.06%
T_{gc} °C	55	T_{ev} °C	0
SH, SC K	0	η_{comp}	1

In conclusion, the optimal pressure for a conventional CO_2 cycle as defined in *Chapter 1,* is a function of T_{ev} and T_{gc} for the control of the optimal high pressure taking into account the effects of the displacement, the rotation speed, the compression ratio, and the pressure drop in the gas cooler and the evaporator. .

Oil is an important factor for CO_2 compressors. The oil must:

- maintain a high level of tightness between the piston and the cylinder although the high pressure difference.
- have a high lubricating capacity and a high viscosity because of the strong constraints on the compressor mechanical parts and the low viscosity of CO_2.
- have a long-term stability with CO_2,which is a powerful solvent of hydrocarbons in a supercritical state to avoid the formation of undesirable compounds or the reaction with components of the installation (seals, flexible lines…) since the CO_2 forms an acid in the presence of water.
- be miscible preferably at low temperature to avoid accumulation in the system low pressure.

For the compressor lubrication, OBRIST propose to use the oil ND8 that is a PAG 46. This oil is polar like the CO_2, and presents adequate viscosity under a large operating range of evaporation and gas cooling temperatures since the CO_2 has low solubility in PAG poly-alkyl-glycols oils. At the compressor suction port, a filter is installed to prevent the entrainment of solid particles into the compressor.

The compressor is entrained by a electric motor through a belt. The electric motor is a Parvex brushless DC current with a power of 10.7 kW. The electric motor is controlled by a driver commanded by a 0-10 V DC. The control is: either the rotation speed or the rotation torque. The control is done by Parvex software and saved on the driver memory. For the electric motor of the test bench, the rotation speed control is programmed to be commanded by a 0-10 V DC, since this method offers the option of simulating driving cycle on the test bench.

The rotation speed and the rotation couple are measured by a MAGTROL sensor.

3.1.3.2 Expansion valve

The expansion valve allows a fluid to expand from high pressure (pressure at the outlet of the gas cooler) to the low evaporating pressure at constant enthalpy, which involves a phase change and a temperature decrease.

The chosen expansion valve is an OBRIST expansion one, presented on Figure 3.19. It comprises a needle valve with an electronic actuator to control the opening. The actuator is supplied with 12 VDC and controlled by a DC voltage signal between 2 and 7 V: 0% open at 7 V and 100% open at 2 V.
Open (%) = 100 (7 – Voltage) / 5.

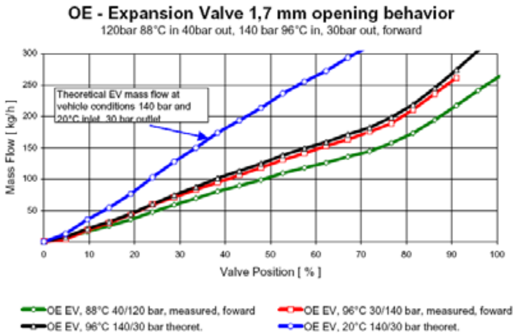

Figure 3.18: OBRIST electronic expansion valve mass flow rate.

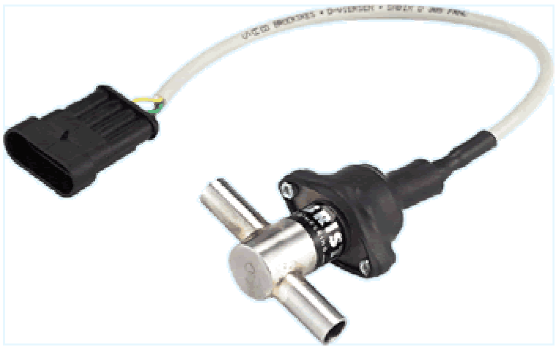

Figure 3.19: OBRIST electronic expansion valve.

The electronic valve could be used either to control either the high pressure, or the evaporation pressure. The mass flow rates of the expansion valve given by the manufacturer are shown on Figure 3.18 as functions of the opening rate and the upstream and downstream pressures.

3.2 Heat exchangers

The sizing of a heat exchanger requires the knowledge of thermal heat transfer coefficients as well as the pressure drop correlations of the internal and the external fluids. Thus the following correlations are needed:

- two-phase evaporation for the evaporator,
- one-phase supercritical CO_2
- two-phase condensation for the gas cooler/ condenser.
- for the external flow, the water liquid phase.

In the following sections, a review of the best available correlations is performed in order to simulate the refrigeration CO_2 systems.

3.2.1 CO_2 Evaporation process

Carbon dioxide has become an important alternative refrigerant in the past few years and thus an accurate heat transfer prediction method for its evaporation inside horizontal tubes is required. The higher operating pressures result in high vapor densities, very low surface tensions, high vapor viscosities, and low liquid viscosities, and thus yield to flow boiling heat transfer and two-phase flow characteristics that are quite different from those of conventional refrigerants. High pressures and low surface tensions have major effects on nucleate boiling heat transfer characteristics. Previous experimental studies have suggested a clear dominance of nucleate boiling heat transfer even at very high mass velocity.

Most up-to-date studies on the two-phase evaporating heat transfer take the model and the evaporation flow pattern map of Kattan-Thome-Favrat [KAT 98a,b,c] as a reference and then they adopt it to be compatible with the carbon dioxide.

Yoon et al. [YOO 04] have performed experimentations on a tube of 7.53 mm internal diameter and have measured the CO_2 evaporating heat transfer. Based on the experiments, Yoon et al. divided the CO_2 two-phase evaporating map in two zones according to the critical quality x_{cr} expressed as a function of the CO_2 properties, heat and mass fluxes. For quality lower than x_{cr}, the zone is totally wet, and for quality higher than x_{cr} the zone is partially wetted, so a dry angle is used to evaluate the two-phase heat transfer coefficient. Yoon et al. express the dry angle as a function of the Reynolds number, the boiling number, and the Bond number. The correlations are validated for circular horizontal tube of 7.53 mm internal diameter.

Yun et al. [YUN 03] have performed experimentations on a tube of 6 mm internal diameter and have measured the CO_2 evaporating heat transfer. By comparing CO_2 to R-134a, Yun et al. have found that the heat transfer coefficient of CO_2 is on average 47% higher than the one of R-134a at the same temperature.

Wojtan et al. [WOJ 05a], [WOJ 05b] have studied the evaporation of R-22 and R-410A, and, using the Kattan et al. flow pattern map, have modified the flow pattern map to describe new evaporation zones. Based on the dynamic void fraction measurements, the stratified–wavy region has been subdivided into three sub-zones: slug, slug/stratified–wavy and stratified–wavy. Furthermore, annular to dry-out and dry-out to mist flow transition curves have been added and integrated into the new flow pattern map, identified by distinct trends of the heat transfer coefficient as a function of vapor quality and by flow pattern observations to determine the inception and completion of dry-out in horizontal tubes. In addition, Wojtan et al. have developed a new heat transfer model for stratified-wavy, dry-out, and mist flow regimes. These flow regimes were not described by Kattan et al.

Thome and El Hajal [THO 04] studied the flow boiling heat transfer of carbon dioxide, and developed correlations, based on Kattan et al. models that predict 73% of their CO_2 database over the vapor quality range of 2–91%. The database covers five tube diameters from 0.79 to 10.06 mm, mass velocities from 85 to 1440 kg m^{-2} s^{-1}, heat fluxes from 5 to 36 kW m^{-2}, and saturation temperatures from –25 °C to 25°C that correspond to saturation pressures from 1.7 to 6.4 MPa. The database is built on five independent experimental studies made by different laboratories in Japan, Korea, Norway, and Denmark. The new correlations affect the nucleation boiling with a linear modification and by introducing a boiling suppression factor that depends on a Reynolds number of the liquid phase and the vapor quality.

Thome and Ribatski [THO 05] have presented a comprehensive review of flow boiling heat transfer and two-phase flow of CO_2 that covers both macro-channel tests (diameters larger than about 3 mm) and micro-channel investigations (diameters lower than 3 mm). The two-phase flow pattern results available in the literature were summarized and compared to some of the leading flow pattern maps, showing significant deviations for CO_2 from the maps prepared for other fluids at lower pressures.

Cheng et al. [CHE 06] have developed a flow boiling heat transfer model and a flow pattern map based on the flow boiling heat transfer mechanisms of Kattan et al. for horizontal tubes specifically for CO_2. The flow boiling heat transfer model predicts 75.5% of the entire CO_2 database within ±30%. The flow boiling heat transfer model and the flow pattern map are applicable to a wide range of conditions: tube diameters (equivalent diameters for noncircular channels) from 0.8 to 10 mm, mass velocities from 170 to 570 kg/m^2 s, heat fluxes from 5 to 32 kW/m^2, and saturation temperatures from -28 to 25°C that correspond to reduced pressures from 0.21 to 0.87.

3.2.2 CO_2 flow vaporization heat transfer correlations

Vaporization can occur in two forms: evaporation and boiling. The nucleate boiling depends on the heat flux, and is characterized by the bubble appearance on the wall. The convective evaporation depends on quality and mass flux, and is characterized by the interface evaporation between liquid and vapor.

Researchers have used several mathematical models for boiling heat transfer, as shown in Table 3.3: superposition model, asymptotic model, and intensification model. The first two models are a function of the nucleating boiling and the convective boiling; the last one is a function of the liquid heat transfer.

Table 3.3: Mathematical model of correlation.

Model	Correlation
Superposition	$h = h_{nb} + h_{cb}$
Asymptotic	$h = \left(h_{nb}^{n} + h_{cb}^{n} \right)^{1/n}$
Intensification	$h = E\, h_l$

The ***n*** exponent of the asymptotic model is generally chosen equal to 2, 2.5 or 3.

The horizontal tubes are classified in three categories: macro-channel, mini-channel, and micro-channel. Based on engineering practice and application areas, Kandlikar [KAN 02] proposed using the following threshold diameters:

- conventional channels: D_h > 3 mm;
- mini-channels: D_h between 600 µm and 3 mm;
- micro-channels: Dh between 50 µm and 600 µm.

Based on the confinement of bubble departure sizes in channels, Kew and Cornwell [KEW 97] proposed an approximate physical criterion for macro- to micro-channel threshold diameter as follows:

$$D_{th} = \left(\frac{4\sigma}{g\left(\rho_l - \rho_v\right)} \right)^{1/2} \tag{3.9}$$

When hydraulic diameters are larger than the threshold diameter, the channels are defined as macro-scale channels; otherwise the channels are defined as micro-scale channels.

For micro-channels, Petterson et al. [PET 00] find that the best correlation is proposed by Kandlikar [KAN 90], which predicts the CO_2 evaporation heat transfer with 0% average deviation and 15% mean deviation for mass flux lower than 300 kg/m^2 s and for heat flux between 600 and 20000 W/ m^2. Petterson has measured CO_2 boiling heat transfer in a flat multi-port extruded aluminum tube with 25 circular channels with 0.79 mm as inner diameter.

The boiling heat transfer coefficient given by Kandlikar is defined by:

$$h = h_l \cdot \left(C_1 \cdot Co^{C_2} \cdot \left(25 \cdot Fr_l \right)^{C_5} + C_3 \cdot Bo^{C_4} F_{fl} \right) \tag{3.10}$$

The factor F_{fl} depends on the fluid, according to Petterson et al. [PET 00] F_{fl} for CO_2 is 1. Constants C_1 to C_5 are shown in Table 3.4.

Table 3.4: Constant values of Kandlikar correlations [PET 00].

Constant	Convective boiling	Nucleate boiling
C_1	1,1360	0,6683
C_2	-0,9	-0,2
C_3	667,2	1058,0
C_4	0,7	0,7
C_5	0	0

The Froude number of liquid phase is expressed by:

$$Fr_l = \frac{G^2}{\rho_l^2 \cdot g \cdot D} \tag{3.11}$$

The boiling number is given by:

$$Bo = \frac{\dot{q}}{G \cdot h_{fg}} \tag{3.12}$$

The convection number based on Martinelli parameter is given by:

$$Co = \left(\frac{1-x}{x}\right)^{0,8} \left(\frac{\rho_v}{\rho_l}\right)^{0,5} \tag{3.13}$$

The liquid heat transfer coefficient proposed by Dittus-Boelter is:

$$h_l = 0,023 \cdot \mathrm{Re}_l^{0.8} \cdot \mathrm{Pr}_l^{0.4} \frac{k_l}{D} \tag{3.14}$$

The highest value of heat transfer calculated using the constant of convective boiling and nucleate boiling is adopted as the evaporating heat transfer coefficient.

For macro and mini-channels, the flow pattern map and correlations proposed by Chen et al. [CHE 06] will be used and explained in details. Many parameters will be presented that contribute to describe the CO_2 evaporation flow map.

The Weber number is given by:

$$We = \frac{G^2 D}{\rho \sigma} \tag{3.15}$$

The critical flux is given by:

$$q_{crit} = 0.131 \rho_V^{1/2} h_{fg} \left[g\sigma \left(\rho_L - \rho_V \right) \right]^{1/4} \tag{3.16}$$

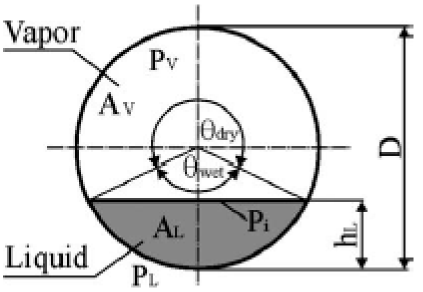

Figure 3.20: Stratified two-phase flow cross-section.

Using Figure 3.20, the dimensionless geometrical variables are defined as:

$$h_{LD} = \frac{h_L}{D}; P_{LD} = \frac{P_L}{D}; P_{VD} = \frac{P_V}{D}; P_{iD} = \frac{P_i}{D}; A_{LD} = \frac{A_L}{D^2}; A_{VD} = \frac{A_V}{D^2}. \tag{3.17}$$

The flow boiling heat transfer model of Kattan et al. [KAT 98] uses the Rouhani–Axelsson drift flux model for horizontal tubes for the cross-sectional void fraction ε:

$$\varepsilon = \frac{x}{\rho_V}\left[\left(1+0.12\left(1-x\right)\right)\left(\frac{x}{\rho_V}+\frac{1-x}{\rho_L}\right)+\frac{1.18\left(1-x\right)\left[g\sigma\left(\rho_L-\rho_V\right)\right]^{0.25}}{G\rho_L^{0.5}}\right]^{-1} \tag{3.18}$$

This drift flux void fraction model gives the void fraction as an explicit function of total mass flux. Using the drift flux void fraction, $\theta_{\mathrm{stratified}}$ is given by:

$$A_L = \frac{R^2}{2}\left[\left(2\pi-\theta_{strat}\right)-\sin\left(2\pi-\theta_{strat}\right)\right] \tag{3.19}$$

$$A_L = A\left(1-\varepsilon\right) \tag{3.20}$$

To avoid any iteration, the geometrical expression for the stratified angle θ_{strat} can be calculated from an approximate expression, evaluated in terms of void fraction, by Biberg as follows:

$$\theta_{strat} = 2\pi - 2\left\{\pi(1-\varepsilon)+\left(\frac{3\pi}{2}\right)^{1/3}\left[1-2(1-\varepsilon)+(1-\varepsilon)^{1/3}-\varepsilon^{1/3}\right]-\frac{1}{200}(1-\varepsilon)\varepsilon\left[1-2(1-\varepsilon)\right]\left[1+4((1-\varepsilon)^2+\varepsilon^2\right]\right\} \tag{3.21}$$

Knowing $\theta_{\mathrm{stratified}}$, generally by iterative method, the liquid height h_{LD} and the perimeter interface P_{iD} are given by:

$$h_{LD} = \frac{1}{2}\left(1-\cos\left(\frac{2\pi-\theta_{strat}}{2}\right)\right) \tag{3.22}$$

$$P_{iD} = \sin\left(\frac{2\pi-\theta_{strat}}{2}\right) \tag{3.23}$$

The other variables are given by:

$$A_{VD} = \frac{\pi}{4} - A_{LD}\,;\; P_{LD} = \frac{2\pi-\theta_{strat}}{2}\,;\; P_{VD} = \pi - P_{LD}\,. \tag{3.24}$$

Using these variables, the mass flux curves of the different evaporation regions are evaluated. Six principal regions form the flow pattern map of pure fluid:

- The intermittent flow region **I**.
- The annular flow region **A**.
- The stratified flow region **S**.
- The stratified wavy flow region **SW**.
- The mist flow region **M**.
- The dry flow regions **D**.

These regions depend on the saturation temperature that affects the thermo-physical properties, the heat flux, and the diameter of the horizontal tube. The map is drawn in a two-axis chart, with vapor quality on the ***x*** axis and mass flux on the ***y*** axis.

The stratified wavy flow region is divided in 3 sub-zones: slug zone, stratified-wavy / slug zone, and stratified zone.

The implementation procedure of the map is as follows.

1. The ‘‘I–A’’ transition is calculated from the original Kattan–Thome–Favrat [KAT 98] boundary:

$$x_{IA} = \left\{ \left[0.34^{1/0.875} \left(\frac{\rho_V}{\rho_L} \right)^{-1/1.75} \left(\frac{\mu_L}{\mu_V} \right)^{-1/7} \right] + 1 \right\}^{-1} \tag{3.25}$$

and extended down to its intersection with G_{strat}.

2. Geometrical parameters ε, A_{LD}, A_{VD}, Θ_{strat}, h_{LD} and P_{iD} are calculated from their equations, respectively.

3. The ‘‘**SW–I/A**’’ transition is first calculated from the following adiabatic version of the original Kattan – Thome – Favrat [KAT 98] boundary:

$$G_{wavy} = \left\{ \frac{16 A_{VD}^3 g D \rho_l \rho_v}{x^2 \pi^2 \left(1 - \left(2h_{LD} - 1\right)^2\right)^{0.5}} \left[\frac{\pi^2}{25 h_{LD}^2} \left(\frac{We}{Fr} \right)_L^{-1} + 1 \right] \right\}^{0.5} + 50 \tag{3.26}$$

The stratified–wavy region is then subdivided into three zones:
- $G > G_{wavy}(x_{IA})$ gives the **SLUG** zone;
- $G_{strat} < G < G_{wavy}(x_{IA})$ and $x < x_{IA}$ give the **SLUG/STRATIFIED-WAVY** zone;
- $x \geq x_{IA}$ gives the **STRATIFIED-WAVY** zone.

4. The ‘‘**S–SW**’’ transition is calculated from the original Kattan–Thome–Favrat [KAT 98] boundary:

$$G_{strat} = \left\{ \frac{226.3^2 A_{LD} A_{VD}^2 \rho_v \left(\rho_L - \rho_v\right) \mu_L g}{\pi^3 x^2 (1 - x)} \right\}^{1/3} \tag{3.27}$$

but now $G_{strat} = G_{strat}(x_{IA})$ at $x < x_{IA}$.

5. The ‘‘A–D’’ boundary is calculated by:

$$G_{dry} = \left\{ \frac{1}{0.67} \left[\ln\left(\frac{0.58}{x} \right) + 0.52 \right] \left(\frac{D}{\rho_V \sigma} \right)^{-0.17} \left(\frac{1}{g D \rho_V \left(\rho_L - \rho_V\right)} \right)^{-0.348} \left(\frac{\rho_V}{\rho_L} \right)^{-0.25} \left(\frac{q}{q_{crit}} \right)^{-0.7} \right\}^{0.965} \tag{3.28}$$

6. The ‘‘D–M’’ boundary is calculated by:

$$G_{mist} = \left[\frac{1}{0.0058} \left[\ln\left(\frac{0.61}{x} \right) + 0.57 \right] \left(\frac{D}{\rho_V \sigma} \right)^{-0.38} \left(\frac{1}{g D \rho_V (\rho_L - \rho_V)} \right)^{-0.15} \left(\frac{\rho_V}{\rho_L} \right)^{0.09} \left(\frac{q}{q_{crit}} \right)^{-0.27} \right]^{0.943} \tag{3.29}$$

7. The following conditions are then applied to define the transitions in the high vapor quality range:

- If $G_{strat}(x) > G_{dryout}(x)$, then $G_{dryout}(x) = G_{strat}(x)$.
- If $G_{wavy}(x) > G_{dryout}(x)$, then $G_{dryout}(x)$ forms the boundary curves.
- If $G_{dry}(x) > G_{mist}(x)$ than $G_{mist}(x)$ forms the boundary curves.

Using this procedure, the flow pattern maps of CO_2 at different evaporation temperatures and heat flux are drawn, Figure 3.21.

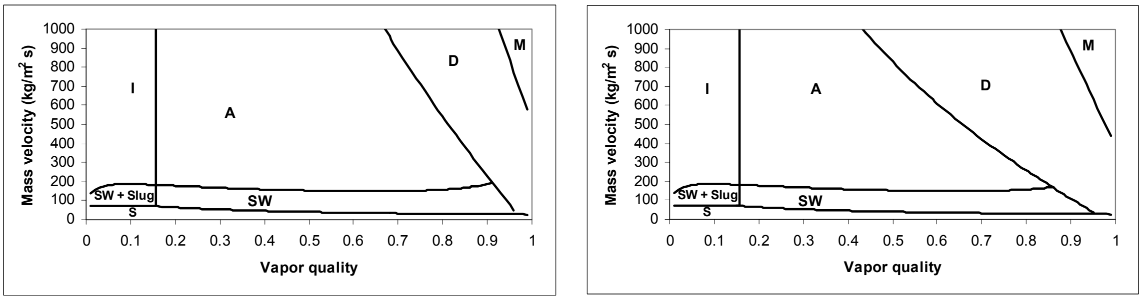

Q = 5 kW/m^2 , T_{evap} = 0°C Q = 15 kW/m^2 , T_{evap} = 0°C

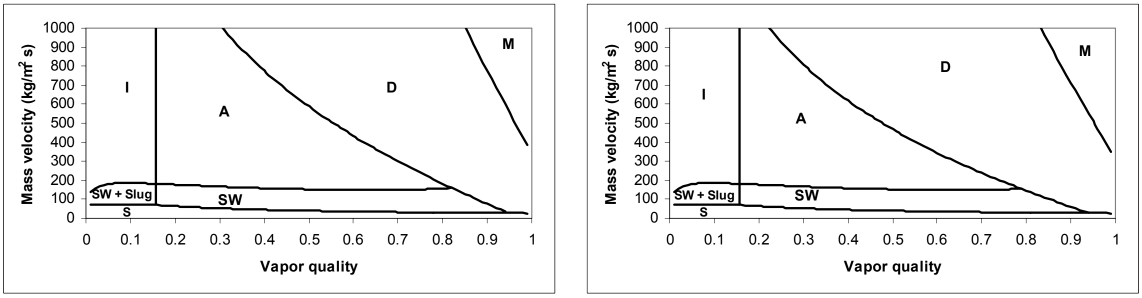

Q = 25 kW/m^2 , T_{evap} = 0°C Q = 35 kW/m^2 , T_{evap} = 0°C

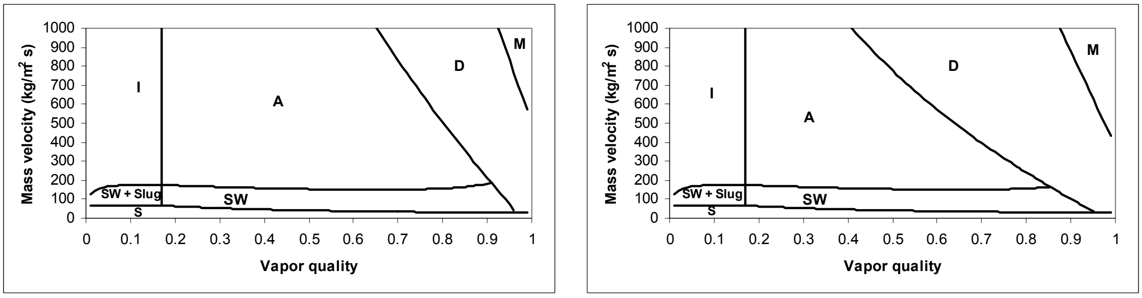

Q = 5 kW/m^2 , T_{evap} = 5°C Q = 15 kW/m^2 , T_{evap} = 5°C

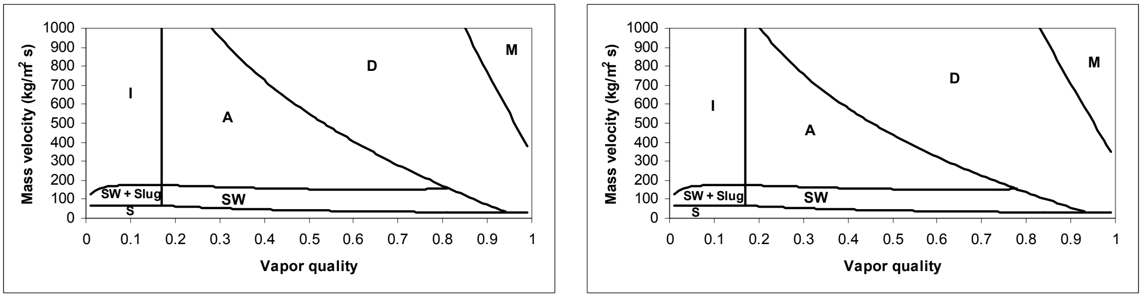

Q = 25 kW/m^2 , T_{evap} = 5°C Q = 35 kW/m^2 , T_{evap} = 5°C

Figure 3.21: Flow pattern map at different evaporation temperature and heat flux for G =300 kg/m^2 s and D = 6 mm.

The dry-out region increases with the evaporation temperature and the heat flux increase.

The flow map depends of three parameters: the mass flux G in kg/m^2 s, the heat flux q in W/m^2, and the evaporation temperature T_{evap} that defines the thermo-physical properties of CO_2.

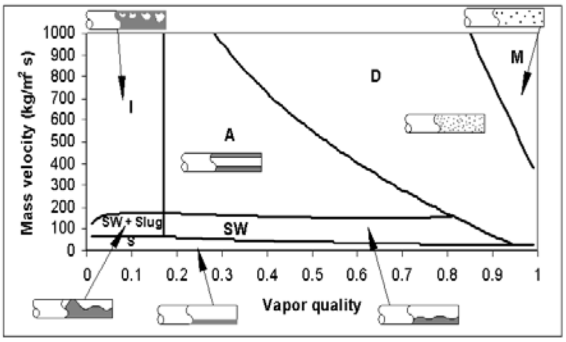

Figure 3.22: Flow shape in different regions.

Based on the flow map, the heat transfer coefficient is evaluated for the different regions, Figure 3.22. According to the dry mass flux, the dry-out inception vapor quality is defined as:

$$x_{di} = 0.58\exp\left(0.52 - 0.67 We_V^{0.17} Fr_V^{0.348}\left(\frac{\rho_V}{\rho_L}\right)^{0.25}\left(\frac{q}{q_{crit}}\right)^{0.7}\right) \tag{3.30}$$

The vapor Froude number is given by:

$$Fr_V = \frac{G^2}{gD\rho_V(\rho_L - \rho_V)} \tag{3.31}$$

According to the mist mass flux, the dry-out completion vapor quality is defined as:

$$x_{de} = 0.61\exp\left(0.57 - 5.8\times10^{-3} We_V^{0.38} Fr_V^{0.15}\left(\frac{\rho_V}{\rho_L}\right)^{-0.09}\left(\frac{q}{q_{crit}}\right)^{0.27}\right) \tag{3.32}$$

If x_{de} is higher then 1, so $x_{de} = 0.999$.

The Kattan-Thome-Favrat general equation for the local two-phase heat transfer coefficients h_{tp} in a horizontal tube is:

$$h_{tp} = \frac{\theta_{dry} h_v + \left(2\pi - \theta_{dry}\right) h_{wet}}{2\pi} \tag{3.33}$$

The vapor phase heat transfer coefficient on the dry perimeter h_V is calculated with Equation 3.14.

The heat transfer coefficient on the wet perimeter is calculated with an asymptotic model that combines the nucleate boiling and convective boiling contributions to the heat transfer by the third power with a suppression factor S for the nucleating boiling:

$$h_{wet} = \left[\left(S.h_{nb}\right)^3 + h_{cb}^3\right]^{1/3} \tag{3.34}$$

The convective contribution is calculated with the following correlation assuming a liquid film flow:

$$h_{cb} = 0.0133\left(\frac{4G\left(1-x\right)\delta}{\mu_L\left(1-\varepsilon\right)}\right)^{0.69} \mathrm{Pr}_L^{0.4}\frac{k_L}{\delta} \tag{3.35}$$

The liquid film thickness is calculated by:

$$\delta = \frac{D}{2} - \sqrt{\frac{D^2}{4} - \frac{2A_L}{2\pi - \theta_{dry}}} \tag{3.36}$$

If δ > D/2 then δ= D/2.

The following new nucleate boiling heat transfer correlation was obtained:

$$h_{nb} = 131 p_{\mathrm{r}}^{-0.0063} \left(-\log_{10} p_{\mathrm{r}}\right)^{-0.55} M^{-0.5} q^{0.58} \tag{3.37}$$

The boiling suppression factor correlation for CO_2 is:

- $x < x_{IA}$, S = 1
- $x \geq x_{IA}$, $S = 1 - 1.14 \left(\frac{D}{D_{ref}}\right)^2 \left(1 - \frac{\delta}{\delta_{IA}}\right)^{2.2}$ (3.38)

where D_{ref} = 7.53 mm; and if D > 7.53 mm then D = 7.53 mm.

The liquid film thickness δ_{IA} is calculated for $\theta_{dry} = 0$.

The heat transfer coefficient in mist flow is calculated as follows:

$$h_{mist} = 0.0117 \, \mathrm{Re}_H^{0.79} \, \mathrm{Pr}_V^{1.06} \, Y^{-1.83} \frac{k_v}{D} \tag{3.39}$$

The homogeneous Reynolds number Re_H is given by:

$$\mathrm{Re}_H = \frac{GD}{\mu_V} \left(x + (1-x) \frac{\rho_V}{\rho_L} \right) \tag{3.40}$$

The correction factor Y is given by:

$$Y = 1 - 0.1 \left[\left(\frac{\rho_L}{\rho_V} - 1 \right) (1-x) \right]^{0.4} \tag{3.41}$$

The heat transfer coefficient in the dry-out region is calculated by:

$$h_{dryout} = h_{tp}(x_{di}) - \frac{x - x_{di}}{x_{de} - x_{di}} \left(h_{tp}(x_{di}) - h_{mist}(x_{de}) \right) \tag{3.42}$$

The dry angle θ_{dry} is defined according to the flow types defined in the flow map:

- For **A**nnular, **I**ntermittent and **Slug** zone: $\theta_{dry} = 0$.
- For **S**tratified-**W**avy zone: $\theta_{dry} = \left(\frac{G_{wavy} - G}{G_{wavy} - G_{strat}} \right)^{0.61} \theta_{strat}$ (3.43)
- For **Slug**-**S**tratified **W**avy zone ($x < x_{IA}$): $\theta_{dry} = \frac{x}{x_{IA}} \left(\frac{G_{wavy} - G}{G_{wavy} - G_{strat}} \right)^{0.61} \theta_{strat}$ (3.44)
- For **S**tratified zone: $\theta_{dry} = \theta_{strat}$.
- For the **D**ry-out inception curve: $\theta_{dry,di} = 0$.

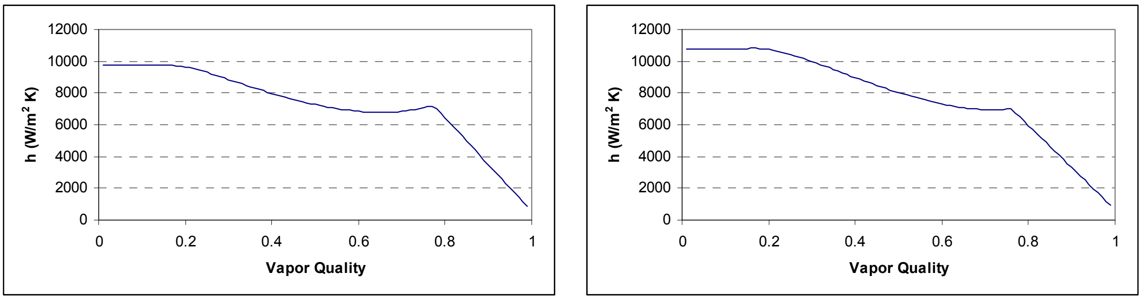

$T_{evap} = 0°C$ $T_{evap} = 5°C$

Figure 3.23: Variation of evaporation heat transfer coefficient with vapor quality at G = 300 kg/m^2 s, Q = 15000 W/m^2 and D = 6 mm.

The liquid Reynolds number function of δ is: $\mathrm{Re}_L = \dfrac{4G(1-x)\delta}{(1-\varepsilon)\mu_L}$. (3.45)

The vapor Reynolds number function of D is: $\mathrm{Re}_V = \dfrac{GxD}{\varepsilon\mu_V}$. (3.46)

These correlations are applicable to the conditions:
-28°C < T_{sat} < 25°C;
5 kW/m^2 < q < 32 kW/m^2,
170 kg/m^2 s < G < 570 kg/m^2 s,
0.8 mm < D < 10 mm.

Using the correlations, the heat transfer coefficient of CO_2 evaporation are presented in Figure 3.23.

According to the respective flow maps, the flow passes successively in the intermittent zone, the annular zone, and the dry zone. In this latter one, the heat transfer coefficient decreases highly due to the presence of vapor.

3.2.3 Evaporation pressure drop

The CO_2 saturation temperature is slightly depending on the pressure, in the range of 1 K for a pressure drop of 0.1 MPa. Thus, few researchers studied the CO_2 pressure drop during the evaporation.

Didi et al. [DID 02] studied seven two-phase models of pressure drop for five refrigerants: R-134a, R-123, R-402A, R-404A, and R-502.

Yoon et al. [YOO 04] studied the CO_2 evaporation in a stainless steel tube with an inner diameter of 7.53 mm, and they elaborate a correlation for the frictional two-phase multiplier $\phi^2_{f,lo}$ on the basis of the B-method [CHI 83].

Petterson et al. [PET 00] have compared 4 models of pressure drop by friction, and they report that the pressure drop calculated by the Thome correlations (THO97), based on the correlation of Friedel for pressure drop by friction, is the more suitable model to calculate the CO_2 pressure drop during evaporation.

The total pressure drop in a tube is the sum of the gravity pressure drop $\Delta P_{gravity}$, the acceleration or momentum pressure drop ΔP_{acc}, and the frictional pressure drop $\Delta P_{fric.}$

$$\Delta P_{acc} = \Delta P_{gravity} + \Delta P_{acceleration} + \Delta P_{frictional}. \quad (3.47)$$

The gravity pressure drop is given by:

$$\Delta P_{gravity} = \rho \cdot g \cdot \Delta L \cdot \sin\theta \tag{3.48}$$

where θ is the inclination angle from the horizontal and ρ is the density given by:

$$\rho = \varepsilon \cdot \rho_{vap} + (1-\varepsilon) \cdot \rho_{liq} \tag{3.49}$$

The void fraction ε is given by the Rouhani–Axelsson drift flux model for horizontal tubes [DID 02].

The acceleration pressure drop for two-phase flow is given by:

$$\Delta P_{acc} = G^2 \cdot \left[\frac{x^2}{\rho_{vap} \cdot \varepsilon} + \frac{(1-x)^2}{\rho_{liq} \cdot (1-\varepsilon)} \right]_{In}^{Out} \tag{3.50}$$

The frictional pressure drop is given by :

$$\left(\frac{\partial P}{\partial L}\right)_l = \left[\frac{2 \cdot f_{l0} G^2}{d_h \cdot \rho_{liq}}\right] \cdot \Phi_{l0}^2 \tag{3.51}$$

Where Φ_{l0}^2 is the diphase multiplier given by:

$$\Phi_{l0}^2 = E + \frac{3{,}24 \cdot F \cdot H}{Fr_h^{0{,}045} \cdot We_h^{0{,}035}} \tag{3.52}$$

The factors E, F et H are defined by:

$$E = (1-x)^2 + x^2 \cdot \frac{f_{V0} \cdot \rho_l}{f_{l0} \cdot \rho_v} \tag{3.53}$$

$$F = x^{0{,}78} \cdot (1-x)^{0{,}224} \tag{3.54}$$

$$H = \left(\frac{\rho_{liq}}{\rho_{vap}}\right)^{0{,}91} \cdot \left(\frac{\mu_{vap}}{\mu_{liq}}\right)^{0{,}19} \cdot \left(1 - \frac{\mu_{vap}}{\mu_{liq}}\right)^{0{,}7} \tag{3.55}$$

The Froude number(Fr_h) and the Webber number (We_h) for a homogeneous flow are defined as:

$$Fr_h = \frac{G^2}{g \cdot d_h \cdot \rho_h^2} \tag{3.56}$$

$$We_h = \frac{G^2 \cdot d_h}{\sigma \cdot \rho_h} \tag{3.57}$$

Where the homogeneous density ρ_h is given by:

$$\rho_h = \left(\frac{x}{\rho_{vap}} + \frac{1-x}{\rho_{liq}}\right)^{-1} \tag{3.58}$$

The Fanning-friction factor is calculated by:

$$f_0 = \frac{0{,}079}{\sqrt[4]{Re}} \tag{3.59}$$

The liquid and vapor friction factors are calculated with the modified Reynolds numbers:

$$\mathrm{Re}_{l0} = \frac{G\, d_h}{\mu_{liq}}. \tag{3.60}$$

$$\mathrm{Re}_{V0} = \frac{G\, d_h}{\mu_{vap}}. \tag{3.61}$$

The volumetric vapor factor β is given by :

$$\beta = \frac{\rho_{liq} \cdot x}{\rho_{liq} \cdot x + \rho_{vap} \cdot (1-x)} \tag{3.62}$$

3.3 Gas cooler / condenser

The sizing of a gas cooler / condenser requests the one-phase correlations (supercritical state) of thermal heat exchange coefficient and of the pressure drop, and the two-phase condensation correlations.

3.3.1 One phase correlation of heat transfer and pressure drop

Many researchers studied the supercritical CO_2 behaviors during cooling.[KRA 05], [DAN 06], [PIT 02], [JIA 06], [YIN 01], [SON 06], [ZHA 06], [HUA 05], [HE 05],[DUF 05], [LIA 02], [ASI 05], [YOO 03], [PIO 04], [DAN 04a], [DAN 04b]. They include many parameters to describe the heat transfer coefficients: the pseudo-critical temperature, the bulk and the wall CO_2 properties: viscosity, conductivity, density; and the mean heat capacity; and they based their correlations on the Dittus–Boelter correlations or to Gnielinski correlations.

After having compared six different correlations for smooth tubes having an internal diameter of 7.8 mm, Rieberer [RIE98] presents the correlation of Gnielinski (VDI) as the most adequate for one phase CO_2 at the supercritical and infra-critical states.

Pettersen et al. [PET 00] also showed the validity of the Gnielinski correlation (VDI) for micro-channel tubes with 0.79 mm as diameter.

Pitla et al. studied different correlations models for supercritical CO_2, and by comparing the correlations to CFD simulations and experiment results, Pitla et al. found that the mean Gnielinski correlation presents the best results. This correlation will be used in this study.

The mean Nusselt number is given by:

$$Nu_{CO_2} = \left(\frac{Nu_{G,wall} + Nu_{G,bulk}}{2} \right) \frac{k_{wall}}{k_{bulk}} \tag{3.63}$$

The Gnielinski Nusselt number is given by:

$$Nu_G = \frac{\left(f_f / 8 \right) (\mathrm{Re} - 1000) \mathrm{Pr}}{1.07 + 12.7 \left(f_f / 8 \right)^{1/2} \left(\mathrm{Pr}^{2/3} - 1 \right)} \tag{3.64}$$

with: $2\,300 < \mathrm{Re} < 5 \times 10^6$ and $0{,}5 < \mathrm{Pr} < 2\,000$.

The friction factor is given by Filonenko:

$$f_f = [0.79 \ln(\mathrm{Re}) - 1.64]^{-2} \tag{3.65}$$

The transfer heat exchange coefficient is given by:

$$h_{CO_2} = \frac{Nu_{CO_2} k_{bulk}}{d_h} \tag{3.66}$$

The friction pressure drop is given by:

$$\left(\frac{\partial P}{\partial L}\right)_l = \frac{2 \cdot f_f G^2}{d_h \cdot \rho} \tag{3.67}$$

The acceleration pressure drop is given by:

$$\Delta P_a = \frac{1}{A}\left[\dot{M} \cdot V\right]_{in}^{out} = G^2 \cdot \left[\frac{1}{\rho_{out}} - \frac{1}{\rho_{in}}\right] \tag{3.68}$$

The gravity pressure drop is negligible for horizontal tubes.

3.3.2 CO$_2$ condensation correlations

The correlations chosen for the condensation of R-744 in a horizontal tube correspond to the recommendations made by Thome (1997) and used by Rieberer [RIE98].

For G < 200 kg/ m^2.s, Akers model (1997) adopted:

$$Nu = \frac{h \cdot d_h}{k_{liq}} = C \cdot \mathrm{Re}_l^{\,n} \cdot \mathrm{Pr}_l^{\,1/3} \tag{3.69}$$

For $\mathrm{Re}_l > 50\,000$: C = 0,0265 and n = 0,8.

For $\mathrm{Re}_l \leq 50\,000$: C = 5,03 and n = 1/3.

The Reynolds number is calculated with the liquid phase properties and for a modified mass flux given by:

$$G_{\mathrm{mod}ified} = G \cdot \left[(1-x) + x \cdot \left(\frac{\rho_{liq}}{\rho_{vap}}\right)^{1/2}\right] \tag{3.70}$$

For G ≥ 200 kg/ m^2.s, the Shah model (1979) adopted:

$$Nu = Nu_{liq} \cdot \left[(1-x)^{0,8} + \frac{3{,}8 \cdot x^{0,76} \cdot (1-x)^{0,04}}{\left(\frac{P}{P_c}\right)^{0,38}}\right] \tag{3.71}$$

with $Nu_{liq} = 0{,}023 \cdot \mathrm{Re}_{liq}^{\;0{,}8} \cdot \mathrm{Pr}_{liq}^{\;0{,}4}$ (3.72)

The friction pressure drop is calculated according to VDI (1994) used by Rieberer [RIE98], and expressed by the linear pressure gradient:

$$\left(\frac{\partial P}{\partial L}\right)_f = 4 \cdot \frac{\tau_{vapor}}{d_h} \tag{3.73}$$

The vapor shearing force is defined by:

$$\tau_{vap} = \frac{f_f}{8} \cdot \frac{x^2 G^2}{\rho_{vap}} \tag{3.74}$$

The condensation friction factor is given by :

$$f_f = f_{1phase} \cdot \left(1 + 2{,}85 \cdot X^{0{,}523}\right)^2 \tag{3.75}$$

Where X is the Lockart-Martinelli parameter :

$$X = \left(\frac{\mu_{liq}}{\mu_{vap}}\right)^{0{,}1} \cdot \left(\frac{1-x}{x}\right)^{0{,}9} \cdot \left(\frac{\rho_{vap}}{\rho_{liq}}\right)^{1/2} \tag{3.76}$$

According to VDI (1994), the one-phase friction factor is given by an asymptotic model function of laminar and turbulent flow:

$$f_{1phase} = \left(f_{la\min ar}^{3} + f_{turbulent}^{3}\right)^{1/3} \tag{3.77}$$

with $f_{la\min ar} = \dfrac{64}{\mathrm{Re}_{vap}}$ (3.78)

and $f_{turbulent} = \dfrac{0{,}184}{\mathrm{Re}_{vap}^{\;0{,}2}}$ (3.79)

where $\mathrm{Re}_{vap} = \dfrac{xGd_h}{\mu_{vap}}$. (3.80)

3.3.3 One phase correlations

For the vapor heating in the evaporator, the Dittus–Boelter correlation is used for heat transfer coefficient. For the vapor cooling and the liquid cooling, the Gnielinski correlations are used for heat transfer coefficient. For pressure drop in vapor and liquid state, the Gnielinski correlations is used.

3.3.4 Water transfer heat coefficient

The Nusselt number for liquid flow between two concentric tubes, Figure 3.24, is given by [PAD]:

$$Nu_{D_h} = 0.023\,\mathrm{Re}_{D_h}^{0.8}\,\mathrm{Pr}^{1/3}\left(\frac{d_o}{d_i}\right)^{0.14} \quad (3.81)$$

where $D_h = d_o - d_i$ and the outer diameter is insulated.

This correlation is used for the water flow into the tube (evaporator) and the shell (condenser / gas cooler).

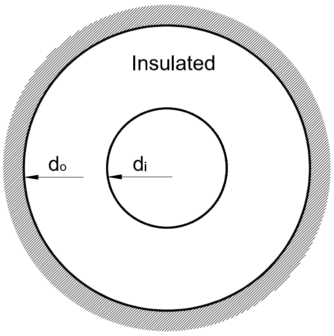

Figure 3.24: Concentric tubes with insulated outer wall.

In addition, other authors give other correlations for liquid flow inside concentric annular ducts.

For the forced convection flow inside concentric annular ducts, turbulent (Re > 2300), the heat transfer coefficient are expressed as follows.

- Heat transfer at the inner wall, outer wall insulated:

$$\frac{\mathrm{Nu}}{\mathrm{Nu}_{\mathrm{tube}}} = 0.86\left(\frac{D_o}{D_i}\right)^{0.16} \quad \text{(Petukhov and Roizen)} \qquad (3.82)$$

- Heat transfer at the outer wall, inner wall insulated:

$$\frac{\mathrm{Nu}}{\mathrm{Nu}_{\mathrm{tube}}} = 1 - 0.14\left(\frac{D_i}{D_o}\right)^{0.6} \quad \text{(Petukhov and Roizen)} \qquad (3.83)$$

- Heat transfer at both walls, same wall temperatures:

$$\frac{\mathrm{Nu}}{\mathrm{Nu}_{\mathrm{tube}}} = \frac{0.86\left(\frac{D_i}{D_o}\right)^{0.84} + \left[1 - 0.14\left(\frac{D_i}{D_o}\right)^{0.6}\right]}{1 + \frac{D_i}{D_o}} \quad \text{(Stephan)} \qquad (3.84)$$

The properties are defined at the fluid bulk mean temperature (arithmetic mean of inlet and outlet temperature) [http://www.cheresources.com/convection.shtml#annular].

3.4 Heat exchanger design

The developed model for heat exchanger is one-dimensional and represents a tube in tube heat exchanger with counter-current flows. The CO_2 tubes are made of stainless steel 316L. The discretization of the heat exchanger is carried out according to the axis length of the exchanger. The heat transfer between the fluid and through the heat exchanger is defined by the relations:

Heat exchanger: $\dot{Q} = UA \cdot \Delta T_{\ln}$ (3.85)

Water flow : $\dot{Q} = \dot{m}_{water} \left(h_{out} - h_{in} \right)_{water}$ (3.86)

CO$_2$ flow : $\dot{Q} = \dot{m}_{CO2} \left(h_{out} - h_{in} \right)_{CO2}$ (3.87)

For a discrete element, the global heat exchange coefficient is:

$$\frac{1}{UA} = \frac{1}{h_i\ A_i} + \frac{\ln\left(\frac{d_o}{d_i}\right)}{2\pi.k.\Delta L} + \frac{1}{h_o\ A_o} \tag{3.88}$$

Figures 3.25 and 3.26 show the fluid flows through the evaporator and the gas cooler.

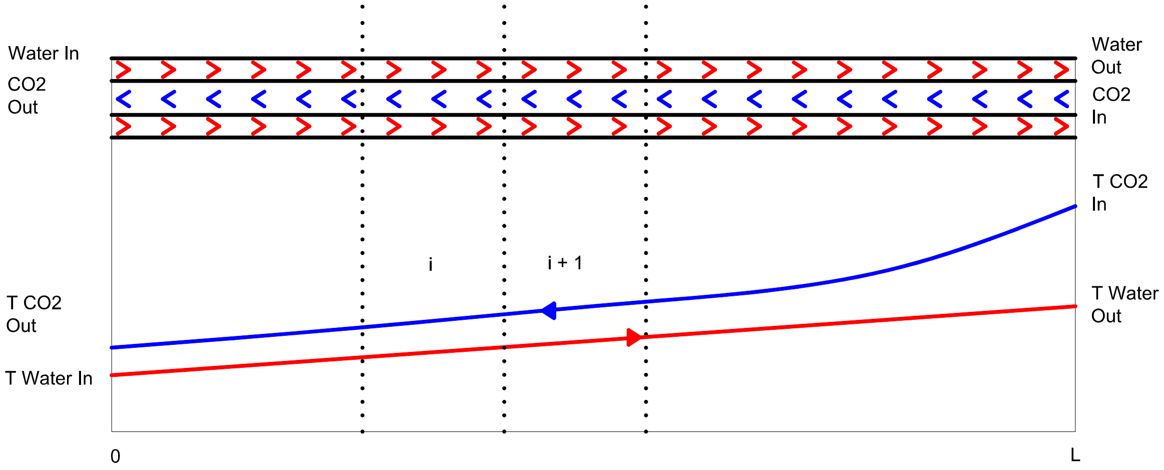

Figure 3.25: Gas cooler flow scheme.

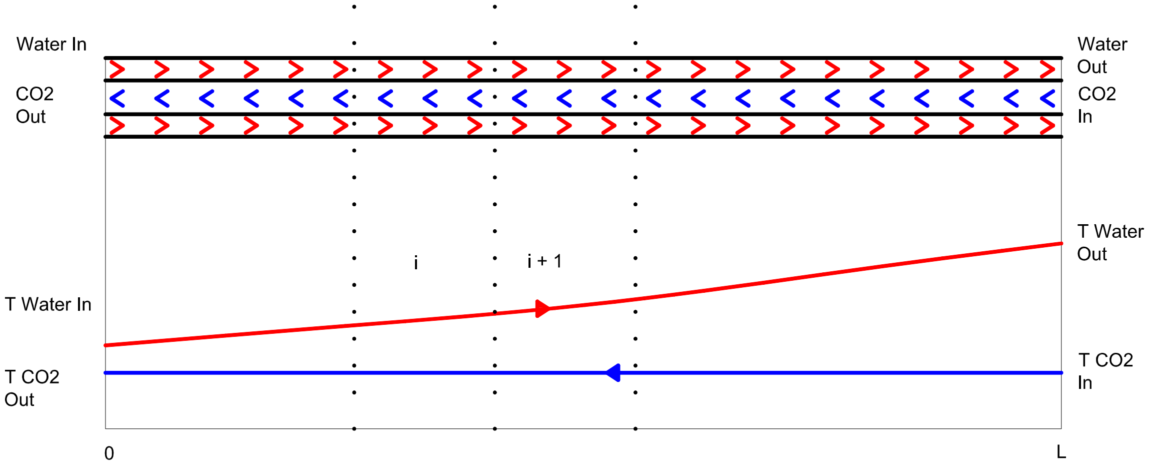

Figure 3.26: Evaporator flow scheme.

Starting at the CO$_2$ inlet, the calculation method consists in estimating the water outlet temperature, then by applying the heat transfer equations, the inlet water temperature is calculated. Thus, an iteration loop is used until the error between the inlet water temperature and the calculated water inlet temperature is lower than 0.01 K. For each element, the heat transfer coefficients are evaluated at the average temperature for each fluid. The CO$_2$ pressure drop of each element is integrated into calculation. The “golden section method” is used to solve the iteration loop.

The evaporator is divided into two sections: a two-phase flow section and a vapor flow one. For the gas cooler, when the CO$_2$ pressure is higher than 7.38 MPa, the gas cooler is modeled as a single section. When the gas cooler pressure is lower than 7.38 MPa, so a condensation process occurs, the gas cooler / condenser is divided into 3 sections: a vapor section to cool vapor down to the saturation phase, a two-phase condensation, and a liquid sub-cooling section.

3.4.1 Evaporator

Since the CO_2 pressure in the evaporator can reach 7 MPa, the adaptable and low cost heat exchanger type is the tube in tube technology. Thus, the inner tube is chosen to be a stainless tube of 8 mm outer diameter and 1 mm thickness. For volume and length constraints, the evaporator is formed by two stainless tubes of a 2.4 m length. For water, a reinforced silicon pipe with 16 mm internal diameter and 2 mm thickness is used as shown in Figure 3.27.

Table 3.5: Tube in tube evaporator.

Water temperature in / out °C	30	22.5
CO_2 inlet enthalpy / pressure kj/kg / MPa	300	3.5
CO_2 evaporation temperature °C	~ 0	
CO_2 mass flow rate g/s	12	
Water mass flow rate g/s	50	
Cooling capacity W	1 560	
Heat exchanger total length m	2.4	
CO_2 outlet quality	~1	
CO_2 pressure drop kPa	10	

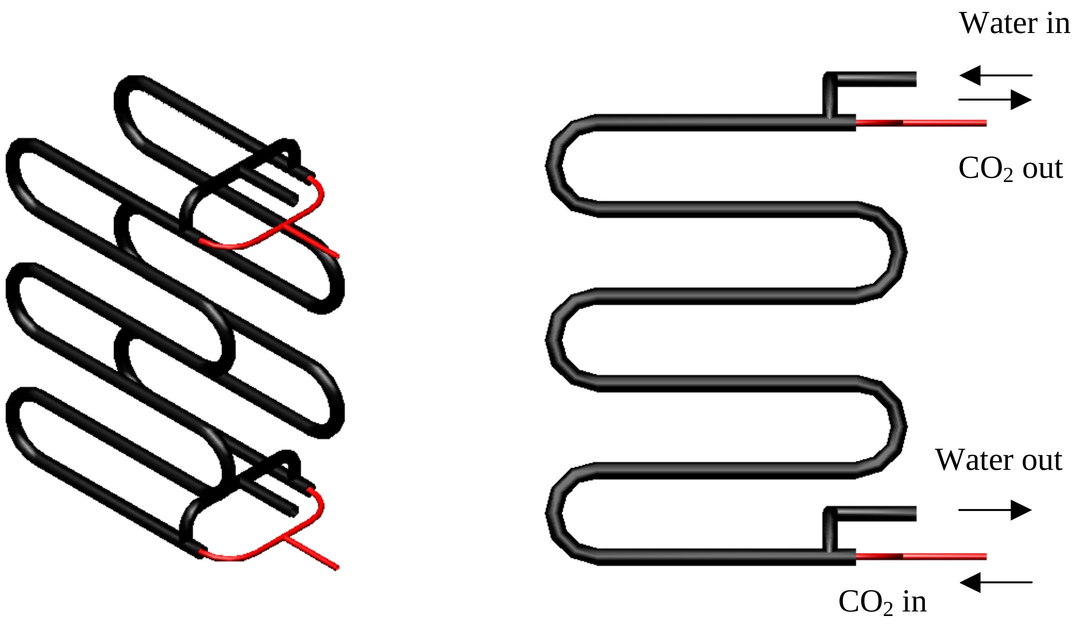

Figure 3.27: CO_2 evaporator.

For the defined parameters of Table 3.5, the evaporator exchanges 1560 W per tube, so a total cooling capacity of 3120 W, the pressure drop is 10 kPa, and the CO_2 outlet quality is 1, so the CO_2 evaporator outlet is at saturated vapor state.

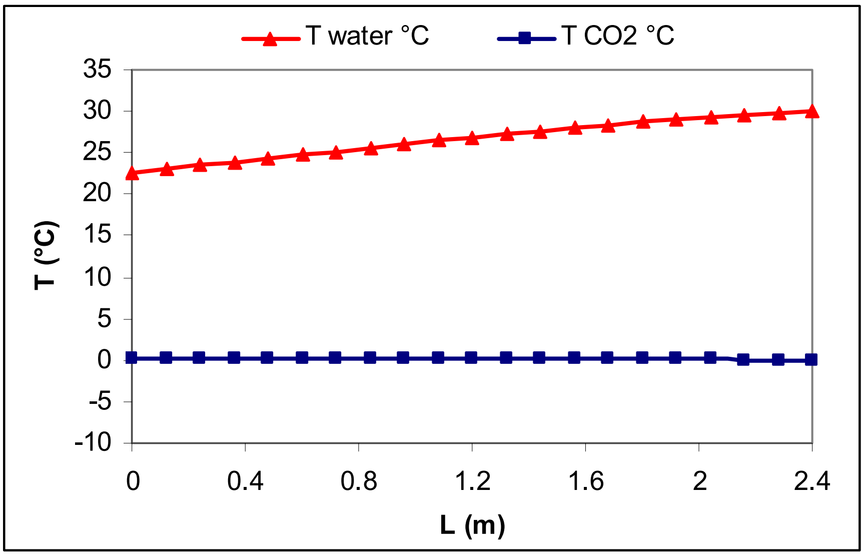

Figure 3.28: Variation of CO_2 and water temperatures through the counter-current tube-in-tube evaporator.

Figure 3.28 shows the variation of water and CO_2 temperatures through the evaporator.

3.4.2 Gas cooler

The explosion energy, defined by the product of the pressure by the internal volume, must be small for safety reasons; that involves a small gas cooler volume occupied by CO_2. Also, the high pressure requires an extra wall thickness.

For a supercritical cycle, the heat exchange is under a significant temperature glide of several tens of Kelvin. The refrigeration cycle performance is sensitive to the gas cooler outlet temperature, which must be close to the cooling fluid, which implies a counter flow configuration.

By respecting these constraints, the gas cooler was divided into two units connected in series. Each unit has a configuration of tube-and-shell type, and is composed of 140 micro-channel tubes with an internal diameter of 0,86 mm brazed on a collector at each end, all in a shell as shown in Figure 3.29. The gas cooler is made of stainless steel 316L. Stainless steel support high pressure but has a low thermal conductivity (15 W /m.K). Taking into account the high heat transfer coefficients for water and CO_2, and the small thicknesses and diameters of tubes, the thermal conduction resistance remains low compared to the internal (CO_2) and external (Water) thermal convective resistances.

Table 3.6: Geometry of the gas cooler prototype.

Characteristics	Values
Micro-channel internal diameter	0,86 mm
Micro-channel thickness	0,36 mm
Shell internal diameter	32,5 mm
Total tubes number per unit	140
Micro-channel useful length	2 * 850 mm
Total exchanger length	≈ 2*950 mm
Micro channel internal volume + collectors	2*0,072 dm^3
Water shell volume	2*0,228 dm^3

The assembly by welding the tubes on the collectors was carried out in a under vacuum oven. The gas cooler characteristics are listed in Table 3.6.

The total useful length of the gas cooler is 1.7 m, the ratio of internal/external heat transfer surface is 0.544.

a. Micro-channel stainless steel tubes. b. Micro-channel collector.

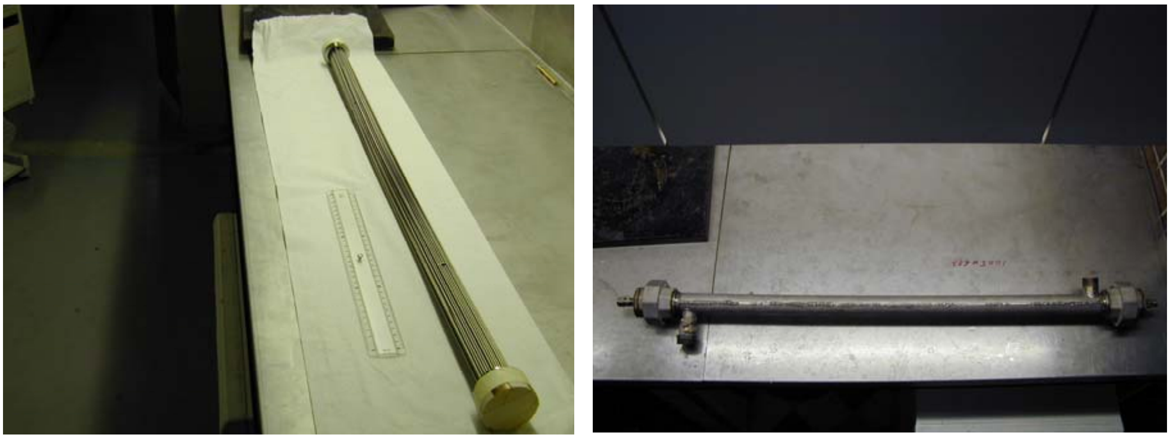

c. A unit of the gas cooler. d. Assembled tubes and collectors.

Figure 3.29: Gas cooler assembly scheme.

Table 7: Tube and shell CO_2 gas cooler.

Water temperature in / out (°C)	15	38.65
CO_2 inlet pressure (MPa)	10	
CO_2 temperature inlet (°C)	140	
CO_2 mass flow rate (g/s)	30	
Water mass flow rate (g/s)	100	
Heating capacity W	9886	
Heat exchanger total length (m)	1.7	
Useful length (m)	1.02	
CO_2 outlet temperature (°C)	15.1	
CO_2 pressure drop (kPa)	33.6	

For the defined parameters of Table 3.7, the gas cooler at supercritical state exchanges about 9.9 kW, the pressure drop is 33.6 kPa, and the CO_2 outlet temperature is 15.1°C, so the CO_2 gas cooler outlet temperature is close to water inlet temperature. Figure 3.30 shows that the useful length of the gas cooler is only 1.02 m, and through the other length no heat exchange occurs.

Table 3.8: Tube and shell CO_2 condenser.

Water temperature in / out (°C)	15	37
CO_2 inlet pressure (MPa)	6.5	
CO_2 temperature inlet (°C)	140	
CO_2 mass flow rate (g/s)	30	
Water mass flow rate (g/s)	100	
Heating capacity (W)	9185	
Heat exchanger total length (m)	1.7	
Useful length (m)	1.7	
CO_2 outlet temperature (°C)	24.5	
CO_2 pressure drop (kPa)	62.5	
CO_2 sub-cooling (K)	0.5	

For the defined parameters of Table 3.8, the gas cooler/ condenser at sub-critical state exchanges 9185 W, the pressure drop is 62.5 kPa, and the CO_2 outlet temperature is 24.5°C, so the CO_2 gas cooler outlet has 0.5 K as sub-cooling. Figure 3.31 shows that all the length of the gas cooler / condenser exchanges heat with water.

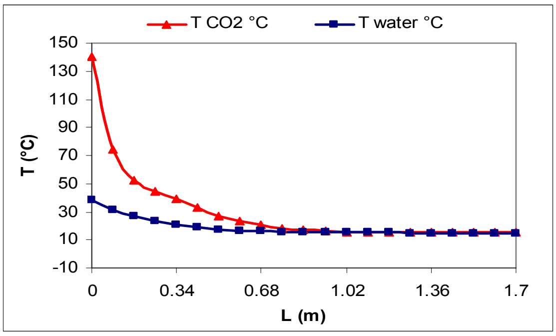

Figure 3.30: Variation of temperature through the gas cooler for supercritical flow.

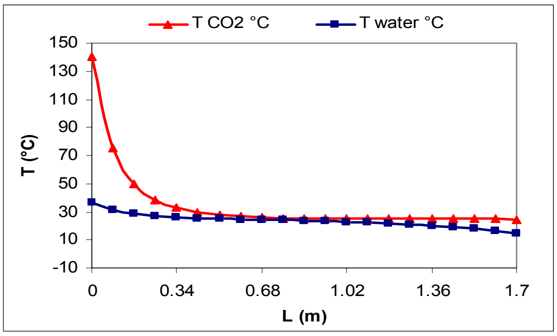

Figure 3.31: Variation of temperature through the condenser for sub-critical flow.

3.5 Design of a two phase CO_2 transcritical ejector

Using the 1D model and with the following input data:
evaporation temperature T_{ev} = 2°C, evaporator outlet superheat SH = 5 K, and gas cooler outlet temperature T_{gc} = 35°C, and by assuming nozzle and diffuser efficiency: $\eta_n = 0.85$; $\eta_s = 0.85$; $\eta_d = 0.75$, $\eta_m = 1$; the following parameters are calculated :

- the cycle COP,
- the entrainment ration w,
- the ratio between the secondary and the primary flows,
- the optimum high pressure,
- the ejector outlet pressure,
- the optimum pressure drop between the mixing chamber and the evaporator, and
- the mixing properties.

Table 3.9: Ejector calculated parameters at fixed inlet values.

T_{ev} °C	2	T_{gc} °C	35	*w*	*0.5410*
SH K	5	COP_c	*3.735*	ΔP MPa	*0.379*
η_n , η_s	0.85	P_{gc} MPa	*8.502*	U_{mix} m/s	*88.54*
η_d	0.75	$T_{out\ ejector}$ °C	*9.00*	P_{mix} MPa	*3.881*
η_{comp}	0.8	$P_{out\ ejector}$ MPa	*4.392*	T_{mix} °C	*4.12*

The following parameters have to be defined for the ejector design:

- Throat diameter of the nozzle.
- Outlet diameter of the nozzle.
- Constant area diameter of the mixing chamber.
- Diffuser outlet diameter.

The 1D model calculates these parameters, but in addition, the divergent and convergent angles: nozzle, constant pressure chamber, diffuser, and the constant area chamber length are determined by referring to the bibliography. Rusly [RUS 05] suggests the nozzle converging and diverging angles: 12° and 7°, the suction chamber converging angle: 10°, the diffuser diverging angle: 3.5°; the constant area chamber length: 5 $D_{\text{cst area}}$; the distance between the nozzle outlet and the constant area chamber: 1.5 $D_{\text{cst area}}$, the diffuser length : 8 $D_{\text{cst area}}$. Due to manufacturing constraints, and to obtain homogeneous flow in the nozzle that improves the nozzle efficiency, and by taking in account the high CO_2 density, the angles are modified, and the distance between the outlet nozzle and the constant area chamber will be modified as shown in Table 3.10.

Table 3.10: Ejector angle.

	Our	Rusly
Convergent nozzle angle	6	12
Divergent nozzle angle	2	7
Convergent constant pressure chamber angle	10	10
Diffuser divergent angle	4	3.5

Two assumptions are made to calculate the nozzle throat diameter:

- There is no phase change in the flow through a convergent tube.
- The maximum flow passes through the orifice separating the two chambers at different pressures: the upstream pressure is higher than the saturation pressure, and the downstream flow is a liquid / vapor two-phase flow.

So, the flow through the nozzle is saturated at the throat, thereby using the expansion efficiency of the nozzle, the thermodynamic properties: density and enthalpy at nozzle throat are evaluated, and by neglecting the inlet velocity, the throat velocity will be:

$$U_{th}=\sqrt{2000(h_{in,nozzle}-h_{throat})} \tag{3.89}$$

where U is in m/s and the enthalpy h in kJ/kg.

For a 4 kW evaporator cooling capacity, the geometrical parameters of the ejector are listed in Table 3.11.

Table 3.11: Ejector parameters for 4 kW evaporator capacity.

Q_{evap} KW	4	$U_{\text{out diffuser}}$ m/s	4.427
d_{throat} mm	1.143	$d_{\text{out diffuser}}$ mm	6.787
d_{out} mm	1.251	m_{evap} g/s	19.36
$d_{\text{constant area}}$ mm	2.212	m_{comp} g/s	35.78

Note that the mass flow rate of CO_2 in the conventional cycle is 31.57 g/s for the same operating conditions.

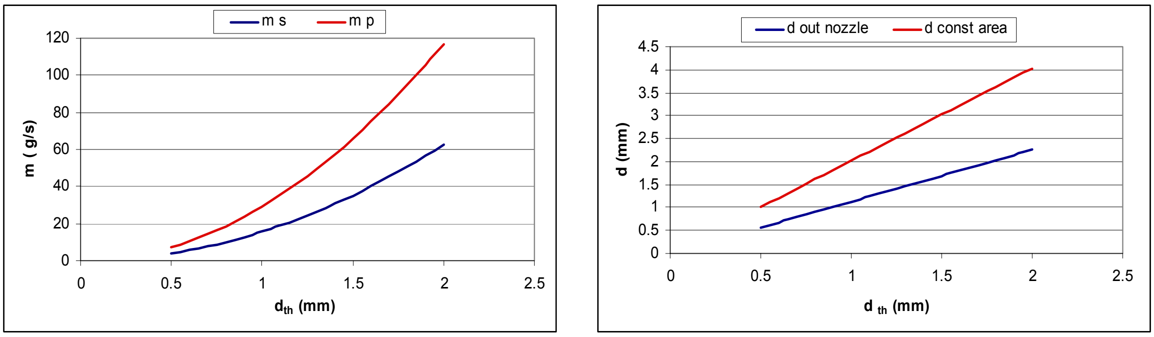

a- Primary and secondary mass flow rate

b- Outlet nozzle diameter and constant area diameter

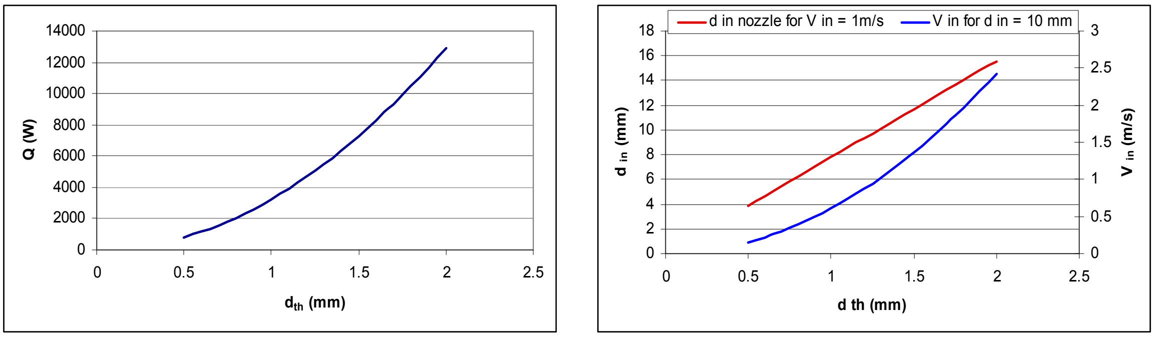

b- Evaporator capacity

d- Nozzle inlet diameter and velocity

Figure 3.32: Variation of ejector geometrical parameters with the nozzle throat diameter for operating parameters defined in Table 3.9.

Figure 3.32 shows the variation of the ejector geometrical parameters and cooling capacity with the nozzle throat diameter. The nozzle outlet diameter, the constant area diameter, the diffuser outlet diameter, and the cooling capacity increase with the throat diameter d_{th}.

For manufacturing constraints, the throat diameter has been set at 1 mm, the other parameters are listed in Table 3.12.

Table 3.12: Produced Ejector parameters (calculated).

Q_{evap} KW	3.062	$U_{out\ diffuser}$ m/s	1.195 (*4.427*)
d_{throat} mm	1	$d_{out\ diffuser}$ mm	10 (*5.195*)
d_{out} mm	1.2 (*1.095*)	m_{eavp} g/s	14.82
$d_{constant\ area}$ mm	2.0 (*1.935*)	m_{comp} g/s	27.39

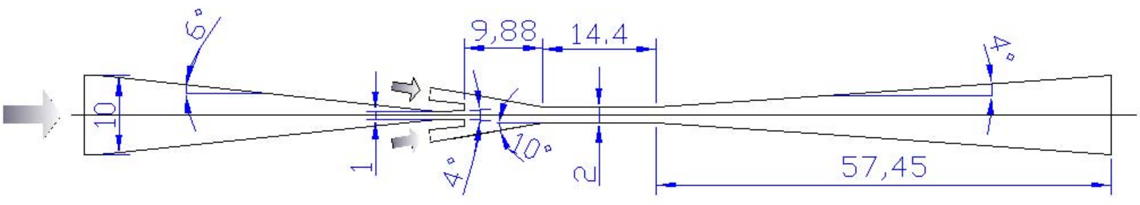

Figure 3.33: Ejector geometrical parameters in mm.

The ejector to be tested is shown in Figure 3.33. The effect of the distance between the nozzle outlet and the constant area chamber, and the effect of the constant area length will be experimentally analyzed.

Two other nozzles are realized with 0.75 mm and 1.25 mm as throat diameters, with same angles already defined. Five body cores other than showed in Figure 3.33, which form the mixing chamber, are produced with 1.5, 2.5, 3.0, 3.5 and 4.0 mm as $D_{const\ area}$. The constant area length varies between 6 $D_{const\ area}$ and 9 $D_{const\ area}$. The scheme and the real ejector is shown in Figure 3.34. Additional figures of the ejector parts as realized are shown in Annex 3.

a. Ejectors parts b. Six different body cores

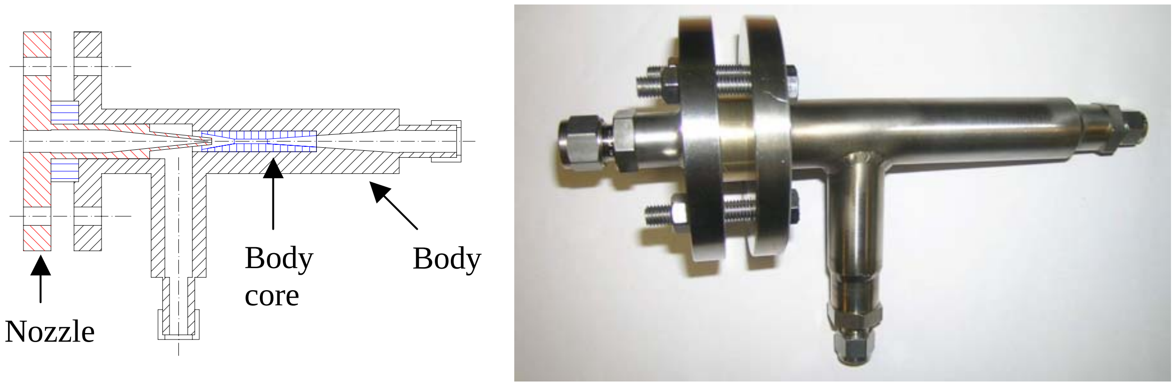

c. Assembled ejector scheme d. Assembled ejector

Figure 3.34: Ejector design.

3.6 Analysis of an ejector

Using Equation 3.89 to calculate the nozzle throat velocity, the analysis of the designed ejector is performed. The input data of the model are:

- The ejector geometry : $d_{th,\ nozzle}$; $d_{nozzle\ divergent\ outlet}$; $d_{const\ area}$.
- The gas cooler outlet temperature T_{gc} , the evaporating temperature T_{ev} .
- The evaporator outlet superheat TS.
- The ejector efficiencies: η_n, η_s, η_d.
- The compressor isentropic efficiency: η_{comp}.

Knowing these inputs, the calculations proceed as follows referring to Figure 2.12b and Figure 2.51:

$$h_2 = f(T_{ev} + TS, P_{ev}) \tag{3.90}$$

Considering a gas cooler pressure P_{gc} gives:

$$h_1 = f(T_{gc},P_{gc}) \tag{3.91}$$
$$s_1 = f(T_{gc},P_{gc}) \tag{3.92}$$

According to the entropy s_1 position compared to the critical entropy s_{cr} = 1.43 kJ/kg.K, two possible calculation options of the saturated enthalpy are possible.

Using polynomial equation:

$$\text{For } s_1 < s_{cr} : h_{sat,\ liq} = 50.51463\ s^2 + 184.392\ s - 34.6345. \tag{3.93}$$
$$\text{For } s_1 > s_{cr} : h_{sat,\ vap} = -323.92032\ s^2 + 1308.1503\ s - 880.807. \tag{3.94}$$

Using an iteration loop to find the saturation enthalpy by varying the throat saturation temperature between the evaporation temperature and the critical temperature. This method is chosen because it is more reliable especially near the critical point:

$$h_{th,\,is} = f(s_1). \tag{3.95}$$

Considering an expansion coefficient in the convergent of the nozzle:

$$h_{th} = h_1 - \eta_n(h_1 - h_{th,is}) . \tag{3.96}$$

Then the saturation throat temperature, velocity and density are calculated by:

$$T_{th} = f(h_{th}) \tag{3.97}$$

$$v_{th} = \sqrt{2(h_1 - h_{th})} . \tag{3.98}$$

$$\rho_{th} = f(T_{th}, h_{th}). \tag{3.99}$$

After the primary mass flow rate is given by:

$$m_p = m_{th} = \rho_{th} v_{th} \frac{\pi d_{th}^2}{4} . \tag{3.100}$$

To evaluate the properties of the flow at the nozzle outlet, an isentropic process from the inlet is used:

$$s_a = s_1 . \tag{3.101}$$

A guessed pressure P_a is considered, and then an iteration calculation is done until the continuity equation is verified:

$$h_{a,is} = f(P_a, s_1) \tag{3.102}$$

$$h_a = h_1 - \eta_n(h_1 - h_{a,is}). \tag{3.103}$$

$$v_a = \sqrt{2(h_1 - h_a)} \tag{3.104}$$

$$\rho_a = f(P_a, h_a) \tag{3.105}$$

$$m_a = \rho_a v_a \frac{\pi \mathrm{d}_{\text{nozzle divergent outlet}}^2}{4} \tag{3.106}$$

The iteration on P_a continues until $m_a = m_p$.

From Equations 2.58, 2.59, and 2.60, the velocity of the secondary flow $v_{b,s}$ is evaluated. The entrainment ratio is an unknown. Using Equations 2.62, 2.63, 2.64', and 2.65', the entrainment ratio is expressed as:

$$w = \rho_{m,s} v_{m,s} \left(\frac{\pi d_{const\ area}^2}{4 m_p} - \frac{1}{\rho_{m,p} v_{m,p}} \right) \tag{3.107}$$

By using Equations 2.66, 2.67, 2.70, and 2.71, the iteration loop gives the mixture pressure P_m and the mixture velocity v_m.

Equations 2.72, 2.73, 2.74, 2.75, and 2.76 give the flow properties at the outlet of the diffuser. To realize the ejector cycle, Equation 2.77' has to be fulfilled, so the gas cooler pressure is now evaluated following Equation 2.77'.

Using the 1D analysis model, the ejector of Figure 3.34 is analyzed by varying the evaporation temperature, the gas cooler outlet temperature, and the constant area diameter $D_{\text{const area}}$.

Results with fixed T_{ev}

By setting three evaporation temperatures: -1, 2, and 5°C, (see Figures 3.35 a to j) and running the program, the following results were obtained:

- The optimum gas cooler pressure increases with T_{gc} for the ejector and the reference refrigeration CO_2 cycle.
- The COP decreases with T_{gc}, but the COP improvement of the ejector refrigeration cycle increases with T_{gc}.
- For the same compressor mass flow rate for the reference cycle and the ejector refrigeration cycle, the cooling capacity of the reference cycle is higher than the ejector cycle one, but the cooling capacity decreases with T_{gc} for both cycle.
- The entrainment ratio w and the pressure drop DP decrease with T_{gc}.
- The compression ratio, the ratio between the ejector outlet pressure and the evaporator outlet pressure, increase with T_{gc}.

By comparing the chart values to those of Table 3.9, a difference exists due to the change of the optimum operating conditions of P_{gc} and ΔP.

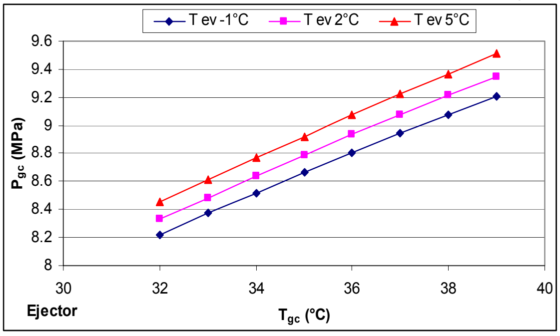

a- Variation of the ejector optimum pressure with T_{gc}

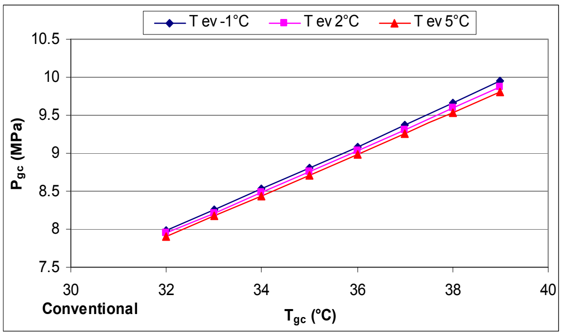

b- Variation of the conventional P_{gc} with T_{gc}.

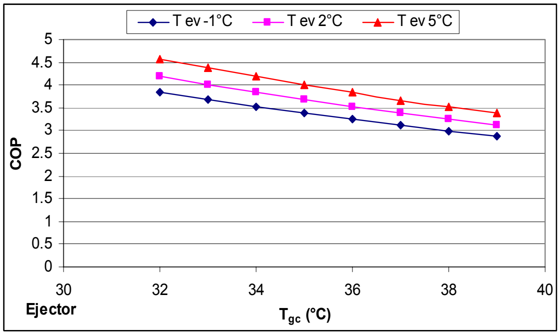

c- Variation of the optimum ejector COP with T_{gc}

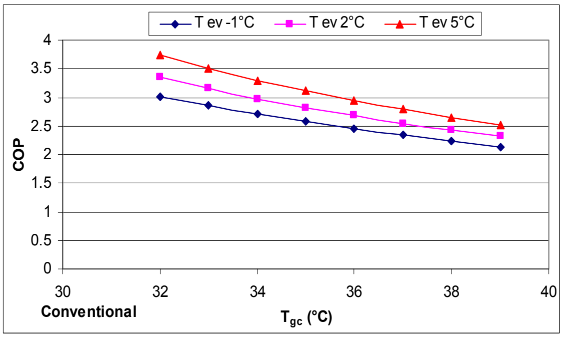

d- Variation of the optimum conventional COP with T_{gc}

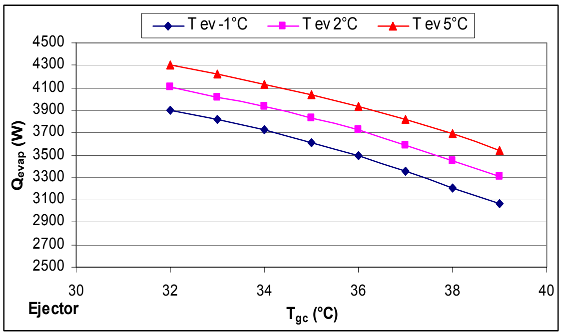

e- Variation of the ejector evaporator capacity with T_{gc}

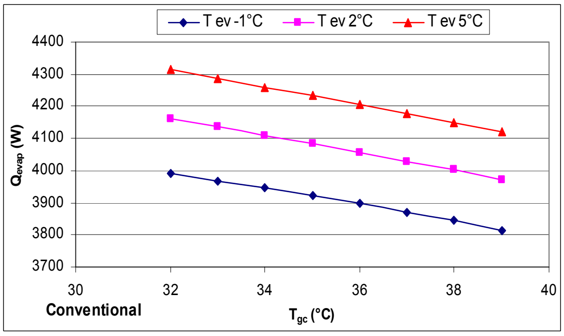

f- Variation of the conventional capacity with T_{gc}

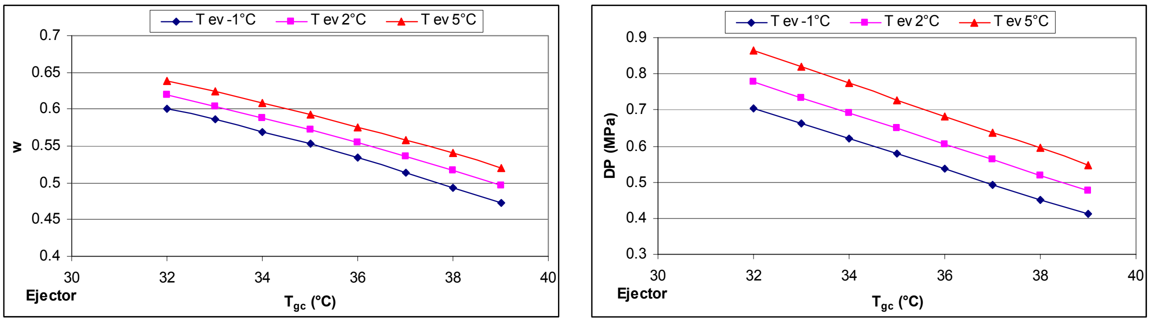

g- Variation of the ejector entrainment ratio with T_{gc}

h- Variation of the pressure drop with T_{gc}

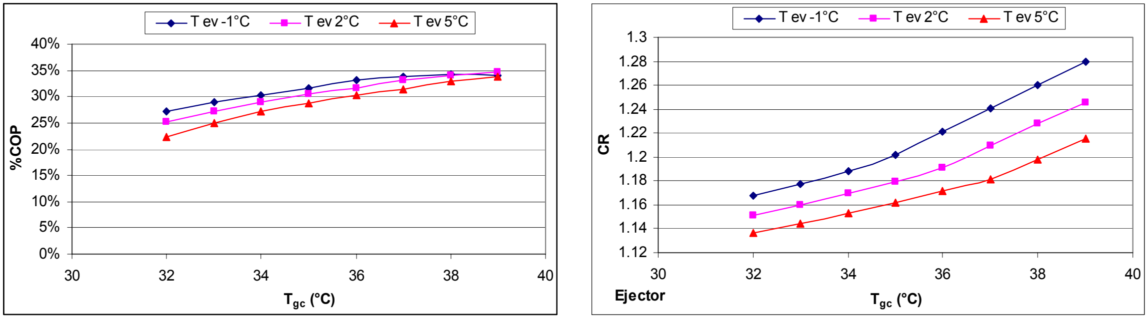

i- Variation of the COP improvement with T_{gc}

j- Variation of the ejector compression ratio with T_{gc}

Figure 3.35: Variation of the ejector parameters with T_{gc}, SH = 5 K, $\eta_{comp} = 0.8$, $\eta_n = \eta_s = 0.85$, $\eta_d = 0.75$.

Results with T_{gc} = 35°C

By fixing T_{gc} at 35°C, (see Figures 3.36 a to d), the variation of T_{ev} shows that the reference P_{gc} decreases with T_{ev}, but the ejector P_{gc} increases with T_{ev}. The COP increases with T_{ev}, and the ejector cycle COP is higher than the reference cycle COP. The cooling capacity increases with T_{ev}, but the reference cooling capacity is higher than the ejector cycle one for similar compressor mass flow rate. The entrainment ratio and the pressure drop PD increases with T_{ev}.

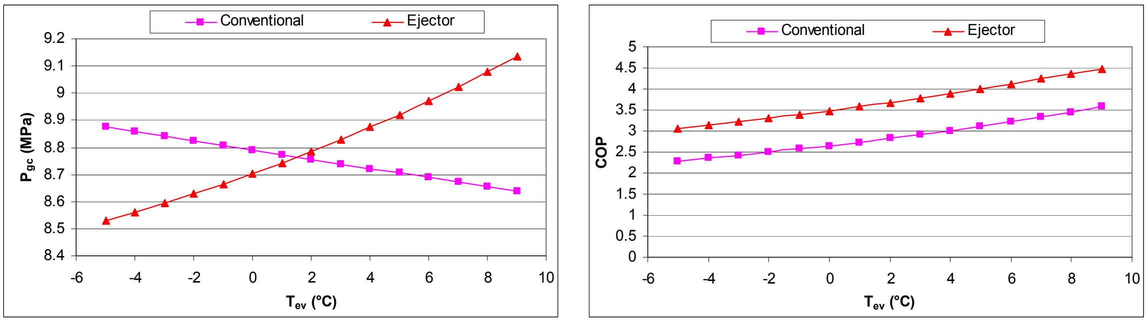

a- Variation of the optimum pressure with T_{ev}

b- Variation of the optimum COP with T_{ev}

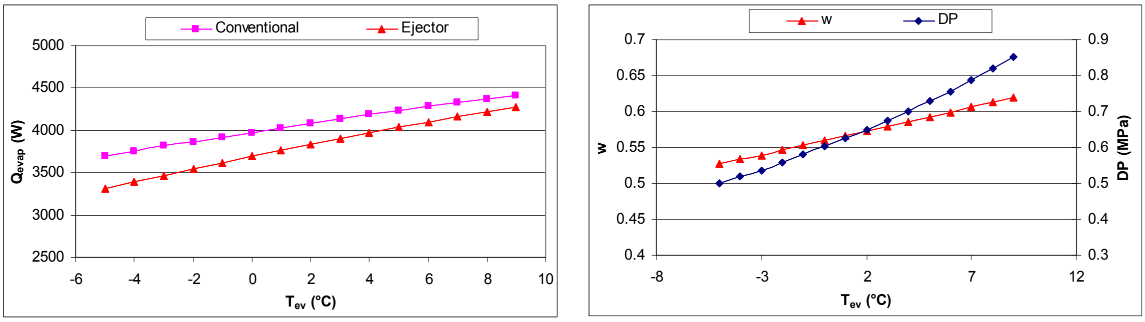

c- Variation of the evaporator capacity with T_{ev}

d- Variation of entrainment ratio w and pressure drop PD with T_{ev}

Figure 3.36: Variation of the ejector parameters with T_{ev}, T_{gc} = 35°C, SH = 5 K, $\eta_{comp} = 0.8$, $\eta_n = \eta_s = 0.85$, $\eta_d = 0.75$.

Analyze of the chamber diameter

For constant operating parameters: T_{ev} = 2°C and T_{gc} = 35°C, the effect of the constant area chamber diameter $D_{cst\ area}$ has been analyzed (see Figure 3.37):

a) The ejector cycle presents an optimum COP near the calculated constant area diameter of Table 4 (1.935 mm).

b) The gas cooler pressure increases with $D_{const\ area}$ up to 3 mm then becomes almost constant.

c) The evaporator capacity increases with $D_{const\ area}$ and becomes equal to the conventional evaporator capacity at $D_{const\ area}$ larger than 4 mm.

d) The entrainment ratio w increases with $D_{const\ area}$ up to 2 mm then becomes nearly constant. The compression ratio, the ratio between the ejector outlet and the evaporator pressure, presents an optimum around $D_{const\ area}$ = 2.2 mm, then decreases with $D_{const\ area}$.

e) The primary mass flow rate increases with $D_{const\ area}$ up to 3 mm then becomes nearly constant. The COP increases with $D_{const\ area}$ up to a maximum near 1.935 mm, then decreases and reaches 10% at 5 mm as $D_{const\ area}$.

f) The pressure-drop ΔP decreases with $D_{const\ area}$.

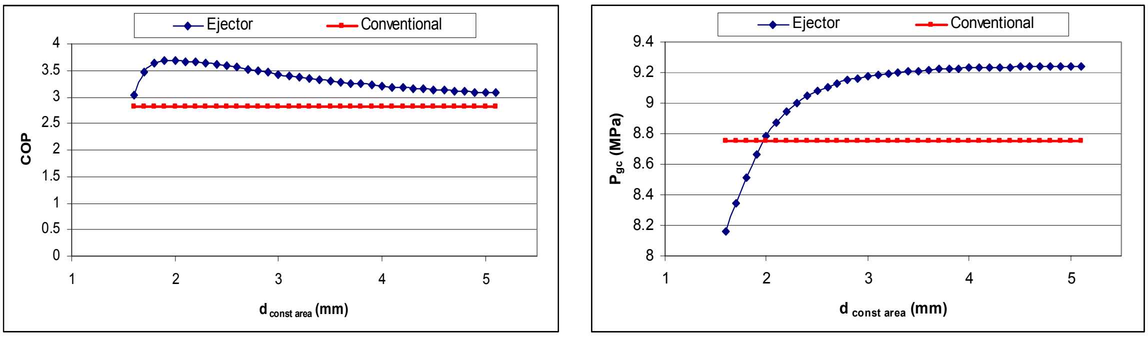

Variation of the optimum ejector COP with $D_{const\ area}$

b- Variation of optimum ejector P_{gc} with $D_{const\ area}$

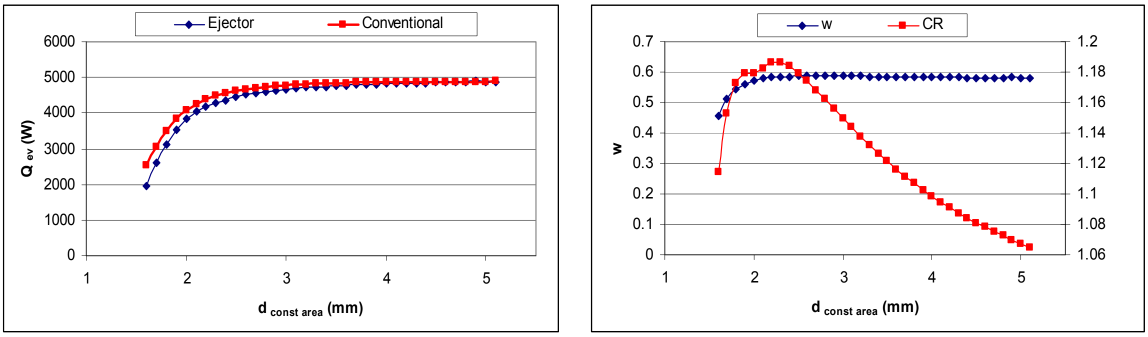

c- Variation of evaporator capacity with $D_{const\ area}$

d- Variation of the entrainment ratio w and the compression ratio with $D_{const\ area}$

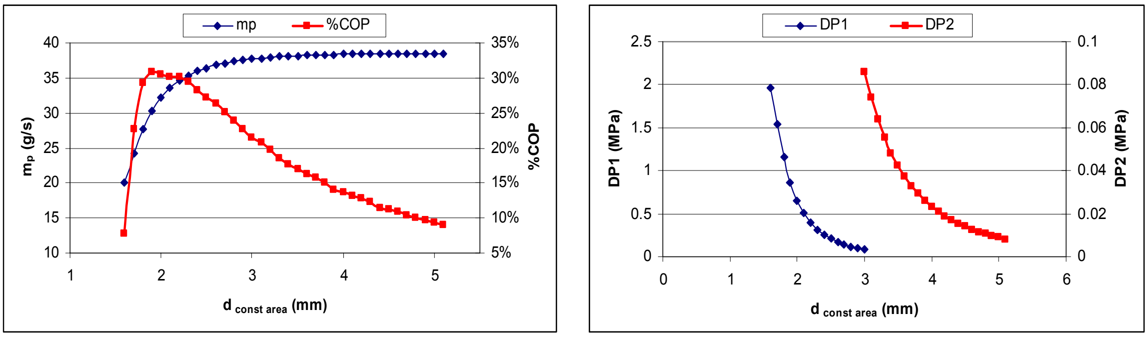

e- Variation of the compressor mass flow rate and the COP improvement with $D_{const\ area}$

f- Variation of ejector pressure drop PD with $D_{const\ area}$

Figure 3.37: Variation of the ejector parameters with constant area diameter $D_{const\ area}$, (T_{ev} = 2°C, T_{gc} = 35°C, SH = 5 K, η_{comp} = 0.8, $\eta_n = \eta_s$ = 0.85, η_d = 0.75).

Table 3.13: Parameters values of the analyzed nozzle with different constant area diameter.

$D_{cst\ area}$ mm	COP_{ej}	W	DP MPa	m_{comp} g/s	% COP	$P_{gc\ ej}$ MPa	CR	$Q_{ev\ conv}$ W	$Q_{ev\ ej}$ W
2	3.681	0.572	0.650	32.176	30.5	8.784	1.179	4081.12	3832.57
2.5	3.590	0.587	0.207	36.432	27.3	9.080	1.180	4621.00	4448.39
3	3.428	0.587	0.086	37.686	21.6	9.176	1.150	4780.06	4663.02
3.5	3.301	0.585	0.042	38.152	17.0	9.212	1.121	4839.12	4764.06
4	3.207	0.583	0.023	38.361	13.7	9.229	1.099	4865.61	4822.62

The values of different ejector characteristics as a function of the constant area diameter are listed in Table 3.13.

3.7 Separator

The separator plays an important role in the ejector refrigeration cycle since it separates the ejector outlet into vapor and liquid. A 1-L high-pressure receiver, with 4-mm thickness for withstanding a 25 MPa operating pressure, has been transformed in a separator by adding a tube (see Figure 3.38).

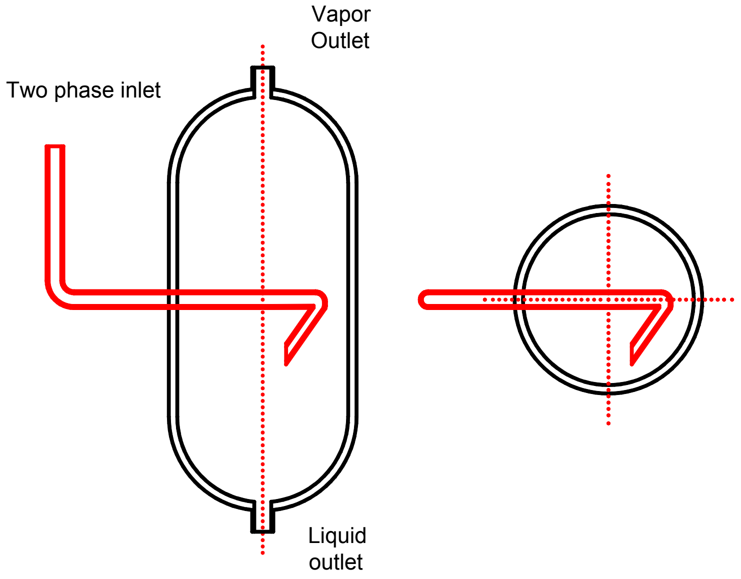

Figure 3.38: Separator lay-out.

The main purpose of a separator is to ensure no entrainment of liquid droplets with the vapor flow. This purpose is achieved by ensuring a vapor velocity in the receiver lower than 0.5 m/s. By varying the saturation temperature between –15 and 15°C, for a vapor mass flow rate of 60 g/s, the vapor velocity is 0.19 m/s. Thus, the separator will operate adequately, but for oil return, the separator will be evacuated after 50 operating hours using a set of ball valves .

3.8 Acquisition system and measurement elements

Temperatures are measured by PT100 resistance sensors, and the pressure is measured by Keller sensors. All the sensors signals are connected to a FIELDPOINT- NATIONAL INSTRUMENTS, that transform the signal (0-10 V DC, 4-20 mA, Hz, Ω) to a computer interface through CVI software. In addition, the system allows the control of the electric motor, the expansion valve, and the compressor electro-valve through a 0-10 V DC signal or a 0 – 10 V PWM signal. The precision of sensors is listed in Table 3.14. The vapor

CO_2 mass flow rate is measured by a Rheonik flowmeter (Coriolis effect type); the torque and the rotation speed are measured by a Magtrol sensor. The water flow volume is measured by Krhone flowmeter.

Table 3.14: Precision and accuracy of sensors.

Sensors	Type	Measure range	Relative precision over all range	Precision
Temperature	PT100	-40°C à +200°C	± 0.5 %	± 0,1 K
Pressure	Keller	0 – 10 MPa	± 0,1 %	± 0,01 MPa
Pressure	Keller	0 – 20 MPa	± 0,1 %	± 0,02 MPa
Mass flow meter	Vapor phase – Corriolis effect	0 – 250 g/ s	± 0,2 %	± 0,5 g/ s
Volume flow meter	Electromagnetic	0 – 1 dm^3/ s	± 0,5 %	± 0,005 dm^3/ s
Torquemeter	Magtrol	0 – 20 N	± 0,2 %	± 0.04 N.m
Tachymeter	Magtrol	0 – 6000 RPM	± 0,2 %	± 12 RPM

Uncertainty on the calculated values

Using the measure parameters by the sensors, the capacity of heat exchanger and the absorbed work of compressor are calculated.

For heat exchanger:

CO_2 side: $$\dot{Q}_{HX} = \dot{m}_{CO_2}\left(h_{in} - h_{out}\right) \quad (3.108)$$

Water side: $$\dot{Q}_{water} = \rho \cdot \dot{V} \cdot C_p \cdot \left(T_{in} - T_{out}\right) \quad (3.109)$$

For compressor:

Absorbed power: $$W_{Comp,eff} = \frac{2\pi NC}{60} \quad (3.110)$$

Isentropic power: $$W_{isent} = \dot{m}_{CO_2}\left(h_{out,comp} - h_{in,comp}\right) \quad (3.111)$$

The cycle performance is: $$COP = \frac{Q_{HX}}{W_{comp}} \quad (3.112)$$

By referring to Refprop7, the uncertainty of P and T gives an uncertainty of 1% on the calculation of the enthalpy and the density.

The uncertainty is given by:

$$\frac{\delta\dot{Q}_{HX}}{\dot{Q}_{HX}} = \frac{\delta W_{Comp,isent}}{W_{Comp,isent}} = \sqrt{\left(\frac{\delta h_{in} + \delta h_{out}}{\Delta h}\right)^2 + \left(\frac{\delta\dot{m}}{\dot{m}}\right)^2} \leq 2\ \% \quad (3.113)$$

$$\frac{\delta Q_{water}}{Q_{water}} = \sqrt{\left(\frac{\delta T_{in} + \delta T_{out}}{\Delta T}\right)^2 + \left(\frac{\delta \rho}{\rho}\right)^2 + \left(\frac{\delta C_p}{C_p}\right)^2 + \left(\frac{\delta \dot{V}}{\dot{V}}\right)^2} \leq 1.8\ \% \tag{3.114}$$

$$\frac{\delta W_{Comp,eff}}{W_{Comp,eff}} = \sqrt{\left(\frac{\delta N}{N}\right)^2 + \left(\frac{\delta C}{C}\right)^2} \leq 0.3\ \%. \tag{3.115}$$

$$\frac{\delta COP}{COP} = \sqrt{\left(\frac{\delta Q_{HX}}{Q_{HX}}\right)^2 + \left(\frac{\delta W_{comp}}{W_{comp}}\right)^2} \leq 3\ \%. \tag{3.116}$$

Thus, the measured error is lower than 3% on the different calculated values. By taking into account the degradation of the accuracy of the instruments, the error is estimated to be lower than 5% on the measured values and the calculated values from measured data.

3.9 Validation of heat exchangers models

Primary tests are done on the test bench to validate the evaporator model and the gas cooler model.

3.9.1 Gas cooler / Condenser model validation

At condensation flow, the pressure was varied between 6 and 7.38 MPa, and the mass flux G between 100 and 500 kg/m^2.s. Figure 3.39 shows that the relative error between the simulated and the measured heating capacity is lower than 5%.

Figure 3.41 shows that the relative error between the simulated pressure drop and the measured pressure drop is lower than 30%, which is the error given by the author of the correlations.

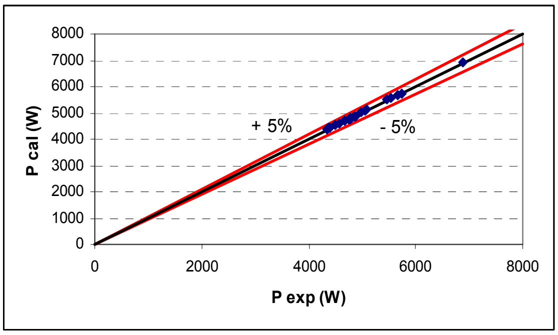

Figure 3.39: Calculated and measured heating capacity at CO$_2$ condensation state.

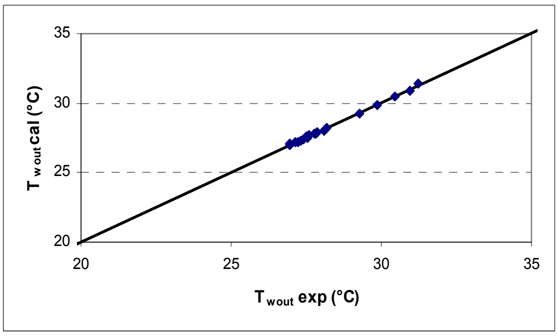

Figure 3.40: Calculated and measured condenser water outlet temperature.

Figure 3.40 shows the condenser outlet calculated temperature versus the measured one; the difference between the two values is lower than 1 K.

In supercritical state, the pressure is varied between 7.4 and 1.2 MPa and the mass flux between 100 and 500 kg/m^2.s. Figure 3.42 shows that the relative error between the simulated and the measured heating capacity is lower than 5 %.

Figure 3.43 shows that the relative error between the simulated pressure drop and the measured pressure drop is about 60%, so a correction factor CF is correlated as a function of the mass flux to decrease the error down to 20% as shown in Figure 3.46.

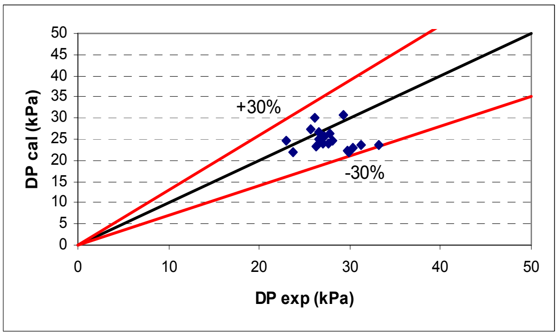

Figure 3.41: Calculated and measured condenser CO_2 pressure drop at condensation state.

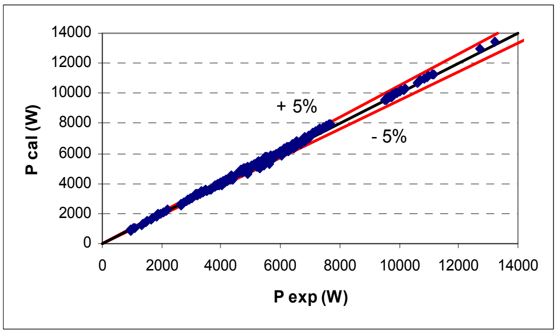

Figure 3.42: Calculated and measured capacity at CO_2 supercritical state.

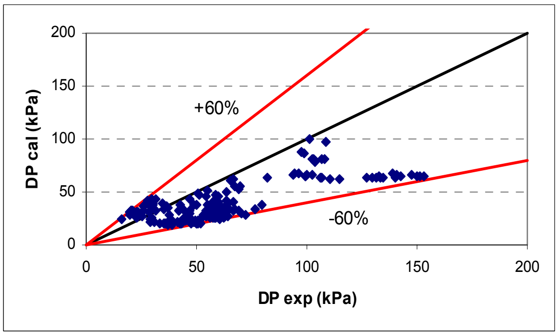

Figure 3.43: Calculated and measured CO_2 pressure drop at supercritical state.

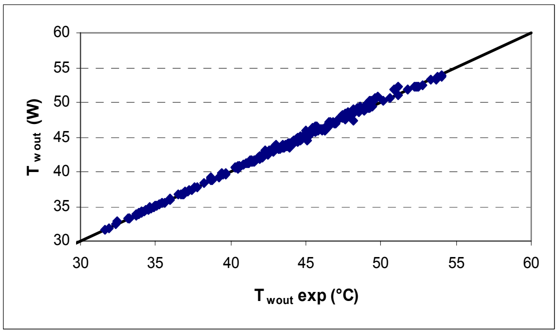

Figure 3.44: Calculated and measured gas cooler water outlet temperature.

The correction factor for the pressure drop at supercritical state, Figure 3.45, is defined by:

$$CF = 5.054.10^{-7}\ G^4 - 1.90356.10^{-4}\ G^3 + 0.026985\ G^2 - 1.731\ G + 44.219. \qquad (3.116)$$

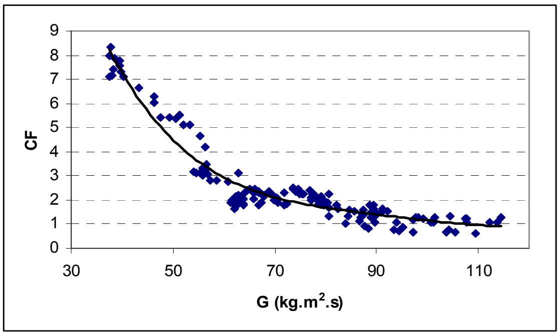

Figure 3.45: Variation of the correction factor CF with the mass flux at CO_2 supercritical state.

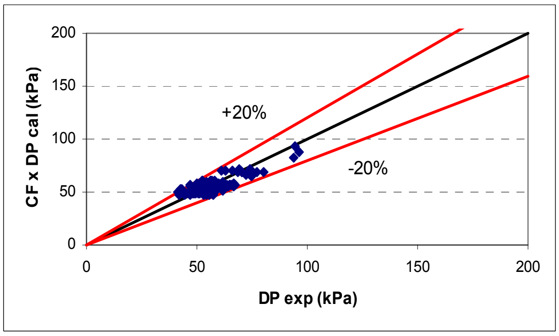

Figure 3.46: Corrected and measured CO_2 pressure drop at supercritical state.

However, the CO_2 properties are sensible to pressure, so a error range of the pressure drop of ±30% is acceptable since the maximum measured error of the pressure sensor is 0.01 MPa. Also, the capacity predicted by the gas cooler/ condenser has an error lower than 5% from the measured values.

Moreover, the effect of the entrained oil is not taken in account in the calculation of the pressure drop. The singular pressure drop at the inlet and the outlet of the gas cooler is not taken in account in the simulations.

Figure 3.44 shows the gas cooler outlet calculated temperature versus the measured one; the difference between the two values is lower than 1 K.

3.9.2 Evaporator model validation

The evaporation temperature is varied between -5 and 20°C, the evaporator outlet superheat between 0 and 25 K, and the mass flux G between 170 and 1000 kg/m^2.s. Figure 3.47 shows that the relative error between the simulated cooling capacity and the measured one is lower than 20%, which is the error range of correlations given by the author [CHE 06]. Also, for an exchanged power lower than 3500 W, the error is lower than 5%.

Figure 3.48 shows that the relative error between the simulated pressure drop and the measured pressure drop is about –80%, so a correction factor CF is elaborated as a function of the mass flux to decrease the error down to 20% as shown in Figure 3.50.

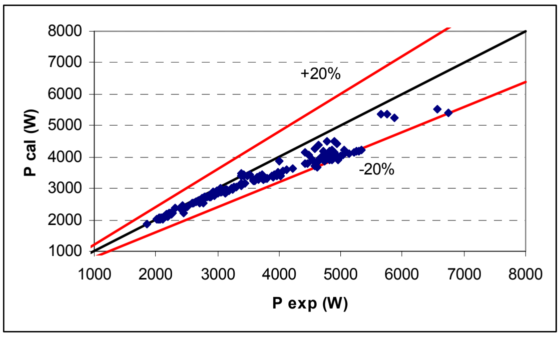

Figure 3.47: Calculated and measured cooling capacity.

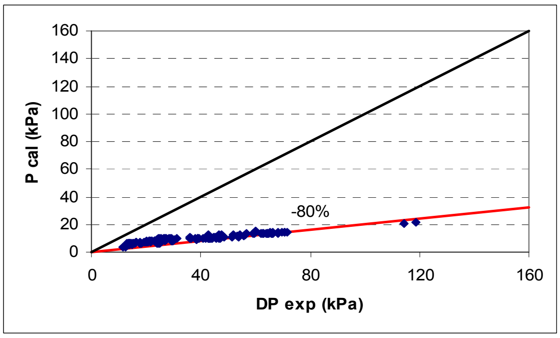

Figure 3.48: Calculated and measured CO$_2$ pressure drop during evaporation

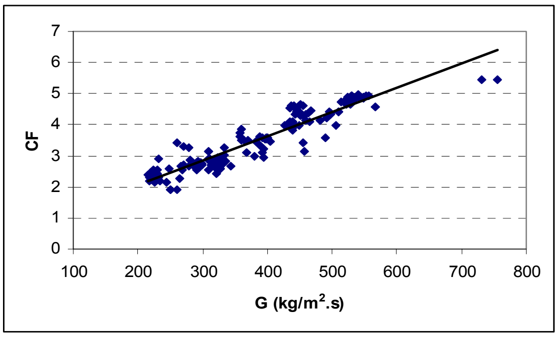

Figure 3.49: Variation of the correction factor CF with the mass flux during CO$_2$ evaporation.

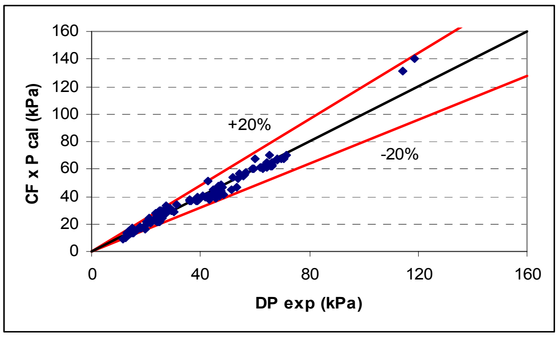

Figure 3.50: Corrected and measured CO$_2$ pressure drop for evaporation

The correction factor of the pressure drop for evaporation, Figure 3.49, is defined by:

$$CF = 7.831.\ 10^{-3}\ G + 0.5. \qquad (3.117)$$

Thus, same comments as those of gas cooler on oil entrainment effect and singular pressure drop are valid for the evaporator.

3.10 Conclusions

In this chapter, a test bench is described to fulfill four objectives:

- Validate the characteristics of the compressor,
- Validate the heat exchanger models: evaporator and gas cooler.
- Control the optimal operation of the CO_2 refrigeration cycle.
- Validate and adapt the ejector model.

The test bench is composed of a water-cooling loop and a CO_2 refrigeration loop. The CO_2 refrigeration loop is designed to test the simple CO_2 refrigeration cycle and the sub-cooled / supercritical CO_2 ejector refrigeration cycle.

The uncertainties of the measured values of the test bench are lower than 5%.

The Obrist compressor is characterized by its different efficiencies: volumetric, isentropic, mechanical, and effective, as a function of the pressure ratio, the rotation speed, and the displacement.

A gas cooler static prototype for CO_2 - water with micro-channel-tube-and-shell type has been designed with a developed simulation model, and the model has been validated with experimental tests.

A tube-in-tube evaporator prototype for CO_2 - water has been sized with a developed simulation model, and the model has been validated with experimental tests.

The simulation calculations predict the heating capacity with a precision better than 5% for condensation and supercritical states, which is the uncertainty range of the used correlations, and a precision better than 20% for evaporation, which is also the error of the correlations given by the authors.

Using the 1D model, an ejector is designed and analyzed for different geometrical and operating parameters. The main assumptions used by the 1D model to analyze the ejectors are:

- The flow is at saturated state at the nozzle throat.
- The flow is fully developed at the nozzle outlet and in the constant area mixing chamber.

Three nozzles are realized with different throat diameters: 0.75, 1, and 1.25 mm; and six different mixing chambers are realized with different diameters: 1.5, 2.0, 2.5, 3.0, 3.5, and 4 mm. The experimental results of the realized ejectors, discussed in Chapter 4, will be used to validate the assumptions and adapt the 1D model.

Also, the control of the CO_2 refrigeration cycle will be discussed in Chapter 4.

References

[ASI 05] Pietro Asinari, “Numerical prediction of turbulent convective heat transfer in mini/micro channels for carbon dioxide at supercritical pressure”, International Journal of Heat and Mass Transfer 48 (2005) 3864–3879.

[CHE 06] Lixin Cheng, Gherhardt Ribatski, Leszek Wojtan, John R. Thome, "New flow boiling heat transfer model and flow pattern map for carbon dioxide evaporating inside horizontal tubes", International Journal of Heat and Mass Transfer 49 (2006) 4082–4094.

[CHI 83] Chisholm D. “Two-phase flow in pipelines and heat exchangers”. Longman; 1983.

[DAN 04a] Chaobin Dang, Eiji Hihara, “In-tube cooling heat transfer of supercritical carbon dioxide. Part 1. Experimental measurement”, International Journal of Refrigeration 27 (2004) 736–747.

[DAN 04b] Chaobin Dang, Eiji Hihara, “In-tube cooling heat transfer of supercritical carbon dioxide. Part 2. Comparison of numerical calculation with different turbulence models”, International Journal of Refrigeration 27 (2004) 748–760.

[DAN 06] Chaobin Dang, Koji Iino, Ken Fukuoka, Eiji Hihara, “Effect of lubricating oil on cooling heat transfer of supercritical carbon dioxide”, International Journal of Refrigeration (2006)

[DID 02] M.B. Ould Didi, N. Kattan, J.R. Thome, “Prediction of two-phase pressure gradients of refrigerants in horizontal tubes”; International Journal of Refrigeration 25 (2002) 935–947.

[DUF 05] Romney B. Duffey, Igor L. Pioro, “Experimental heat transfer of supercritical carbon dioxide flowing inside channels”, Nuclear Engineering and Design 235 (2005) 913–924.

[HE 05] S. He, Pei-Xue Jiang, Yi-Jun Xu, Run-Fu Shi, W.S. Kim, J.D. Jackson, “A computational study of convection heat transfer to CO2 at supercritical pressures in a vertical mini tube”, International Journal of Thermal Sciences 44 (2005) 521–530.

[HUA 05] X.L. Huai, S. Koyama, T.S. Zhao, “An experimental study of flowand heat transfer of supercritical carbon dioxide in multi-port mini channels under cooling conditions”, Chemical Engineering Science 60 (2005) 3337 – 3345.

[JIA 06] Pei-Xue Jiang, Run-Fu Shi , Yi-Jun Xu, S. Heb, J.D. Jackson , “Experimental investigation of flow resistance and convection heat transfer of CO2 at supercritical pressures in a vertical porous tube”, J. of Supercritical Fluids (2006).

[KAN 02] S.G. Kandlikar, "Fundamental issues related to flow boiling in minichannels and microchannels", Exp. Thermal Fluid Sci. 26 (2002) 38–47.

[KAN90] KANDLIKAR S.G. "A general correlation for saturated two phase glow boiling heat transfer inside horizontal and vertical tubes", ASME Journal of Heat Transfer, Vol.112, 1990, p. 219-228.

[KAT 98a] N. Kattan, J.R. Thome, D. Favrat, "Flow boiling in horizontal tubes. Part 1: Development of a diabatic two-phase flow pattern map", J. Heat Transfer 120 (1998) 140–147.

[KAT 98b] N. Kattan, J.R. Tome et D. Favrat, "Flow boiling in horizontal tubes : Part 2 - New Heat Transfer Data for Five Refrigerants", J. Heat Transfer, Vol. 120, p 148-155, 1998.

[KAT 98c] N. Kattan, J.R. Thome, D. Favrat, "Flow boiling in horizontal tubes. Part 3: Development of a new heat transfer model based on flow patterns", J. Heat Transfer 120 (1998) 156–165.

[KEW 97] P.A. Kew, K. Cornwell, "Correlations for the prediction of boiling heat transfer in small-diameter channels", Appl. Thermal Eng. 17 (1997) 705–715.

[KRA 05] M. van der Kraan, M.M.W. Peeters, M.V. Fernandez Cid, G.F. Woerlee, W.J.T. Veugelers, G.J. Witkamp, “The influence of variable physical properties and buoyancy on heat exchanger design for near- and supercritical conditions”,J. of Supercritical Fluids 34 (2005) 99–105.

[LIA 02] S.M. Liao, T.S. Zhao, “An experimental investigation of convection heat transfer to supercritical carbon dioxide in miniature tubes”, International Journal of Heat and Mass Transfer 45 (2002) 5025–5034.

[PAD] Jacques PADET, “Convection thermique et massique: Nombre de Nusselt: partie 1”; Technique de l’ingénieur, BE 8 206-1.

[PET 00] PETTERSEN J., RIEBERER R., MUNKEJORD S.T., Heat transfer and pressure drop for flow of supercritical and subcritical CO_2 in microchannel tubes, Report TR A5127, SINTEF Energy Research,, Norway, February 2000.

[PIO 04] Igor L. Pioro, Hussam F. Khartabil, Romney B. Duffey, ”Heat transfer to supercritical fluids flowing in channels—empirical correlations”, Nuclear Engineering and Design 230 (2004) 69–91.

[PIT 00] S.S. Pitla, D.M. Robinson, A. Zingerli, E.A. Groll, S. Ramadhayani, “Heat transfer and pressure drop characteristics during in tube gas cooling of supercritical carbon dioxide”; Ray W. Herrick Laboratories, Purdue University, August 2000.

[PIT 02] Srinivas S. Pitla, Eckhard A. Groll, Satish Ramadhyani, “New correlation to predict the heat transfer coefficient during in-tube cooling of turbulent supercritical CO2", International Journal of Refrigeration 25 (2002) 887–895.

[RIE 98] René Rieberer, “CO_2 as working fluid for heat pumps”, Institute of Thermal Engineering, Craz University of Technology, Austria, December 1998.

[SON 06] Chang-Hyo Son, Seung-Jun Park, “An experimental study on heat transfer and pressure drop characteristics of carbon dioxide during gas cooling process in a horizontal tube”, International Journal of Refrigeration 29 (2006) 539–546.

[THO 04] John R. Thome, Jean El Hajal," Flow boiling heat transfer to carbon dioxide: general prediction method", International Journal of Refrigeration 27 (2004) 294–301.

[THO 05] John R. Thome, Gherhardt Ribatski, "State-of-the-art of two-phase flow and flow boiling heat transfer and pressure drop of CO2 in macro- and micro-channels", International Journal of Refrigeration 28 (2005) 1149–1168.

[WOJ 05a] Leszek Wojtan, Thierry Ursenbacher, John R. Thome," Investigation of flow boiling in horizontal tubes: Part I—A new diabatic two-phase flow pattern map", International Journal of Heat and Mass Transfer 48 (2005) 2955–2969.

[WOJ 05b] Leszek Wojtan, Thierry Ursenbacher, John R. Thome," Investigation of flow boiling in horizontal tubes: Part II - Development of a new heat transfer model for stratified-wavy, dryout and mist flow regimes". International Journal of Heat and Mass Transfer 48 (2005) 2970–2985.

[YIN 01] Jian Min Yin, Clark W. Bullard, Predrag S. Hrnjak, “R-744 gas cooler model development and validation”. International Journal of refrigeration 24 (2001) 692-701.

[YOO 03] Seok Ho Yoon, Ju Hyok Kim, Yun Wook Hwang, Mm Soo Kim, Kyoungdoug Minb, Yongchan Kim, “Heat transfer and pressure drop characteristics during the in-tube cooling process of carbon dioxide in the supercritical region”International Journal of Refrigeration 26 (2003) 857–864.

[YOO 04] Seok Ho Yoon, Eun Seok Cho, Yun Wook Hwang, Min Soo Kim,Kyoungdoug Min, Yongchan Kim , "Characteristics of evaporative heat transfer and pressure drop of carbon dioxide and correlation development", International Journal of Refrigeration 27 (2004) 111–119.

[YUN 03] Rin Yun, Yongchan Kim, Min Soo Kim, Youngdon Choi, "Boiling heat transfer and dryout phenomenon of CO_2 in a horizontal smooth tube"; International Journal of Heat and Mass Transfer 46 (2003) 2353–2361.

[ZHA 06] Xin Rong Zhang , Hiroshi Yamaguchi; “Forced convection heat transfer of supercritical CO2 in a horizontal circular tube”, J. of Supercritical Fluids (2006).

Chapter 4. CO_2 system operation: control strategy and experimental results

4.1 Introduction

As already presented in chapter 3, the test bench is designed to realize three objectives:

- The experimental analysis of the simple CO_2 refrigeration system.
- The elaboration of a control strategy of the evaporation temperature and the high side pressure of a CO_2 refrigeration system.
- The experimental analysis of the two-phase ejector CO_2 refrigeration system.

In this chapter those three objectives are discussed in details.

4.2 The simple CO_2 refrigeration system

In Chapter 1, the simple theoretical CO_2 refrigeration system; composed of a condenser/gas cooler, a compressor, an evaporator, and an expansion valve has been studied in details. When the outdoor temperature is higher than 31°C, the COP of the system depends on the high pressure side. To verify those results, several tests are performed at T_{ev} ~ 0°C and T_{gc} ~ 35°C.

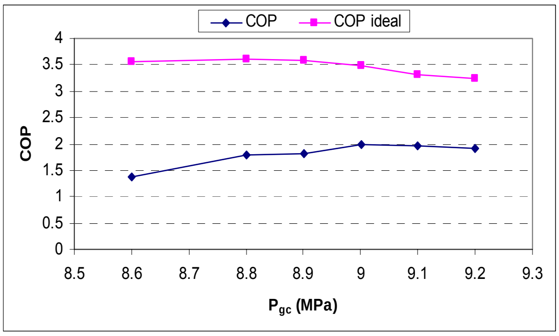

Figure 4.1: Variation of experimental and ideal COPs with P_{gc}

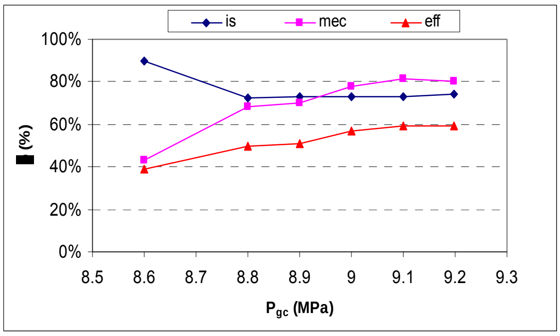

Figure 4.2: Compressor efficiencies variation with P_{gc}

Figure 4.1 shows that the experimental COP presents an optimum around 9 MPa. As the effective compressor efficiency is not constant during the tests as shown in Figure 4.2, so the ideal COP is calculated by dividing the real COP by the effective efficiency. The ideal COP presents an optimum around 8.8 MPa. By assuming a high pressure interval ±0.3 MPa around the optimum high pressure calculated in Chapter 1, the real COP of the CO_2 refrigeration system will be in the optimum interval.

4.3 Design of the control strategies of the high pressure and the evaporation temperature

4.3.1 Global system control

The main objective of this section is the development of a control logic that governs the control parameters of the refrigeration system: the compressor electro-valve (CEV) of an externally controlled compressor, and the electronic expansion valve. The control logic has to ensure an efficient operation of the system, for different thermal conditions and for different compressor rotation regimes.

The use of an externally control compressor allows to ensure:

- an optimum operating range of high pressures.
- a temperature level of evaporation to control the evaporator outlet temperature.

Also, the use of electronic expansion valve (EEV) ensures the optimum high pressure and the desired evaporation temperature.

In a mobile air-conditioning system with an externally controlled compressor, the compressor speed is directly related to the motor rotation speed, which varies rapidly during accelerations and decelerations of the vehicle. The relation between the compressor and the motor speed is function of their pulley diameter ratio. The pulley ratio is the ratio of the motor pulley diameter over the compressor pulley diameter. Figures 4.3 and 4.4 illustrate respectively the evolution of motor rotation speed and vehicle speed during a NEDC cycle.

The European NEDC regulatory cycle is composed of four successive urban cycles (195 s each) with fast engine speed variations and an extra urban cycle (400 sec), the total duration is about 20 min. As indicated on Figures 4.3 and 4.4, those quick speed variations imply fast variations of the compressor rotation speed. The typical variations are of more than 250% compared to the reference line, making the same variations of the refrigerant mass flow rates whatever the cooling needs.

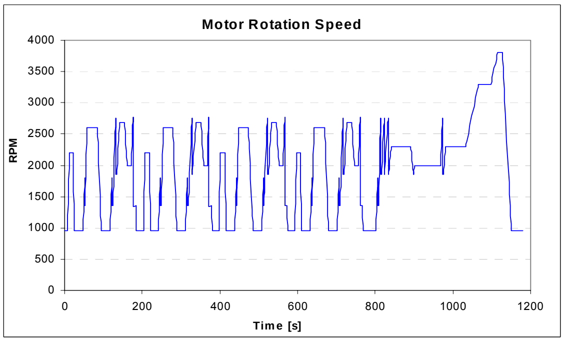

Figure 4.3: Evolution of motor rotation speed during a MVEG cycle.

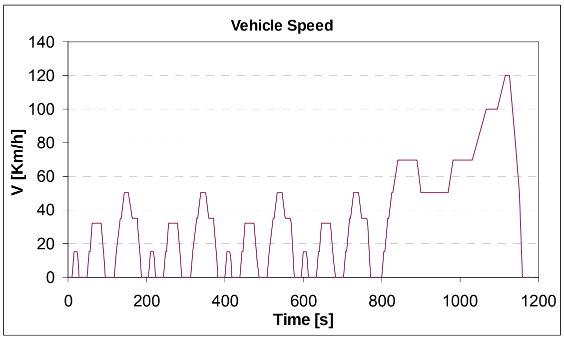

Figure 4.4: Evolution of vehicle speed during a MVEG cycle.

Smart control permits very fast answer of the compressor that can adapt the necessary swept volume whatever the engine speed variations.

The solenoid valve controls the compressor swept volume from 0 to 100%. The tension variation of the solenoid valve allows fine-tuning of the refrigerant mass flow rate according to the cooling needs of the vehicle. This solenoid valve is able to manage the fast variation of the engine rotation speed in order to avoid discharge pressure and evaporating temperature out of the optimum ranges.

A control algorithm has been developed for the externally control compressor taking into account the fast variations of the engine speed of typical urban driving cycles.

The control system, Figure 4.5, shall take into account the following input parameters:

- The evaporation temperature (EV Tem). For the test bench, this temperature is the evaporation temperature, but for the real system, the air outlet temperature at the evaporator is the reference parameter.
- The optimum high-pressure side is evaluated as a function of the evaporation temperature and the gas cooler outlet temperature. In mobile air-conditioning systems, the gas cooler outlet temperature is related to the outdoor temperature, the vehicle speed, and the cooling capacity.

The controlled parameters are the high pressure and the evaporating temperature. The output of the control system are:

- the tension of the CEV of the external control compressor
- the expansion valve opening (EVO).

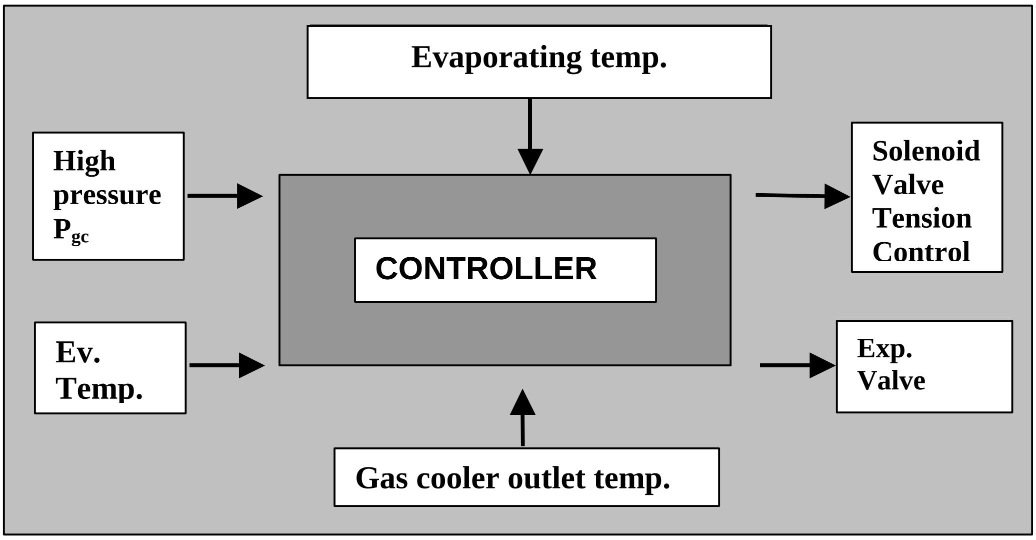

Figure 4.5: Schematic diagram of the controller.

The strategy elaborated to control the system is based on a PID method (Proportional, Integrator, Derivative). Since there are two tensions to be controlled: CEV and the EEV actuators, two PID controllers are used to adapt separately the evaporation temperature and the gas cooler pressure to the reference values.

4.3.2 PID control description and tuning

A PID controller allows the adjustment of the CEV voltage and the EEV opening to maintain the defined references of high-side pressure and evaporation temperature. The role of a controller is to maintain the controlled parameters at reference point whatever the system perturbations.

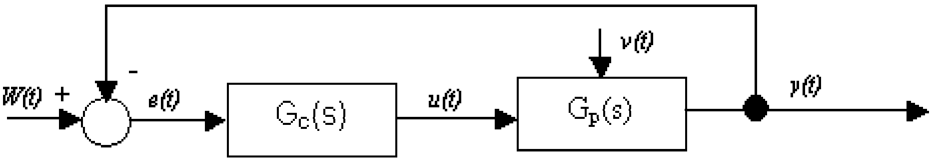

Figure 4.6: Working diagram of a closed loop regulated by a PID.

The working diagram of a closed loop system regulated PID is represented on Figure 4.6. It allows:

- to provide a control signal **u(t)** by taking into account the evolution of the output signal **y(t)** compared to the reference instruction **w(t)**
- to eliminate the static error e(t) due to the integrating term
- to anticipate the variations of the exit value **y(t)** due to the closed loop.

The temporal description of a PID is defined as follows:

$$u(t) = K_p\left(e(t) + \frac{1}{T_i}\int_0^t e(t)\,dt + T_d\,\frac{de(t)}{dt}\right) \tag{4.1}$$

The variable ***e(t)*** represents the tracking error, the difference between the desired input value ***w(t)*** and the actual output ***y(t)***. The error signal ***e(t)*** will be sent to the PID controller, and the controller computes both the derivative and the integral of the error signal.

The signal ***u(t)*** at the controller outlet is the sum of:

- the proportional gain times, the magnitude of the error

- the integral gain times, the integral of the error.
- the derivative gain times, the derivative of the error.

The general form of a numerical PID is given by:

$$u(k) = u(k-1) + \mathrm{A} \,.\, e(k) - B \,.\, e(k\text{-}1) + C \,.\, e(k-2) \tag{4.2}$$

With :

$$A = K_p\left(1 + \frac{\Delta}{T_i} + \frac{T_d}{\Delta}\right) \tag{4.3}$$

$$B = K_p\left(1 + 2\,\frac{T_d}{\Delta}\right) \tag{4.4}$$

$$C = K_p\left(\frac{T_d}{\Delta}\right) \tag{4.5}$$

Δ	sampling period
Ti	integral time
Td	derivative time
Kp	proportional gain.

The adequate control strategy allows attenuating the strong and sudden variation of the controlled parameters.

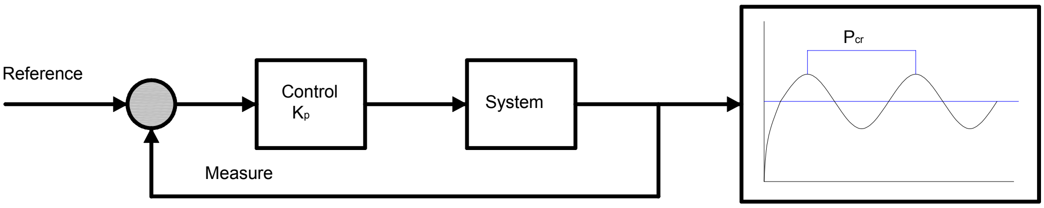

Figure 4.7: Working diagram of a closed loop regulated by a PID.

Generally, for characterized system with a transfer function $G_p(s)$, many analytical methods exist to calculate the constant of the PID controller. But for the system where the characterization with a transfer function is difficult or inexistent (extremely non-linear), the parameters A, B, and C are empirically given by the method of Ziegler-Nichols in closed loop.

The method consists in increasing gradually the pure proportional gain k_p until the oscillation of the system (see Figure 4.7), with $T_i = \alpha$ and $T_d = 0$. Thus, the critical gain K_{cr} and the critical period P_{cr} are experimentally determined. Ziegler and Nichols suggested values for the controller parameters given in Table 4.1.

Table 4.1: PID parameters.

Controller	P.	P.I.	P.I.D.
K_p	0,5 K_{cr}	0,45 K_{cr}	0,6 K_{cr}
T_i	α	0,83 P_{cr}	0,5 P_{cr}
T_d	0	0	0,125 P_{cr}

The larger the value of K_p, the less stable the system. Moreover a pure proportional does not eliminate the static error. The integrator action eliminates the static error and improves the robustness, but it slows down the system and makes it unstable. The derivative action makes the system more dynamic, stabilizes it but, on the other hand, makes it very sensitive to noises.

The PID controller tuned by the Ziegler-Nichols rules has the following mathematical formula:

$$G_c(s) = \mathrm{k_p}\left(1 + \frac{1}{\mathrm{T_i\ s}} + T_d\ s\right) = 0.075 K_{cr} P_{cr} \frac{\left(s + \frac{4}{P_{cr}}\right)^2}{s} \tag{4.6}$$

Thus, the PID controller has a pole at the origin and double zeros at s = - 4/ P_{cr}. However, if the Ziegler-Nichols tuning parameters do not respond to the required results, a small modification of the parameters can improve the results.

On the other hand, generally, for a PID controllers, the parameters are chosen to extract the small poles from the system mathematical equation, so 4/ P_{cr} should be less than 1.

In addition, if the PID controllers do not respond to the requested values, a proportional parameter D in the control signal equation is introduced to increase or decrease the effect of the previous signal:

$$u(k) = D.u(k-1) + \mathrm{A}.e(k) - B.e(k\text{-}1) + C.e(k-2) \tag{4.7}$$

Using the numerical PID controller, the evaporation temperature and the high-side pressure will be controlled by the EEV and the CEV. Four cases are studied:

- Control of the evaporation temperature by the CEV.
- Control of the gas cooler outlet pressure by the EEV.
- Control of the evaporation temperature by the EEV.
- Control of the gas cooler outlet pressure by the CEV.

Each case will be discussed, and the superposition of the control of the evaporation temperature by the EEV and the gas cooler outlet pressure with the CEV will be the optimal solution.

The CEV is controlled by a DC voltage between 3 and 8 volts. The middle of the interval control voltage is chosen to be the initial control signal, so the control signal Y_{comp} of the CEV is:

Y_{comp} (V) = (55 + u(k))/10. (4.8)

The expansion valve is controlled by a 0-10 DC voltage, so the control signal Y_{exp} is:

Y_{exp} = 50 - u(k). (4.9)

$$Voltage = 7 - \frac{5Y_{exp}}{100} \tag{4.10}$$

The error is calculated by:
e(t) = Reference – measured value. (4.11)

4.3.4 Control of the evaporation temperature by the CEV

The reference is the evaporation temperature, so the error is:

e(t) = $T_{ev,ref} - T_{iev}$. (4.12)

The determination of the controller parameters k_p, T_i, and T_d begins by fixing initial values that give poles near zero: $k_p = 1$, $T_i = 4$, $T_d = 1$. Then, by varying these parameters, the required parameters are determined on the test bench for different perturbations:

compressor rotation speed, gas cooler outlet temperature, expansion valve opening (EVO), and the change of the reference.

For a rotation speed of 2000 RPM, the optimum control parameters reached are:

k_p	T_i	T_d	D
-4	3	1	1

Figure 4.8 is divided into four intervals:

1- $T_{ev,\,ref}$ = 2°C, EVO = 50%.
2- $T_{ev,\,ref}$ = 2°C, EVO = 25%.
3- $T_{ev,\,ref}$ = 0°C, EVO = 25%.
4- $T_{ev,\,ref}$ = 0°C, EVO = 50%.

Also, the gas cooler outlet temperature varies between 32 and 37°C as additional perturbation.

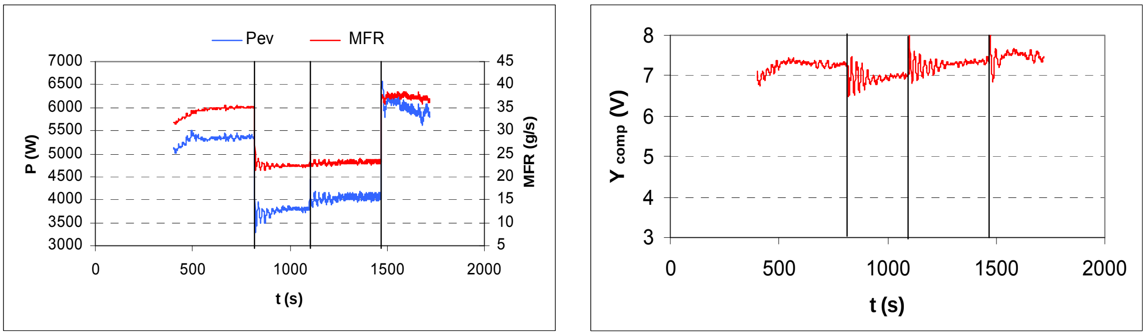

a- Cooling capacity and CO_2 mass flow rate　　b- Compressor control signal

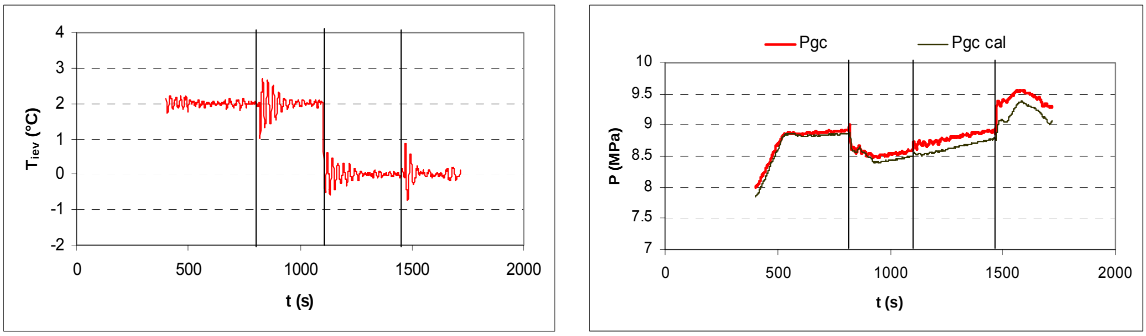

c- Evaporation temperature　　d- Gas cooler outlet pressure

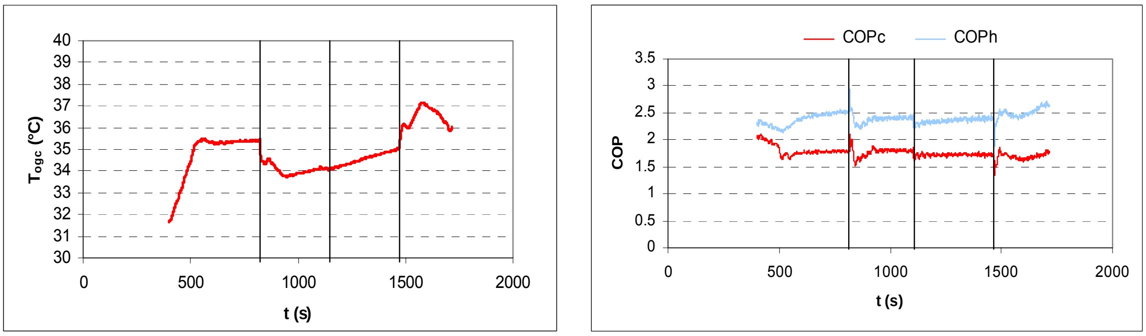

e- Gas cooler outlet temperature　　f- Cold and hot COP

Figure 4.8: Variation of evaporating capacity, CO_2 mass flow rate, compressor control signal, evaporation temperature, gas cooler pressure, gas cooler outlet temperature, and COP with the control strategy.

The cooling capacity depends on the EVO:

- 5.4 kW for interval 1,
- 3.8 kW for interval 2,
- 4 kW for interval 3 a
- nd 6 kW for interval 4,

since the mass flow rate is directly related to the EEV.

The gas cooler pressure is higher than the calculated optimal pressure as shown in Figure 4.8-d. The CEV control signal varies around 7 V. Figure 4.8-c shows that the control strategy presents small fluctuations of the evaporation temperature lower than 1 K around the reference value. The COP is constant after reaching the reference value.

The control logic, described above, can be used also to control the air blown temperature with finned tube evaporator: small fluctuation, and rapid response. The compressor presents rapid response to the control signal, so the parameter D is set to 1.

4.3.4 Control of P_{gc} with the EEV

The reference is the gas cooler temperature, so the error is:

$$e(t) = P_{gc,ref} - P_{ogc} \quad (4.13)$$

By fixing the CEV signal to 7 V, and for a high perturbation coming from the variation of the compressor rotation speed following an ECE driving cycle and a variation of the gas cooler outlet temperature, the optimum control parameters are:

k_p	T_i	T_d	D
-6	3	0.75	1

The compressor rotation speed follows the rotation signal coming from the acquisition data (see Figure 4.9.a). Also, the measured mass flow rate matches the calculated mass flow rate from the cooling capacity with fluctuation coming from the sudden variation of the compressor rotation speed (Figure 4.9.b). The evaporator cooling capacity varies from 2.5 to 3.5 kW. The gas cooler outlet temperature varies from 35 to 37°C. The evaporation temperature presents a periodic oscillation between 11 and 15°C, following the compressor rotation speed. The evaporation temperature could be decreased by increasing the CEV signal above 7 V. Also, the EEV control signal presents a periodic variation, Figure 4.9.e. The instantaneous COP varies from 2 to 3, Figure 4.9.f.

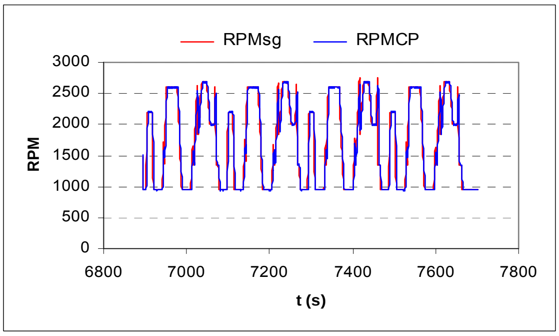

a- Compressor rotation speed

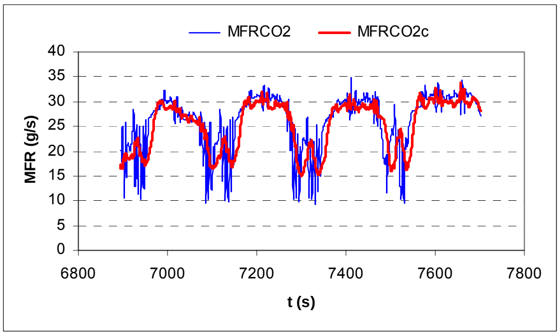

b- Measured and calculated CO_2 mass flow rate

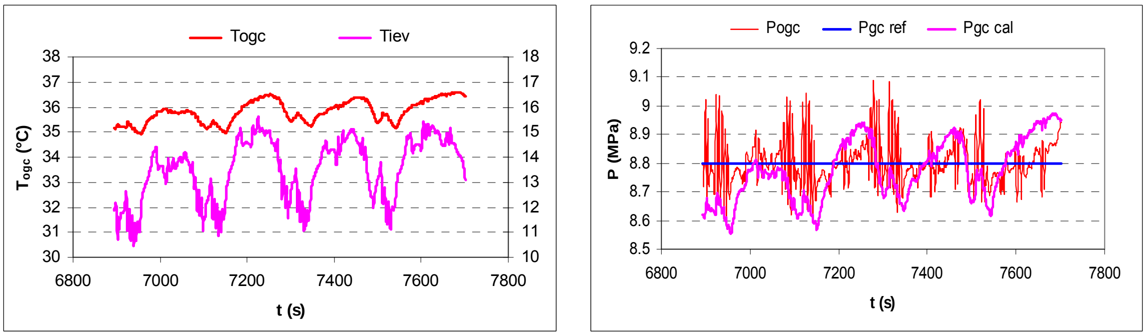

c- Gas cooler outlet temperature and evaporation temperature.

d- Calculated and measured gas cooler pressure.

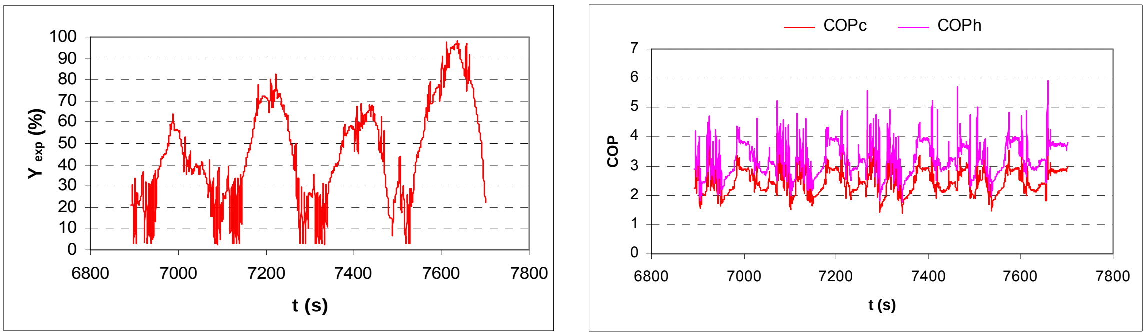

e- Expansion valve control signal.

f- Cold and hot COP.

Figure 4.9: Variation of compressor rotation speed, CO_2 mass flow rate, EEV control signal, evaporation temperature, gas cooler pressure, gas cooler outlet temperature, and COP with the control strategy.

The reference gas cooler pressure is fixed at 8.8 MPa, the controlled P_{gc} varies by less than 0.2 MPa from the set point, and by less than 0.1 MPa from the optimal gas cooler pressure.

4.3.5 Control of T_{ev} with EEV and control of P_{gc} with the CEV

After the determination of the two controller parameters: EEV controller of evaporation temperature and the CEV controller of gas cooler pressure, separately. They are tested together to control the evaporation temperature and the gas cooler pressure.

The error for the EEV controller is:

$$e(t) = T_{ev,ref} - T_{iev} \qquad (4.14)$$

The error for the CEV controller is:

$$e(t) = P_{gc,ref} - P_{ogc} \qquad (4.15)$$

In case of high perturbation coming from the variation of the compressor rotation speed following an ECE driving cycle, the optimum control parameters reached are as follows:

CEV controller parameters			
k_p	T_i	T_d	D
4	3	0.75	1

EEV controller parameters			
k_p	T_i	T_d	D
-12	1	0.5	0.9

The compressor rotation speed follows the rotation signal coming from the acquisition, Figure 4.10.a. Also, the measured mass flow rate matches the calculated mass flow rate from the cooling capacity with fluctuation coming from the sudden variation of the compressor rotation speed. The cooling capacity varies from 1.5 to 2.5 kW as shown in Figure 4.10-f. The gas cooler outlet temperature is fixed around 35.5°C.

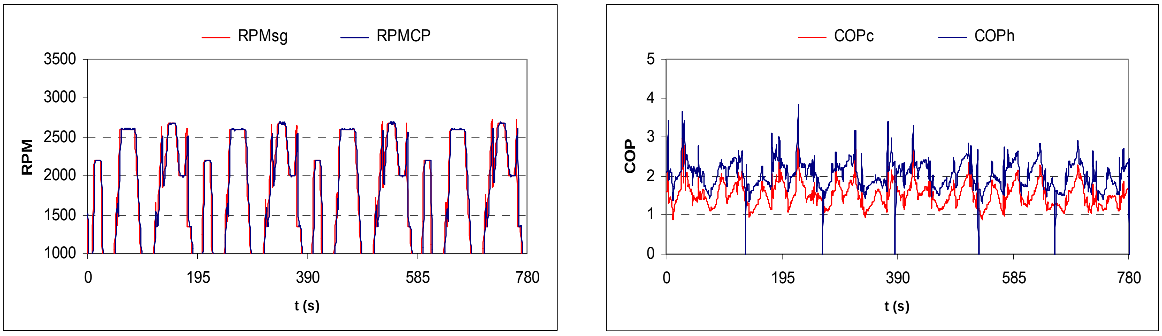

a- Compressor rotation speed

b- Cold and hot COP.

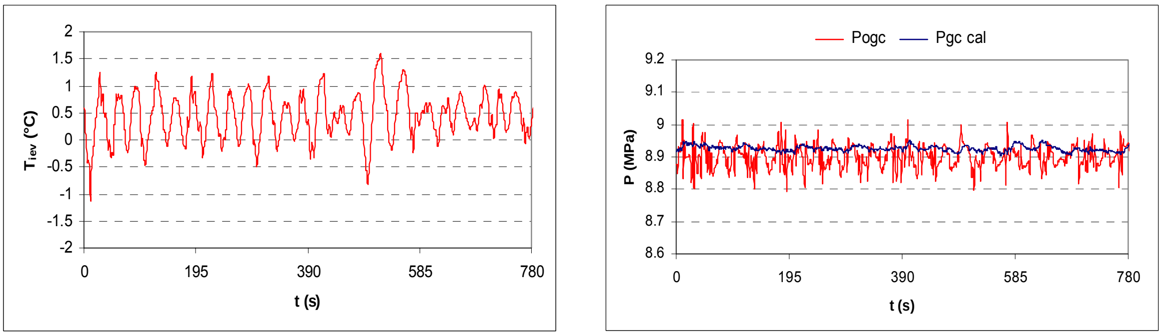

c- Evaporation temperature

d- Calculated and measured gas cooler pressure.

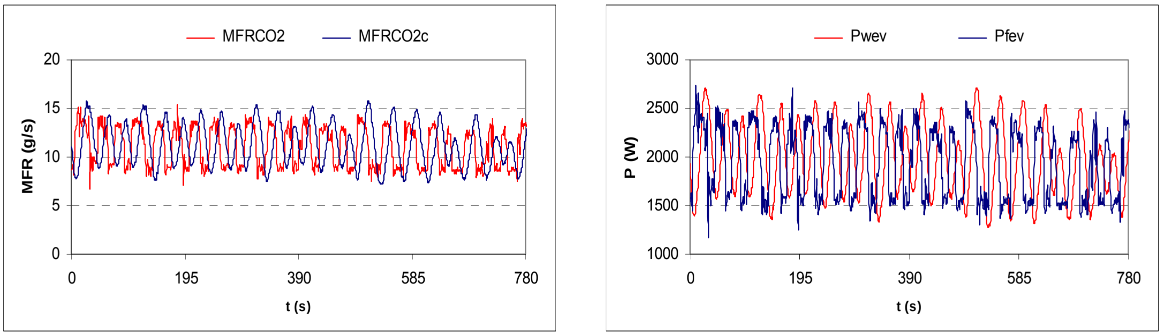

e- Measured and calculated CO_2 mass flow rate

f- Water and CO_2 measured cooling capacity

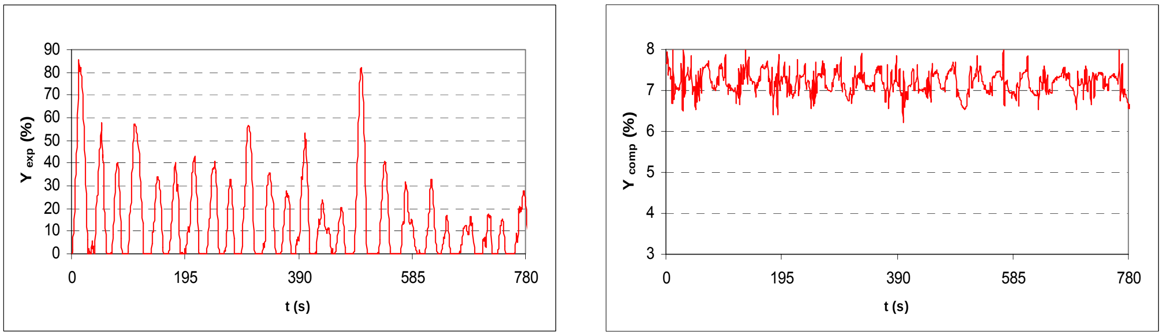

g- EEV control signal.

h- CEV control signal.

Figure 4.10: Variation of compressor rotation speed, CO_2 mass flow rate, CEV control signal, evaporation temperature, gas cooler pressure, EEV control signal, and COP with the control strategy.

The evaporation temperature set point is fixed at 0.5°C. The evaporation temperature presents a fluctuation between –0.5 and 1.5°C as shown in Figure 4.10-c. The EEV control signal presents a high variation between 0 and 60%, Figure 4.10-g.

The gas cooler pressure reference is fixed at 8.9 MPa. The gas cooler outlet pressure swings around the reference with amplitude lower than 0.1 MPa. The optimal calculated gas cooler pressure is slightly above 8.9 MPa. The compressor control signal varies between 6.5 and 7.5 V. The instantaneous COP varies between 1 and 2, Figure 4.10-b.

4.3.6 Conclusion

Four different control strategies were described. The control by the CEV presents more accurate results than the control by the EEV, since the effect of the compressor is dominant over the expansion valve effect in a vapor refrigeration system.

The superheat at the evaporator outlet could also be controlled by adapting the PID parameters. Usually, the control of the evaporator superheat is performed for finned tube evaporator to determine the air blown temperature. The water circuit of the test bench is a closed loop that makes the control strategy more complex, therefore the evaporation temperature is used instead of the evaporator outlet temperature.

Those control strategies are used to perform the ejector tests on the bench test.

4.4 Ejector test results and 1D model adaptation

The objectives of the tests are:

- Adaptation of the 1D model of the ejector.
- Characterization of the effect of the constant pressure chamber length.
- Characterization of the effect of the constant area chamber length.

The CFD study of vapor ejector, in Chapter 2, showed that the diffuser length should be more than 9 $D_{\text{const area}}$ and the constant area chamber more than 3 $D_{\text{const area}}$. Therefore, the ejector bodies that have been realized, have a constant area chamber length between 6.3 and 8.6 $D_{\text{const area}}$, and the diffuser has a length between 10.8 and 40.7 $D_{\text{const area}}$ as presented in Table 4.2.

Table 4.2: Variation of constant area chamber length and diffuser length with $D_{\text{const area}}$.

$D_{\text{const area}}$ mm	$L_{\text{const area}}$ mm	L_{diffuser} mm	$L_{\text{const area}} / D_{\text{const area}}$	$L_{\text{diff}} / D_{\text{const area}}$
1.5	9.4	61	6.27	40.67
2	14.4	57.4	7.20	28.70
2.5	19.4	53.9	7.76	21.56
3	24.4	50.3	8.13	16.77
3.5	29.4	46.7	8.40	13.34
4	34.4	43.2	8.60	10.80

Using variable thickness discs, the length of the constant pressure chamber can be varied between 0 and 10.2 $D_{\text{const area}}$ as shown in Table 4.3.

Table 4.3: Variation of the constant pressure chamber length.

Variable thickness discs	8	12	16	8	12	16
$D_{\text{const area}}$ mm	Constant pressure chamber length L_{cp}			Ratio $L / D_{\text{const area}}$		
1.5	7.3	11.3	15.3	4.87	7.53	10.20
2	5.9	9.9	13.9	2.95	4.95	6.95
2.5	4.5	8.5	12.5	**1.80**	**3.40**	**5.00**
3	3.1	7.1	11.1	1.03	2.37	3.70
3.5	1.6	5.6	9.6	0.46	1.60	2.74
4	0.2	4.2	8.2	0.05	1.05	2.05

Therefore, the effect of the constant area length and the diffuser length will not be characterized because the ejectors as realized, have optimal lengths.

4.5 Tests

54 different ejectors can be assembled based on the different parts, which have been realized for the tests:

- **6** body cores (1.5, 2.0, 2.5, 3.0, 3.5, and 4.0 mm as constant area diameter)
- **3** nozzles (0.75, 1.0, and 1.25 as throat diameter)
- **3** disc thicknesses (8, 12, and 16 mm).

For the tests results, **18** assembled ejectors were sufficient to adapt the 1D model and to characterize the non tested ejectors. The tested ejectors are listed in Table 4.4.

The test result interpretation is divided in two parts: nozzle characterization and ejector body characterization.

Table 4.4: Tested ejectors parameters.

Ejector number	d_{throat} mm	Disc thickness mm	$D_{const\ area}$ mm
1	0.75	12	1.5
2	0.75	12	2
3	0.75	8	2.5
4	0.75	12	2.5
5	0.75	16	2.5
6	0.75	12	3
7	1	12	1.5
8	1	12	2
9	1	8	2.5
10	1	12	2.5
11	1	16	2.5
12	1	12	3
13	1	12	3.5
14	1.25	12	2
15	1.25	8	2.5
16	1.25	12	2.5
17	1.25	16	2.5
18	1.25	12	3

4.6 Nozzle characterization

Three nozzles with different throat diameters (0.75, 1.0, and 1.25 mm) are tested with variable inlet parameters of temperature and pressure: $25 < T_{o,gc} < 50$ °C, and $6 < P_{o,gc} < 12.5$ MPa.

The tested points cover the two side of the saturated dome: saturated liquid and saturated vapor states. The critical entropy (at the critical point), s_{crit} = 1.42 kJ/kg K, divides the expansion flow states.

The experiments results of the nozzle show that the expansion efficiency in the nozzle convergent is close to **1**, so **the expansion can be considered as isentropic**, and **the maximum flow passes through the nozzle at the throat**, **phase change can occur in the nozzle convergent as shown in Figure 4.11.c**. The flow quality at the throat varies from zero, if the maximum flow is saturated liquid, to one if the maximum flow is saturated vapor.

Figure 4.11.b shows the relative error between the measured mass flow rates and the calculated mass flow rates according to the following assumptions:

- saturated flow at the throat. This assumption presents a high relative error up to 50% at some points,
- maximum flow rate: this assumption presents a relative error ±2% from the measured mass flow rate as shown in Figure 4.11.d.

Therefore, the proposed assumptions to analyze the ejector are not always true, so the new flow characteristics through a nozzle are:

- the expansion through our convergent nozzle is isentropic (efficiency = 1),
- the maximum flow passes through an orifice separating two chambers at different pressures: the upstream pressure is higher than the saturation pressure, and CO_2 is in two-phase flow downstream the nozzle, as shown in Figures 4.11.b and 4.11.d.
- If the downstream pressure is higher than the calculated throat pressure, the throat pressure will be the downstream pressure.

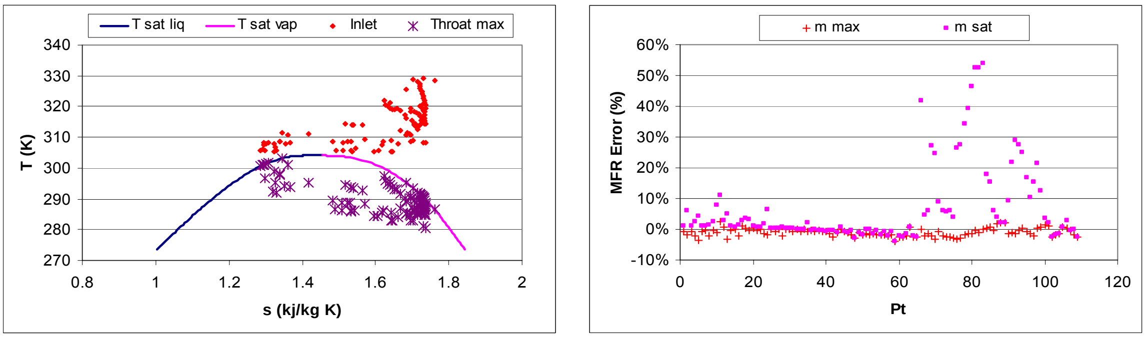

a- Position of test points in CO_2 T-s diagram

b- Relative Mass Flow Rate error between calculate and measured values

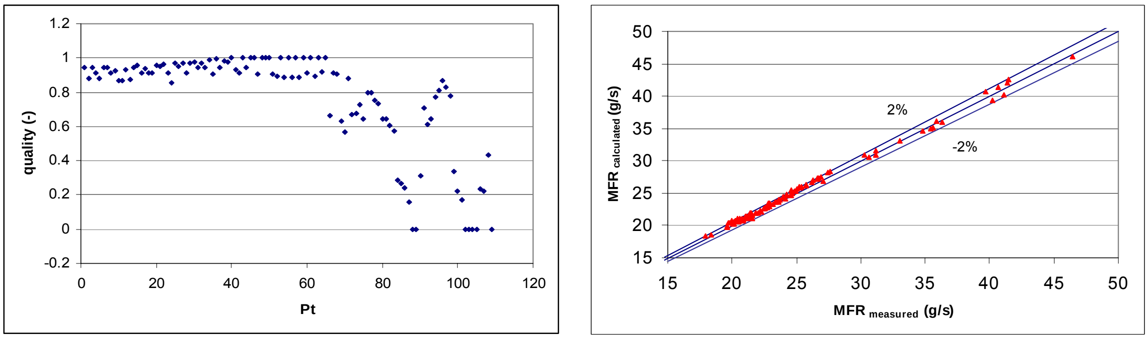

c- Throat flow quality of the calculated values

d- Comparison of measured and calculated mass flow rate

Figure 4.11: Experiments results of the ejector nozzles.

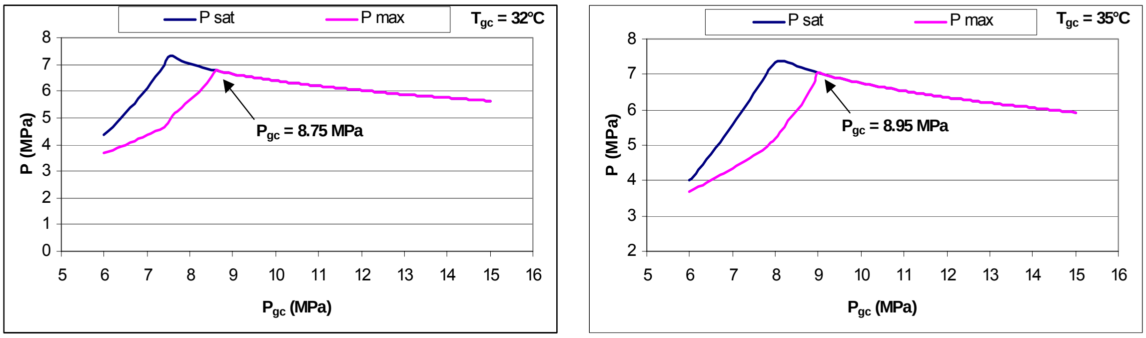

a. T_{gc} = 32°C, P_s = 8.75 MPa.

b. T_{gc} = 35°C, P_s = 8.95 MPa.

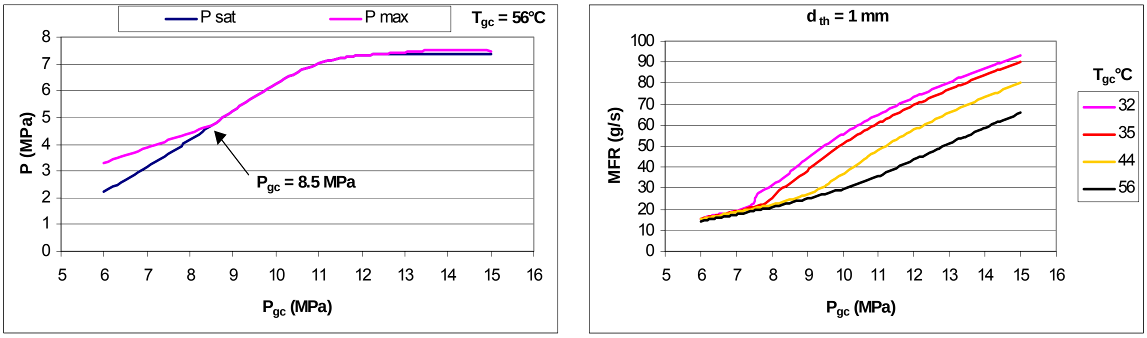

c. T_{gc} = 56°C, P_s = 8.75 MPa.

d. Variation of nozzle mass flow rate with P_{gc} at different inlet temperatures.

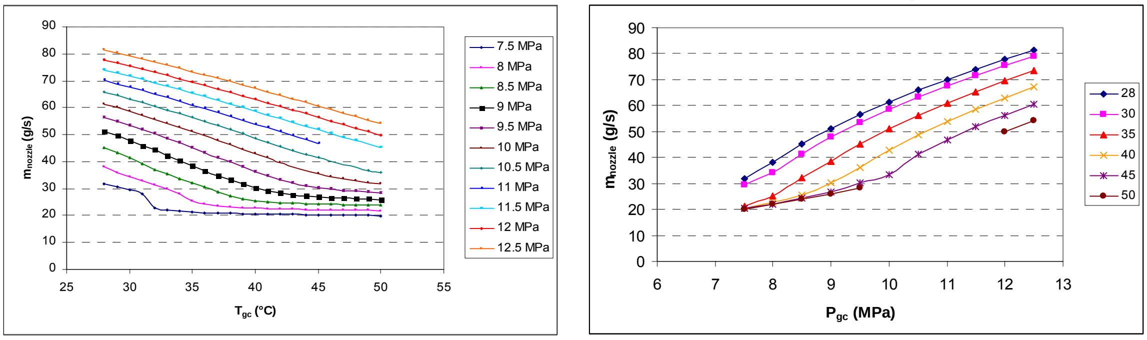

e. Variation of nozzle mass flow rate with T_{gc} at different inlet pressures higher than the critical pressure for d_{th} =1 mm.

f. Variation of nozzle mass flow rate with P_{gc} higher than the critical pressure at different inlet temperatures for d_{th} =1 mm.

Figure 4.12: Variation of saturated flow and the maximum flow throat pressure with P_{gc}.

By fixing the gas cooler outlet temperature, and by varying the high-side pressure P_{gc}, the nozzle inlet pressure, the throat pressure is drawn in Figures 4.12 (a, b, c) assuming:

- saturated state at the throat for P_{sat},
- maximum mass flow rate for P_{max},
- isentropic expansion in the nozzle (η_n = 1).

For each T_{gc}, there is a threshold gas cooler pressure $P_{gc,s}$:
- where the two assumptions are true: $P_{gc} \geq P_{gc,s}$, and
- a P_{gc} range in which only the maximum flow assumption is true: $P_{gc} < P_{gc,s}$.

Figures 4.12 (d, e, f) show that the mass flow rate of the nozzle increases with P_{gc} and decreases with T_{gc}.

Figure 4.12.d shows that for P_{gc} lower than the CO_2 critical pressure 7.38 MPa, the mass flow rate is slightly dependent on the inlet temperature.

The new adapted nozzle assumptions will be used to characterize the ejector body operation.

Comparison with other authors

To compare and validate the assumptions, two comparisons are made with two different published results.

Martin et al. [MAR 06] have studied the expansion of CO_2 through a short tube orifice, Figure 4.13. Two lengths of tubes have been experimentally tested and a mathematical model has been elaborated.

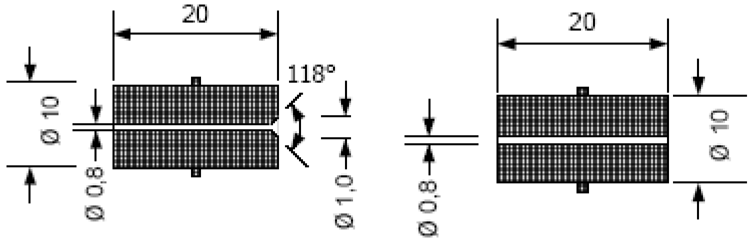

Figure 4.13: Short orifice tube tested by Martin et al [MAR 06].

By applying the new assumptions to the experimental results of the tube with 20 mm length, the isentropic efficiency is determined to be 0.68 and the relative error is lower than 10% as shown in Figure 4.14.

For the 10-mm length tube, the isentropic efficiency is determined to be 0.73 and the relative error is lower than 10% as shown in Figure 4.15.

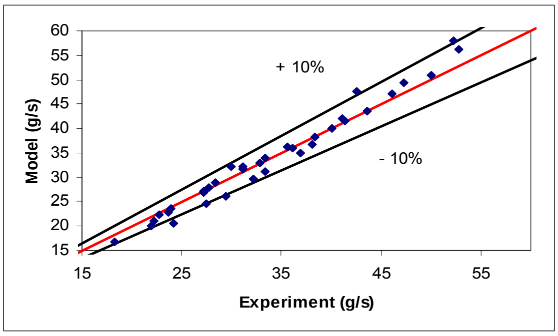

Figure 4.14: Relative error on mass flow rate for 20-mm length orifice tube.

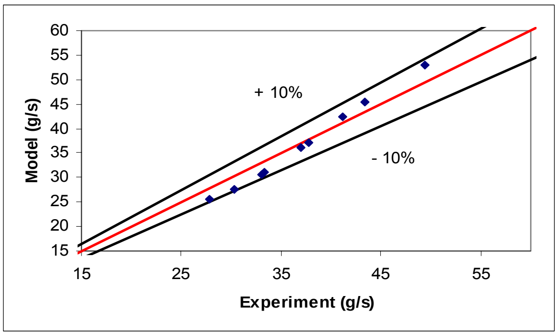

Figure 4.15: Relative error on mass flow rate for 10-mm length orifice tube.

Also, Martin et al. report that the mass flow rate through an orifice tube increases when a chamfer is created at the orifice inlet. So, the chamfer increases the expansion efficiency by decreasing the singular losses, and the orifice length decreases the expansion efficiency by increasing the friction losses.

Chen et al. [CHE 04] study the CO_2 expansion through a short tube orifice, Figure 4.16. Several diameters and lengths have been experimented: 0.82 and 1.35 mm for orifice diameter, and 8 to 26 mm for tube length. By applying the new assumptions to the experimental results, the isentropic efficiency is determined to be 0.61 and the relative error is lower than 5% as shown in Figure 4.17.

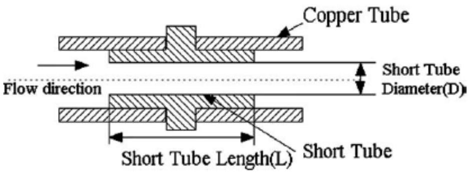

Figure 4.16: Short tube orifice tested by Chen et al. [CHE 04].

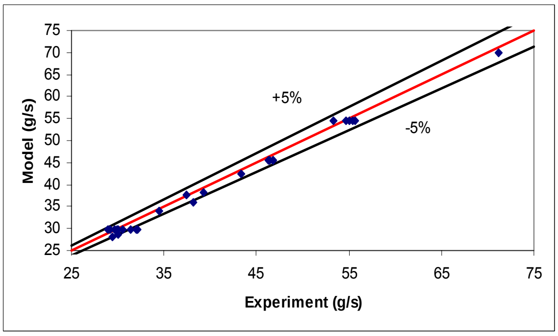

Figure 4.17: Relative error on mass flow rate of Chen orifice tube.

In conclusion, for each orifice tube, an expansion efficiency coefficient can be determined. This coefficient depends on the geometrical shapes that affect the minor head losses and linear friction losses.

The mass flow rate at the throat is calculated using the throat velocity v_{th} and the throat density ρ_{th}:

$$v_{th} = \sqrt{2000\eta_{is,\exp}(h_{in} - h_{th,is})} \tag{4.16}$$

$$\rho_{th} = f(P_{th,is}, h_{in} - \eta_{is,\exp}(h_{in} - h_{th,is})) \tag{4.17}$$

4.7 Body characterization

According to the ejector 1D model, four parameters should be determined:

- The nozzle divergent expansion efficiency: η_n.
- The secondary flow expansion efficiency: η_s.
- The mixture efficiency: η_m.
- The diffuser efficiency: η_d.

Assuming $\eta_n = \eta_s$ and a fully developed flow in the constant area chamber, the ejector outlet parameters: pressure and quality, are much lower than the measured ones.
The following assumptions are made:

- The nozzle and secondary flows are considered isentropic: $\eta_n = \eta_s = 1$.
- The diffuser compression is isentropic: $\eta_d = 1$.
- The two flows occupy an effective area in the constant area chamber. This effective area is characterized by an effective surface efficiency, that will be called **ettas,** defined as: $ettas = \frac{effective\ area}{\text{area}} = \left(\frac{d_{\ effective}}{d_{\ const\ area}}\right)^2$. (4.18)
- The constant pressure chamber pressure is calculated assuming that the maximum entrainment ratio, w, is sucked.
- The mixture efficiency η_m is calculated to meet the measured ejector outlet pressure.

The measured values considered in the calculations are:

- The temperatures and pressures of the primary and secondary flows measured by temperature and pressure sensors.
- The entrainment ratio, w, calculated from the cooling capacity measured on the water side. The evaporator CO_2 inlet enthalpy is considered as saturated liquid leaving the separator at the saturated temperature measured at three points: separator liquid outlet, separator vapor outlet, and the separator inlet from the ejector. Steady state is reached during the experimental test when the temperature difference between these three temperatures is lower than 0.2 K.
- The ejector outlet pressure is considered as the saturated pressure at the separator liquid temperature.

The calculation of **ettas** and η_m are as follows:

- From P_{ogc} and T_{ogc}, the mass flow rate through the nozzle is calculated by considering the maximum mass flow rate with $\eta_n = 1$.
- An iteration is used to calculate the maximum flow by varying the throat pressure between the evaporation pressure (P_{ev}) and the nozzle inlet pressure (P_{gc}), (see Figure 4.18), using the following equation:

$$m_p = \rho(P_{th}, s_{o,gc}).\sqrt{2(h_{o,gc} - h(P_{th}, s_{o,gc}))}.\frac{\pi d_{th}^2}{4} \tag{4.20}$$

- The mixing chamber pressure and the entrainment ratio, are calculated based on the assumption made for the vapor ejector: **the maximum entrained ratio is absorbed without passing the sonic level (Mach = 1).**
- An iteration loop is used to calculate the maximum entrainment ratio **w** by varying the mixing chamber pressure between 0.6 MPa and the evaporation pressure (see Figure 4.19).

$$w = \rho_{m,s} v_{m,s} \left(\frac{ettas.\pi d^2_{const\ area}}{4 m_p} - \frac{1}{\rho_{m,p} v_{m,p}} \right) \qquad (4.21)$$

- The surface efficiency **ettas** is varied so that the **calculated** entrainment ratio is equal to the **measured** one.
- After the calculation of the entrainment ratio, the mixture efficiency ratio η_m is calculated by an iteration loop between 0 and 1 so that the calculated ejector outlet pressure is equal to the **measured** one by applying Equations 2.66 to 2.75.

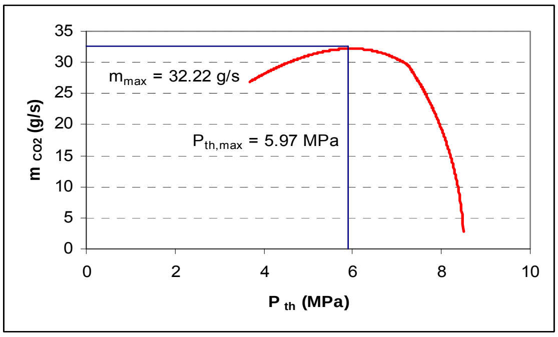

Figure 4.18: Variation of CO_2 mass flow rate with the throat pressure (for P_{gc} = 8.5 MPa and T_{gc} = 35°C).

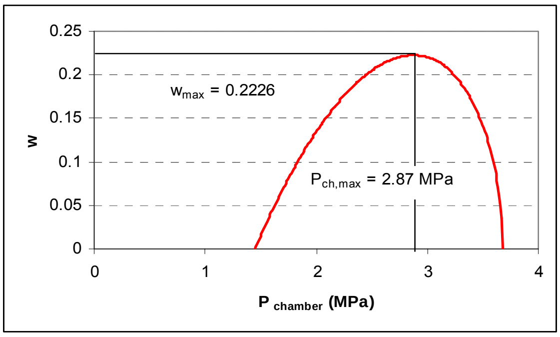

Figure 4.19: Variation of CO_2 mass flow rate with the mixing chamber pressure (for P_{gc} = 8.5 MPa, T_{gc} = 35°C, ettas = 1, T_{oev} = 7°C and P_{oev} = 3.673 MPa).

Analyzing **ettas** and η_m values lead to the elaboration of empirical equations expressing these values as a function of the flow and ejector parameters:

$$\mathrm{Re}_{ettas} = \frac{\rho_{th} \cdot v_{th} \cdot d_{th}}{\mu_{vap,th} \cdot 10^6} \cdot (1 - x_{th}) \cdot \left(\frac{\mu_{\sec} \cdot 10^6}{\rho_{\sec}} \right)^{0.05} \cdot \left(\frac{P_{in,\sec}}{P_{cr}} \right)^{0.05} \qquad (4.21)$$

$$\mathrm{Re}_m = \left(\frac{\rho_{th} \cdot v_{th} \cdot d_{th}}{\mu_{vap,th} \cdot 10^6} \right)^{0.1} \cdot \frac{1}{(1+w)} \qquad (4.22)$$

$$ettas = 2.542\ 10^{-3}\ \mathrm{Re}_{ettas}^{-0.1351} \left(0.6394\, \mathrm{Re}_{ettas} + 0.47875 \right) \frac{d_{th}}{d^2_{cst\ area}} \qquad (4.23)$$

$$\eta_m = -0.81.\mathrm{Re}_m + 1.3704 \qquad (4.24)$$

4.8 Constant pressure chamber length

The effect of the constant pressure chamber length has been investigated to define the optimal length to be used in the experiments.

Three different lengths L_{cp} of the constant pressure chamber are analyzed for three different nozzle diameters (0.75 mm, 1 mm, 1.25 mm).

The comparison of ettas and η_m for different nozzle throat diameters, Figure 4.20, show that these two parameters were not affected by L_{cp}. Therefore, the experimental results prove that the tested constant pressure chamber length L_{cp} , between 1.8 and 5 $d_{cst\ area}$ and between 3.6 and 16.6 d_{th}, do not affect the ejector performance.

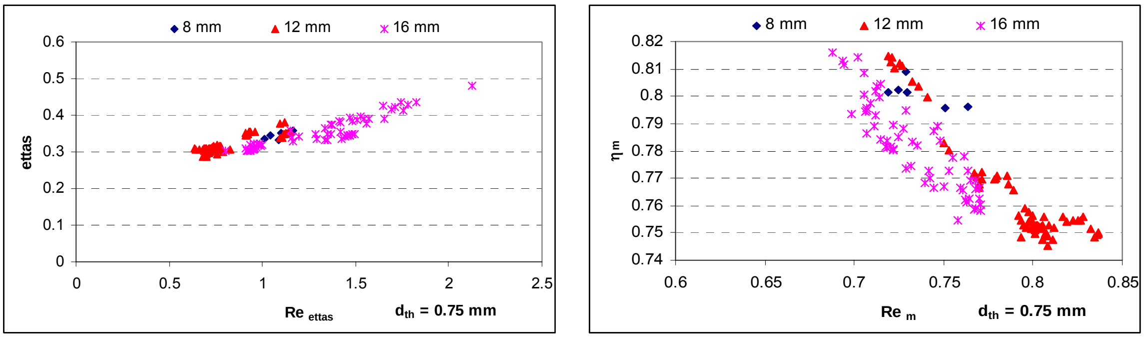

a. ettas for d_{th} = 0.75 mm

b. η_m for d_{th} = 0.75 mm

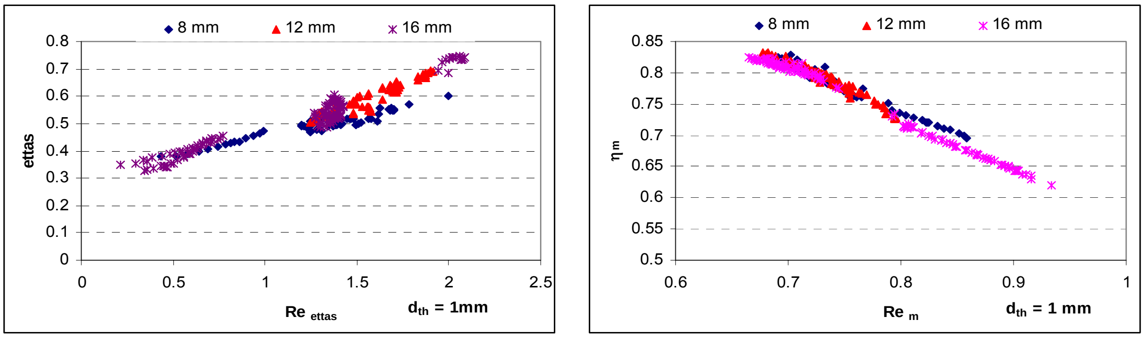

a. ettas for d_{th} = 1.0 mm

b. η_m for d_{th} = 1.0 mm

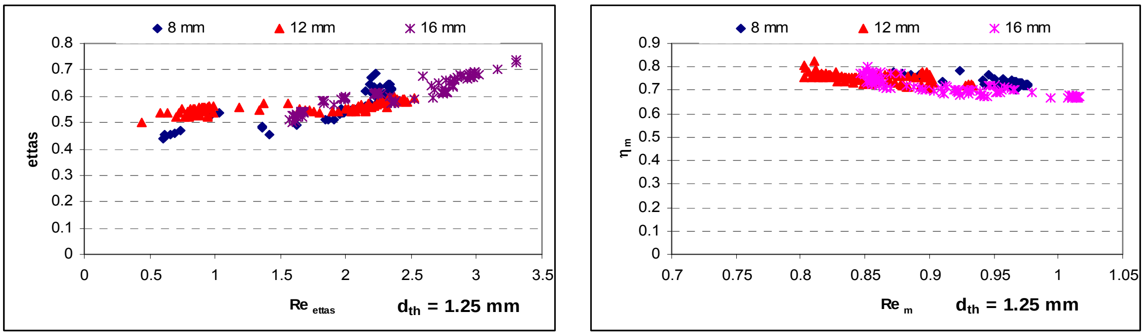

a. ettas for d_{th} = 1.25 mm

b. η_m for d_{th} = 1.25 mm

Figure 4.20: Variation of ettas and η_m with L_{cp} for different throat diameters.

Thus a disk thickness of 12 mm is used to complete the ejector tests with different geometrical parameters.

The effect of the constant length L_{cp} on the ejector efficiency is very low in the test length range. The constant pressure chamber length of the ejector should be studied with different diffuser lengths (lower than 9 $d_{cst\ area}$) to characterize the length impact if any.

4.9 Experimental result reliability

For the experimental tests, the gas cooler pressure is varied between 6 and 12.5 MPa and the gas cooler outlet temperature between 26 and 45 °C to cover the sub-critical and the supercritical operation modes of the ejector.

The error between the measured and the calculated values ranges between ±5 and ±15%.

For the ejector with nozzle throat diameter d_{th} = 0.75 mm, the error of ettas is lower than 10% while the error of η_m is lower than 7%, Figures 4.21.b and 4.21.d. Four different constant area diameters are studied: 1.5, 2, 2.5, and 3 mm.

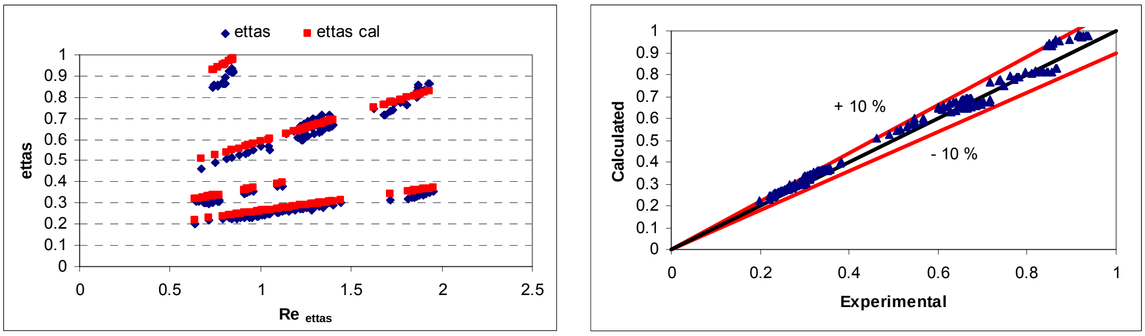

a. Variation of ettas with Re_{ettas} for different $d_{cst\ area}$: 1.5, 2, 2.5, and 3 mm.

b. Error between the calculated and the measured ettas.

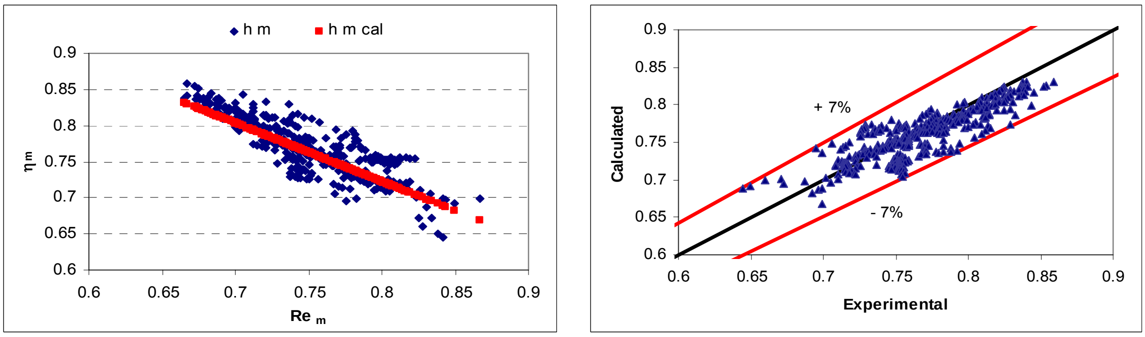

c. Variation of η_m with Re_m for different $d_{cst\ area}$: 1.5, 2, 2.5, and 3 mm.

d. Error between the calculated and the measured η_m.

Figure 4.21: Reliability of ettas and η_m for d_{th} = 0.75 mm.

For the ejector with nozzle throat diameter d_{th} = 1 mm, the error of ettas is lower than 10% and the error of η_m is lower than 5%, Figures 4.22.b and 4.22.d. Four different constant area diameters are studied: 2, 2.5, 3, and 3.5 mm.

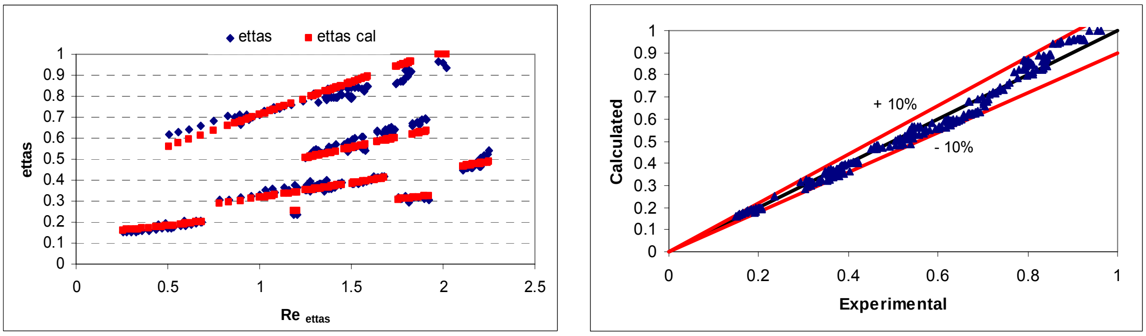

a. Variation of ettas with Re_{ettas} for different $d_{cst\ area}$: 2, 2.5, 3, and 3.5 mm.

b. Error between the calculated and the measured ettas.

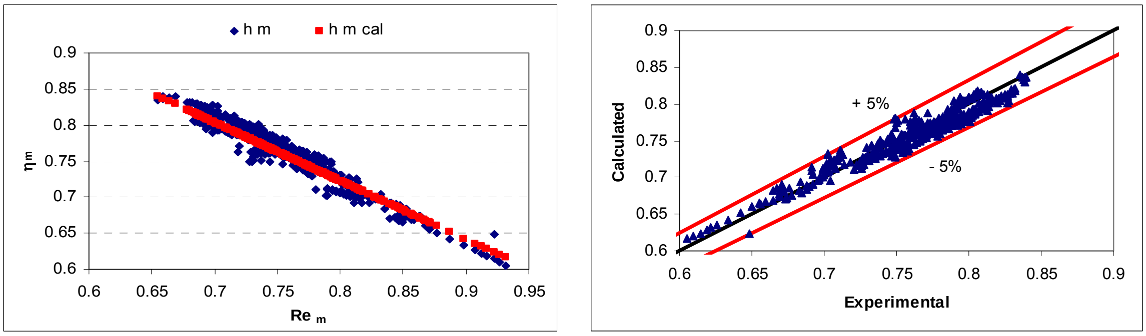

c. Variation of η_m with Re_m for different $d_{cst\ area}$: 2, 2.5, 3, and 3.5 mm.

d. Error between the calculated and the measured η_m.

Figure 4.22: Reliability of ettas and η_m for d_{th} = 1.0 mm.

For the ejector with a nozzle throat diameter d_{th} = 1.25 mm, the error of ettas is lower than 15% and the error of η_m is lower than 10%, Figures 4.23.b and 4.23.d. Three different constant area diameters are studied: 2, 2.5 and 3 mm.

The mass flow rate of the nozzle d_{th} =1.25 is high (>60 g/s), so an additional CO_2 mass is required (to be charged in the system) to guarantee a steady operation. In addition, the velocity in the tube increases and so the pressure drop and the ejector performances are hampered. Errors for the 1.25 mm nozzle throat diameter ejector are higher than those found for the other ejectors.

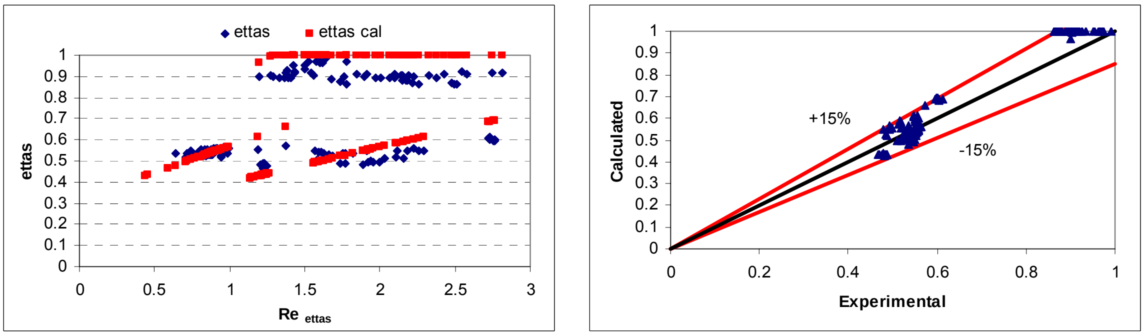

a. Variation of ettas with Re_{ettas} for different $d_{cst\ area}$: 2, 2.5, and 3 mm.

b. Error between the calculated and the measured ettas.

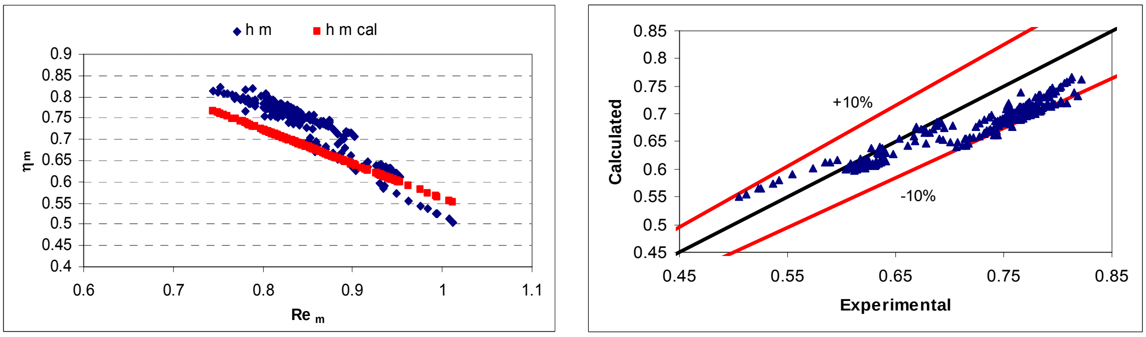

c. Variation of η_m with Re_m for different $d_{cst\ area}$: 2, 2.5, and 3 mm.

d. Error between the calculated and the measured η_m.

Figure 4.23: Reliability of ettas and η_m for d_{th} = 1.25 mm.

The increase in $d_{cst\ area}$ decreases the area efficiency ettas.

4.10 Effect of ettas and η_m on ejector performance

The ejector operation is studied using the new adapted 1D model. The gas cooler outlet pressure $P_{o,gc}$ is calculated to meet the mass balance (see Equation 2.77). When the mass balance is not respected, a pumping phenomenon occurs with high fluctuation of the cooling capacity, the evaporation temperature, and the gas cooler pressure.

The variation of ettas, Figure 4.24.a, shows that the ejector performance is not proportional to the variation of ettas:

- if ettas decreases, the ejector COPs decrease three times the ettas decrease.
- If ettas increases, the ejector COP increases in the same range.

The variation of ettas is done by considering:

- the mixture efficiency as defined by Equation 4.24.
  - the surface efficiency ettas as defined by Equation 4.23 and multiplied by a factor between 0.85 for –15% variation and 1.15 for 15% variation.

Table 4.5: Variation of COP improvement with ettas and η_m.

% ettas	% COP ej		% η_m	% COP ej
-15%	-47.76%			
-10%	-32.35%		-10%	-10.41%
-5%	-14.03%		-5%	-5.78%
0%	0.00%		0%	0.00%
5%	4.19%		5%	6.62%
10%	11.73%		10%	14.32%
15%	13.24%			

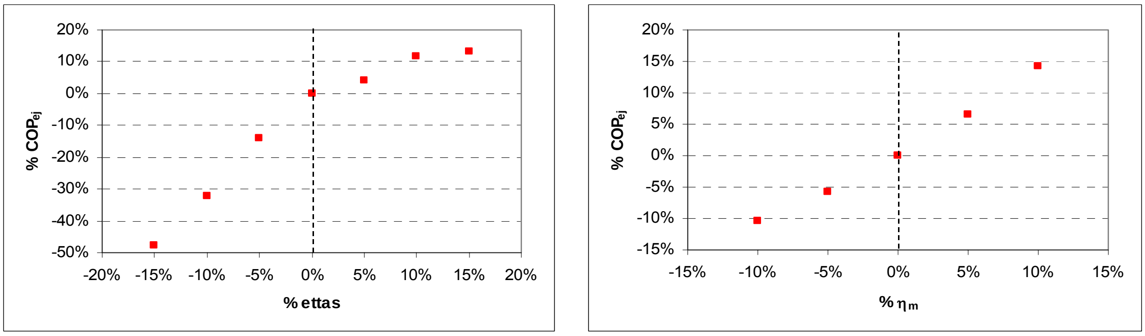

a. Variation of ettas

b. Variation of η_m

Figure 4.24: Variation of the ejector performance with ettas and η_m for $T_{o,ev}$ =7°C, P_{oev}=3.677 MPa, T_{gc} = 35°C, SH = 5 K.

The variation of η_m, Figure 4.24.b, shows that the ejector performance is not proportional to the variation of η_m:

- if η_m decreases, the ejector COP decreases in the same range,
- if η_m increases, the ejector COP increases about 1.5 times the η_m increases.

The variation of η_m is done by considering:

- the surface efficiency ettas as defined by Equation 4.23,
- the mixture efficiency η_m as defined by Equation 4.24 and multiplied by a factor between 0.9 for –10% and 1.10 for 10%.

So, the increase of ettas and η_m improves the ejector performance for T_{ev} = 2°C, T_{gc} = 35°C and SH = 5 K.

Considering an ideal mixing between the primary and secondary flows, η_m = 1, Figure 4.25 shows that the ideal COP improvement varies between 40 and 60%. The ratio between the ejector COP with variable η_m and the ideal ejector COP is around 65% as shown in Figure 4.26.

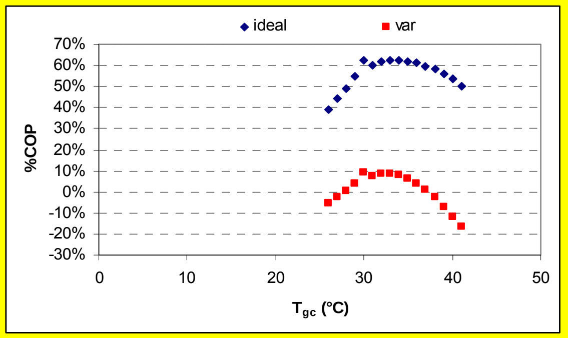

Figure 4.25: Variation of the COP improvement with T_{gc} for variable η_m (ideal η_m = 1, T_{ev} = 2°C, SH = 5 K).

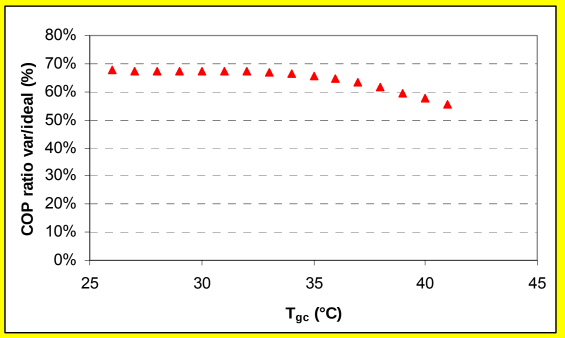

Figure 4.26: Variation of the ejector COP ratio with T_{gc} for variable η_m (ideal η_m = 1, T_{ev} = 2°C, SH = 5 K).

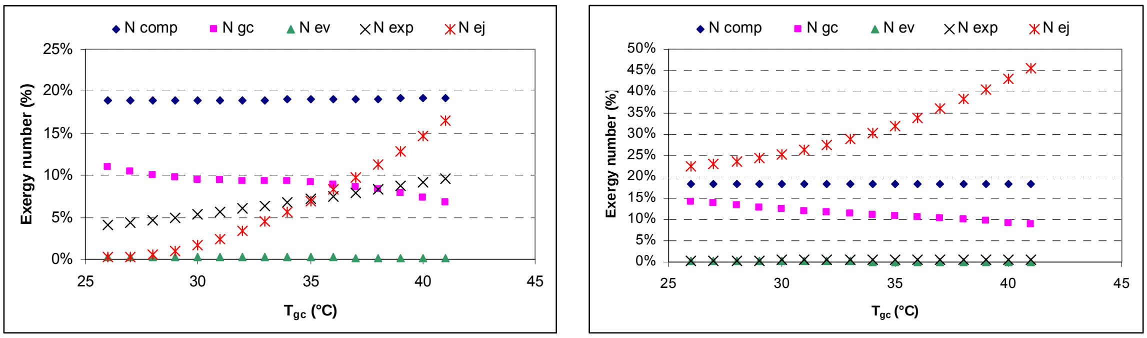

a. Ideal ejector refrigeration cycle, $\eta_m = 1$. b. Ejector refrigeration cycle with variable η_m.

Figure 4.27: Variation of exergy numbers of different components of the ejector refrigeration cycle ($\eta_{comp} = 80\%$ and $T_{ev} = 2°C$).

The exergy study of the ejector refrigeration system shows the component efficiency loss variation with T_{gc}.

- For the ideal ejector, Figure 4.27, the ejector loss increases with T_{gc} from around 1% in sub-critical operation to 15% at T_{gc} =40 °C, but the compression loss is the highest around 19%. The expander loss is higher than 5%, so the use of the isentropic expansion will improve the ejector cycle. The gas cooler loss is around 10%.
- For the ejector with variable η_m, the ejector loss is the highest and increases with T_{gc} from around 21% in sub-critical operation to 45% at T_{gc} = 41 °C, the compression loss is around 19%. The expander loss is around 0%, so the use of an isentropic expansion will not improve the ejector cycle. The gas cooler loss decreases from15% for sub-critical operation to 10% at T_{gc} = 40°C.

Thus, the improvement of the mixing efficiency η_m improves the ejector performances.

4.11 Effect of $d_{cst\ area}$ and d_{th}

The 1D model is adapted by including ettas and η_m. These efficiencies are expressed as a function of the ejector geometrical parameters: $d_{cst\ area}$ and d_{th}, and the flow thermodynamic parameters.

4.11.1 Variation of $d_{cst\ area}$

For T_{ev} = 2°C, d_{th} = 1 mm, and T_{gc} = 35°C, the variation of the constant area diameter, Figure 4.28, shows the existence of a critical diameter d_{cr}:

- if d_{cst} area < d_{cr}, the surface efficiency ettas is 1, and the ejector does not operate correctly.
- If $d_{cst\ area}$ > d_{cr}, the ejector operates with constant performances.

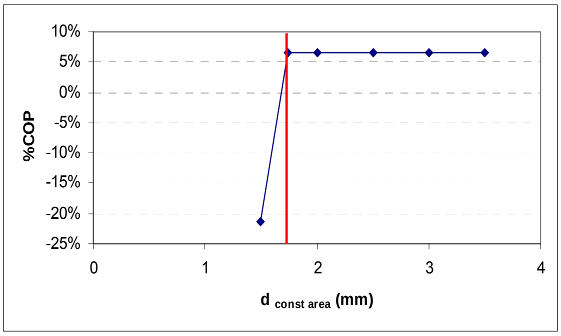

Figure 4.28: Variation of COP improvement ($d_{cst\ area}$ for T_{ev} = 2°C, T_{gc} = 35 °C, SH = 5 K).

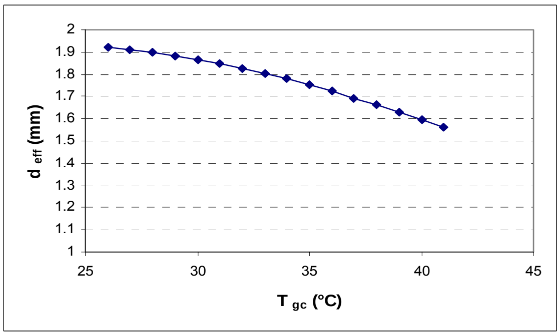

Figure 4.29: Variation of d_{eff} (T_{gc} for T_{ev} = 2°C, SH = 5 K).

For T_{ev} = 2°C, the effective critical diameter is drawn as a function of T_{gc}, (see Figure 4.29). The effective critical diameter decreases with the increase of T_{gc}.

Considering Equation 4.21, the replacement of ettas shows that the calculation of the entrainment ratio w is independent of $d_{cst\ area}$ if ettas is lower than 1. For this reason, the ejector operation is independent of the constant area diameter.

So, due to the high velocity of the primary flow and the entrained secondary flow, the flow is centered at the center of the constant area region, surrounded by a dead zone in which the velocity is equal to the wall velocity, Figure 4.30. In the dead zone, a closed circulation loop can occur without affecting the flows.

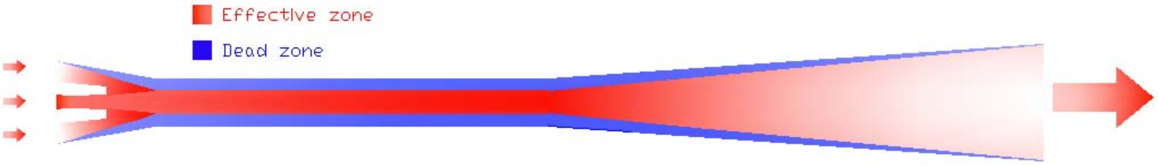

Figure 4.30: Ejector effective flow.

To be sure of the good operation of the ejector without disturbance, the constant area diameter should be chosen higher than 1.1 times the critical effective diameter. The chosen diameter will cover an operating range around the design parameters: evaporating and gas cooler outlet temperatures.

4.11.2 Variation of d_{th}

For T_{ev} = 2°C, Figure 4.31 shows that the ejector cycle performance varies with the nozzle throat diameter d_{th} according to the gas cooler outlet temperature. For T_{gc} = 30°C, the optimum COP is reached for d_{th} around 1 mm, and for T_{gc} higher than 35°C, the optimal COP is reached for d_{th} around 0.8 mm. Also, Figure 4.32 shows the variation of the ejector COP improvement with T_{gc} for different nozzle throat diameters.

By varying the nozzle throat diameter, the ejector can operate always with positive COP improvement. The variation of the nozzle diameter can be done by installing a converging cone in the nozzle controlled by a translated motor like the electronic needle valve actuator. However, for d_{th} = 1 mm, the COP improvement is positive for a range of T_{gc} between 27 and 37°C.

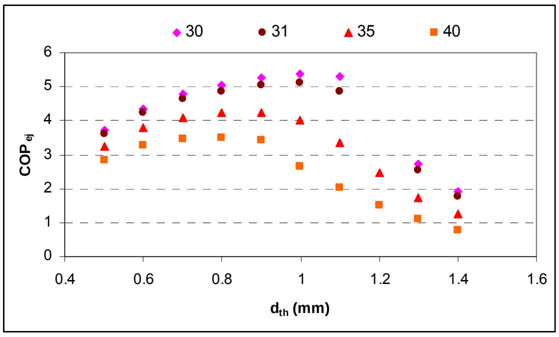

Figure 4.31: Variation of ejector efficiency (d_{th} for T_{ev} = 2°C, SH = 5 K, and η_{comp}= 1).

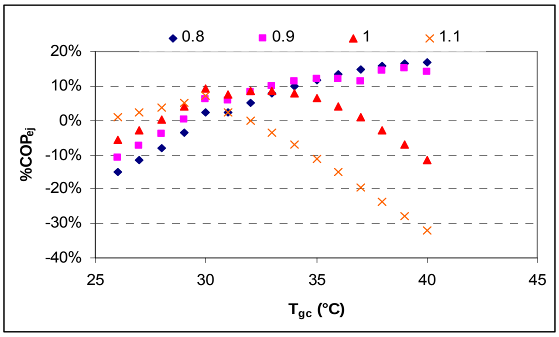

Figure 4.32: Variation of the ejector COP improvement with T_{gc} for different d_{th} (0.8, 0.9, 1, 1.1) (T_{ev} = 2°C and SH = 5 K).

The following comments can be made on effective surface efficiency ettas and the mixture efficiency η_m correlations.

For ettas, Equations 4.21 and 4.23:

- The motive flow in the ejector is the primary flow that is defined by the nozzle throat diameter, so the efficiencies depend mainly on the primary flow: throat velocity, throat diameter, and throat density.

- The liquid expansion dominates the vapor expansion, which explains the term (1 – x) that expresses the amount of the liquid in the primary flow at the throat.
- The secondary flow is an entrained flow, so its effect on ettas is very low; this effect is expressed by the low power of the second flow term: 0.05.
- The increase of the primary mass flow rate increases the surface efficiency, for that ettas increases with Re_{ettas} and d_{th}.

Table 6: Comparison of the ejector COP.

d_{th} (mm)	0.8	0.9	1	1.1
T_{gc} °C	Ejector COP comparison versus d_{th} = 1 mm			
26	90.12%	94.58%	100.00%	106.95%
27	90.79%	95.10%	100.00%	105.34%
28	91.55%	95.68%	100.00%	103.31%
29	92.50%	96.42%	100.00%	100.88%
30	93.68%	97.31%	100.00%	98.13%
31	95.12%	98.40%	100.00%	95.04%
32	96.91%	99.72%	100.00%	91.89%
33	99.10%	101.29%	100.00%	88.85%
34	101.79%	103.15%	100.00%	86.04%
35	105.02%	105.26%	100.00%	83.56%
36	108.92%	107.66%	100.00%	81.50%
37	113.58%	110.30%	100.00%	79.82%
38	119.04%	117.67%	100.00%	78.52%
39	125.29%	123.75%	100.00%	77.61%
40	132.35%	129.33%	100.00%	77.06%

Table 7: Comparison of the ejector performance improvement.

d_{th} (mm)	0.8	0.9	1	1.1
T_{gc} °C	%COP improvement			
26	-14.91%	-10.71%	-5.59%	0.97%
27	-11.73%	-7.53%	-2.77%	2.42%
28	-8.11%	-3.96%	0.38%	3.70%
29	-3.73%	0.35%	4.08%	5.00%
30	2.30%	6.26%	9.20%	7.15%
31	2.39%	5.92%	7.64%	2.31%
32	5.21%	8.27%	8.57%	-0.24%
33	7.71%	10.10%	8.69%	-3.43%
34	9.92%	11.39%	7.99%	-7.09%
35	11.81%	12.06%	6.46%	-11.05%
36	13.41%	12.10%	4.13%	-15.14%
37	14.72%	11.41%	1.01%	-19.38%
38	15.73%	14.40%	-2.78%	-23.66%
39	16.44%	15.01%	-7.06%	-27.87%
40	16.85%	14.19%	-11.71%	-31.96%

For η_m, Equations 4.22 and 4.24:

- The mixture occurs between two flows, so η_m depends of the primary flow: throat velocity, throat diameter, and throat density; and the secondary flow: entrainment ratio w.

4.12 Variation of T_{gc} , T_{ev} and SH

Considering the ejector composed of a nozzle of 1 mm throat diameter, the ejector performance is studied as a function of the evaporating temperature, the gas cooler outlet temperature and the evaporator outlet superheat.

The effect of the gas cooler outlet temperature on the COP improvement, the cooling capacity, the effective diameter, and the gas cooler outlet pressure of the ejector transcritical CO_2 cycle are shown in Figure 4.33.

It can be seen that the gas cooler pressure increases with the gas cooler outlet temperature T_{gc}, but the cooling capacity and the effective diameter d_{eff} decreases with T_{gc}. The COP improvement presents an optimum value for a defined T_{gc} and T_{ev}. The optimal T_{gc} increases with the increase of T_{ev}. For T_{ev} = 2°C, the COP improvement is positive in an interval of T_{gc} between 27 and 37 °C, the maximal improvement is 10% around T_{gc} = 30°C.

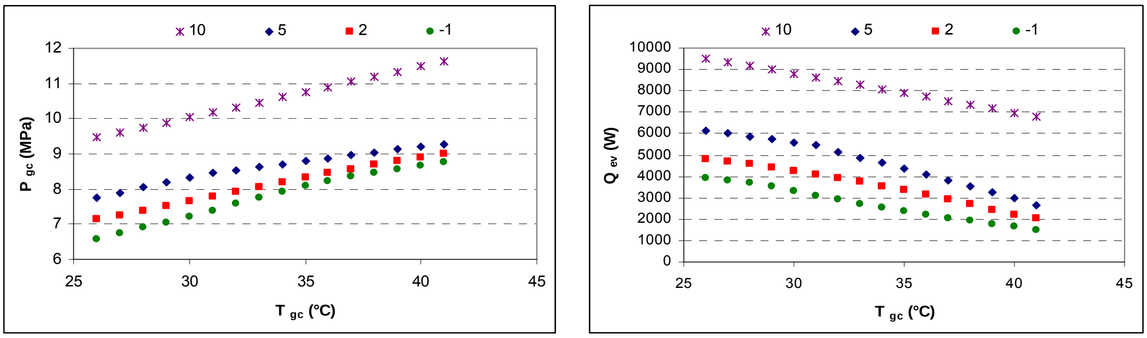

a. Gas cooler outlet pressure b. Cooling capacity

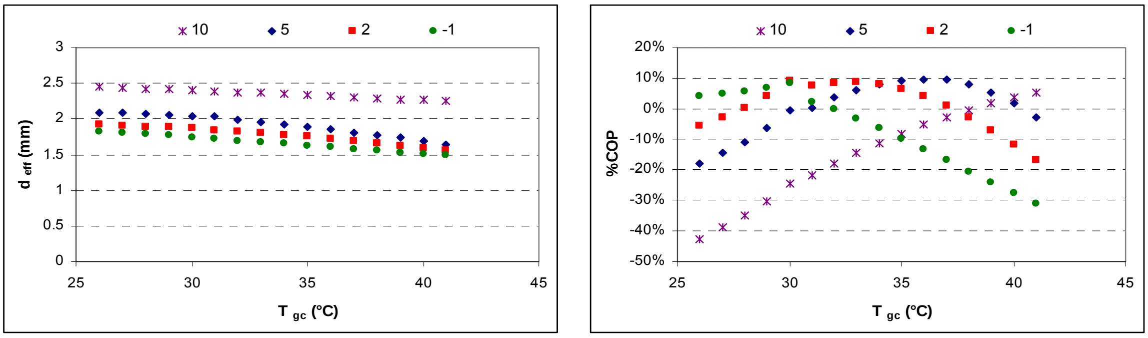

c. Effective diameter d. COP improvement

Figure 4.33: Variation of ejector parameters with the gas cooler outlet temperature T_{gc} for different evaporation temperatures, SH = 5 K.

The effect of the evaporation temperature on the COP improvement, the cooling capacity, the effective diameter, and the gas cooler outlet pressure of the ejector transcritical CO_2 cycle are shown in Figure 4.34.

It can be seen that the gas cooler pressure increases with the evaporation temperature T_{ev}, also the cooling capacity and the effective diameter d_{eff} increase with T_{gc}. The COP improvement presents an optimum value for a defined T_{ev} and T_{gc}. The optimal T_{ev} increases with the increase of T_{gc}. For T_{gc} = 35°C, the COP improvement is positive in an interval of T_{ev} between 0 and 8 °C, the maximal improvement is 10% around T_{ev} = 4°C.

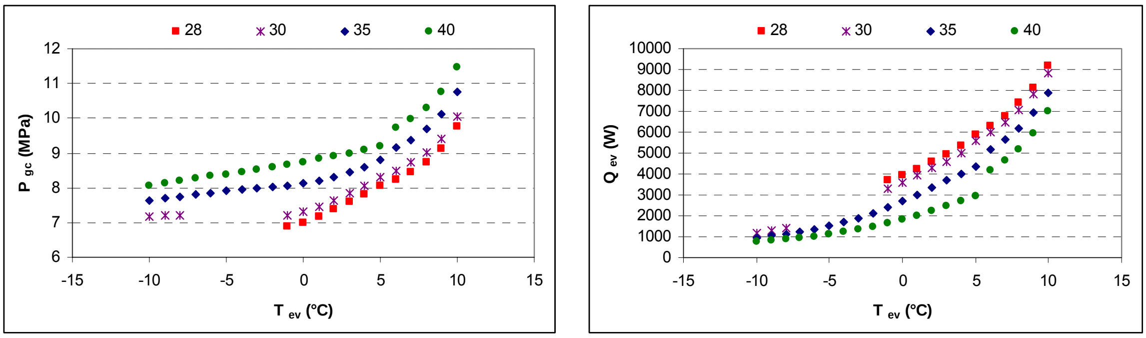

a. Gas cooler outlet pressure b. Cooling capacity

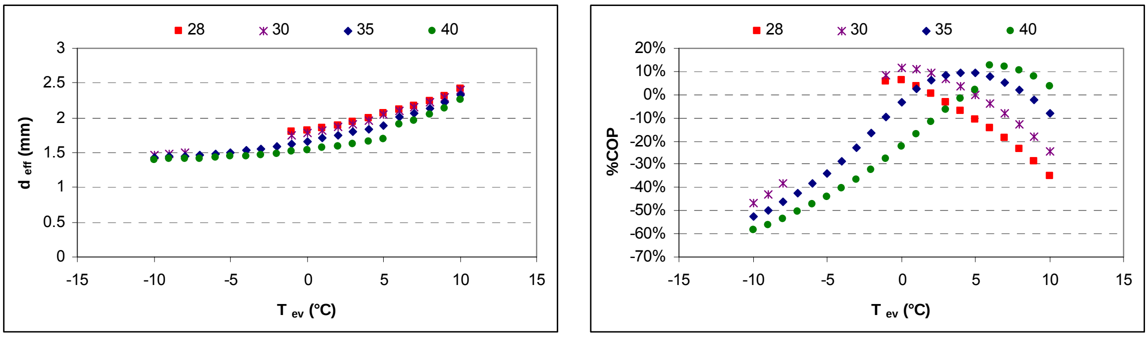

c. Effective diameter d. Cop improvement

Figure 4.34: Variation of ejector parameters with the evaporation temperature T_{ev} for different gas cooler outlet temperatures, SH = 5 K.

The COP improvement and the cooling capacity are presented in Figures 4.35 and 4.36 for a variation of T_{ev} between –2 and 10°C and a variation of T_{gc} between 26 and 41°C. The COP improvement map shows a region of T_{ev} and T_{gc} in which the COP improvement is positive:

- The blue region gives a COP improvement between 0 and 5%.
- The magenta region gives a COP improvement between 5 and 10%.
- The red region gives a COP improvement more than 10%.

The COP improvement is higher than 10% around 0°C evaporation and around the critical temperature due to the high values of the upstream density and enthalpy. Also, for evaporation between 6 and 9°C, and a gas cooler outlet temperature higher than 36°C, the COP improvement is higher than 10%.

The cooling capacity map shows that the capacity decreases with T_{gc} and increases with T_{ev}.

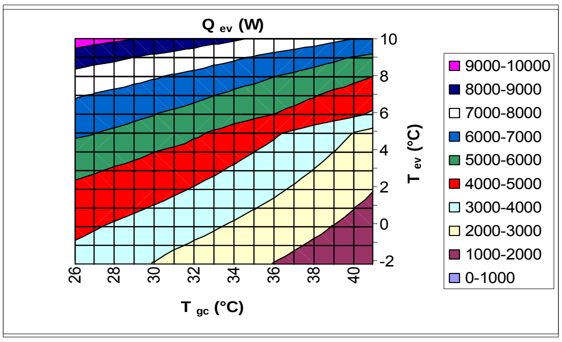

Figure 4.35: Variation of cooling capacity with T_{ev} and T_{gc}, SH = 5 K.

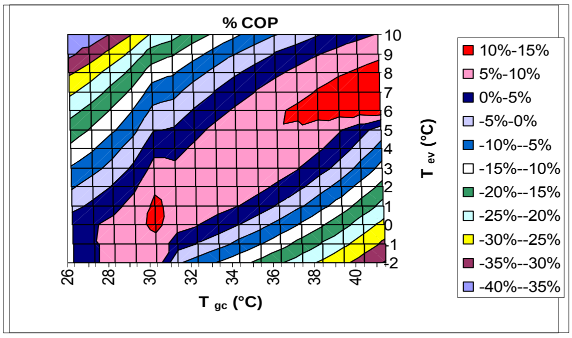

Figure 4.36: Variation of COP improvement with T_{ev} and T_{gc}, SH = 5 K.

The CO_2 ejector refrigeration cycle operates continuously by respecting a constant system mass balance. By respecting the system mass balance and varying the evaporation temperature T_{ev} between –10 and 10°C, and the gas cooler outlet temperature T_{gc} between 26 and 45°C, and by considering a superheat of 5 K, the gas cooler operating pressure is calculated by the 1D model, and a correlation is elaborated to express P_{gc} as a function of T_{ev} and T_{gc}.

The error between the model values and the correlation is lower than 3% as shown in Figure 4.37. The correlation is used as reference value to control the high-side pressure of the ejector refrigeration system.

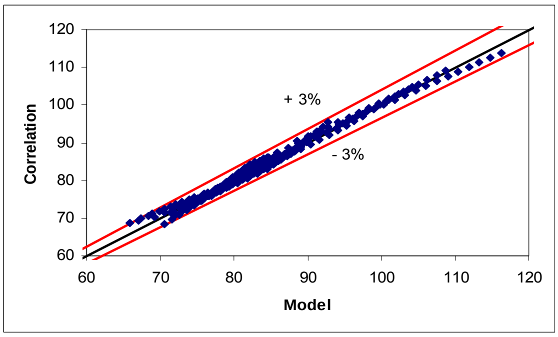

Figure 4.37: Error of the calculation of P_{gc}.

$$P_{gc} = a + b\,T_{gc} + c\,T_{ev} + d\,T_{ev}^{2} + e\,T_{ev}^{3}\ . \tag{4.25}$$

a	b	c	d	e
3.70416	0.1245456	0.076715	0.01052402	0.000752

The effect of the evaporator outlet superheat on the COP improvement, the cooling capacity, the effective diameter, and the gas cooler outlet pressure of the ejector transcritical CO_2 cycle are shown in Figure 4.38 for T_{ev} = 2°C. The evaporator superheat is considered as useful superheat and so is included in the cooling capacity.

It can be seen that the gas cooler pressure increases with the evaporator outlet superheat SH, also the cooling capacity and the effective diameter d_{eff} increase with SH. For sub-critical cycle operation, the COP improvement decreases with SH, but for transcritical cycle operation, the COP improvement presents an optimum value for a superheat around 10 K.

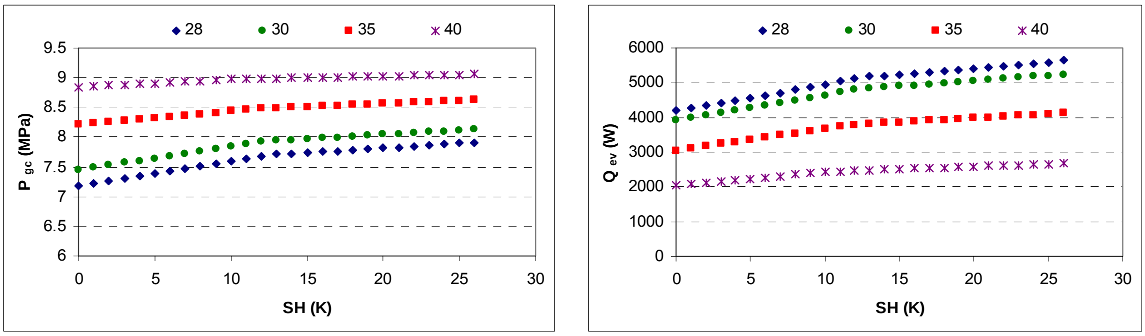

a. Gas cooler outlet pressure b. Cooling capacity

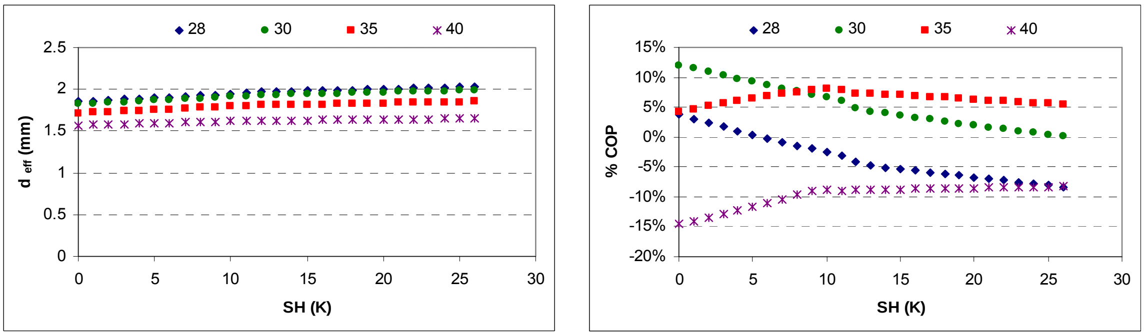

c. Effective diameter d. Cop improvement

Figure 4.38: Variation of ejector parameters with the evaporator outlet superheat SH for different gas cooler outlet temperatures and T_{ev} = 2°C.

Considering a superheat of 10 K, a gas cooler outlet temperature of 35°C and an evaporation temperature of 4°C, the COP improvement is 9.4%.

4.13 Ejector refrigeration system with integral IHX

The increase in the gas cooler outlet pressure increases the liquid hold-up in the separator, due to the quality decrease of ejector outlet flow. To ensure the constant system mass balance, the excess liquid should be evaporated. The excess liquid evaporation could be ensured by two methods:

- Using the ambient temperature as heat source.
- Using the gas cooler outlet flow as a heat source by installing what we call an integral heat exchanger (IgHX.) The Integral heat exchanger is used to evaporate the excess liquid in the separator by cooling the high-pressure flow coming from the gas cooler.
- Note: **integral** is used to differentiate the heat exchange of an **Internal** where no liquid is evaporated and only vapor is superheated at evaporator outlet to cool the gas or the liquid leaving the gas cooler or the condenser.

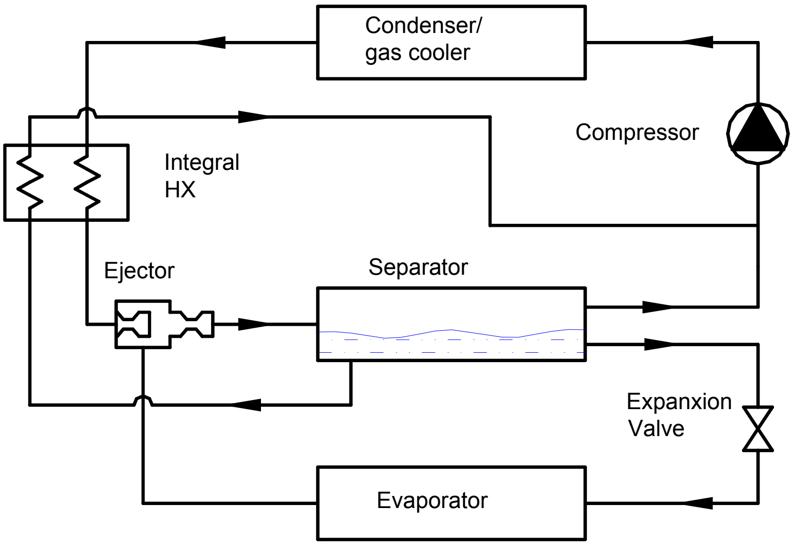

Figure 4.39: Ejector refrigeration cycle with integral heat exchanger (IgHX).

The first method penalizes the ejector performance by loosing cooling capacity, whereas the second method may improve the performance due to the use of an IgHX. The ejector refrigeration system with IgHX is shown in Figure 4.39. The excess liquid in the separator will be evaporated by cooling the gas cooler outlet flow, the vapor meets the separator vapor at the compressor suction.

Considering an evaporation temperature T_{ev} = 2°C and a gas cooler outlet temperature T_{gc} = 35°C, the system mass balance is traced as a function of the gas cooler pressure for an ejector cycle without an integral heat exchanger, Figure 4.40. The system mass balance decreases with P_{gc} down to the nozzle throat quality is zero, then the system mass balance increases to an optimal value than continue to decrease. The application of the IgHX when the system mass balance is lower than 1, shows an optimal COP improvement. This optimal COP improvement corresponds to the maximal COP in the P_{gc} interval when the nozzle throat flow is sub-cooled, Figures 4.42 and 4.43.

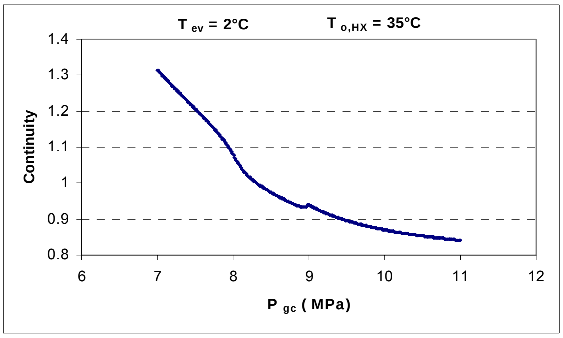

Figure 4.40: Variation of the system mass balance (P_{gc} for T_{ev} = 2°C and T_{gc} = 35°C, for the ejector refrigeration system).

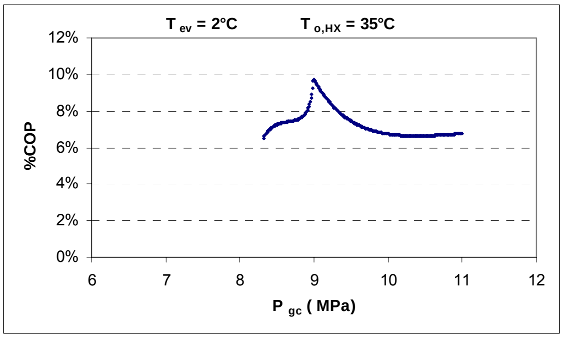

Figure 4.41: Variation of the COP improvement with P_{gc} (for T_{ev} = 2°C and ejector inlet temperature $T_{o,HX}$ = 35°C, for the ejector refrigeration system with IgHX).

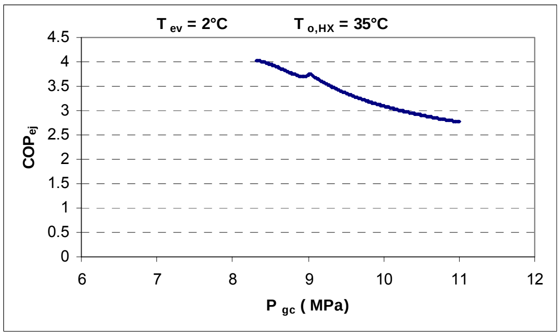

Figure 4.42: Variation of the ejector COP with P_{gc} (for T_{ev} = 2°C and T_{gc} = 35°C, for he ejector refrigeration system, η_{comp} = 1).

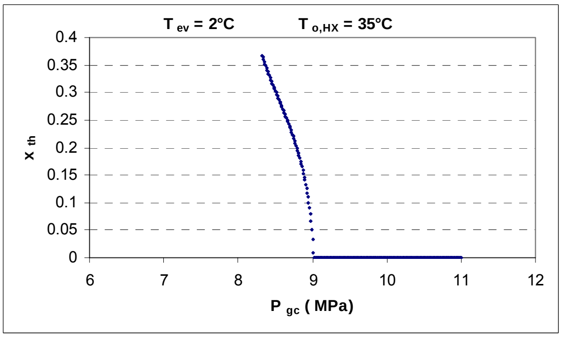

Figure 4.43: Variation of the throat nozzle quality with P_{gc} (for T_{ev} = 2°C and T_{gc} = 35°C, for he ejector refrigeration system).

Considering the maximal COP improvement with the IgHX ejector system, the ejector refrigeration cycle with IgHX will be characterized.

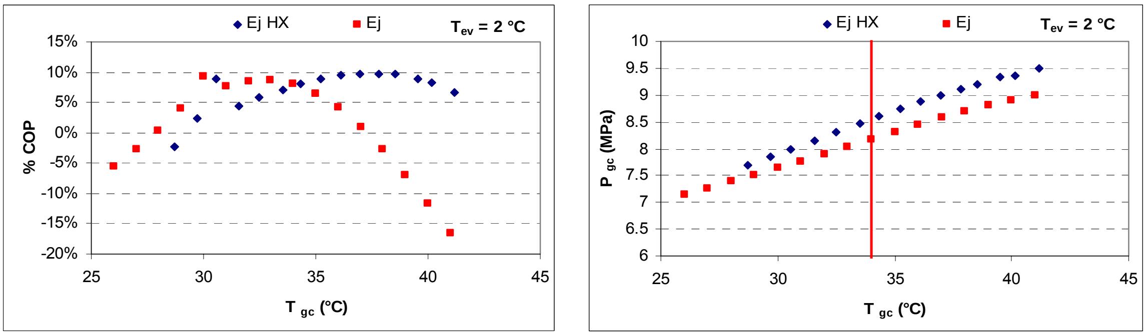

a. COP improvement.

b. Gas cooler outlet pressure .

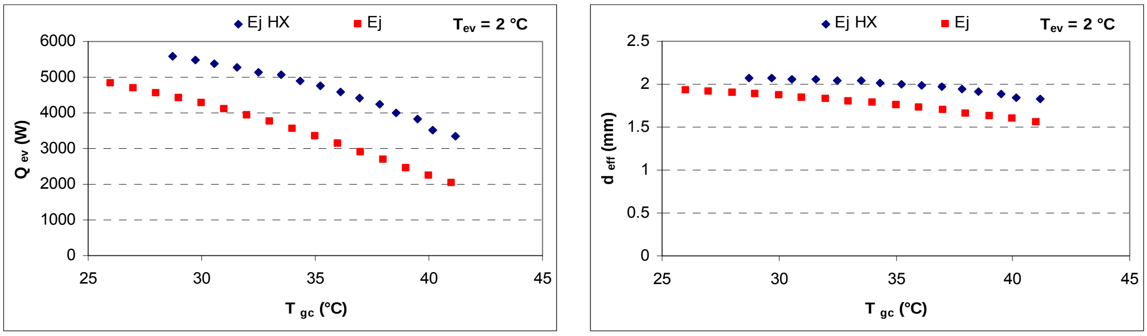

c. Cooling capacity.

d. Effective diameter.

Figure 4.44: Variation of ejector parameters with the evaporation temperature T_{ev} for different gas cooler outlet temperatures, SH = 5 K.

The effects of the gas cooler outlet temperature on the COP improvement, the cooling capacity, the effective diameter, and the gas cooler outlet pressure of the ejector transcritical CO_2 cycle with IgHX are shown in Figures 4.44 and 4.45 for different evaporating temperatures (-4, -1, 2, 4).

It can be seen that for T_{ev} = 2°C, the gas cooler pressure increases with T_{gc} and is higher than the pressure of the ejector cycle, but the cooling capacity and the effective diameter d_{eff} decrease with T_{gc} and they are higher than those of the ejector cycle.

The COP improvement of the ejector cycle with IgHX shows the same trend as the COP improvement of the ejector cycle, but there is a critical gas cooler outlet temperature above which the COP improvement with IgHX is higher:

- for T_{ev} = -4°C, $T_{gc,cr}$ ~ 28°C.
- for T_{ev} = -1°C, $T_{gc,cr}$ ~ 31°C.
- for T_{ev} = 2°C, $T_{gc,cr}$ ~ 34°C.
- for T_{ev} = 4°C, $T_{gc,cr}$ ~ 37°C.

For optimal operation, the IgHX should be used only when the gas cooler outlet temperature is higher than the critical gas cooler outlet temperature.

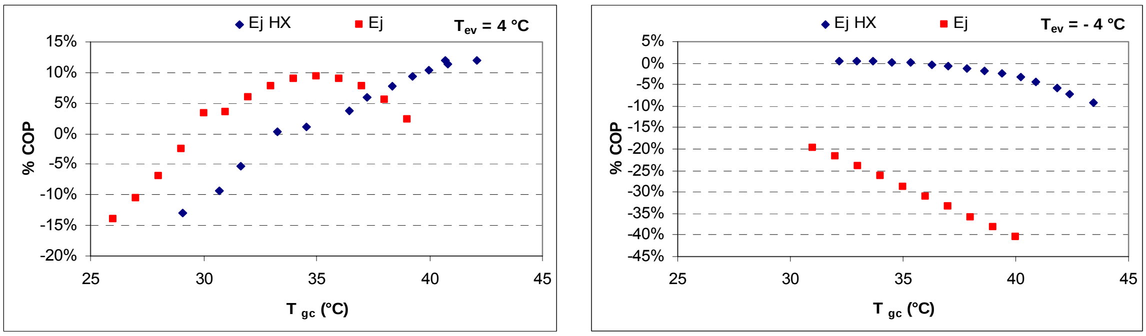

a. COP improvement for T_{ev} = 4°C. b. COP improvement for T_{ev} = -4°C.

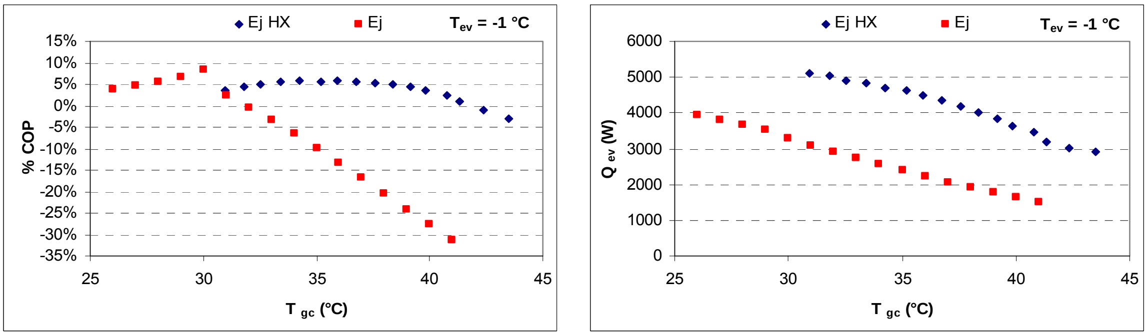

c. COP improvement for T_{ev} = -1°C. d. Cooling capacity for T_{ev} = -1°C.

Figure 4.45: Variation of ejector parameters with gas cooler outlet temperature for different evaporation temperatures, SH = 5 K.

4.14 Ejector refrigeration system with an IHX

The ejector refrigeration system with an IHX is shown on Figure 4.46. The saturated vapor leaving the separator is superheated by the high-pressure flow coming from the gas cooler in a counter flow configuration. The superheated vapor is sucked by the compressor and the sub-cooled high pressure flow is expand through the ejector.

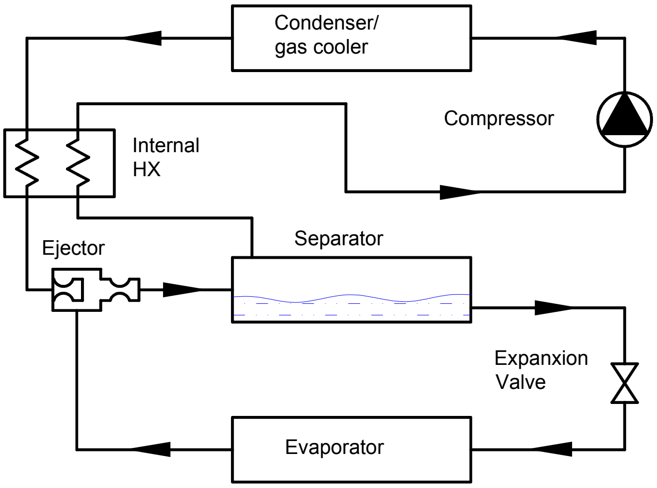

Figure 4.46: Ejector refrigeration system with IHX.

Considering an efficiency of the IHX of 80%, the ejector refrigeration system with IHX will be characterized.

The effect of the gas cooler outlet temperature on the COP improvement and the cooling capacity of the ejector transcritical CO_2 cycle with IHX are shown in Figures 4.47 for different evaporating temperatures (-5, -1, 2, 5, 10). It can be seen that the cooling capacity decreases with T_{gc} but it is higher than the cooling capacity of the ejector system, Figure 4.47.d.

The COP improvement of the ejector system with IHX varies with T_{gc}, but there is a critical gas cooler outlet temperature above which the COP improvement with IHX is higher:

- for T_{ev} = -5°C, $T_{gc,cr}$ ~ 36°C.
- for T_{ev} = -1°C, $T_{gc,cr}$ ~ 39°C.
- for T_{ev} = 2°C, $T_{gc,cr}$ ~ 40°C.
- for T_{ev} = 5°C, $T_{gc,cr}$ ~ 40°C.
- for T_{ev} = 10°C, $T_{gc,cr}$ ~38°C.

For the studied ejector, d_{th} = 1 mm, the use of an IHX is not recommended because the IHX performance improvement is for operating parameters where the ejector system performance is lower than the conventional system.

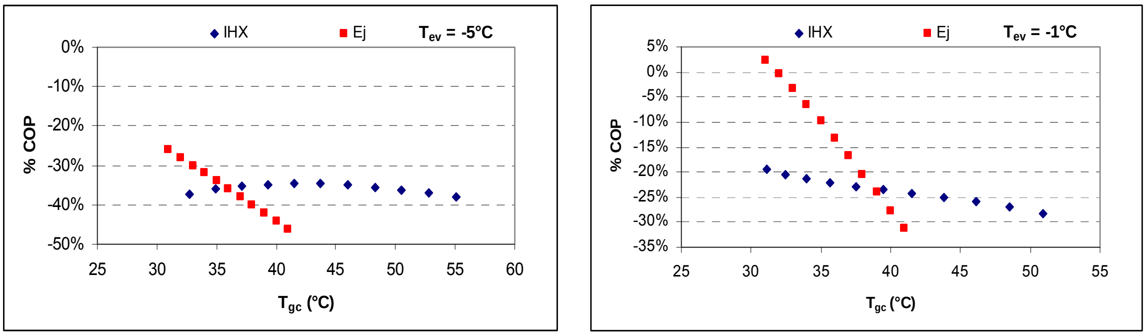

a. COP improvement for T_{ev} = -5°C.

b. COP improvement for T_{ev} = -1°C.

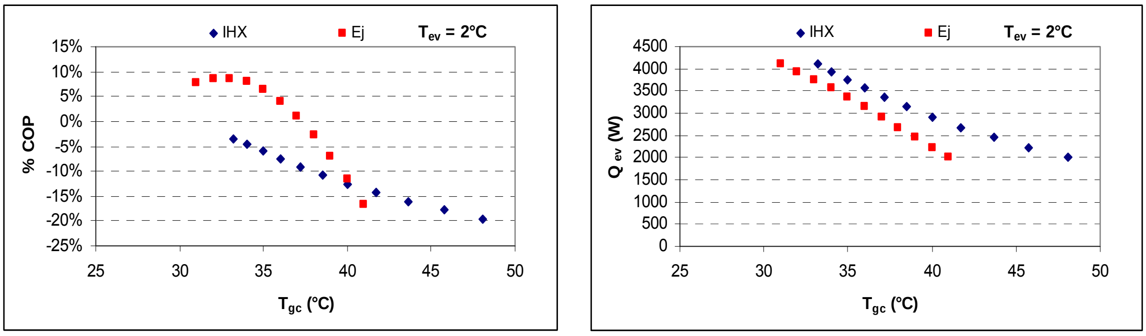

c. COP improvement for T_{ev} = 2°C. d. Cooling capacity for T_{ev} = 2°C.

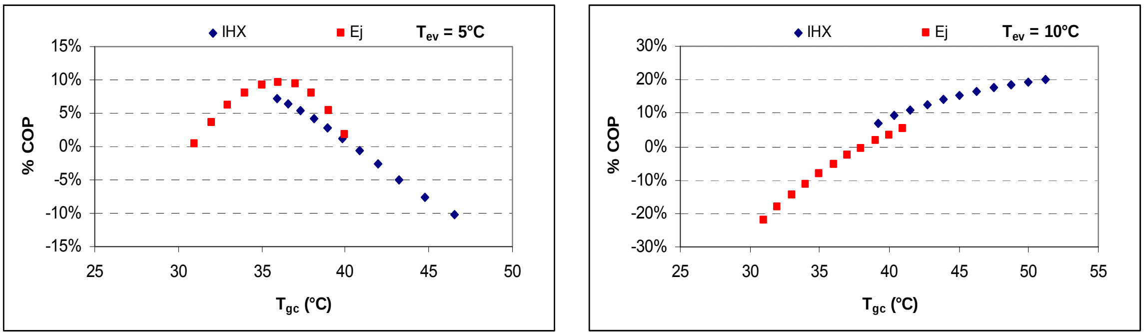

e. COP improvement for T_{ev} = 5°C. f. COP improvement for T_{ev} = 10°C.

Figure 4.47: Variation of ejector parameters with gas cooler outlet temperature for different evaporation temperatures, (SH = 5 K, SH = 5 K, η_{IHX} = 80%).

The decreasing of the IHX efficiency decreases the IHX ejector system performance down to the ejector system without an IHX.

The ejector system with IgHX and IHX is shown on Figure 4.48. The saturated vapor flow leaving the separator and the IgHX will be superheated in the IHX then sucked by the compressor.

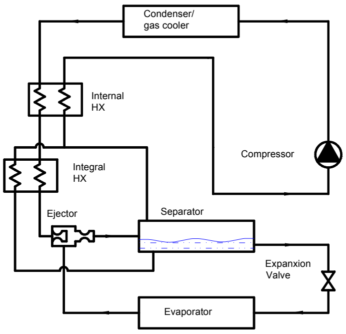

Figure 4.48: Ejector refrigeration system with IgHX and IHX.

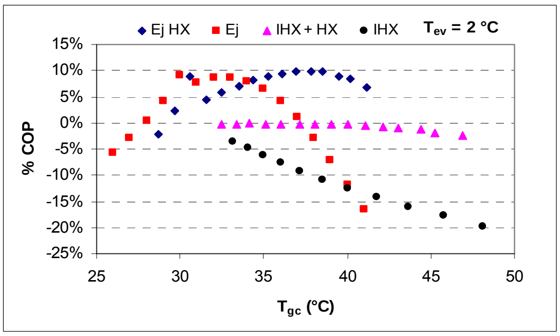

Figure 4.49: Variation of COP improvement for T_{ev} = 2°C and SH = 5 K., η_{IHX} = 75%.

Figure 4.49 shows that the superposition of an IgHX and an IHX, η_{IHX} = 75%, penalizes the system performance for T_{gc} lower than 45°C. So, this system can be used only with T_{gc} higher than 45°C.

4.16 ettas improvement

Since the length of the constant pressure chamber does not affect the ejector performance, the geometrical parameter that can affect the performance is the divergent shape of the nozzle: length and inclination angle.

Due to manufacturing constraints, the divergent was not able to be longer. So an additional tube with internal diameter of 1.2 mm and a length of 10 mm is welded on the nozzle with throat diameter of 1mm. The ejector composed of the modified nozzle, with a body of constant area diameter of 2.5 mm, and a constant pressure chamber length of 6.5 mm is tested on the test bench.

The experimental results show an improvement of ettas by **5%,** and the correlation of η_m still valid without modification.

Thus, the increasing of the nozzle length increases the expansion of the primary flow without external perturbation coming from the secondary entrained flow.

a. Scheme of the modified nozzle

b. Nozzle and annular tube

Figure 4.49: The modified nozzle.

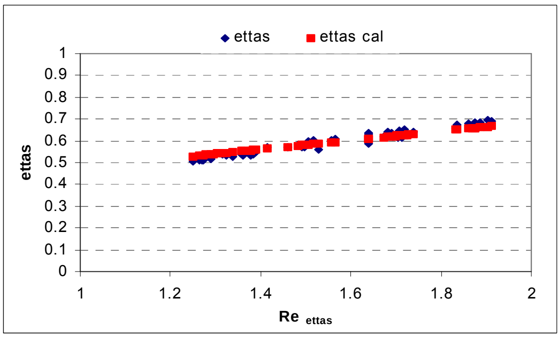

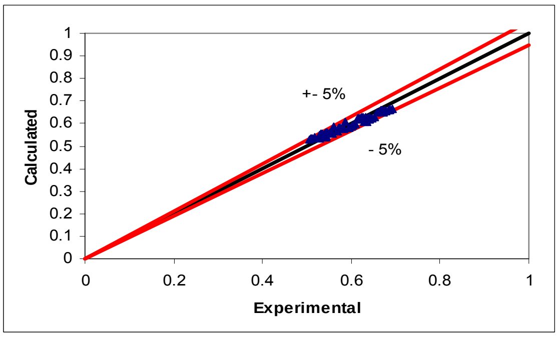

Figure 4.50: Variation of ettas with Re_{ettas} for the modified nozzle.

Figure 4.51: Error between the calculated and the measured ettas of the modified nozzle.

Figures 4.50, 4.51 and 4.52 show that the error between the experimental test and the correlation is lower than 5% for ettas and lower than 3% for η_m.

For T_{ev} = 2°C, SH = 5 K, and T_{gc} = 35°C, the COP improvement increases from 6.5% up to 10.9 % with the modified nozzle.

Increasing ettas will increase η_m due to the increase in the entrainment ratio, w, see Equations 4.22 and 4.24.

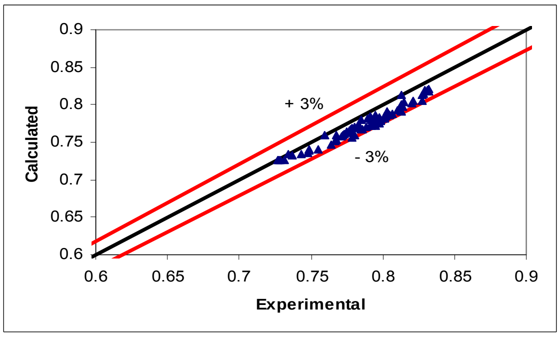

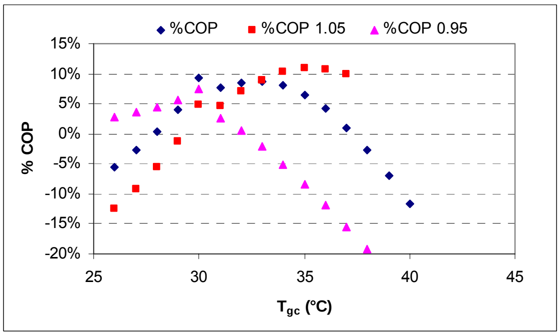

Figure 4.52: Error between the calculated and the measured η_m of the modified nozzle.

Figure 4.53: Variation of COP improvement with ettas.

Contrary to the improvement of η_m, the improvement of ettas enhances the ejector performances for a T_{gc} range higher than a critical $T_{gc,cr}$, and penalizes the ejector performances for T_{gc} lower than $T_{gc,cr}$, Figure 4.53.

According to the operation conditions, the nozzle will be designed. Many divergent lengths with different inclination angles should be tested to reach the optimal improvement.

4.17 Conclusions

The CO_2 refrigeration system has been tested on a test bench, and an optimal high pressure has been determined experimentally.

Four different control strategies have been described to control the evaporation temperature and the gas cooler high pressure with either the EEV or the CEV. The control by the CEV was found to be more accurate.

For the ejector refrigeration system, 18 ejectors have been tested. The experimental results were used to characterize the ejector operation: nozzle and body.

For the tested nozzles, the expansion through the convergent nozzle has been found to be isentropic. It also has been proven that the maximum flow passes through an orifice separating two chambers at different pressures: the upstream pressure is higher than the saturation pressure, and downstream the throat CO_2 is in two-phase flow.

For the tested bodies, it has been found that:

- The constant pressure chamber length does not affect the ejector performance.
- The 1D model of the ejector has been adapted by introducing a surface efficiency **ettas** and a mixing efficiency η_m. These efficiencies are expressed as functions of the flow and the ejector parameters.
- There is a critical constant area diameter above which the ejector performance is constant. For constant area diameter lower than the critical diameter, the ejector performance will decrease. The surface efficiency **ettas** determines the effective area of the constant area chamber.

A parametric study of the ejector refrigeration system has been performed as a function of the evaporation temperature, the gas cooler outlet temperature, and the evaporator outlet superheat. The COP improvement of the ejector refrigeration system is about 12% for T_{gc} = 30°C, T_{ev} = 2°C and SH = 5 K.

Also, an ejector refrigeration system with integral heat exchanger has been studied and it has been found that for a certain gas cooler outlet temperature, the performance of this system is higher than the ejector refrigeration system.

References

[CHE 04] J.P. Chen , J.P. Liu, Z.J. Chen, Y.M. Niu: “Trans-critical R744 and two-phase flow through short tube orifices”, International Journal of Thermal Sciences 43 (2004) 623–630.

[CHE 05] Y. Chen, J. Gu: “Non-adiabatic capillary tube flow of carbon dioxide in a novel refrigeration cycle”, Applied Thermal Engineering (2005).

[MAR 06] KLAUS MARTIN, RENÉ RIEBERER, JOSEF HAGER : "Modelling of Short Tube Orifices for CO_2”, R111, International Refrigeration and Air Conditioning Conference at Purdue, July 17-20, 2006.

General conclusion

Carbon dioxide, with a global warning potential of 1 is a candidate to replace the current refrigerants with high global warming potential like R-134a (GWP = 1300). Many technical developments have been launched on CO_2 MAC systems by car makers and suppliers all over the world.

In this work, CO_2 refrigeration systems are characterized. The thermo-physical and thermodynamic properties of R-744 present several advantages compared to current refrigerants: the CO_2 volumetric capacity is about 8 times higher than R-134a, which decreases the compressor swept volume.

In sub-critical operation, when the condensing temperature is lower than 31°C, the CO_2 refrigeration cycle is a vapor compression cycle with condensation. When the sink temperature is higher than 31°C, the CO_2 refrigeration cycle is trans-critical and has an optimum operating high pressure with a maximum coefficient of performance.

A detailed exergy analysis of the CO_2 cycle shows that the main performance losses in the conventional CO_2 refrigeration cycle are related to the expansion and the discharge temperature of the compressor.

Many refrigeration cycles were investigated to improve the CO_2 refrigeration performances, and were studied at different heat source and heat sink temperatures. The comparison between these cycles shows that the indirect injection cycle, with isentropic expansion and two compression stages, presents the best performance at 0°C evaporation temperature and 28°C as condenser outlet temperature in sub-critical operation, and 35°C gas cooler outlet temperature in trans-critical operation.

The system under study is taking into account the automobile air conditioning constraints that have to be respected. The system has to be kept simple, at the lowest costs, and so with a single compressor. Thereby, the ejector refrigeration cycle was chosen to be studied and characterized because it respects the automotive constraints.

A bibliography review about the CO_2 isentropic expansion is presented to show the energy performances, which are currently reached, and the possible improvements with different expanders types: scroll, rolling piston, and reciprocating piston technologies.

The ejector is composed of two parts: a nozzle and a body. A primary flow expands through the nozzle and absorbs a secondary flow from the evaporator, then the two flows are mixed in the body before exiting the ejector. The role of the ejector is to compress the vapor flow of the evaporator.

Two possible types of ejector refrigeration cycle can be designed:

- superheated vapor ejector cycle: a liquid compression cycle with vapor mixing between two vapor flows.
- sub-cooled / supercritical ejector cycle: a vapor compression cycle with a mixing process between a two-phase flow and a vapor flow.

The sub-cooled / supercritical ejector cycle is not fully studied and characterized by researchers, but the superheated vapor ejector cycle had been studied and characterized by several researchers with different refrigerants: water, R-718, R-141b, and R-134a. Also, the vapor flow can be described by CFD simulations. In this thesis a 1D model was elaborated for the superheated vapor ejector refrigeration cycle and adapted using literature experimental results and CFD simulations. The main assumption validated by the vapor 1D model is that **the entrainment ratio, w, is optimized to a maximum value by evaluating the optimum pressure drop**.

A CFD analysis of an ejector with R-141b vapor flow was done by studying the internal flow properties at different ejector sections. Also, using CFD, a parametric study of the ejector geometry was performed to optimize the ejector geometry: diffuser length and constant area chamber length.

Using the assumptions of the vapor ejector model, a 1D model for the sub-cooled / supercritical ejector cycle has been elaborated. The 1D model is used to characterize the ejector with two-phase flows, and to study the effect of different cycle parameters. The refrigeration performance improvements reach more than 10% for the sub-cooled ejector cycle with CO_2 as refrigerant.

A comparison between CO_2 and R-134a for the conventional refrigeration cycle and sub-cooled/supercritical ejector refrigeration cycle has shown that the ejector cycle improves the CO_2 system energy performances more than a R-134a system.

The 1D two-phase model has been used to design different ejectors. To characterize the effect of the geometrical parameters of the ejector cycle, several ejectors parts were produced: three nozzles with different throat diameters (0.75, 1.0, and 1.25 mm), and six bodies with different constant area chamber diameters (1.5, 2.0, 2.5, 3.0, 3.5, and 4.0 mm).

The 1D two-phase model has been used to analyze the ejector composed of the nozzle with a throat diameter of 1 mm and of different bodies. The assumptions used in the 1D model to analyze the ejectors are:

- The flow is at the saturated state at the nozzle throat.
- The flow is fully developed at the nozzle outlet and in the constant area mixing chamber.

A test bench has been realized to analyze the performances of CO_2 refrigeration cycles: simple and sub-cooled / supercritical ejector cycles. The uncertainties of the measured values on the test bench are lower than 5 %.

The Obrist compressor has been characterized by its different efficiencies: volumetric, isentropic, mechanical, and effective, as functions of the pressure ratio, the rotation speed, and the displacement.

A CO_2 to water gas cooler prototype for with micro-channel-tube-and-shell type has been designed and realized using a simulation model validated with experimental results.

A tube-in-tube evaporator prototype for CO_2 - water has been sized with a simulation model validated with experimental tests.

The objectives of the bench test have been:

- The characterization of the CO_2 compressor with CEV,
- The validation of the heat exchanger models: evaporator and gas cooler.
- The control of the optimal operation of the CO_2 refrigeration cycle.
- The validation and the adaptation of sub-cooled / supercritical ejector model.

The simulation results predict the heating capacity with a precision better than 5 % for condensation and supercritical state, which is the uncertainty range of applications of the used correlations, and a precision better than 20% for evaporation, which is also the error of the correlations given by the authors.

The CO_2 simple refrigeration cycle has been tested on the test bench, and an optimal high pressure has been determined experimentally.

Four different control policies have been described to control the evaporation temperature and the gas cooler high pressure with either the CEV or the EEV. The control by the CEV was found to be more accurate, and was used to test the ejectors.

For the ejector refrigeration cycle, 18 ejectors have been tested on the test bench. The experimental results have been used to characterize the ejector operation: nozzle and body.

The expansion through the convergent nozzle prototypes has been found to be isentropic. Also, It has been found that for the maximum flow crossing an orifice separating two chambers at different pressures: the upstream pressure is higher than the CO_2 saturation pressure, and downstream the nozzle CO_2 is in two-phase flow.

For the tested bodies, it has been found that:

- The constant pressure chamber length does not affect the ejector performance.
- The 1D model of the ejector has been adapted by introducing a surface efficiency ettas and a mixing efficiency η_m. These efficiencies have been expressed as functions of the flow and the ejector parameters.
- There is a critical constant area diameter above which the ejector performance is constant. For constant area diameter smaller than the critical diameter, the ejector performance is penalized.

Using the adapted 1D model, a parametric study of the ejector refrigeration cycle has been established as a function of the evaporation temperature, the gas cooler outlet temperature and the evaporator outlet superheat. The COP improvement of the ejector refrigeration cycle is about 12% for T_{gc} = 30°C, T_{ev} = 2°C, and SH = 5 K, which is the maximum reached improvement with the in-house tested ejector.

An ejector refrigeration cycle with integral heat exchanger has been studied and it is found that, for a certain gas cooler outlet temperature, the performance of this cycle is higher than the ejector refrigeration cycle.

The effect of using an internal heat exchanger on the ejector refrigeration cycle has been discussed. The internal heat exchanger can improve the ejector cycle performance for some operating conditions.

The ejector sensitivity analysis has shown that the improvement of the mixing efficiency increases the performance of the ejector cycle, but the improvement of ettas increases the performances only for specific operating parameters.

As future works, the effect of the constant pressure chamber, the diffuser, the constant area chamber, and the nozzle divergent lengths on the ejector performance could be experimentally evaluated out of the studied range.

The nozzle could be used with a wheel to form an impulsion turbine that can be used to improve the CO_2 refrigeration cycle as isentropic expander.

The realized ejector could be installed on an mobile air conditioning to evaluate the dynamic refrigeration performances, and compare the results with a simple CO_2 MAC system.

Once the CFD simulation of a two-phase flow is available, the optimization of the sub-cooled CO_2 ejector cycle will be established.

ANNEX 1. CO_2 two-stage compression cycles

The energy performances of the single-stage CO_2 cycle can be significantly improved by using multistage compression and by inter-cooling of liquid and vapor refrigerant. Installing intermediate heat exchangers may enhance the two-stage cycle by decreasing the gas cooler inlet temperature that decreases the irreversibility of the gas cooler. This annex presents the detailed simulations of different structures of 2 stage CO2 systems and also to cooled compressor.
The main configurations of two-stage compression refrigeration cycles are:

- Two-stage compression in series with intercooler between the stages TSCSI.
- Two-stage compression with injection between the stages as integrated cascade TSCI.
- Two-stage compression with economizer TSCE.

For two-stage systems, the optimum HP is related to a number of parameters of the system, the pressure ratio affects the isentropic compression efficiency of the compressor, the ratio between the expander generated work and the compression work determines the uses of the generated work in the cycle, the swept volumes of the compressors determine the intermediate pressure.

1. Two-stage compression in series with intercooler between the stages TSCSI

The TSCSI, showed in Figure1.1, is composed of: an evaporator, a LP compressor, an intercooler, a HP compressor, a gas cooler and a throttling device (valve or turbine). An internal heat exchanger could be installed as showed in Figure 1.1.e between the suction line of the LP compressor and the gas cooler outlet line.

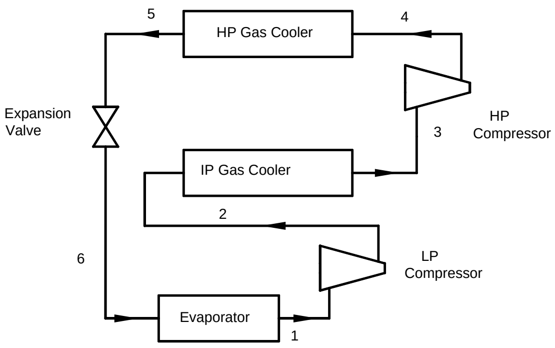

a. Two-stage compression in series

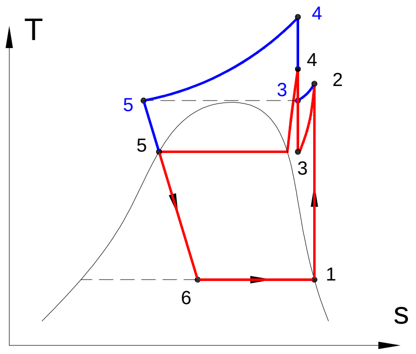

b. T-S diagram of TSCSI

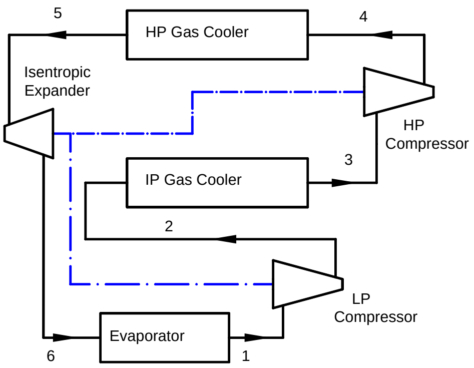

c. TSCSI with isentropic expansion

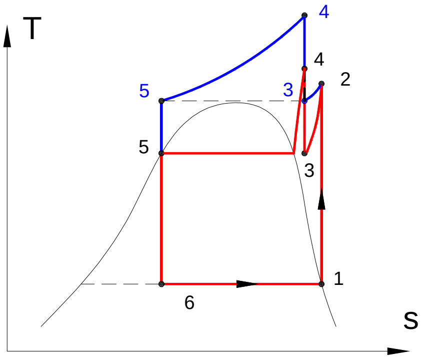

d. T-S diagram of TSCSI with isentropic expansion

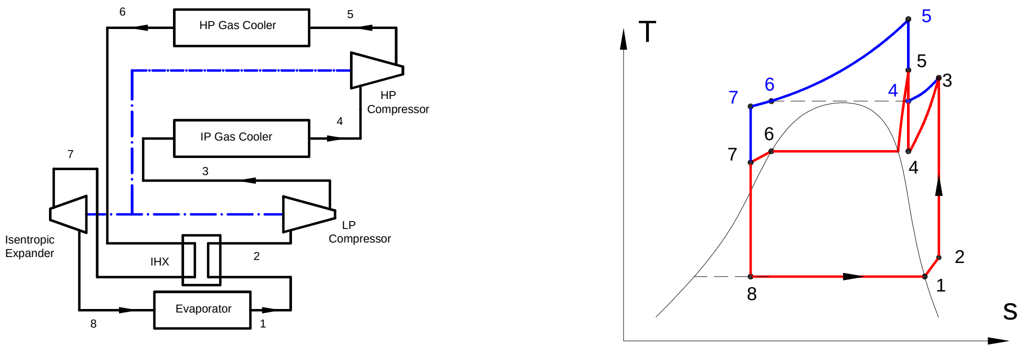

e. TSCSI with IHX and isentropic expansion

f. T-S diagram of TSCSI with IHX and isentropic expansion

Figure 1.1: Two-stage compression cycle in series with intercooler.

1.1 TSCSI with isenthalpic expansion

By applying the first law of thermodynamic, and using Refprop7 to calculate the properties of CO_2 at different conditions, Figures 1.2 to 1.6 show several operating parameters.

- **Variation of the evaporating temperatures on the low pressure side**

Simulation conditions: expansion is isenthalpic, the superheat at the low pressure (LP) compressor suction is 5 K and 0 K for the HP (HP) compressor, no sub-cooling, the isentropic compression efficiency is 1, the gas cooler/ condenser outlet temperature is equal to 35, 45 and 55°C, the evaporating temperature is varied.

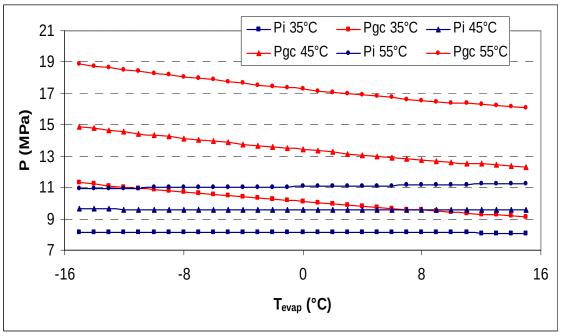

-a-

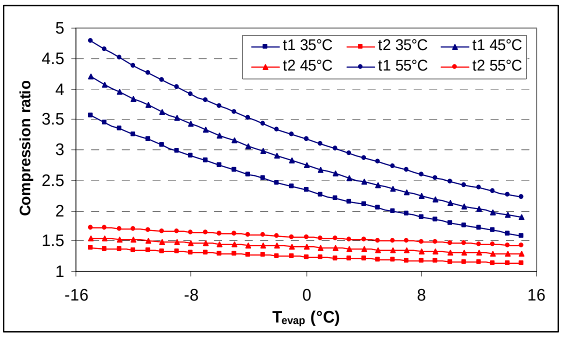

-b-

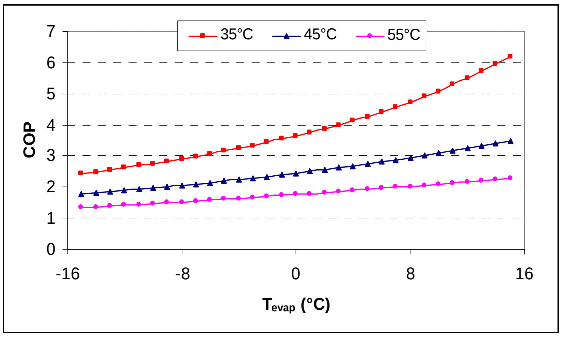

-c-

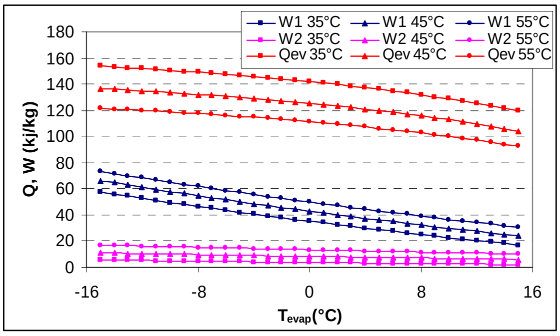

-d-

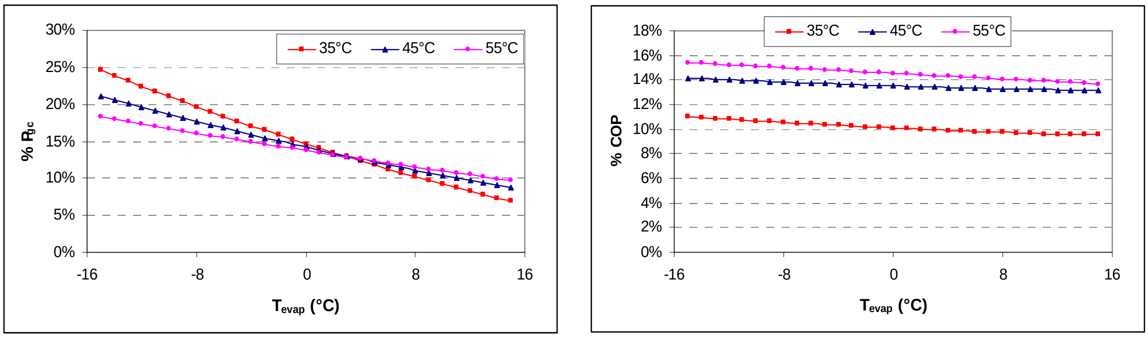

-e- -f-

Figure 1.2: Variation of P_i, P_{gc}, CR, COP, COP, and P_{gc} comparison, cooling capacity and compression work with evaporation temperature for TSCSI. ($\eta_{comp} = 1$, $T_{SH} = 5$ K).

Results

Figure 1.2 shows the results with an isenthalpic expansion with different gas cooler outlet temperatures (35, 45, 55°C). The variation of the evaporating temperature (Figure 1.2.a) shows that the optimum high pressure (HP) decreases with the increase of the evaporation temperature; on the other hand, the optimum intermediate pressure (IP) is quasi-constant with the increase of the evaporating temperature. As the evaporating temperature increases, the compression ratio (CR) of the LP compressor (t1) decreases (Figure 1.2.b), the CR of the HP compressor (t2) decreases also slightly with the evaporating temperature.

The HP and IP are independent of the isentropic compression efficiency of the compressor, but depend slightly of the pressure drop in the evaporator and the gas cooler.

The cooling capacity (Figure 1.2.d) decreases with T_{ev} because the saturated vapor enthalpy decreases with T_{ev}. The compression work of the HP compressor (W2) slightly decreases with T_{ev}, and the compression work of the LP compressor (W1) decreases with T_{ev} at constant gas cooler outlet temperature.

The COP of TSCSI increases (Figure 1.2.c) with T_{ev} as the temperature difference between the heat source and the heat sink decreases.

Comparison with the single-stage cycle

- By comparing the P_{gc} of TSCSI to the conventional P_{gc}, ($\%P_{gc,TSCSI} = (P_{gc,TSCSI} - P_{gc,conv}) / P_{gc,\,conv}$), the gas cooler HP variation $\%P_{gc}$ is positive and decreases with T_{ev}, so the HP of TSCSI is higher than the one of conventional cycle (Figure 1.2.e).
- By comparing the COP of TSCSI to the conventional COP, ($\%COP_{TSCSI} = (COP_{TSCSI} - COP_{conv}) / COP_{conv}$), the COP variation $\%COP_{TSCSI}$ is positive and slightly decreases with T_{ev}, so the TSCSI cycle improves the energy performance of the cycle by 15% at $T_{gc} = 35$°C, by 13% at $T_{gc} = 45$°C, and by 10% at $T_{gc} = 55$°C (Figure 1.2.f).

- **Variation of the outdoor temperatures on the high-pressure side**

Simulation conditions: expansion is isenthalpic, evaporating temperature equals 0°C, the gas cooler/ condenser outlet temperature is varied and Figure 1.3 is drawn.

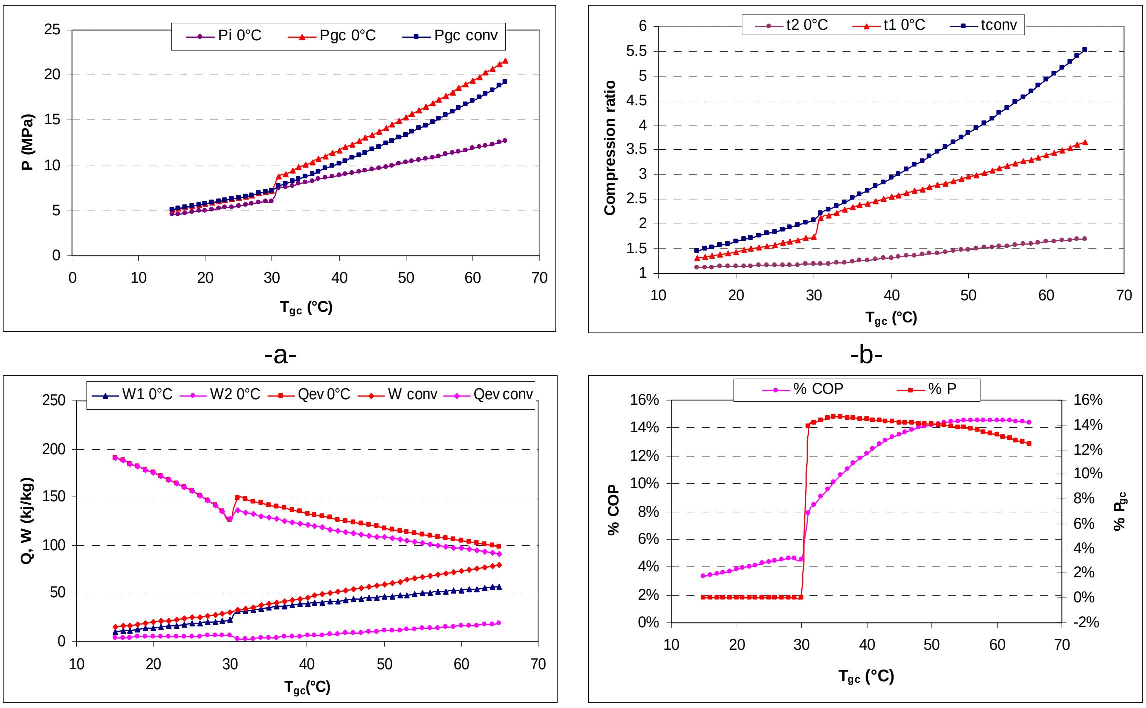

-a- -b-

-c- -d-

Figure 1.3: Variation of P_i, P_{gc}, CR, COP and P_{gc} comparison, cooling capacity and compression work with gas cooler outlet temperature for TSCSI (evaporation temperature = 0°C, η_{comp} = 1, T_{SH} = 5 K).

Results

In sub-critical operating conditions, T_{gc} < 31°C, the HP is the saturated pressure at T_{gc}, and the IP slightly increases with T_{gc} (Figure 1.3.a). As the gas cooler outlet temperature increases, the CR of the LP compressor (t1) increases; on the other hand, the CR of the HP compressor (t2) increases slightly, however the CR of the conventional cycle (tconv) is larger than the two CRs (Figure 1.3.b).

The cooling capacity decreases with T_{gc} because the evaporator inlet enthalpy increases with T_{gc}, also the cooling capacity of TSCSI cycle is equal to the conventional cycle in sub-critical cycle. The compression work of the HP compressor (W2) and the compression work of the LP compressor (W1) slightly increase with T_{gc}, at constant evaporating temperature, 0°C (Figure 1.3.c).

Comparison with the single stage cycle

- By comparing, the gas cooler outlet pressure variation $\%P_{gc}$ is zero in sub-critical cycle.
- By comparing, the COP variation $\%COP_{TSCSI}$ is positive and slightly increases with T_{gc}, so the TSCSI cycle improves the energy performance of the cycle in sub-critical cycle, by 3% at T_{gc} = 15°C, and by 4.5% at T_{gc} = 30°C (Figure 1.3.d).

By passing from sub-critical cycle to transcritical, a jump occurs in the different presented values due to the high change of the CO_2 properties near the critical point.

In trans-critical operating conditions, T_{gc} > 31°C, the HP and the IP increase with T_{gc} (Figure 1.3.a). As the gas cooler outlet temperature increases, the CR of the LP compressor (t1) increases with a jump near the critical point; on the other hand, the CR of the HP compressor (t2) continuously increases, however the CR of the conventional cycle (tconv) continuously increases and is larger than the two CRs (Figure 1.3.b).

The HP and the IP are independent of the isentropic compression efficiency of the compressor, but slightly depend of the pressure drop in the evaporator and the gas cooler.

The cooling capacity decreases with T_{gc} because the evaporator inlet enthalpy increases with T_{gc}, but the cooling capacity of TSCSI cycle is larger than the conventional cycle because the $P_{gc,TSCSI}$ is higher than $P_{gc,conv}$. The compression work of the HP compressor (W2) and the compression work of the LP compressor (W1) slightly increase with T_{gc}, at constant evaporating temperature, 0°C (Figure 1.3.c).

Comparison with the single stage cycle

- By comparing the P_{gc} of TSCSI to the conventional P_{gc}, the gas cooler outlet pressure variation $\%P_{gc}$ is positive in trans-critical cycle and slightly decreases with T_{gc} around 14% (Figure 1.3.d).
- By comparing the COP of TSCSI to the conventional COP, the COP variation $\%COP_{TSCSI}$ is positive and increases with T_{gc} from 8 to 14% at 31°C to 50°C, and then become quasi-constant equal to 14%, so the TSCSI cycle enhances the energy performance of the cycle in trans-critical cycle, by more than 8% (Figure 1.3.d).

1.2 TSCSI with isentropic expansion

- **Variation of the evaporating temperatures on the low pressure side**

Simulation conditions: isentropic expansion, gas cooler outlet temperature T_{gc} is set at different temperatures (35, 45, 55°C).

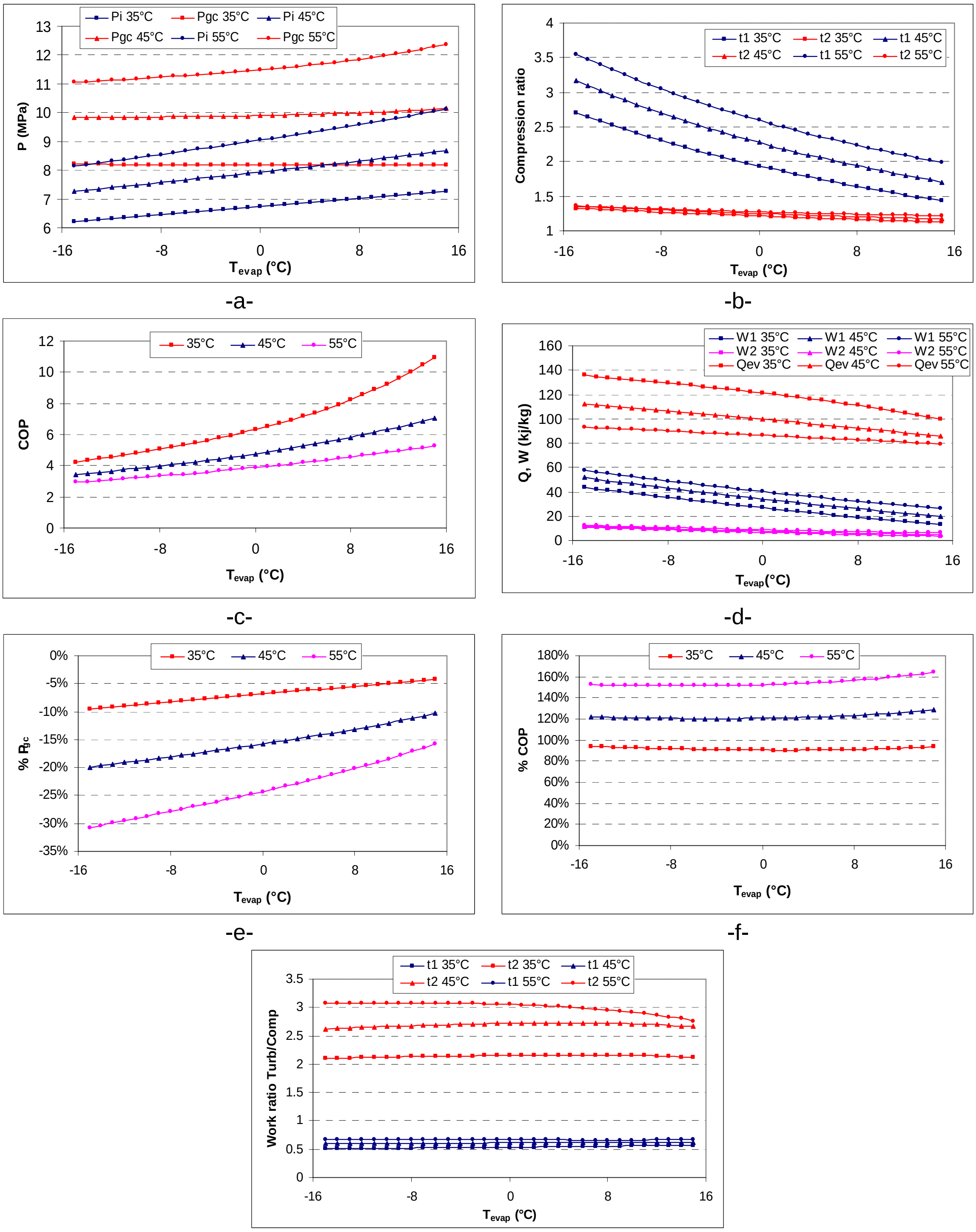

-a- -b-

-c- -d-

-e- -f-

-g-

Figure 1.4: Variation of P_i, P_{gc}, CR, COP, COP and P_{gc} improvement, cooling capacity and compression work with evaporation temperature
for TSCSI (isentropic expansion, η_{comp} = 1, $\eta_{turbine}$ = 1and T_{SH} = 5 K).

Results

The variation of the evaporating temperature shows that the high side optimum pressure slightly increases with the increase of the evaporation temperature; on the other hand, the intermediate optimum pressure increases with the increase of the evaporating temperature (Figure 1.4.a). As the evaporating temperature increases, the evaporating pressure increases that decreases the CR of the LP compressor; on the other hand, the CR of the HP compressor is quasi-constant with the evaporating temperature (Figure 1.4.b).

The HP and the IP depend of the isentropic expansion efficiency of the expander and the isentropic compression efficiency, but depends slightly on the pressure drop in the evaporator and the gas cooler.

The cooling capacity decreases with T_{ev} because the saturated vapor enthalpy decreases with T_{ev}. The compression work of the HP compressor (W2) is quasi-constant with T_{ev}, and the compression work of the LP compressor (W1) decreases with T_{ev} at constant gas cooler outlet temperature (Figure 1.4.d).

The COP of TSCSI increases with T_{ev} as the temperature difference between the heat source and the heat sink decreases (Figure 1.4.c); the COP is calculated by subtracting the turbine-generated work from the compression work of the two compression stages.

By comparing the available generated work from the isentropic expansion to the required work of the two compressors, the variation of T_{ev} shows that the turbine work is larger than the HP compression work (t2), more than two times at 35°C as T_{gc} and three times at 55°C as T_{gc}; on the other hand, the variation of T_{ev} shows that the turbine work is lower than the LP compression work (t1), around 0.5 time at 35°C to 55°C as T_{gc}; however the work ratio is quasi-constant with the variation of T_{ev} (Figure 1.4.g).

Comparison with the single stage CO_2 cycle

- By comparing the P_{gc} of TSCSI with isentropic expansion to the conventional P_{gc}, the gas cooler outlet pressure variation $\%P_{gc}$ is negative and increases with T_{ev}, so the HP of TSCSI is lower than the conventional cycle, also $\%P_{gc}$ decrease with T_{gc} (Figure 1.4.e).

- By comparing the COP of TSCSI with isentropic expansion to the conventional COP, the COP variation $\%COP_{TSCSI}$ is positive and is quasi-constant with T_{ev} but increases with T_{gc}, so the TSCSI with isentropic expansion cycle improves the energy performance of the cycle by 90% at T_{gc} = 35°C, by 120% at T_{gc} = 45°C, and by 150% at T_{gc} = 55°C (Figure 1.4.f).

  - **Variation of the outdoor temperature on the high-pressure side**

Simulation conditions: expansion is isentropic, evaporating temperature equals 0°C, the gas cooler/ condenser outlet temperature is varied and Figure 1.5 is drawn.

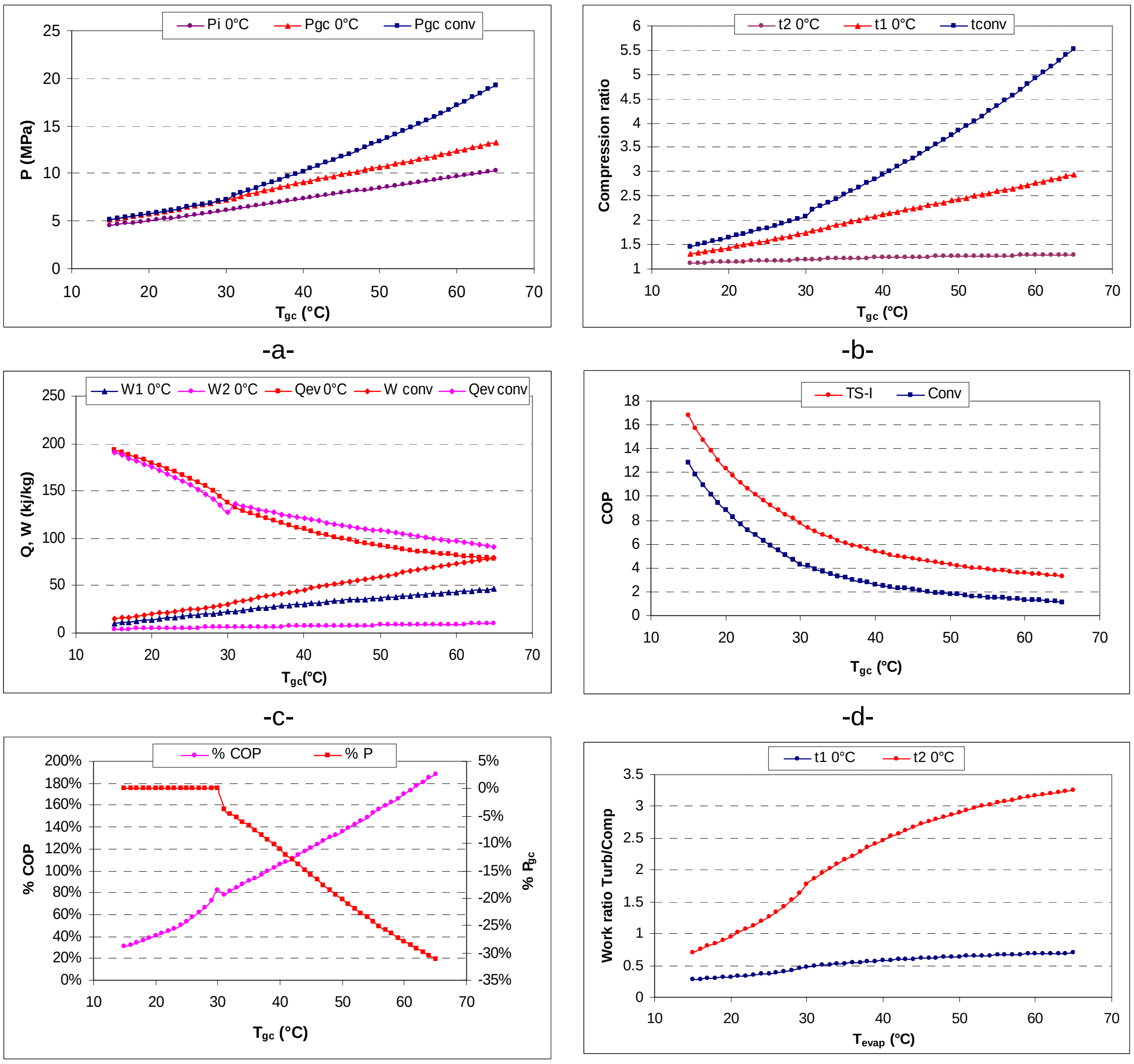

-a-

-b-

-c-

-d-

-e-

-f-

Figure 1.5: Variation of P_i, P_{gc}, CR, COP and P_{gc} improvement, cooling capacity and compression work with gas cooler outlet temperature for TSCSI with isentropic expansion at 0°C evaporation temperature, ($\eta_{comp} = 1$, $\eta_{turbine} = 1$ and $T_{SH} = 5$ K).

Results

In sub-critical operating conditions, $T_{gc} < 31°C$, the HP is the saturated pressure at T_{gc}, and the IP slightly increases with T_{gc} (Figure 1.5.a). As the gas cooler outlet temperature increases, the CR of the LP compressor increases; on the other hand, the CR of the HP compressor slightly increases, however the CR of the conventional cycle is larger than the two CRs (Figure 1.5.b).

The cooling capacity decreases with T_{gc} because the evaporator inlet enthalpy increases with T_{gc}, but the cooling capacity of TSCSI with isentropic expansion cycle is larger than the conventional cycle in sub-critical cycle due to the generated work by the turbine that decreases the inlet enthalpy of the evaporator. The compression work of the HP compressor (W2) and the compression work of the LP compressor (W1) increases slightly with T_{gc}, at constant evaporating temperature, 0°C (Figure 1.5.c).

The COP of TSCSI with isentropic expansion decreases with T_{gc} as the temperature difference between the heat source and the heat sink increases (Figure 1.5.d); the COP is calculated by subtracting the turbine-generated work from the compression work of the two compression stages.

By comparing the available generated work from the isentropic expansion to the required work of the two compressors, the variation of T_{gc} shows that the turbine work is lower than the HP compression work for T_{gc} <22°C and is larger than the HP compression work for T_{gc} >22°C; on the other hand, the variation of T_{gc} shows that the turbine work is lower than the LP compression work, around 0.45 time; however the work ratio increases with the variation of T_{gc} (Figure 1.5.f).

Comparison with the single stage CO_2 cycle

- The gas cooler outlet pressure variation %P_{gc} is zero in sub-critical cycle (Figure 1.5.e).
- By comparing the COP of TSCSI with isentropic expansion to the conventional COP, the COP variation %$COP_{TSCSI\ is}$ is positive and increases with T_{gc}, so the TSCSI with isentropic expansion cycle enhances the energy performance of the sub-critical cycle, by 30% at T_{gc} = 15°C, and by 80% at T_{gc} = 30°C (Figure 1.5.e).

In trans-critical operating conditions, T_{gc} > 31°C, the HP and the IP increase with T_{gc} (Figure 1.5.a). As the gas cooler outlet temperature increases, the CR of the LP compressor (t1) continuously increases; on the other hand, the CR of the HP compressor (t2) increases slightly, however the CR of the conventional cycle (tconv) increases continuously and is larger than the two-CRs (Figure 1.5.b).

The HP and the IP are dependent of the isentropic compression efficiency of the compressor and the isentropic expansion efficiency, but slightly depend of the pressure drop in the evaporator and the gas cooler.

The cooling capacity decreases with T_{gc} because the evaporator inlet enthalpy increases with T_{gc}, but the cooling capacity of TSCSI with isentropic expansion cycle is lower than the conventional cycle because $P_{gc,TSCSI\ is}$ is lower than $P_{gc,conv}$. The compression work of the HP compressor (W2) and the compression work of the LP compressor (W1) increases slightly with T_{gc}, at constant evaporating temperature, 0°C (Figure 1.5.c).

By comparing the available generated work from the isentropic expansion to the required work of the two compressors, the variation of T_{gc} shows that the turbine work is larger than the HP compression work more than 1.5 times at 31°C; on the other hand, the variation of T_{gc} shows that the turbine work is lower than the LP compression work, around 0.6 time; however the work ratio increases with the variation of T_{gc} (Figure 1.5.f).

Comparison with the single stage CO_2 cycle

- By comparing the P_{gc} of TSCSI with isentropic expansion to the conventional P_{gc}, the gas cooler HP variation %P_{gc} is negative in trans-critical cycle and decreases with T_{gc} from - 4% at 31°C to –30% at 65°C (Figure 1.5.e).
- By comparing the COP of TSCSI with isentropic expansion to the conventional COP, the COP variation %$COP_{TSCSI\ is}$ is positive and increases with T_{gc} from 80 to 190% at 31°C to 65°C, so the TSCSI with isentropic expansion cycle improves the energy performance of the trans-critical cycle by more than 80% (Figure 1.5.e).

The most available expanders are directly connected to a compressor. By considering the generated work of the turbine is equal to the required work of a compression stage: LP compressor or the HP compressor, Figure 1.6 is drawn for optimal HP. The COP and P_{gc} are compared to the conventional values.

Using the turbine work, as LP compressor, decreases the COP by 20% in sub-critical and transcritical operations, in addition the HP is lower than 10 % compared to the optimal P_{gc} of the TSCSI with isentropic expansion, and the cooling capacity is lower because of the decrease of the HP in transcritical operation.

Using the turbine work, as HP compressor, presents same performance of the TSCSI with isentropic expansion in sub-critical operation, but the COP improvement begins to decrease in trans-critical operation and becomes less than the previous case around 47°C as T_{gc}. In addition the high pressure is higher than the optimal P_{gc} of the TSCSI with isentropic expansion that gives a higher evaporator capacity and becomes higher than the conventional evaporator capacity for T_{gc} higher than 40°C.

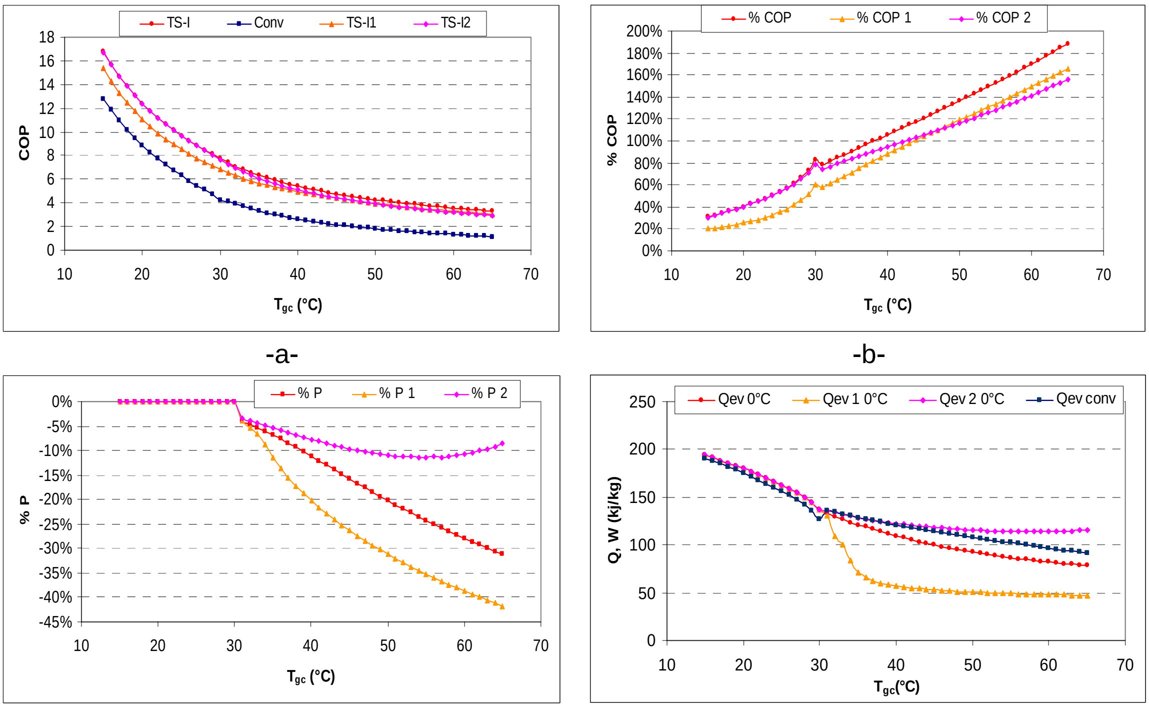

-a- -b-

-c- -d-

Figure 1.6: Variation of COP, COP and P_{gc} improvement, cooling capacity with gas cooler outlet temperature for TSCSI with isentropic expansion at 0°C as evaporation temperature.

Note: η_{comp} = 1, $\eta_{turbine}$ = 1 and T_{SH} = 5 K. Indice "1" refers to using the generated work from the expansion device as low pressure compression work, and indice "2" refers to using the generated work from the expansion device as HP compression work. The IP is not optimized but P_{gc} is optimized.

2. Two-stage compression with injection between the stages TSCII

The two-stage compression cycle with indirect injection TSCII, showed in Figure1.7 (Figure 1.10), is composed of: an evaporator, a LP compressor, a two phase separator, a HP compressor, a gas cooler and a throttling device (valve or turbine). An internal heat exchanger could be installed between the suction line of the HP compressor and the gas cooler outlet line, and between the suction line of the LP compressor and the separator liquid outlet line. The suction of the HP compressor is in saturated vapor.

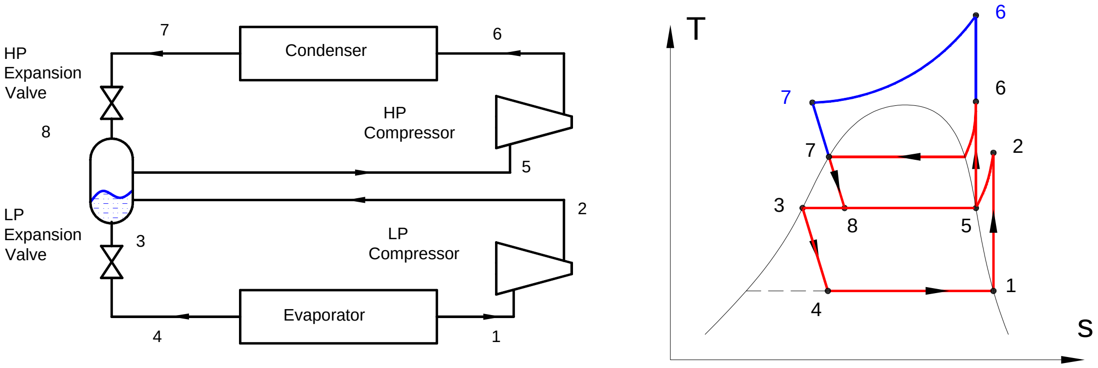

a. TSCII: Integrated cascade b. T-S diagram of TSCII

Figure 1.7: Two-stage compression cycle with indirect injection TSCII.

By applying the first law of thermodynamic, and using Refprop to calculate the properties of CO_2 at different conditions, Figures 1.8 to 1.18 are drawn for several operating parameters: the superheat at the LP compressor suction port is 5 K, no sub-cooling, the isentropic compression efficiency is 1 as well as the isentropic expansion efficiency of the expander. The separator outlets are saturated liquid and saturated vapor.

2.1 TSCII with isenthalpic expansion

▪ Variation of the evaporating temperatures on the low pressure side

Simulations conditions: expansion is isenthalpic, the gas cooler outlet temperature is set at different temperatures (35, 45, 55°C), and the evaporating temperature is varied.

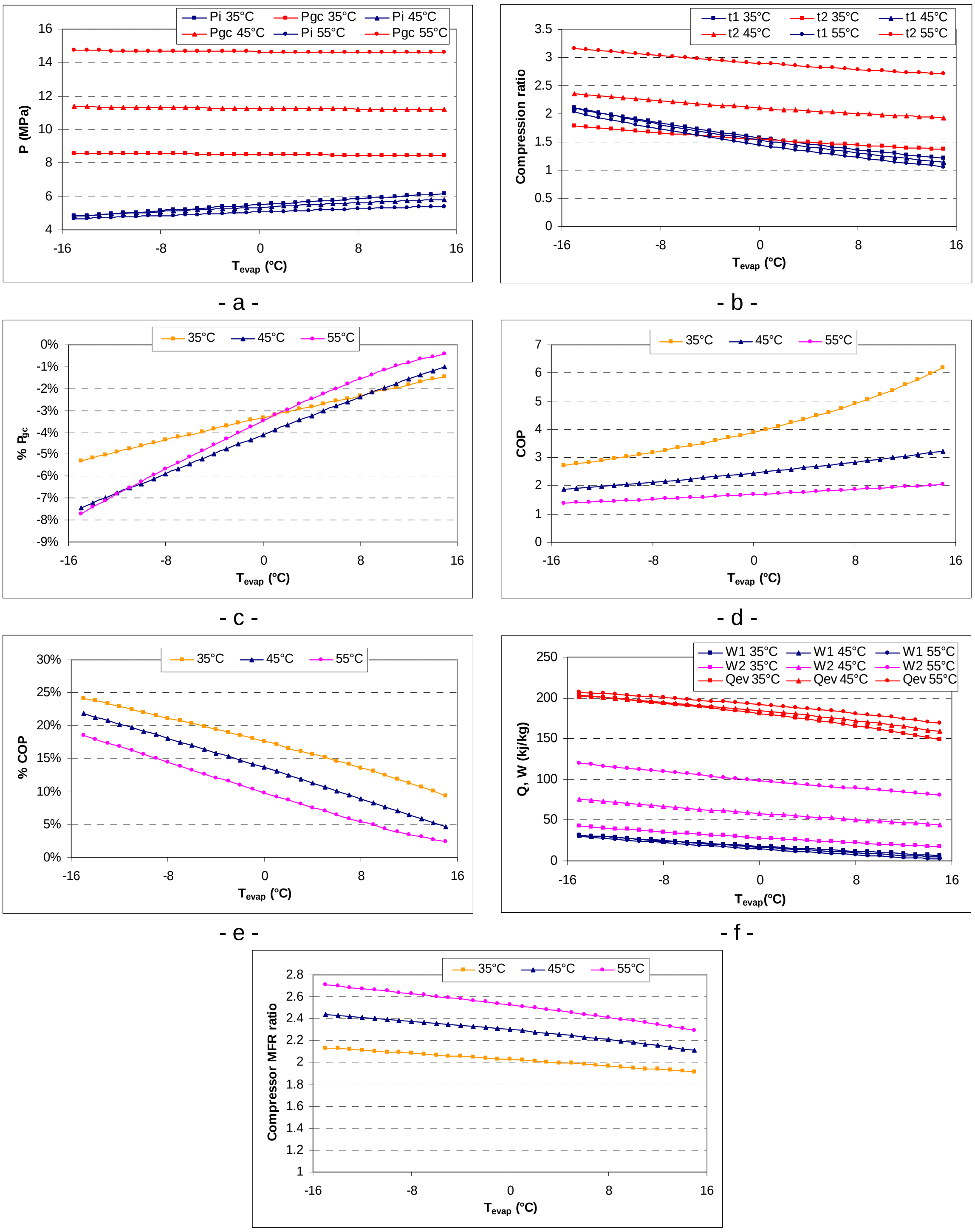

- a -

- b -

- c -

- d -

- e -

- f -

- g -

Figure 1.8: Variation of P_i, P_{gc}, CR, COP, COP and P_{gc} improvement, cooling capacity and compression work, and compressor mass flow rate ratio with evaporation temperature for TSCII. (η_{comp} = 1 and T_{SH} =5 K).

Results

The variation of the evaporating temperature shows that the HP optimum pressure is quasi-constant with the increase of the evaporation temperature but increases with T_{gc}; on the other hand, the IP optimum pressure increases with the increase of the evaporating temperature (Figure 1.8.a). As the evaporating temperature increases, the evaporating pressure increases that decreases the CR of the LP compressor (t1); on the other hand, the CR of the HP compressor (t2) decreases slightly with the evaporating temperature due to the slight increase of the IP (Figure 1.8.b).

The HP and the IP depend slightly on the isentropic compression efficiency of the compressor, and depend slightly on the pressure drop in the evaporator and the gas cooler.

The cooling capacity decreases with T_{ev} because the saturated vapor enthalpy decreases with T_{ev}, but increases slightly with T_{gc} due to the HP. The compression work of the HP (W2) and the LP (W1) compressors decrease with T_{ev} at constant gas cooler outlet temperature (Figure 1.8.f).

The COP of TSCSI increases with T_{ev} as the temperature difference between the heat source and the heat sink decreases (Figure 1.8.d).

The mass flow rate MFR ratio between the HP compressor and the LP compressor decreases with the increase of the evaporating temperature T_{ev}, however, the MFR of HP compressor is at least two times the MFR of the LP compressor (Figure 1.8.g).

Comparison with single-stage CO_2 cycle

- By comparing the P_{gc} of TSCII to the conventional P_{gc}, the gas cooler outlet pressure variation $\%P_{gc}$ is negative and increases with T_{ev}, so the HP of TSCII is lower than the conventional cycle by less than 8% (Figure 1.8.c).
- By comparing the COP of TSCII to the conventional COP, the COP variation $\%COP_{TSCII}$ is positive and decreases with T_{ev}, so the TSCII cycle enhances the energy performance of the cycle (Figure 1.8.e).

  - **Variation of the outdoor temperature on the high pressure side**

Simulations conditions: expansion is isenthalpic, the evaporating temperature equals 0°C, the gas cooler/ condenser outlet temperature is varied and Figure 1.9 is drawn.

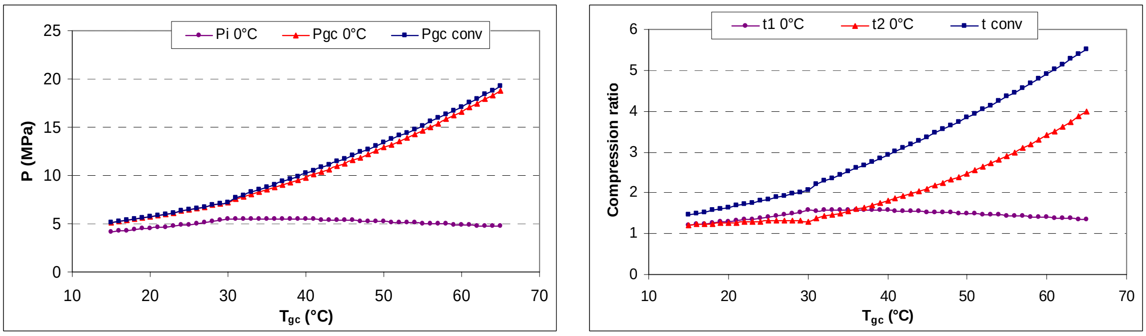

- a - - b -

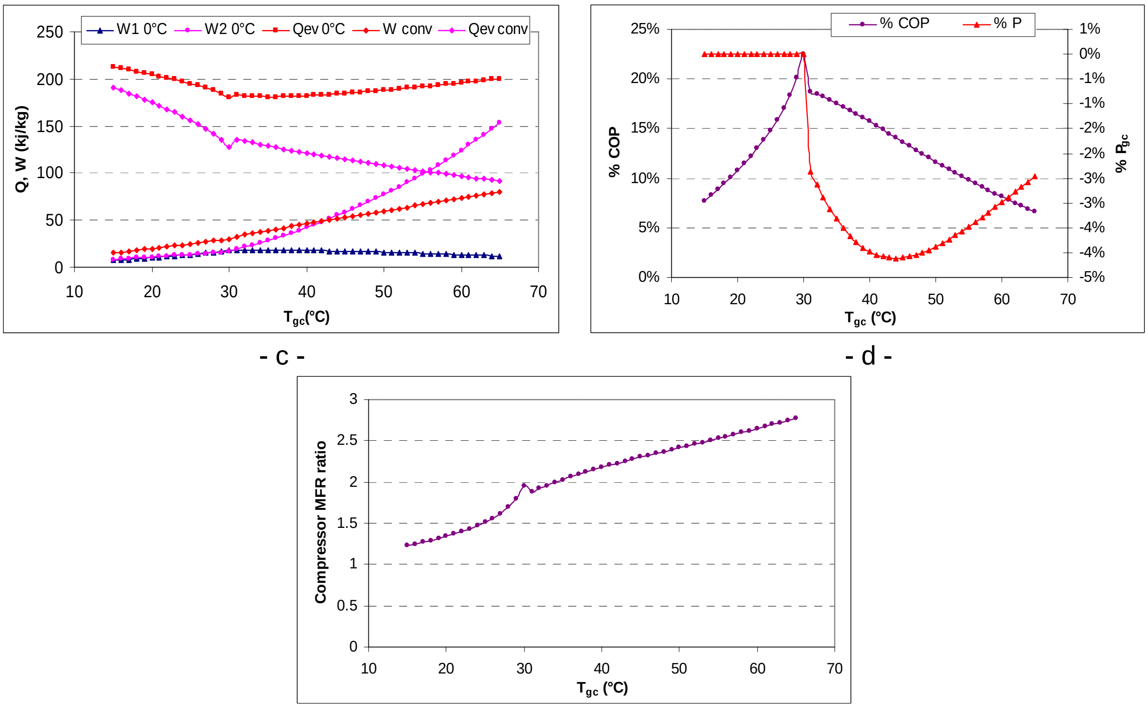

- c -

- d -

- e -

Figure 1.9: Variation of P_i, P_{gc}, CR, COP and P_{gc} improvement, cooling capacity and compression work, and compressor mass flow rate ratio with gas cooler outlet temperature for TSCII at 0°C evaporation temperature ($\eta_{comp} = 1$ and $T_{SH} = 5$ K).

Results

In sub-critical operating conditions, $T_{gc} < 31°C$, the HP is the saturated pressure at T_{gc}, and the IP slightly increases with T_{gc} (Figure 1.9.a). As the gas cooler outlet temperature increases, the CR of the LP compressor (t1) increases slightly; on the other hand, the CR of the HP compressor (t2) is quasi-constant, however the CR of the conventional cycle (tconv) is larger than the two-CRs (Figure 1.9.b).

The cooling capacity decreases with T_{gc} because the evaporator inlet enthalpy increases with T_{gc}, also the cooling capacity of TSCII cycle is larger than the conventional cycle in sub-critical cycle due to the low enthalpy of the evaporator inlet. The compression work of the HP and LP compressors increase slightly with T_{gc}, at constant evaporating temperature, 0°C (Figure 1.9.c).

The mass flow rate MFR ratio between the HP compressor and the LP compressor increases with the increase of the gas cooler temperature T_{gc}, however, the MFR of HP compressor vary by 1.2 to 2 times the MFR of the LP compressor at 15 to 30°C as T_{gc} (Figure 1.9.e).

Comparison with single stage CO_2 cycle

- The gas cooler outlet HP variation $\%P_{gc}$ is zero in sub-critical cycle.
- By comparing the COP of TSCII to the conventional COP, the COP variation $\%COP_{TSCII}$ is positive and increases with T_{gc}, so the TSCII cycle enhances the energy performance of the sub-critical cycle, by 8% at $T_{gc} = 15°C$, and by 23% at $T_{gc} = 30°C$.

In trans-critical operating conditions, $T_{gc} > 31°C$, the HP increases with T_{gc} but the IP slightly decreases with T_{gc} (Figure 1.9.a). As the gas cooler outlet temperature increases, the CR of the LP compressor (t1) decreases slightly, but the CR of the HP compressor (t2) continuously increases, however the CR of the conventional cycle (tconv) continuously increases and is larger than the two CRs (Figure 1.9.b).

The HP and the IP slightly depend of the isentropic compression efficiency of the compressor, and of the pressure drop in the evaporator and the gas cooler.

The cooling capacity slightly increases with T_{gc}, but the cooling capacity of TSCII cycle is larger than the conventional cycle due to the low enthalpy of the evaporator inlet. The compression work of the LP compressor (W1) slightly decrease with T_{gc}, at constant evaporating temperature, 0°C, or the compression work of the HP compressor (W2) increases with T_{gc} and becomes larger than the conventional work for T_{gc} > 43°C (Figure 1.9.c).

The mass flow rate MFR ratio between the HP compressor and the LP compressor increases with the increase of the gas cooler temperature T_{gc}, however, the MFR of HP compressor vary by 2 to 2.8 times the MFR of the LP compressor at 31 to 65°C as T_{gc} (Figure 1.9.e).

Comparison with single stage CO_2 cycle

- By comparing the P_{gc} of TSCII to the conventional P_{gc}, the gas cooler outlet pressure variation $\%P_{gc}$ is negative in trans-critical cycle and vary between –3% and -5% (Figure 1.9.d).
- By comparing the COP of TSCII to the conventional COP, the COP variation $\%COP_{TSCII}$ is positive and decreases with T_{gc} from 18 to 8% at 31°C to 65°C, so the TSCII cycle enhances the energy performance of the trans-critical cycle, by more than 8% (Figure 1.9.d).

2.2 TSCII with isentropic expansion

Figure 1.10 presents the lay-out (1.10.a) and the thermodynamic evolutions (1.10.b) in a T-S diagram of the two-stage compression cycle with indirect injection TSCII and isentropic expansion.

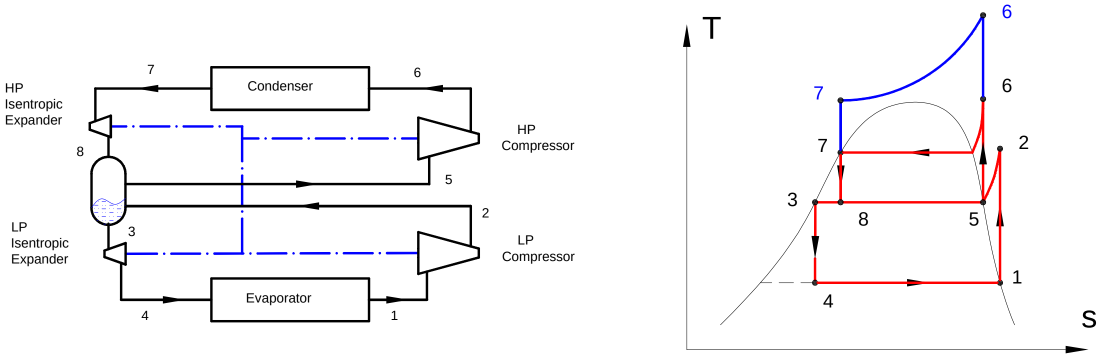

a. TSCII with isentropic expansion.

b. T-S diagram of TSCII with isentropic expansion.

Figure 1.10: Two-stage compression cycle with indirect injection TSCII and isentropic expansion.

- **Variation of the evaporating temperatures on the low-pressure side**

Simulations conditions: expansion is isentropic, the gas cooler outlet temperature is set at different temperatures (35, 45, 55°C), and the optimization of COP does not take intoto account the work generated by the turbine.

Results

The variation of the evaporating temperature shows that the optimum HP is quasi-constant with the increase of the evaporation temperature but increases with T_{gc}; on the other hand, the optimum IP increases with the increase of the evaporating temperature

(Figure 1.11.a). As the evaporating temperature increases, the evaporating pressure increases that decrease the CR of the LP compressor (t1); on the other hand, the CR of the HP compressor (t2) decreases with the evaporating temperature due to the increase of the IP (Figure 1.11.b).

The HP and the IP depend on the isentropic compression efficiency of the compressor and the isentropic expansion efficiency of the expander, and depend slightly on the pressure drop in the evaporator and the gas cooler.

The cooling capacity decreases with T_{ev} because the saturated vapor enthalpy decreases with T_{ev}, but increases slightly with T_{gc}. The compression work of the HP (W2) and the LP compressors (W1) decrease with T_{ev} at constant gas cooler outlet temperature (Figure 1.11.c).

The COP of TSCII with isentropic expansion increases with T_{ev} as the temperature difference between the heat source and the heat sink decreases (Figure 1.11.d).

The mass flow rate MFR ratio between the HP compressor and the LP compressor decreases slightly with the increase of the evaporating temperature T_{ev} and increases with T_{gc}, however, the MFR of HP compressor is at least 1.8 times the MFR of the LP compressor (Figure 1.11.g).

By comparing the available generated work from the isentropic expansion to the required work of the two compressors, the variation of T_{ev} shows that the turbine work is larger than the LP compression work for T_{gc} > 45°C, but for T_{gc} = 35°C the CR (t1) varies with T_{ev} between 0.6 and 1.5; on the other hand, the variation of T_{ev} shows that the turbine work is lower than the HP compression work (W2), around 0.5 time at 35°C to 55°C as T_{gc}; however the work ratio (R2) is quasi-constant with the variation of T_{ev} (Figure 1.11.h).

Comparison with the single stage CO_2 cycle

- By comparing the P_{gc} of TSCII with isentropic expansion to the conventional P_{gc}, the gas cooler outlet pressure variation $\%P_{gc}$ is negative and increases with T_{ev}, so the HP of TSCII with isentropic expansion is lower than the conventional cycle by less than 11% (Figure 1.11.e).
- By comparing the COP of TSCII with isentropic expansion to the conventional COP, the COP variation $\%COP_{TSCII}$ is is positive and is quasi-constant with T_{ev}, so the TSCII with isentropic expansion cycle enhances the energy performance of the cycle by 90% at 35°C, by 110% at 45°C and 135% at 55°C (Figure 1.11.f).

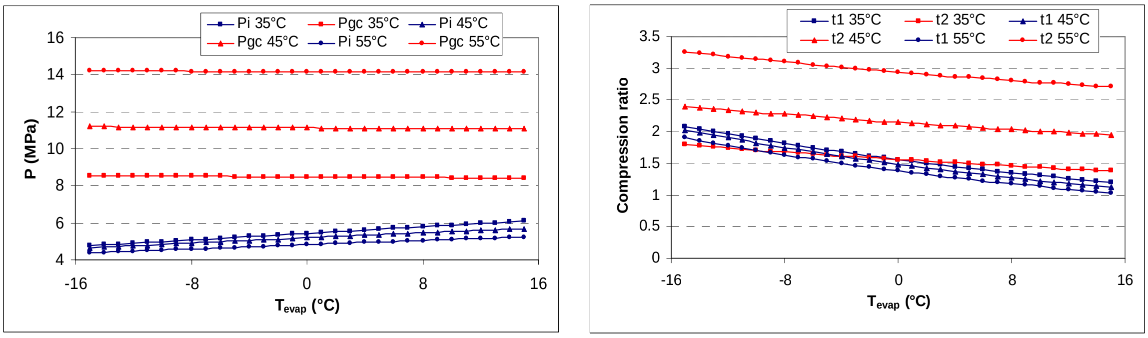

- a - - b -

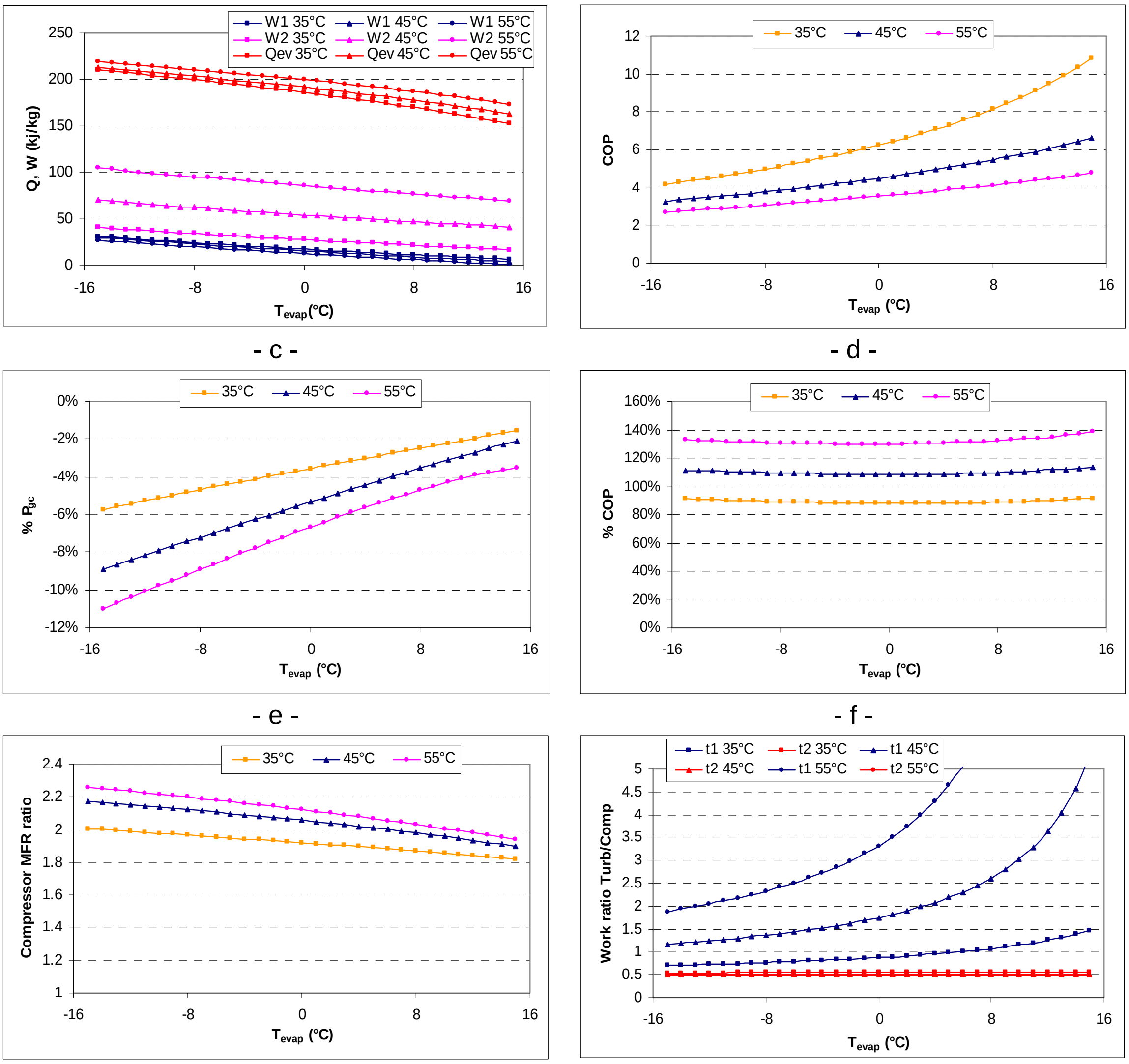

- c - - d -

- e - - f -

- g - - h -

Figure 1.11: Variation of P_i, P_{gc}, CR, COP, COP and P_{gc} improvement, cooling capacity and compression work, compressor mass flow rate ratio and turbine work to compression work ratio with evaporation temperature for TSCII (isentropic expansion. $\eta_{comp} = 1$, $\eta_{turbine} = 1$and $T_{SH} = 5$ K).

- **Variation of the outdoor temperature on the high-pressure side**

Simulations conditions: expansion is isentropic, the evaporating temperature equals 0°C, the gas cooler/ condenser outlet temperature is varied and Figure 1.12 is drawn.

Results

In sub-critical operating conditions, $T_{gc} < 31$°C, the HP is the saturated pressure at T_{gc}, and the IP slightly increases with T_{gc} (Figure 1.12.a). As the gas cooler outlet temperature increases, the CR of the LP compressor (t1) slightly increases; on the other hand, the CR of the HP compressor (t2) is quasi-constant, however the CR of the conventional cycle (tconv) is larger than the two-CRs (Figure 1.12.b).

The cooling capacity decreases with T_{gc} because the evaporator inlet enthalpy increases with T_{gc}, also the cooling capacity of TSCII with isentropic expansion cycle is larger than the conventional cycle in sub-critical cycle due to the low enthalpy of the evaporator inlet and the work generation. The compression work of the HP and LP compressors slightly increase with T_{gc}, at constant evaporating temperature, 0°C, and are almost equal (Figure 1.12.c).

The mass flow rate MFR ratio between the HP compressor and the LP compressor increases with the increase of the gas cooler temperature T_{gc}, however, the MFR of HP compressor vary by 1.2 to 1.9 times the MFR of the LP compressor at 15 to 30°C as T_{gc} (Figure 1.12.e).

By comparing the available generated work from the isentropic expansion to the required work of the two compressors, the variation of T_{gc} shows that the turbine work, compared to the LP and the HP compression work, varies around 0.5, however the work ratio is quasi-constant with the variation of T_{gc} (Figure 1.12.f).

Comparison with the single stage CO_2 cycle

- By comparing the P_{gc} of TSCII with isentropic expansion to the conventional P_{gc}, the gas cooler outlet pressure variation $\%P_{gc}$ is zero in sub-critical cycle (Figure 1.12.d).
- By comparing the COP of TSCII with isentropic expansion to the conventional COP, the COP variation $\%COP_{TSCII\ is}$ is positive and increases with T_{gc}, so the $TSCII_{\ is}$ cycle enhances the energy performance of the sub-critical cycle, by 30% at T_{gc} = 15°C, and by 90% at T_{gc} = 30°C (Figure 1.12.d).

In trans-critical operating conditions, T_{gc} > 31°C, the HP increases with T_{gc} but the IP slightly decreases with T_{gc} (Figure 1.12.a). As the gas cooler outlet temperature increases, the CR of the LP compressor (t1) slightly decreases, but the CR of the HP compressor (t2) continuously increases, however the CR of the conventional cycle (tconv) continuously increases and is larger than the two CRs (Figure 1.12.b).

The HP and the IP depend of the isentropic expansion efficiency of the expander, and slightly depend of the pressure drop in the evaporator and the gas cooler.

The cooling capacity increases with T_{gc}, but the cooling capacity of $TSCII_{is}$ cycle is larger than the conventional cycle due to the low enthalpy of the evaporator inlet. The compression work of the LP compressor (W1) slightly decreases with T_{gc}, at constant evaporating temperature, 0°C, or the compression work of the HP compressor (W2) increases with T_{gc} and becomes larger than the conventional work for T_{gc} > 43°C (Figure 1.12.c).

The mass flow rate MFR ratio between the HP compressor and the LP compressor slightly increases with the increase of the gas cooler temperature T_{gc}, however, the MFR of HP compressor vary by 1.8 to 2.2 times the MFR of the LP compressor at 31 to 65°C as T_{gc} (Figure 1.12.e).

By comparing the available generated work from the isentropic expansion to the required work of the two compressors, the variation of T_{gc} shows that the generated work, compared to the LP compression work (W1), varies from 0.7 at 31°C, becomes 1 around 38°C, than highly increases to 6 at 65°C; on the other hand, the variation of T_{gc} shows that the generated work is lower than the HP compression work (W2), around 0.5 time; however the work ratio (t2) is quasi-constant with the variation of T_{gc} (Figure 1.12.f).

Comparison with the single stage CO_2 cycle

- By comparing the P_{gc} of $TSCII_{is}$ to the conventional P_{gc}, the gas cooler outlet pressure variation $\%P_{gc}$ is negative in trans-critical cycle and vary between –2% and -9% (Figure 1.12.d).
- By comparing the COP of $TSCII_{is}$ to the conventional COP, the COP variation $\%COP_{TSCIIis}$ is positive and increases with T_{gc} from 80 to 160% at 31°C to 65°C, so the $TSCSII_{is}$ cycle enhances the energy performance of the trans-critical cycle, by more than 80% (Figure 1.12.d).

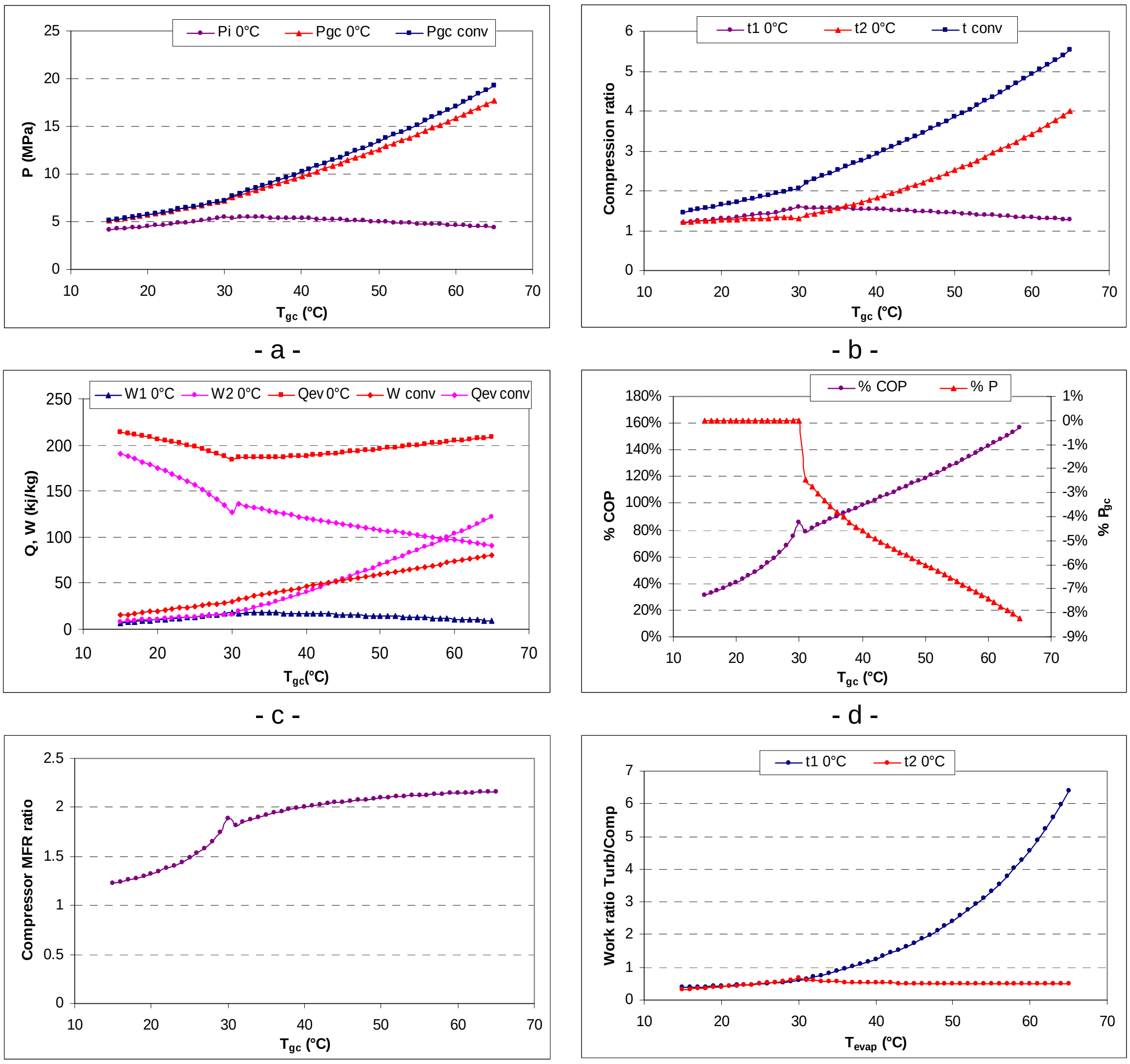

- a -

- b -

- c -

- d -

- e -

- f -

Figure 1.12: Variation of P_i, P_{gc}, CR, COP and P_{gc} improvement, cooling capacity and compression work, and compressor mass flow rate ratio and turbine work to compression work ratio with gas cooler outlet temperature for TSCII with isentropic expansion at 0°C as evaporation temperature $\eta_{comp} = 1$, $\eta_{turbine} = 1$and $T_{SH} = 5$ K.

3. Two-stage compression cycle with direct injection TSCDI

By modifying the connection of the HP compressor suction and the LP compressor discharge, the two-stage compression cycle with direct injection TSCDI is presented, and showed in Figure1.13. It is composed of an evaporator, a LP compressor, a two-phase separator, a HP compressor, a gas cooler and a throttling device (valve or turbine). An internal heat exchanger could be installed between the suction line of the HP compressor and the gas cooler outlet line, and between the suction line of the LP compressor and the separator liquid outlet line. The inlet of the HP compressor is a mixture of saturated vapor coming from the separator and the superheated vapor of the LP compressor discharge. The separator outlets are saturated liquid and saturated vapor.

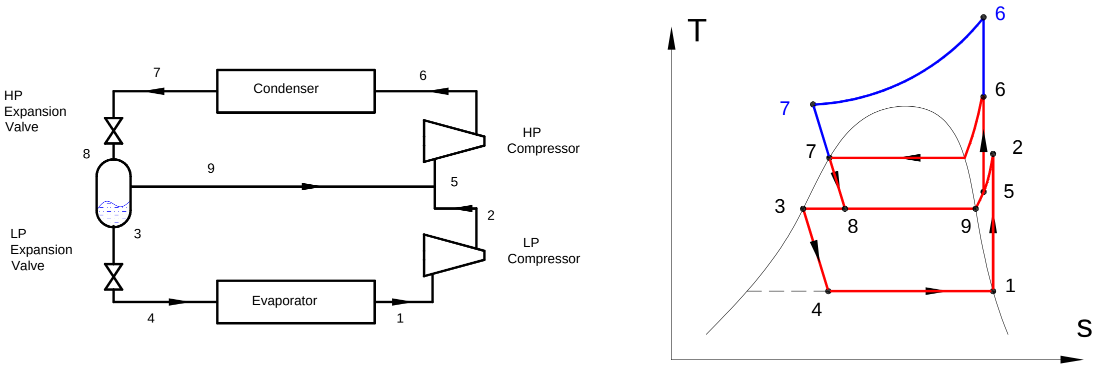

a. TSCDI b. T-S diagram of TSCDI

Figure 1.13: Two-stage compression cycle with direct injection TSCDI.

3.1 TSCDI with isenthalpic expansion

- **Variation of the evaporating temperatures on the low pressure side**

Simulations conditions: expansion is isenthalpic, the gas cooler outlet temperature is set at different temperatures (35, 45, 55°C).

Results

The variation of the evaporating temperature shows that the high side optimum pressure is quasi-constant with the increase of the evaporation temperature but increases with T_{gc}; on the other hand, the intermediate optimum pressure increases with the increase of the evaporating temperature but is quasi-constant with T_{gc} (Figure 1.14.a).

As the evaporating temperature increases, the evaporating pressure increases that decrease the CR of the LP compressor (t1) but it is quasi-constant with T_{gc}; on the other hand, the CR of the HP compressor (t2) slightly decreases with the evaporating temperature due to the slightly increase of the IP, in addition it increases with T_{gc} (Figure 1.14.b).

The HP and the IP depend slightly on the isentropic compression efficiency of the compressor, and depend slightly of the pressure drop in the evaporator and the gas cooler.

The cooling capacity decreases with T_{ev} because the saturated vapor enthalpy decreases with T_{ev}, but it is quasi-constant with T_{gc}. The compression work of the HP compressor (W2) decreases with T_{ev} at constant gas cooler outlet temperature, and increases with T_{gc}, on the other hand the work of the LP compressor (W1) decreases with T_{ev} at constant gas cooler outlet temperature, and it is quasi-constant with T_{gc} (Figure 1.14.c).

The COP of TSCSI increases with T_{ev} as the temperature difference between the heat source and the heat sink decreases (Figure 1.14.c).

The mass flow rate MFR ratio between the HP compressor and the LP compressor slightly decreases with the increase in the evaporating temperature T_{ev} but increases with T_{gc}, however, the MFR of HP compressor is at least 1.5 times the MFR of the LP compressor (Figure 1.14.g).

Comparison with the single stage CO_2 cycle

- By comparing the P_{gc} of TSCDI to the conventional P_{gc}, the gas cooler outlet pressure variation $\%P_{gc}$ is negative and increases with T_{ev}, so the HP of TSCDI is lower than the conventional cycle by less than 13% (Figure 1.14.f).
- By comparing the COP of TSCDI to the conventional COP, the COP variation $\%COP_{TSCDI}$ is positive and decreases with T_{ev}, so the TSCDI cycle improves the energy performance of the cycle by 27% at –15°C and by more than 10% at 15°C as T_{ev} (Figure 1.14.e).

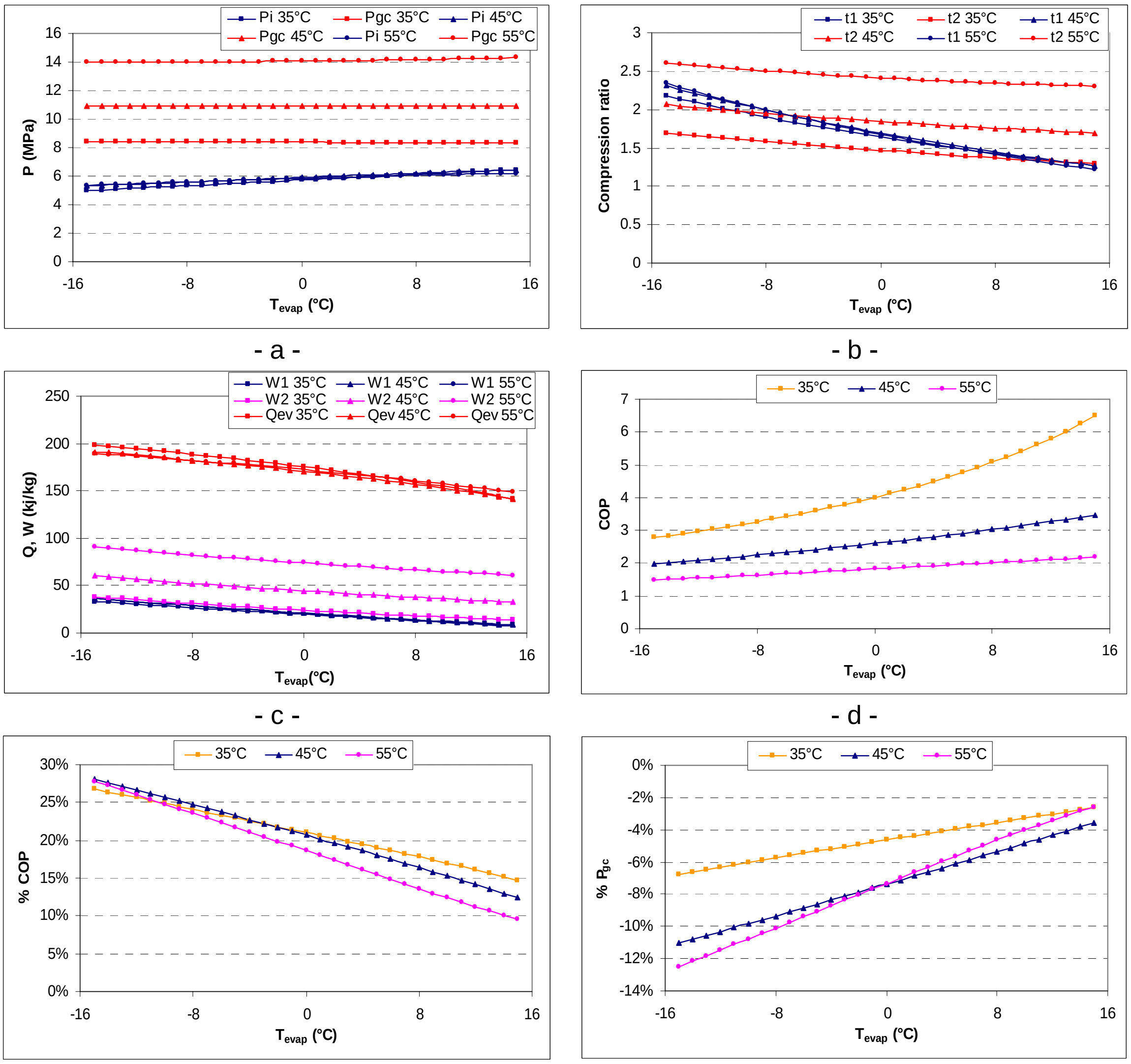

- a -

- b -

- c -

- d -

- e -

- f -

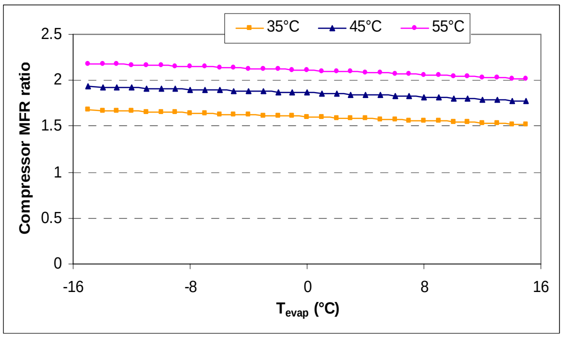

- g -

Figure 1.14: Variation of P_i, P_{gc}, CR, COP, COP and P_{gc} improvement, cooling capacity and compression work, and compressor mass flow rate ratio with evaporation temperature for TSCDI. (η_{comp} = 1 and T_{SH} = 5 K).

- **Variation of the outdoor temperature on the high pressure side**

Simulations conditions: expansion is isenthalpic, the evaporating temperature equals to t 0°C, the gas cooler/ condenser outlet temperature is varied and Figure 1.15 is drawn.

Results

In sub-critical operating conditions, T_{gc} < 31°C, the HP is the saturated pressure at T_{gc}, and the IP slightly increases with T_{gc} (Figure 1.15.a). As the gas cooler outlet temperature increases, the CR of the LP compressor (t1) is quasi-constant; on the other hand, the CR of the HP compressor (t2) is quasi-constant and close to the CR of the LP compressor, however the CR of the conventional cycle is larger than the two-CRs (Figure 1.15.b).

The cooling capacity decreases with T_{gc} because the evaporator inlet enthalpy increases with T_{gc} that increases the IP; also the cooling capacity of TSCDI cycle with isentropic expansion is larger than the conventional cycle in sub-critical cycle due to the low enthalpy at the evaporator inlet. The compression work of the HP (W2) and LP (W1) compressors are close and increase slightly with T_{gc}, at constant evaporating temperature, 0°C (Figure 1.15.c).

The mass flow rate MFR ratio between the HP compressor and the LP compressor increases with the increase of the gas cooler temperature T_{gc}, however, the MFR of HP compressor varies by 1.1 to 1.5 times the MFR of the LP compressor at 15 to 30°C as T_{gc} (Figure 1.15.e).

Comparison with the single stage CO_2 cycle

The gas cooler outlet pressure variation $\%P_{gc}$ is zero in sub-critical cycle (Figure 1.15.d).. By comparing the COP of TSCDI cycle to the conventional COP, the COP variation $\%COP_{TSCDI}$ is positive and increases with T_{gc}, so the TSCDI cycle improves the energy performance of the sub-critical cycle by 6% at T_{gc} = 15°C, and by 24% at T_{gc} = 30°C (Figure 1.15.d).

In trans-critical operating conditions, T_{gc} > 31°C, the HP increases with T_{gc} but the IP is quasi-constant with T_{gc} (Figure 1.15.a). As the gas cooler outlet temperature increases, the CR of the LP compressor (t1) is quasi-constant, but the CR of the HP compressor (t2) increases continuously, however the CR of the conventional cycle (tconv) increases continuously also and is larger than the two CRs (Figure 1.15.b).

The cooling capacity is quasi-constant with T_{gc}, but the cooling capacity of TSCDI cycle is larger than the conventional cycle due to the low enthalpy at the evaporator inlet. The compression work of the LP compressor (W1) is quasi-constant with T_{gc}, at constant evaporating temperature, 0°C, or the compression work of the HP compressor (W2) increases with T_{gc} and becomes larger than the conventional work for $T_{gc} > 51°C$ (Figure 1.15.c).

The mass flow rate MFR ratio between the HP compressor and the LP compressor increases with the increase of the gas cooler temperature T_{gc}, however, the MFR of HP compressor varies by 1.5 to 2.5 times the MFR of the LP compressor at 31 to 65°C as T_{gc} (Figure 1.15.e).

Comparison with the single stage CO_2 cycle

- By comparing the P_{gc} of TSCDI to the conventional P_{gc}, the gas cooler outlet pressure variation $\%P_{gc}$ is negative in trans-critical cycle and varies between –3% and -8% (Figure 1.15.d).
- By comparing the COP of TSCDI to the conventional COP, the COP variation $\%COP_{TSCDI}$ is positive and decreases with T_{gc} from 22 to 15% at 31°C to 65°C, so the TSCSDI cycle improves the energy performance of the trans-critical cycle, by more than 15% (Figure 1.15.d).

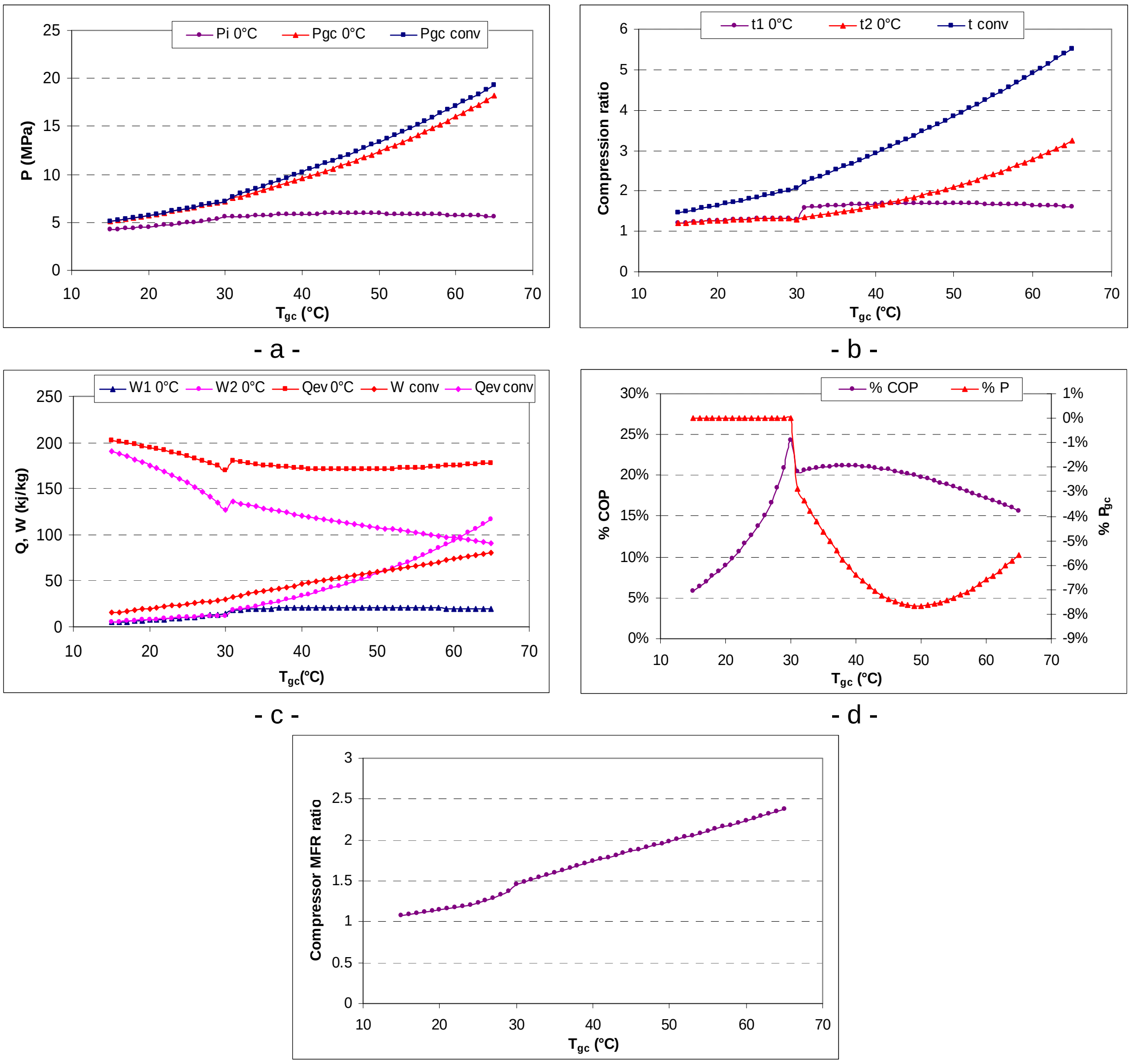

- a -

- b -

- c -

- d -

- e -

Figure 1.15: Variation of P_i, P_{gc}, CR, COP and P_{gc} improvement, cooling capacity and compression work, and compressor mass flow rate ratio with gas cooler outlet temperature for TSCDI at 0°C evaporation temperature, (η_{comp} = 1and T_{SH} = 5 K).

3.2 TSCDI with isentropic expansion

Figure 1.16 presents the lay-out (1.16.a) and the thermodynamic evolutions (1.16.b) in a T-S diagram of the two-stage compression cycle with direct injection TSCDI and isentropic expansion.

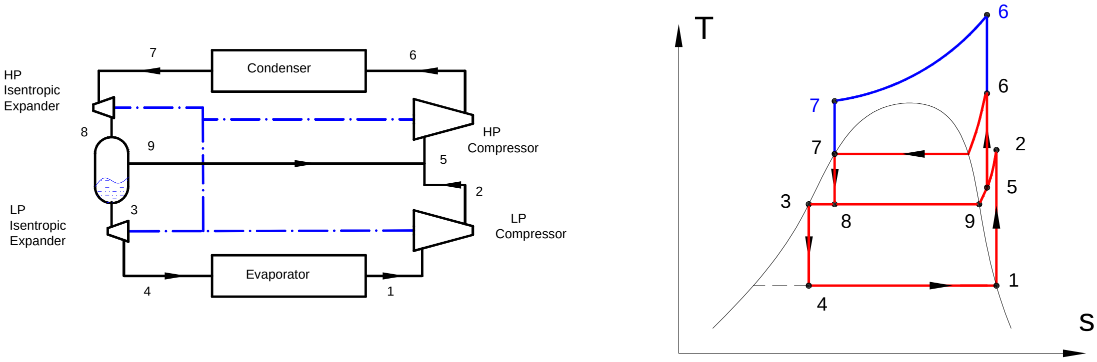

a. TSCDI with isentropic expansion.

b. T-S diagram of TSCDI with isentropic expansion.

Figure 1.16: Two-stage compression cycle with direct injection TSCDI and isentropic expansion.

- **Variations of the outdoor temperature at the high-pressure side**

Simulations conditions: expansion is isentropic, the gas cooler outlet temperature is set at different temperatures (35, 45, 55°C). The optimization of COP does not take into account the work generated by the turbine.

Results

The variation of the evaporating temperature shows that the high side optimum pressure is quasi-constant with the increase of the evaporation temperature but increases with T_{gc}; on the other hand, the intermediate optimum pressure slightly increases with the increase of the evaporating temperature, but it is quasi-constant with T_{gc} (Figure 1.17.a). As the evaporating temperature increases, the evaporating pressure increases that decrease the CR of the LP compressor (t1); on the other hand, the CR of the HP compressor (t2) decreases slightly with the evaporating temperature due to the increase of the IP (Figure 1.17.b).

The HP and the IP depend of the isentropic compression efficiency of the compressor and the isentropic expansion efficiency of the expander, and depend slightly on the pressure drop in the evaporator and the gas cooler.

The cooling capacity decreases with T_{ev} because the saturated vapor enthalpy decreases with T_{ev}, but is quasi-constant with T_{gc}. The compression works of the HP (W2) and the LP (W2) compressors decrease with T_{ev} at constant gas cooler outlet temperature (Figure 1.17.f).

The COP of TSCDI with isentropic expansion increases with T_{ev} as the temperature difference between the heat source and the heat sink decreases (Figure 1.17.d).

The mass flow rate MFR ratio between the HP compressor and the LP compressor decreases slightly with the increase of the evaporating temperature T_{ev} and increases with T_{gc}, however, the MFR of HP compressor is at least 1.5 times the MFR of the LP compressor (Figure 1.17.g).

By comparing the available generated work from the isentropic expansion to the required work of the two compressors, the variation of T_{ev} shows that the generated work is larger than the LP compression work for T_{gc} > 45°C and T_{ev} > -2°C, but for T_{gc} = 35°C the ratio is lower than one and varies with T_{ev} between 0.5 and 0.9; on the other hand, the variation of T_{ev} shows that the generated work is lower than the HP compression work, around 0.5 time at 35°C to 55°C as T_{gc}; however the work ratio is quasi-constant with the variation of T_{ev} (Figure 1.17.h).

Comparison with the single stage CO_2 cycle

- By comparing the P_{gc} of TSCDI with isentropic expansion to the conventional P_{gc}, the gas cooler outlet pressure variation %P_{gc} is negative and increases with T_{ev}, so the HP of TSCDI with isentropic expansion is lower than the conventional cycle by less than 16% (Figure 1.17.c).
- By comparing the COP of TSCDI with isentropic expansion to the conventional COP, the COP variation %$COP_{TSCDI\ is}$ is positive and is quasi-constant with T_{ev}, so the TSCDI with isentropic expansion cycle improves the energy performance of the cycle by 80% at 35°C, by 100% at 45°C and 130% at 55°C (Figure 1.17.e).

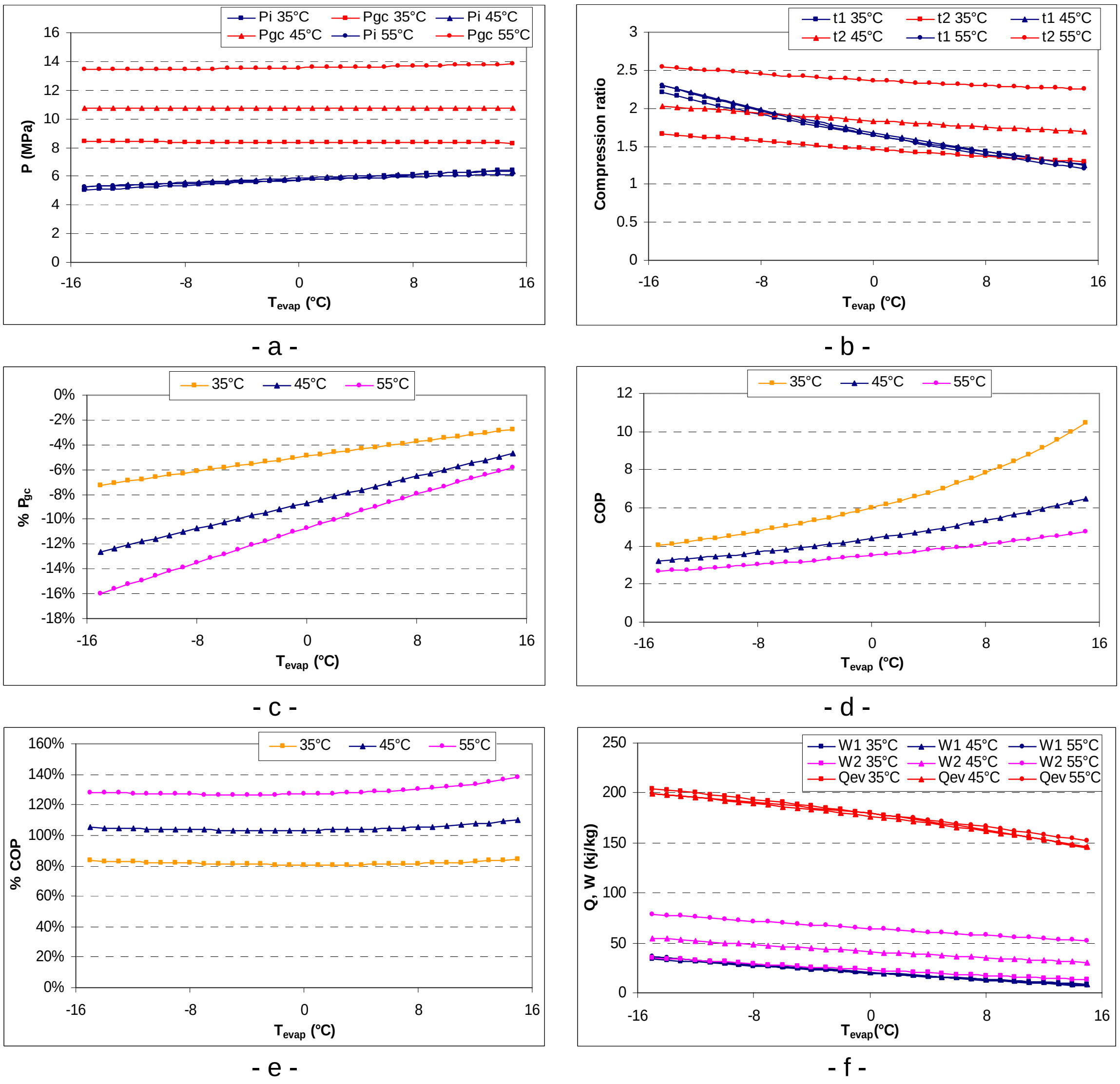

- a -

- b -

- c -

- d -

- e -

- f -

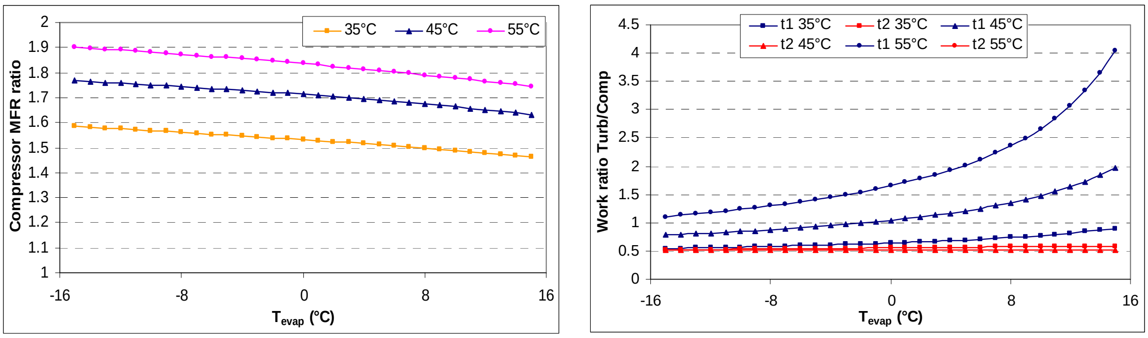

- g - - h -

Figure 1.17: Variation of P_i, P_{gc}, CR, COP, COP and P_{gc} improvement, cooling capacity and compression work, compressor mass flow rate ratio and turbine work to compression work ratio with evaporation temperature for TSCDI
(isentropic expansion. $\eta_{comp} = 1$ and $\eta_{turbine} = 1$).

- **Variation of outdoor temperatures on the high pressure side**

Simulations conditions: expansion is isentropic, 0°C evaporating temperature, the gas cooler/ condenser outlet temperature is varied and Figure 1.18 is drawn.

Results

In sub-critical operating conditions, T_{gc} < 31°C, the HP is the saturated pressure at T_{gc}, and the IP increases slightly with T_{gc} (Figure 1.18.a). As the gas cooler outlet temperature increases, the CR of the LP compressor (t1) is quasi-constant; as well as CR of the HP compressor (t2) The CR of the conventional cycle (tconv) is larger than the two-CRs (Figure 1.18.b).

The cooling capacity decreases with T_{gc} because the evaporator inlet enthalpy increases with T_{gc}, also the cooling capacity of TSCDI with isentropic expansion cycle is larger than the conventional cycle in sub-critical cycle due to the low enthalpy of the evaporator inlet and the work generation. The compression work of the HP and LP compressors increase slightly with T_{gc}, and are almost equal (Figure 1.18.c).

The mass flow rate MFR ratio between the HP compressor and the LP compressor increases with the increase of the gas cooler temperature T_{gc}, however, the MFR of HP compressor varies by 1.1 to 1.5 times the MFR of the LP compressor at 15 to 30°C as T_{gc} (Figure 1.18.e).

By comparing the available generated work from the isentropic expansion to the required work of the two compressors, the variation of T_{gc} shows that the generated work, compared to the LP and the HP compression works, is lower than 0.5, however the work ratio slightly increases with the variation of T_{gc} (Figure 1.18.f).

Comparison with the single stage CO_2 cycle

- The gas cooler outlet pressure variation %P_{gc} is zero in sub-critical cycle (Figure 1.18.d).
- By comparing the COP of TSCDI with isentropic expansion to the conventional COP, the COP variation %$COP_{TSCDI\ is}$ is positive and increases with T_{gc}, so the TSCII $_{is}$ cycle improves the energy performance of the sub-critical cycle, by 25% at T_{gc} = 15°C, and by 80% at T_{gc} = 30°C (Figure 1.18.d).

In trans-critical operating conditions, T_{gc} > 31°C, the HP increases with T_{gc} but the IP is quasi-constant with T_{gc} (Figure 1.18.a). As the gas cooler outlet temperature increases, the CR of the LP compressor (t1) is quasi-constant, but the CR of the HP compressor (t2) continuously increases, however the CR of the conventional cycle (tconv) increases also and is higher than the two CRs (Figure 1.18.b).

The cooling capacity is quasi-constant with T_{gc}, but the cooling capacity of TSCDI$_{is}$ cycle is larger than the conventional cycle due to the low enthalpy at the evaporator inlet. The compression work of the LP compressor (W1) is quasi-constant with T_{gc}, and the compression work of the HP compressor (W2) increases with T_{gc} and becomes larger than the conventional work for T_{gc} > 55°C (Figure 1.18.c).

The mass flow rate MFR ratio between the HP compressor and the LP compressor increases with the increase of the gas cooler temperature T_{gc}, however, the MFR of HP compressor vary by 1.5 to 2 times the MFR of the LP compressor at 31 to 65°C as T_{gc} (Figure 1.18.e).

By comparing the available generated work from the isentropic expansion to the required work of the two compressors, the variation of T_{gc} shows that the generated work, compared to the LP compression work, varies from 0.5 at 31°C, becomes 1 around 45°C, than increases significantly to 2.5 at 65°C; on the other hand, the variation of T_{gc} shows that the generated work is lower than the HP compression work, around 0.5 time; however the work ratio (t2) is quasi-constant with the variation of T_{gc} (Figure 1.18.f).

Comparison with the single stage CO_2 cycle

- By comparing the P_{gc} of TSCDI$_{is}$ to the conventional P_{gc}, the gas cooler outlet pressure variation %P_{gc} is negative in trans-critical cycle and decreases from –3% to -12% at 31°C to 65°C (Figure 1.18.d).
- By comparing the COP of TSCDI$_{is}$ to the conventional COP, the COP variation %COP$_{TSCIIis}$ is positive and increases with T_{gc} from 75 to 160% at 31°C to 65°C, so the TSCSDI$_{is}$ cycle improves the energy performance of the trans-critical cycle by more than 75% (Figure 1.18.d).

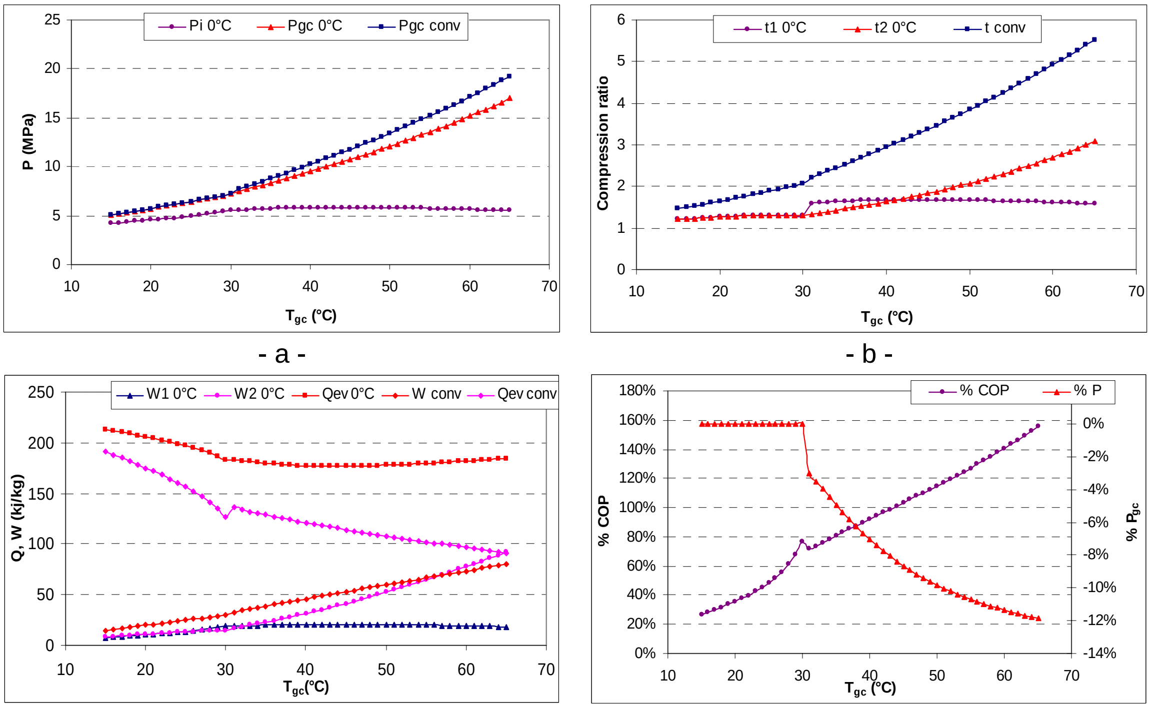

- a -

- b -

- c -

- d -

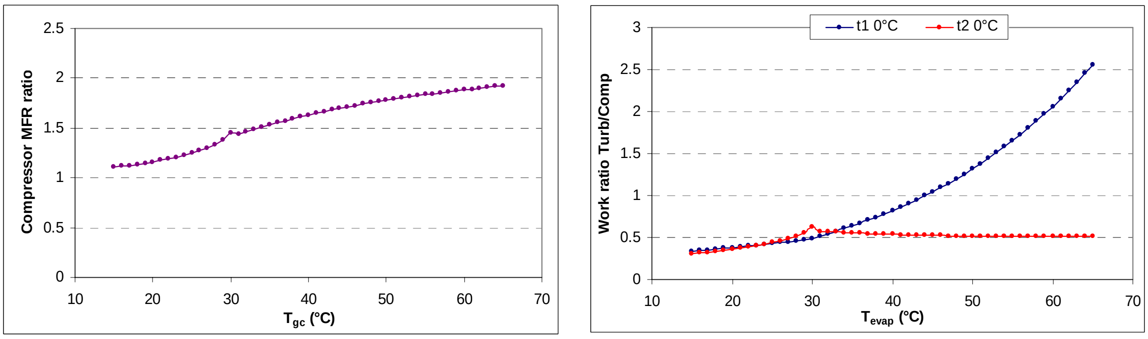

- e - - f -

Figure 1.18: Variation of P_i, P_{gc}, CR, COP and P_{gc} improvement, cooling capacity and compression work, and compressor mass flow rate ratio and turbine work to compression work ratio with gas cooler outlet temperature for TSCDI with isentropic expansion at 0°C evaporation temperature ($\eta_{comp} = 1$, $\eta_{turbine} = 1$ and $T_{SH} = 5$ K).

4. Two-stage compression with economizer TSCE

The two-stage compression cycle with economizer, showed in Figure1.19, is composed of an evaporator, a LP compressor, a two-phase separator, a HP compressor, two gas coolers and a throttling device (valve or turbine). An internal heat exchanger could be installed between the suction line of the HP compressor and the gas cooler outlet line, and between the suction line of the LP compressor and the separator liquid outlet line or the gas cooler outlet line. The inlet of the compressors is saturated vapor coming from the separator or the evaporator. The separator outlets are saturated liquid and saturated vapor.

Since there are two gas coolers, so in transcritical refrigeration cycle, there is two possibilities to connect them to the separator: even considering a common HP side for the two compressors, or considering each gas cooler separated from the other and then each gas cooler has its HP. Calculations show that in the two cases, same energy performances are achieved but at different HPs, so in this study, the outlet of the gas coolers are connected and the two compressors have the same HP.

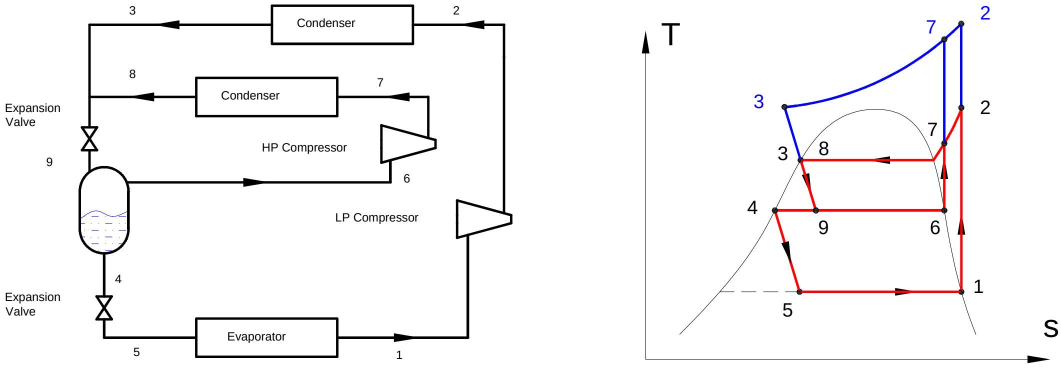

a. TSCE cycle b. T-S diagram of TSCE

Figure 1.19: Two-stage refrigeration compression cycle with economizer TSCE.

4.1 TSCE with isenthalpic expansion

- **Variation of the evaporating temperatures on the low-pressure side**

Simulations conditions: expansion is isenthalpic, the gas cooler outlet temperature is set at different temperatures (35, 45, 55°C).

Results

The variation of the evaporating temperature shows that the optimum HP is quasi-constant with the increase of the evaporation temperature but increases with T_{gc}; on the other hand, the optimum IP increases with the increase of the evaporating temperature but is quasi-constant with T_{gc} (Figure 1.20.a). As the evaporating temperature increases, the evaporating pressure increases that decrease the CR of the LP compressor (t1) but (t1) increases with T_{gc}; on the other hand, the CR of the HP compressor (t2) is quasi-constant with the evaporating temperature due to the slightly increase of the IP, in addition t_2 is increases with T_{gc} (Figure 1.20.b).

The HP and the IP are independent of the isentropic compression efficiency of the compressor, and depend slightly on the pressure drop in the evaporator and the gas cooler.

The cooling capacity decreases with T_{ev} because the saturated vapor enthalpy decreases with T_{ev}, but it is quasi-constant with T_{gc}. The compression works of the HP (W2) and LP (W1) compressors decrease with T_{ev} at constant gas cooler outlet temperature, and increase with T_{gc} (Figure 1.20.c).

The COP of TSCE increases with T_{ev} as the temperature difference between the heat source and the heat sink decreases (Figure 1.20.d).

The mass flow rate MFR ratio between the HP compressor and the LP compressor decreases with the increase of the evaporating temperature T_{ev} but increases with T_{gc}, however, the MFR of HP compressor is at least 0.4 times the MFR of the LP compressor at 35°C as T_{gc}, and lower than 1.2 at 55°C as T_{gc}. The MFR ratio depends on the quality inlet of the separator that depends of T_{gc} and P_{gc} (Figure 1.20.g).

Comparison with the one stage CO_2 cycle

- By comparing the P_{gc} of TSCE to the conventional P_{gc}, the gas cooler outlet pressure variation %P_{gc} is negative and increases with T_{ev}, so the HP of TSCE is lower than the conventional cycle by less than 12% (Figure 1.20.f).
- By comparing the COP of TSCE to the conventional COP, the COP variation %COP_{TSCE} is positive and decreases with T_{ev}, so the TSCE cycle improves the energy performance of the cycle by 25% at –15°C and by more than 2 % at 15°C as T_{ev} (Figure 1.20.e).

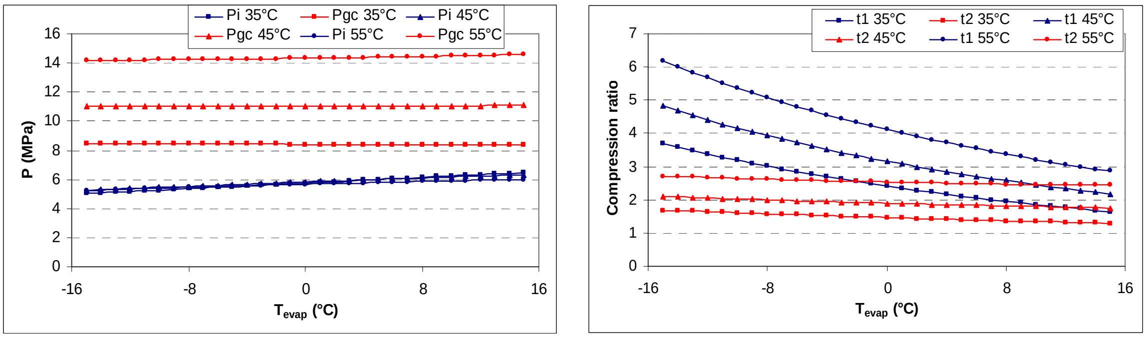

- a - - b -

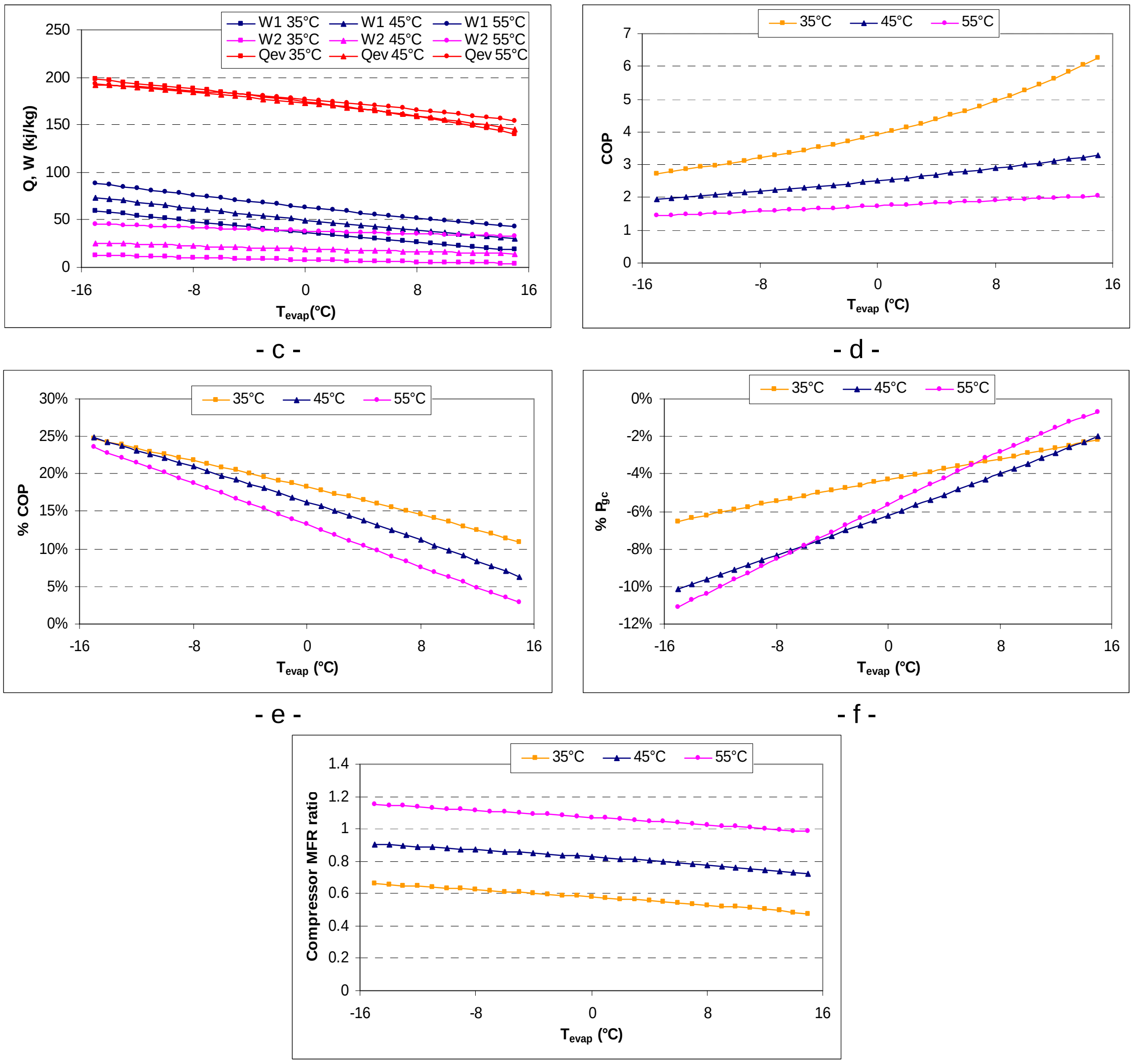

- c -

- d -

- e -

- f -

- g -

Figure 1.20: Variation of P_i, P_{gc}, CR, COP, COP and P_{gc} improvement, cooling capacity and compression work, and compressor mass flow rate ratio with evaporation temperature for TSCE. (η_{comp} = 1and T_{SH} = 5 K)

.

- **Variation of outdoor temperature on the high-pressure side**

Simulation conditions: expansion is isenthalpic, evaporating temperature = 0°C, the gas cooler/ condenser outlet temperature is varied.

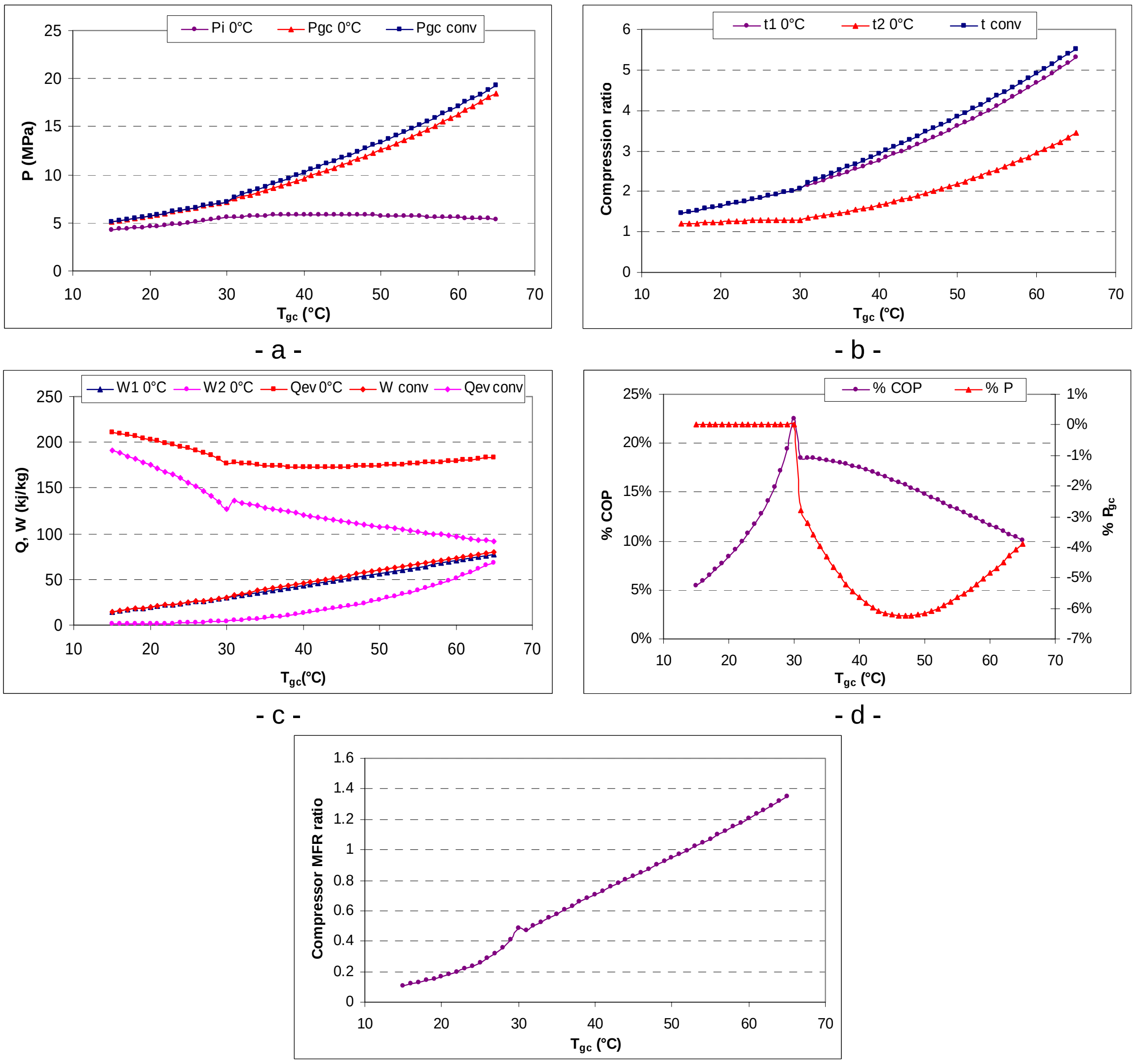

- a -

- b -

- c -

- d -

- e -

Figure 1.21: Variation of P_i, P_{gc}, CR, COP and P_{gc} improvement, cooling capacity and compression work, and compressor mass flow rate ratio with gas cooler outlet temperature for TSCE at 0°C evaporation temperature, (η_{comp} = 1and T_{SH} = 5 K).

Results

In sub-critical operating conditions, T_{gc} < 31°C, the HP is the saturated pressure at T_{gc}, and the IP slightly increases with T_{gc} (Figure 1.21.a). As the gas cooler outlet temperature increases, the CR of the LP compressor (t1) increases; on the other hand, the CR of the HP compressor (t2) is quasi-constant, however the CR of the conventional cycle (tconv) is equal to (t1) and larger than t2 (Figure 1.21.b).

The cooling capacity decreases with T_{gc} because the evaporator inlet enthalpy increases with T_{gc} that increases the IP; also the cooling capacity of TSCE cycle with isenthalpic expansion is larger than the conventional cycle in sub-critical cycle due to the low enthalpy of the evaporator inlet. The compression work of the LP compressor (W1) increases with T_{gc}, at constant evaporating temperature, 0°C, but the work of the HP compressor (W2) is very small lower than 10 kJ/kg (Figure 1.21.c).

The mass flow rate MFR ratio between the HP compressor and the LP compressor increases with the increase of the gas cooler temperature T_{gc}, however, the MFR of HP compressor vary from 0.1 to 0.5 times the MFR of the LP compressor at 15 to 30°C as T_{gc} (Figure 1.21.e).

Comparison with the one stage CO_2 cycle

- The gas cooler outlet pressure variation $\%P_{gc}$ is zero in sub-critical cycle (Figure 1.21.d).
- By comparing the COP of TSCE cycle to the conventional COP, the COP variation $\%COP_{TSCE}$ is positive and increases with T_{gc}, so the TSCE cycle with isenthalpic expansion improves the energy performance of the sub-critical cycle by 6% at T_{gc} = 15°C, and by 22% at T_{gc} = 30°C (Figure 1.21.d).

In trans-critical operating conditions, T_{gc} > 31°C, the HP increases with T_{gc} but the IP is quasi-constant with T_{gc} (Figure 1.21.a). As the gas cooler outlet temperature increases, the CR of the LP (t1) and HP (t2) compressors continuously increase, however the CR of the conventional cycle continuously increases and is larger than the two CRs (Figure 1.21.b).

The cooling capacity is quasi-constant with T_{gc}, but the cooling capacity of TSCE cycle is larger than the conventional cycle due to the low enthalpy of the evaporator inlet. The compression work of the LP compressor (W1) is close to the conventional cycle work and increases with T_{gc}, or the compression work of the HP compressor (W2) increases with T_{gc} and is close to the conventional work at 65°C as T_{gc} (Figure 1.21.c).

The mass flow rate MFR ratio between the HP compressor and the LP compressor increases with the increase of the gas cooler temperature T_{gc}, however, the MFR of HP compressor is 0.5 at 31°C as T_{gc}, becomes 1 at 52°C, then it achieves 1.4 for T_{gc} higher than 65°C (Figure 1.21.e).

Comparison with the one stage CO_2 cycle

- By comparing the P_{gc} of TSCE to the conventional P_{gc}, the gas cooler outlet pressure variation $\%P_{gc}$ is negative in trans-critical cycle and vary between –2% and -7% (Figure 1.21.d).
- By comparing the COP of TSCE to the conventional COP, the COP variation $\%COP_{TSCE}$ is positive and decreases with T_{gc} from 18 to 10% at 31°C to 65°C, so the TSCE cycle improves the energy performance of the trans-critical cycle, by more than 10% (Figure 1.21.d)..

4.2 TSCE with isentropic expansion

Figure 1.22 presents the lay-out (1.22.a) and the thermodynamic evolutions (1.22.b) in a T-S diagram of the two-stage compression cycle with economizer TSCE and isentropic expansion.

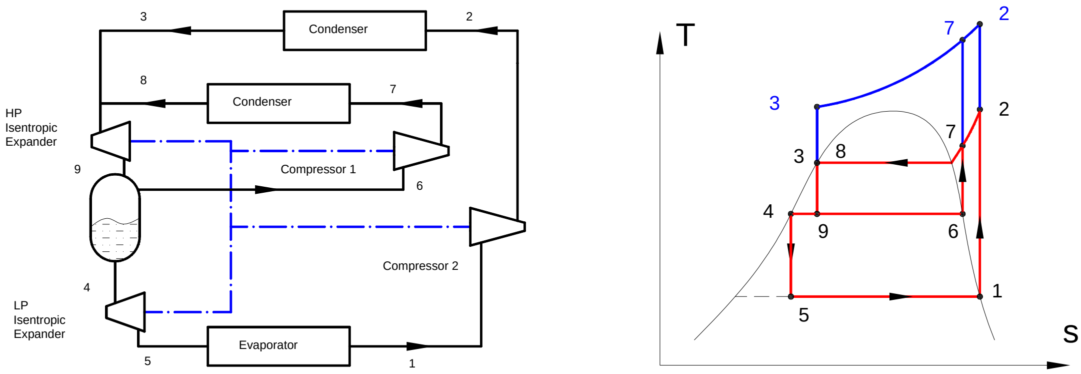

a. TSCE with isentropic expansion

b. T-S diagram of TSCE with isentropic expansion

Figure 1.22: Two-stage compression cycle with economizer TSCE and isentropic expansion.

- **Variation of the evaporating temperatures on the low pressure side**

Simulation conditions: expansion is isentropic and by fixing the gas cooler outlet temperature at different temperature (35, 45, 55°C). The optimization of COP takes in account the work generated by the turbine.

Results

The variation of the evaporating temperature shows that the optimum HP is quasi-constant with the increase of the evaporation temperature but increases with T_{gc}; on the other hand, the optimum IP slightly increases with the increase of the evaporating temperature and with T_{gc} (Figure 1.23.a). As the evaporating temperature increases, the evaporating pressure increases that decrease the CR of the LP compressor (t1); on the other hand, the CR of the HP compressor (t2) is quasi-constant with the evaporating temperature (Figure 1.23.b).

The HP and the IP depend on the isentropic expansion efficiency of the expander, and depend slightly on the pressure drop in the evaporator and the gas cooler.

The cooling capacity decreases with T_{ev} because the saturated vapor enthalpy decreases with T_{ev}, but it increases with T_{gc}. The compression works of the HP (W2) and the LP (W1) compressors decrease with T_{ev} at constant gas cooler outlet temperature (Figure 1.23.c).

The COP of TSCE with isentropic expansion increases with T_{ev} as the temperature difference between the heat source and the heat sink decreases (Figure 1.23.d).

The mass flow rate MFR ratio between the HP compressor and the LP compressor decreases slightly with the increase of the evaporating temperature T_{ev} and increases with T_{gc}, however, the MFR of HP compressor is lower than 1 for 35°C as T_{gc}, and it is superior to 1 for T_{gc} higher than 45°C (Figure 1.23.g).

By comparing the available generated work from the isentropic expansion to the required work of the two compressors, the variation of T_{ev} shows that the generated work is larger than the LP compression work for T_{gc} = 50°C, but for T_{gc} lower than 50°C the ratio is lower than one and it is around 0.4 for T_{gc} = 35°C, and it varies with T_{ev} between 0.6 and 1 for

T_{gc} = 45°C; on the other hand, the comparison with HP compression work shows that the turbine work is quasi-constant with T_{ev} and decreases with T_{gc}, in addition it is lower than the HP compression work for T_{gc} higher than 45°C, for T_{gc} = 35°c, the ratio is around 1.55 (Figure 1.23.h).

Comparison with the one stage CO_2 cycle

- By comparing the P_{gc} of TSCE with isentropic expansion to the conventional P_{gc}, the gas cooler outlet pressure variation $\%P_{gc}$ is negative and increases with T_{ev}, so the HP of TSCE with isentropic expansion is lower than the conventional cycle from 6% to 35% (Figure 1.23.f).
- By comparing the COP of TSCE with isentropic expansion to the conventional COP, the COP variation $\%COP_{TSCEis}$ is positive and is quasi-constant with T_{ev}, so the TSCE with isentropic expansion cycle improves the energy performance of the cycle by 80% at 35°C, by 100% at 45°C and 130% at 55°C (Figure 1.23.e).

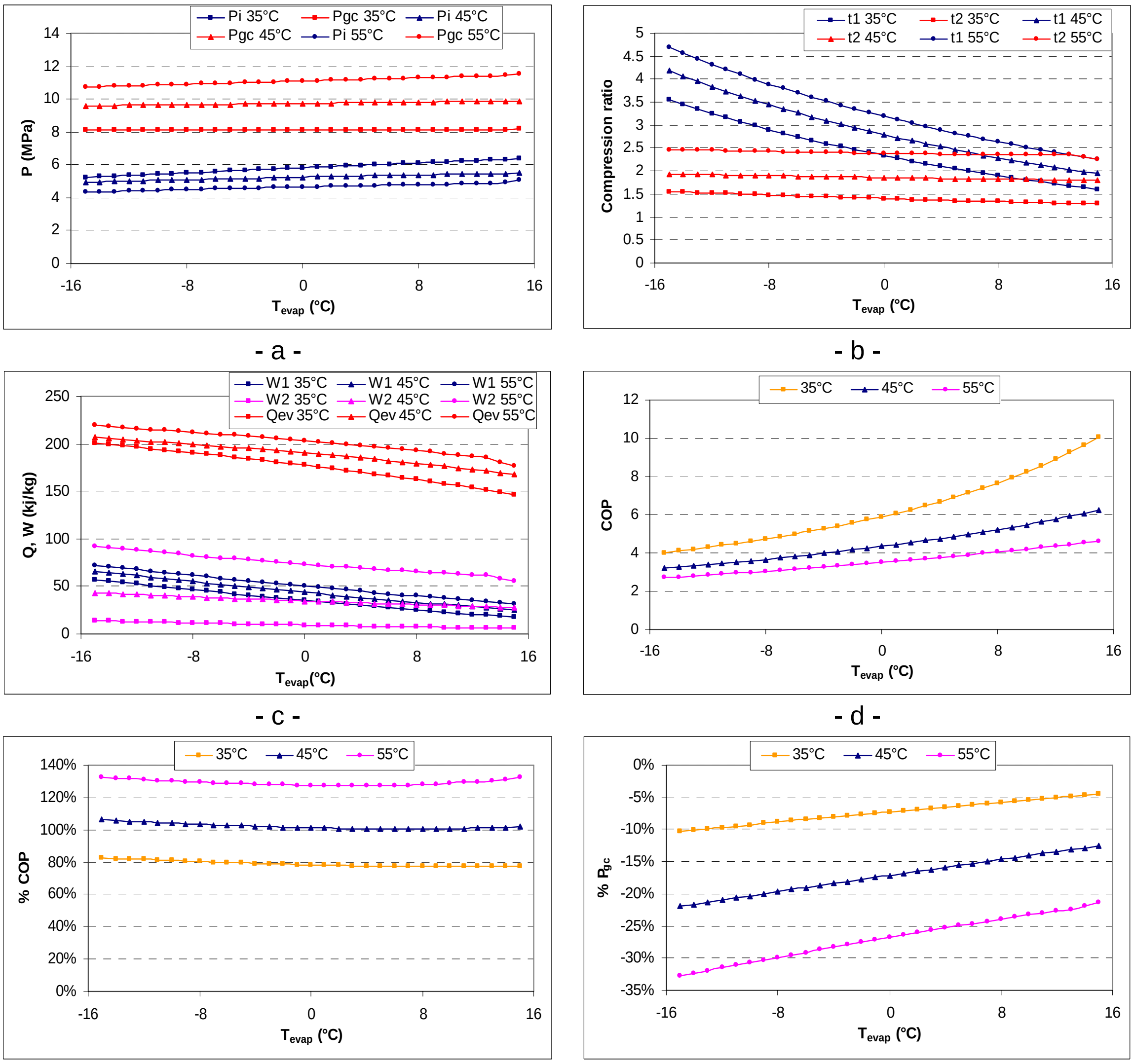

- a -

- b -

- c -

- d -

- e -

- f -

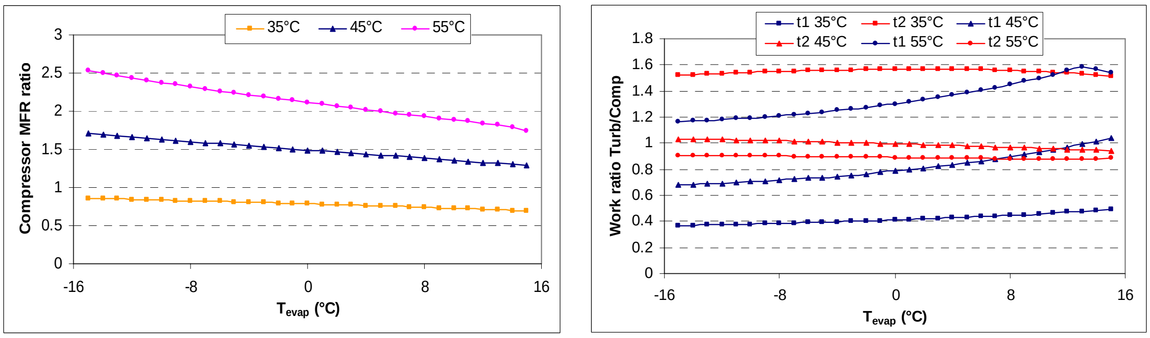

- g - - h -

Figure 1.23: Variation of P_i, P_{gc}, CR, COP, COP and P_{gc} improvement, cooling capacity and compression work, compressor mass flow rate ratio and turbine work to compression work ratio with evaporation temperature for TSCE with isentropic expansion.
$\eta_{comp} = 1$, $\eta_{turbine} = 1$ and $T_{SH} = 5$ K.

- **Variation of outdoor temperatures on the high pressure side**

Simulation conditions: expansion is isentropic, evaporating temperature = 0°C, the gas cooler/ condenser outlet temperature is varied.

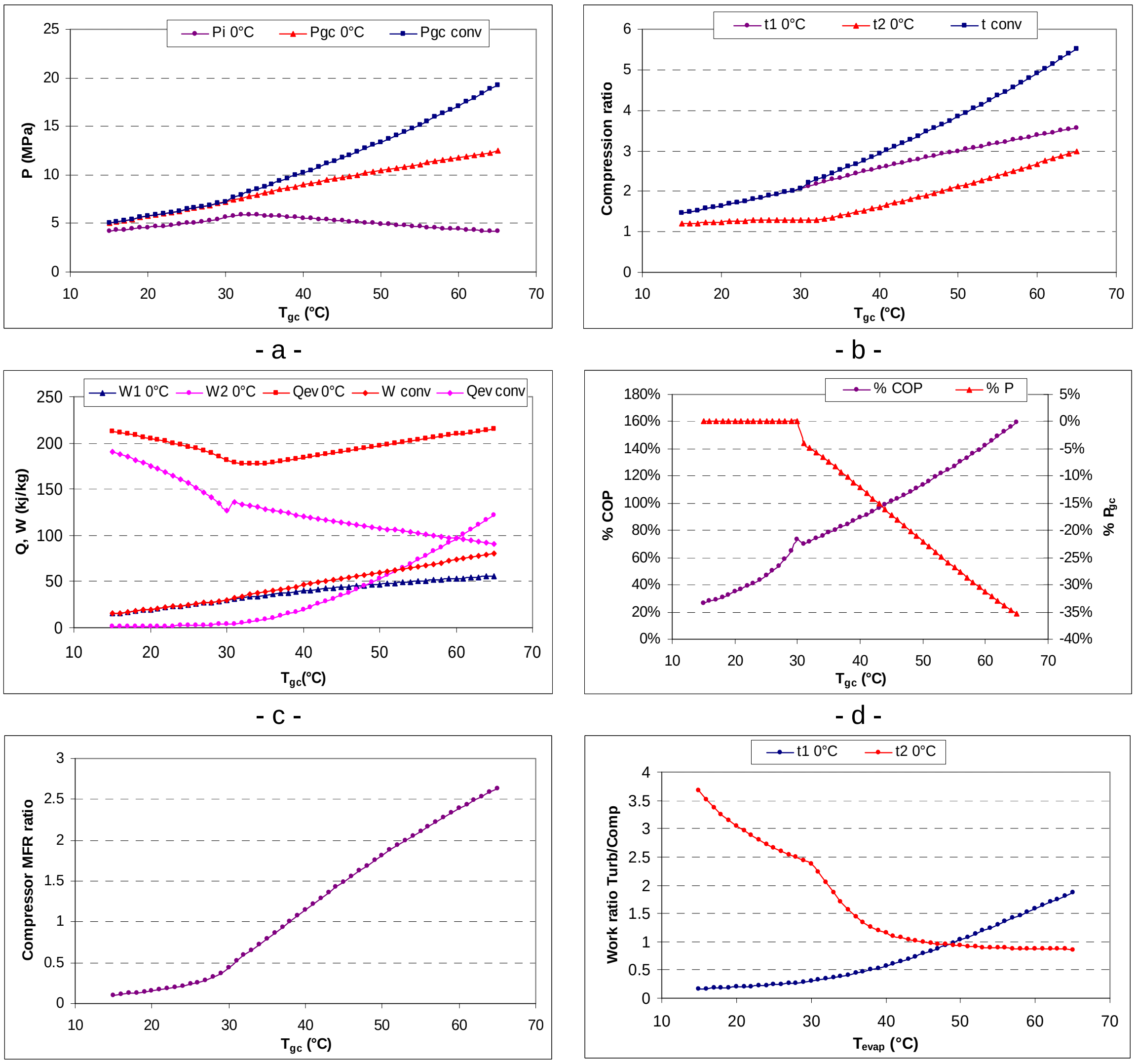

- a - - b -

- c - - d -

- e - - f -

Figure 1.24: Variation of P_i, P_{gc}, CR, COP and P_{gc}, cooling capacity and compression work, and compressor mass flow rate ratio and turbine work to compression work ratio with gas cooler outlet temperature for TSCE with isentropic expansion at 0°C as evaporation temperature $\eta_{comp} = 1$, $\eta_{turbine} = 1$ and $T_{SH} = 5$ K.

Results

In sub-critical operating conditions, T_{gc} < 31°C, the HP is the saturated pressure at T_{gc}, and the IP increases with T_{gc} (Figure 1.24.a). As the gas cooler outlet temperature increases, the CR of the LP compressor (t1) increases and it is close to the conventional CR (tconv); on the other hand, the CR of the HP compressor (t2) is quasi-constant, however the CR of the conventional cycle (tconv) is larger than the two-CRs (Figure 1.24.b).

The cooling capacity decreases with T_{gc} because the evaporator inlet enthalpy increases with T_{gc}, also the cooling capacity of TSCE with isentropic expansion cycle is larger than the conventional cycle in sub-critical cycle due to the low enthalpy of the evaporator inlet and the work generation. The LP compression work (W1) increases with T_{gc}, at constant evaporating temperature, 0°C, and is almost equal to the conventional work, but the HP compression work (W2) is very small lower than 10 kJ/kg (Figure 1.24.c).

The mass flow rate MFR ratio between the HP compressor and the LP compressor increases with the increase of the gas cooler temperature T_{gc}, however, the MFR of HP compressor varies from 0.1 to 0.5 at 15 to 30°C as T_{gc} (Figure 1.24.e).

By comparing the available generated work from the isentropic expansion to the required work of the two compressors, the variation of T_{gc} shows that the generated work, compared to the LP compression work, slightly increases and is lower than 0.4, on the other hand, the generated work, compared to the HP compression work, decreases with T_{gc} from 3.5 at 15°C to 2.5 at 30°C (Figure 1.24.f).

Comparison with the one stage CO_2 cycle

- The gas cooler outlet pressure variation $\%P_{gc}$ is zero in sub-critical cycle (Figure 1.24.d).
- By comparing the COP of TSCE with isentropic expansion to the conventional COP, the COP variation $\%COP_{TSCE\ is}$ is positive and increases with T_{gc}, so the TSCE $_{is}$ cycle improves the energy performance of the sub-critical cycle, by 25% at T_{gc} = 15°C, and by 75% at T_{gc} = 30°C (Figure 1.24.d).

In trans-critical operating conditions, T_{gc} > 31°C, the HP increases with T_{gc} but the IP slightly decreases with T_{gc} (Figure 1.24.a). As the gas cooler outlet temperature increases, the CR of the LP (t1) and the HP (t2) compressors increase, however the CR of the conventional cycle (tconv) continuously increases and is larger than the two CRs (Figure 1.24.b).

The cooling capacity increases with T_{gc}, but the cooling capacity of $TSCE_{is}$ cycle is larger than the conventional cycle due to the low enthalpy of the evaporator inlet. The compression work of the LP compressor (W1) increases with T_{gc}, the compression work of the HP compressor (W2) increases with T_{gc} and becomes larger than the conventional work for T_{gc} > 52°C (Figure 1.24.c).

The mass flow rate MFR ratio between the HP compressor and the LP compressor increases with the increase of the gas cooler temperature T_{gc}, however, the MFR of HP compressor varies from 0.5 to 2.6 times the MFR of the LP compressor at 31 to 65°C as T_{gc} (Figure 1.24.e).

By comparing the available generated work from the isentropic expansion to the required work of the two compressors, the variation of T_{gc} shows that the generated work, compared to the LP compression work (t1), varies from 0.4 at 31°C, becomes 1 around 48°C, then increases to 1.9 at 65°C; on the other hand, the variation of T_{gc} shows that the generated work, compared to the HP compression work (t2), decreases with T_{gc} from 2.5 at 31°C as T_{gc}, then becomes lower than one around 48°C and achieves 0.9 at 65°C (Figure 1.24.f).

Comparison with the one stage CO_2 cycle

- By comparing the P_{gc} of $TSCE_{is}$ to the conventional P_{gc}, the gas cooler outlet pressure variation $\%P_{gc}$ is negative in trans-critical cycle and decreases from –5% to -35% at 31°C to 65°C (Figure 1.24.d).
- By comparing the COP of $TSCE_{is}$ to the conventional COP, the COP variation $\%COP_{TSCEis}$ is positive and increases with T_{gc} from 75 to 160% at 31°C to 65°C, so the $TSCE_{is}$ cycle improves the energy performance of the trans-critical cycle by more than 75% (Figure 1.24.d).

4.3 TSCE with Internal Heat exchanger IHX

Another refrigeration cycle with economizer could be used to improve the performance of the conventional cycle. Two compressors, a gas cooler, an evaporator, an internal heat exchanger and a throttle device compose this cycle, shown in Figure 1.25.

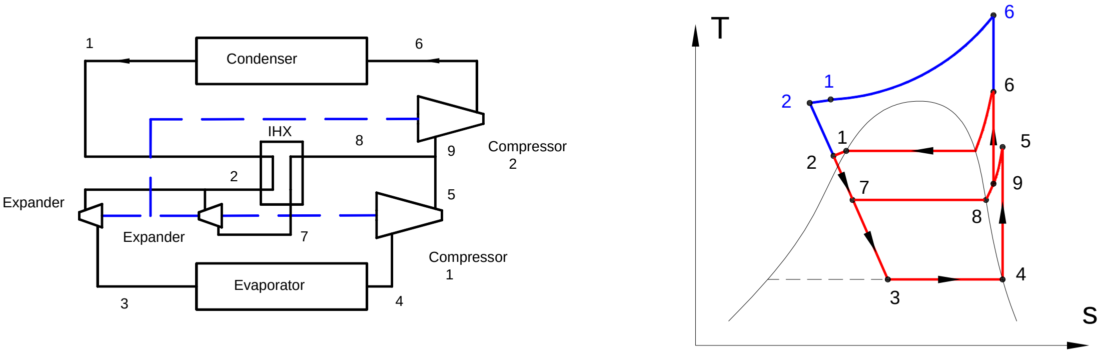

a. Second TSCE with isentropic expansion.

b. T-S diagram of the second TSCE with isentropic expansion.

Figure 1.25: Second economizer refrigeration cycle.

Simulation conditions: the IHX efficiency is the ratio between the temperature difference of the HP and its maximal value.

Results

The improvement given by the second economizer reaches more than 20% the COP of the conventional cycle with isenthalpic expansion, and more than 80% with an isentropic expansion (Figure 1.26.b).

The comparison between the second economizer refrigeration cycle with the indirect injection cycle shows that the first one is better with isenthalpic expansion (Figure 1.26.b), whereas the injection cycle is better with isentropic expansion for an ideal internal heat exchanger ($\eta_{IHX} = 1$).

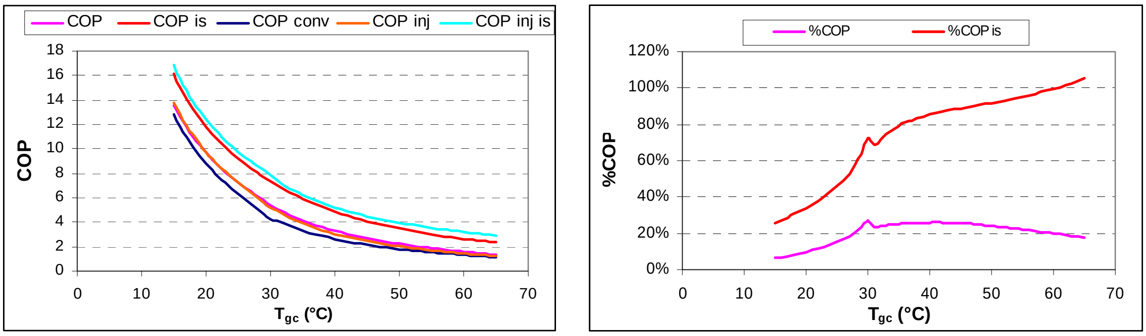

a. COP comparison

b. COP improvement

Figure 1.26: Comparison of the second economizer cycle with the conventional and the indirect injection refrigeration cycle, with variation of T_{gc} for $T_{ev} = 0°C$, $\eta_{comp} = 1$, $\eta_{IHX} = 1$, $T_{SH} = 5$ K and $\eta_{turb} = 1$.

5. Cooling of the compressor

Since the high discharge compressor temperature increases the exergy numbers of the gas cooler and the compression work, so by limiting this temperature, the performance of the cycle is improved. To limit the discharge temperature of the compressor, an external cold source should be used to absorb the energy generated by the compression work. Therefore, the compression is done in two stages: the poly-tropic compression from the evaporator pressure to an IP, and the cooled compression from the IP to the HP. The intermediate temperature varies between the gas cooler outlet temperature and the conventional compressor discharge temperature with poly-tropic compression. In this study, two intermediate temperatures are considered: the gas cooler outlet temperature and the gas cooler outlet temperature plus 15 K.

In the poly-tropic compression stage, the work is calculated in the same way as the conventional cycle; or in the cooled compression, the work is calculated by:

$$w_{isothermal} = \int_{P_{int}}^{P_{gc}} v\,dP = \sum_{i=1}^{100} \frac{2}{\frac{1}{v_i} + \frac{1}{v_{i-1}}} \Delta P$$

$$\Delta P = \frac{(P_{gc} - P_{int})}{100}$$

$$v_i = f(T_{int}, P_{int} + i\,\Delta P)$$

The refrigeration compression cycle with compressor cooling RCC, shown in Figure1.27, is composed of: an evaporator, a cooled-compressor, a gas cooler and a throttling device (valve or turbine). An internal heat exchanger could be installed between the suction line of the compressor and the gas cooler outlet line.

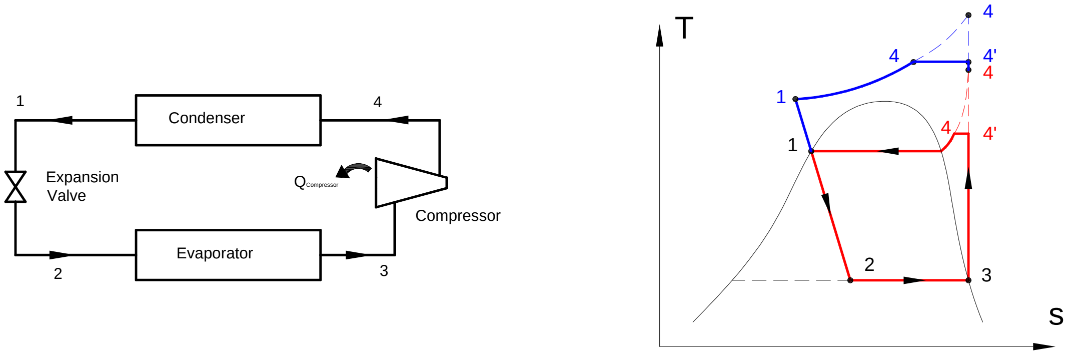

a. RCC scheme. b. T-S diagram of RCC.

Figure 1.27: Refrigeration compression cycle with compressor cooling RCC.

5.1 RCC and isenthalpic expansion

- **Variation of the evaporating temperatures on the low-pressure side**

Simulation conditions: expansion is isenthalpic, the gas cooler outlet temperature is set at three different temperatures (35, 45, 55°C).

Results

The variation of the evaporating temperature shows that the optimum HP decreases with the increase of the evaporation temperature; on the other hand, the optimum IP increases with T_{ev} (Figure 1.28.a). As the evaporating temperature increases, the evaporating pressure increases and so the CR of the poly-tropic compression (t1) decreases; also the

CR of the cooled compression (t2) decreases with the evaporating temperature, on the other hand, the CR increases with T_{gc} (Figure 1.28.b).

The HP and the IP depend strongly on the isentropic compression efficiency of the compressor, but depend slightly on the pressure drop in the evaporator and the gas cooler.

The cooling capacity decreases with T_{ev} and with T_{gc}. Also, the compression work of the poly-tropic compression (W1) and the cooled compression (W2) decrease with T_{ev} at constant gas cooler outlet temperature, but they increase with T_{gc} (Figure 1.28.c).

The COP of RCC increases with T_{ev} as the temperature difference between the heat source and the heat sink decreases (Figure 1.28.d).

Comparison with the one stage CO_2 cycle

- By comparing the P_{gc} of RCC to the conventional P_{gc}, the gas cooler outlet pressure variation $\%P_{gc}$ is positive and decreases with T_{ev}, so the HP of RCC is larger than the conventional cycle (Figure 1.28.f).
- By comparing the COP of RCC to the conventional COP, the COP variation $\%COP_{RCC}$ is positive and slightly decreases with T_{ev}, so the RCC cycle improves the energy performance of the cycle by more than 25% at T_{gc} higher than 35°C (Figure 1.28.e).

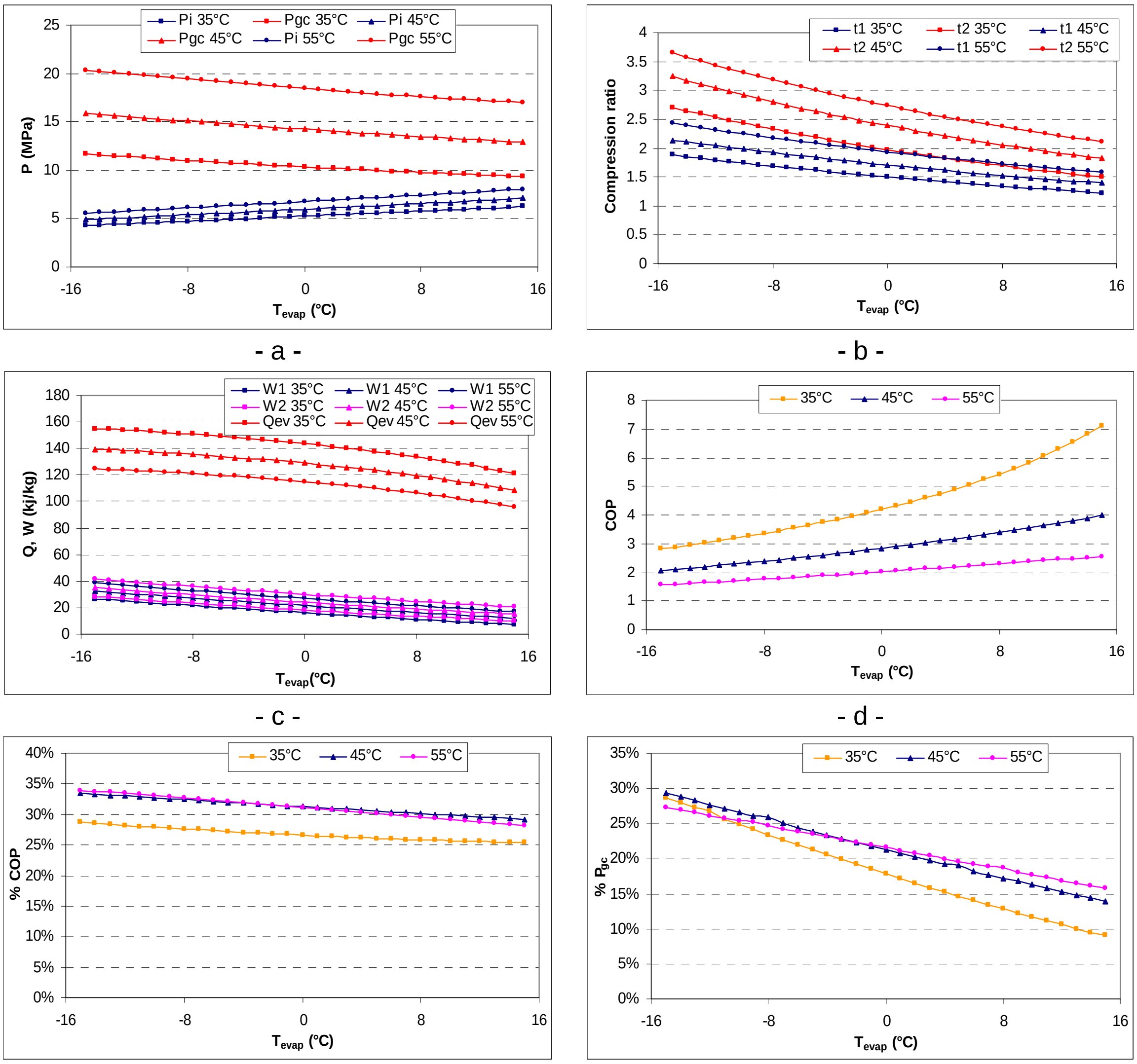

- a -

- b -

- c -

- d -

- e -

- f -

Figure 1.28: Variation of P_i, P_{gc}, CR, COP, COP and P_{gc} improvement, cooling capacity and compression work with evaporation temperature for RCC. ($\eta_{comp} = 1$, $\Delta T = 0$ K and $T_{SH} = 5$ K).

- **Variation of the outdoor temperature on the high pressure side**

Simulation conditions: expansion is isenthalpic, evaporating temperature = 0°C, the gas cooler/ condenser outlet temperature is varied.

Results

In sub-critical operating conditions, T_{gc} < 31°C, the HP is the saturated pressure at T_{gc}, and the IP slightly increases with T_{gc} (Figure 1.29.a). As the gas cooler outlet temperature increases, the CRs of the poly-tropic compression (t1) and the cooled compression (t2) are close and slightly increases; however the CR of the conventional cycle is larger than the two CRs (Figure 1.29.b).

The cooling capacity decreases with T_{gc} because the evaporator inlet enthalpy increases with T_{gc}, and it is equal to the conventional cycle cooling capacity in sub-critical cycle. The works of the poly-tropic compression (W1) and of the cooled compression (W2) are close and they slightly increase with T_{gc}, at constant evaporating temperature, 0°C (Figure 1.29.c).

Comparison with the one stage CO_2 cycle

- The gas cooler outlet pressure variation $\%P_{gc}$ is zero in sub-critical cycle (Figure 1.29.d).
- By comparing the COP of RCC to the conventional COP, (the COP variation $\%COP_{RCC}$ is positive and increases with T_{gc}, so the RCC cycle improves the energy performance of the sub-critical cycle, by 7% at T_{gc} = 15°C, and by 11% at T_{gc} = 30°C (Figure 1.29.d).

In trans-critical operating conditions, T_{gc} > 31°C, the HP and the IP increase with T_{gc} (Figure 1.29.a). As the gas cooler outlet temperature increases, the CR of the poly-tropic compression (t1) increases; also the CR of the cooled compression (t2) increases with a jump at the critical temperature, however the CR of the conventional cycle increases continuously and is larger than the two CRs (Figure 1.29.b).

The HP and the IP are dependent of the isentropic compression efficiency of the compressor, but depends slightly on the pressure drop in the evaporator and the gas cooler.

The cooling capacity decreases with T_{gc} because the evaporator inlet enthalpy increases with T_{gc}, but the cooling capacity of RCC cycle is larger than the conventional cycle because the $P_{gc,RCC}$ is higher than $P_{gc,conv}$. The work of the poly-tropic compression (W1) and the cooled compression (W2) increase with T_{gc}, at constant evaporating temperature, 0°C, and they are close (Figure 1.29.c).

Comparison with the one stage CO_2 cycle

- By comparing the P_{gc} of RCC to the conventional P_{gc}, the gas cooler outlet pressure variation $\%P_{gc,\ RCC}$ is positive in trans-critical cycle and varies between 15% and 21% with T_{gc} (Figure 1.29.d).
- By comparing the COP of RCC to the conventional COP, the COP variation $\%COP_{RCC}$ is positive and increases with T_{gc} from 22% at 31°C to 30% at 40°C, and then become quasi-constant around 30%, so the RCC cycle improves the energy performance of the trans-critical cycle, by more than 20% (Figure 1.29.d).

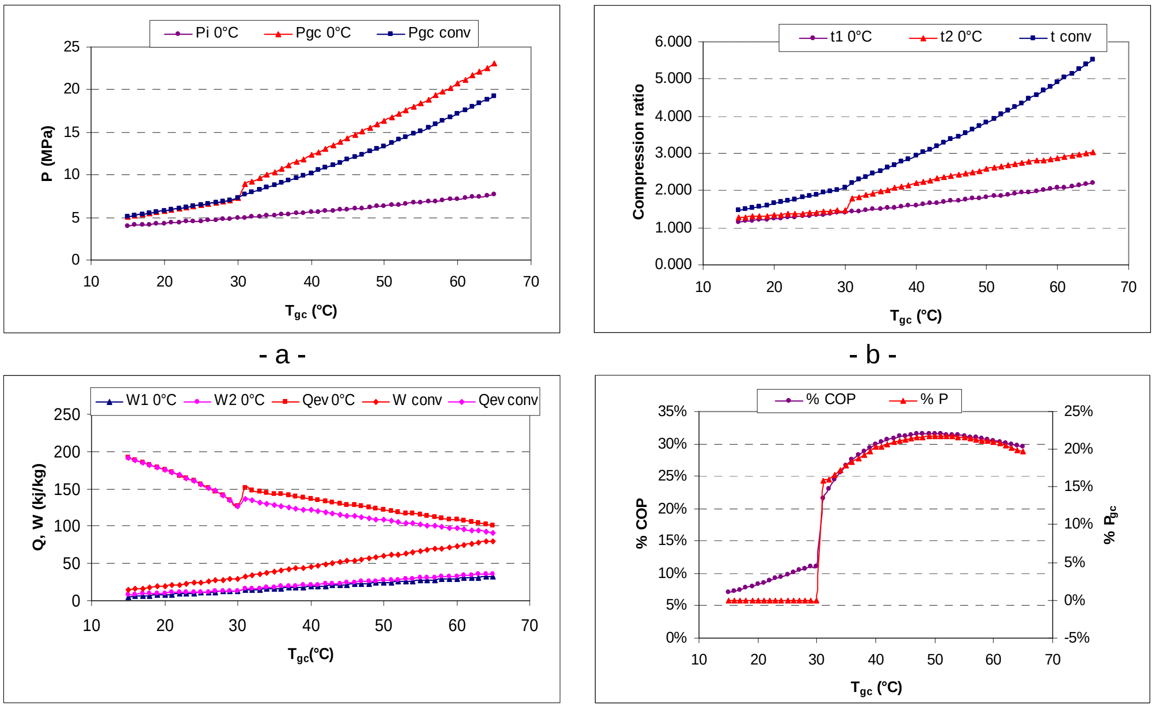

- a - - b -

- c - - d -

Figure 1.29: Variation of P_i, P_{gc}, CR, COP and P_{gc} improvement, cooling capacity and compression work with gas cooler outlet temperature for RCC at 0°C as evaporation temperature, $\eta_{comp} = 1$, $T_{SH} = 5$ K and $\Delta T = 0$ K.

5.2 RCC with isentropic expansion

The RCC with isentropic expansion lay-out is presented on Figure 1.30.a and the corresponding thermodynamic evolutions in Figure 1.30.b

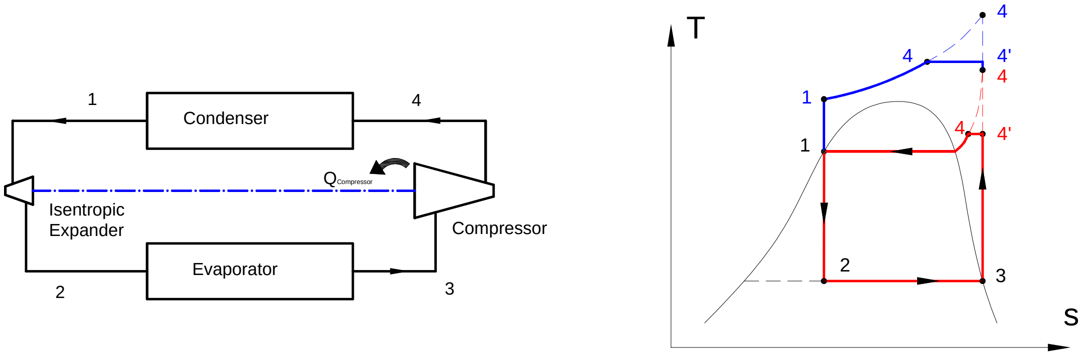

a. RCC with isentropic expansion.

b. T-S diagram of RCC with isentropic expansion.

Figure 1.30: Refrigeration compression cycle with compressor cooling RCC and isentropic expansion.

- **Variation of the evaporating temperatures on the low-pressure side**

Simulation conditions: expansion is isentropic, the gas cooler outlet temperature is set at 3 different temperatures (35, 45, 55°C). The generated work is considered directly used by the compressor.

Results

The variation of the evaporating temperature shows that the high-side optimum pressure decreases with the increase of the evaporation temperature; on the other hand, the intermediate optimum pressure increases with T_{ev} (Figure 1.31.a). As the evaporating temperature increases, the evaporating pressure increases that decrease the CR of the poly-tropic compression (t1); also the CR of the cooled compression (t2) decreases with the evaporating temperature (Figure 1.31.b).

The HP and the IP depend on the isentropic expansion efficiency of the expander and of the isentropic compression efficiency, but depend slightly on the pressure drop in the evaporator and the gas cooler.

The cooling capacity decreases with T_{ev} and with T_{gc}. Also, the compression work of the poly-tropic compression (W1) and the cooled compression (W2) decrease with T_{ev} at constant gas cooler outlet temperature, but they increase with T_{gc} (Figure 1.31.c).

The COP of RCC with isentropic expansion increases with T_{ev} as the temperature difference between the heat source and the heat sink decreases (Figure 1.31.d); the COP is calculated by subtracting the expander-generated work from the compression work of the two compression stages (poly-tropic and cooled).

By comparing the available generated work from the isentropic expansion to the required work of the two compression stages, the variation of T_{ev} shows that the generated work is lower than the cooled compression work (t2), and also it is lower than the poly-tropic compression work (t1) but the ratio t1 approaches one as T_{gc} increases; however the work ratio increases with T_{ev} and T_{gc} (Figure 1.31.g).

Comparison with the one stage CO_2 cycle

- By comparing the P_{gc} of RCC with isentropic expansion to the conventional P_{gc}, the gas cooler outlet pressure variation $\%P_{gc}$ is positive and decreases with T_{ev}, so the HP of RCC is higher than the conventional cycle (Figure 1.31.f).
- By comparing the COP of RCC with isentropic expansion to the conventional COP, the COP variation $\%COP_{RCC\ is}$ is positive and is quasi-constant with T_{ev} but increases with T_{gc}, so the RCC cycle with isentropic expansion improves the energy performance of the cycle by 130% at T_{gc} = 35°C, by 170% at T_{gc} = 45°C, and by 200% at T_{gc} = 55°C (Figure 1.31.e).

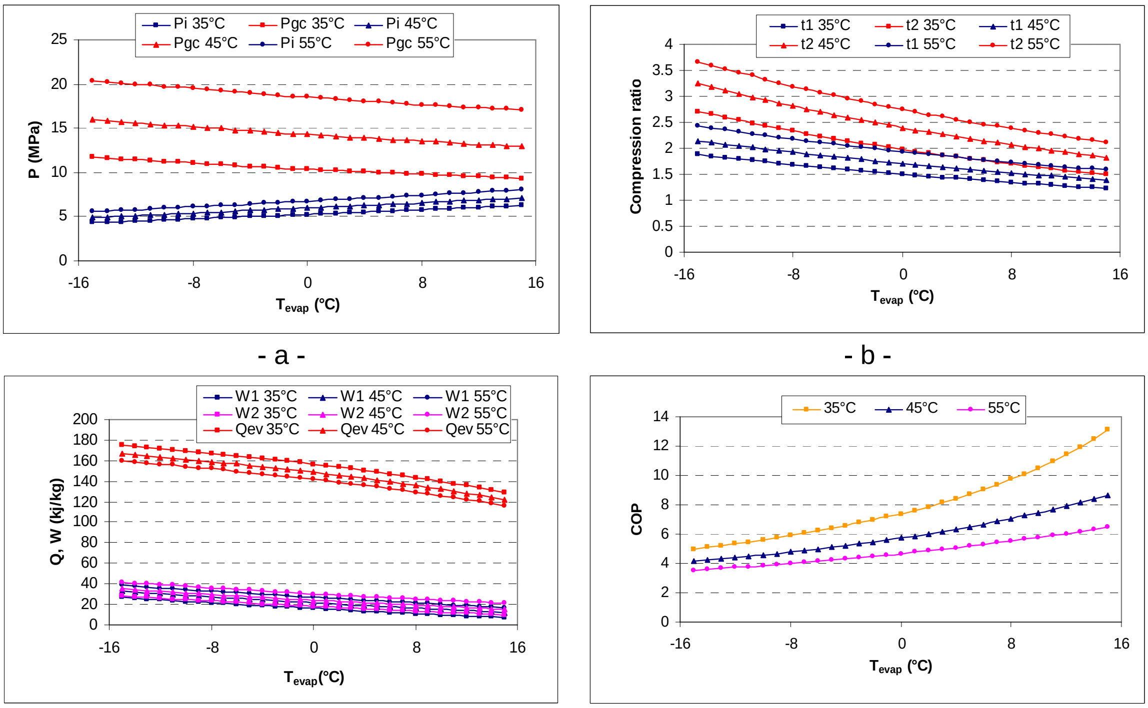

- a -

- b -

- c -

- d -

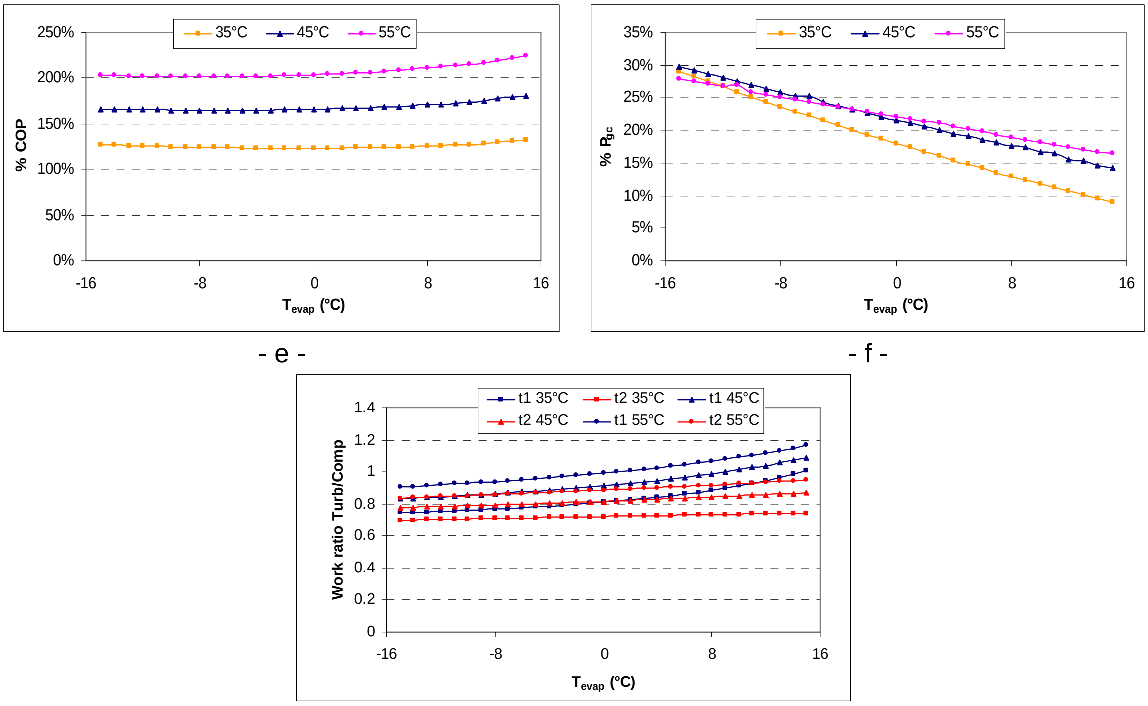

- e -

- f -

- g -

Figure 1.31: Variation of P_i, P_{gc}, CR, COP, COP and P_{gc} improvement, cooling capacity and compression work, turbine work to compression work ratio with evaporation temperature for RCC with isentropic expansion.
$\eta_{comp} = 1$, $\eta_{turbine} = 1$, $T_{SH} = 5$ K, $\Delta T = 0$ K.

- **Variation of the outdoor temperatures at the high-pressure side**

Simulation conditions: the expansion is isentropic, the evaporating temperature = 0°C, the gas cooler/ condenser outlet temperature is varied.

Results

In sub-critical operating conditions, $T_{gc} < 31$°C, the HP is the saturated pressure at T_{gc}, and the IP slightly increases with T_{gc} (Figure 1.32.a). As the gas cooler outlet temperature increases, the CRs of the poly-tropic compression (t1) and the cooled compression (t2) are close and slightly increases; however the CR of the conventional cycle is larger than the two CRs (Figure 1.32.b).

The cooling capacity decreases with T_{gc} because the evaporator inlet enthalpy increases with T_{gc}, and it is slightly larger than the conventional cycle cooling capacity in sub-critical cycle due to the generated work by the expander that decreases the inlet enthalpy of the evaporator. The works of the poly-tropic compression (W1) and of the cooled compression (W2) are close and they increase slightly with T_{gc}, at constant evaporating temperature, 0°C (Figure 1.32.c).

By comparing the available generated work from the isentropic expansion to the required work of the two compression stages, the variation of T_{gc} shows that the generated work is lower than the poly-tropic compression work (t1), and also it is lower than the cooled compression work (t2); however the work ratios increases with T_{gc} (Figure 1.32.e).

Comparison with the one stage CO_2 cycle

- The gas cooler outlet pressure variation %P_{gc} is zero in sub-critical cycle (Figure 1.32.d).

- By comparing the COP of RCC cycle with isentropic expansion to the conventional COP, the COP variation $\%COP_{RCC\ is}$ is positive and increases with T_{gc}, so the RCC cycle with isentropic expansion improves the energy performance of the sub-critical cycle, by 40% at T_{gc} = 15°C, and by 100% at T_{gc} = 30°C (Figure 1.32.d).

In trans-critical operating conditions, T_{gc} > 31°C, the HP and the IP increase with T_{gc} (Figure 1.32.a). As the gas cooler outlet temperature increases, the CR of the poly-tropic compression (t1) increases; also the CR of the cooled compression increases, with a jump at the critical temperature, however the CR of the conventional cycle continuously increases and is larger than the two CRs (Figure 1.32.b).

The cooling capacity decreases with T_{gc} because the evaporator inlet enthalpy increases with T_{gc}, but the cooling capacity of RCC cycle is larger than the conventional cycle because the $P_{gc,RCC}$ is higher than $P_{gc,conv}$. The works of the poly-tropic compression (W1) and of the cooled compression (W2) increase with T_{gc}, at constant evaporating temperature, 0°C, and they are close (Figure 1.32.c).

By comparing the available generated work from the isentropic expansion to the required work of the two compression stages, the variation of T_{gc} shows that the generated work is lower than the cooled compression work (t2), and the ratio t2 increases with Tgc from 0.7 at 31°C to 0.95 at 65°C; also, the variation of T_{gc} shows that the generated work is lower than the poly-tropic compression work (t1) for T_{gc} < 55°C, and the ratio t1 increases with T_{gc} from 0.75 at 31°C to 1.05 at 65°C (Figure 1.32.e).

Comparison with the one stage CO_2 cycle

- By comparing the P_{gc} of RCC cycle with isentropic expansion to the conventional P_{gc}, the gas cooler outlet pressure variation $\%P_{gc,\ RCC\ is}$ is positive in trans-critical cycle and varies between 15% and 23% with T_{gc} (Figure 1.32.d).
- By comparing the COP of RCC cycle with isentropic expansion to the conventional COP, the COP variation $\%COP_{RCC\ is}$ is positive and increases with T_{gc} from 100% at 31°C to 250% at 65°C so the RCC cycle with isentropic expansion improves the energy performance of the trans-critical cycle, by more than 100% (Figure 1.32.d).

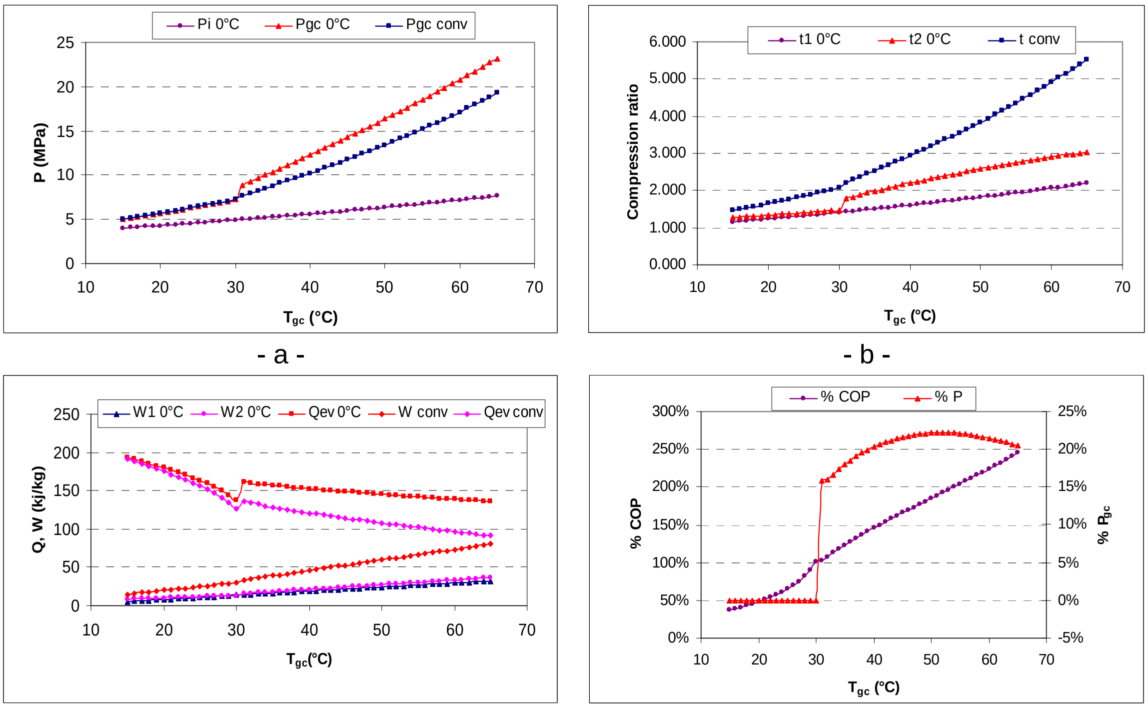

- a -

- b -

- c -

- d -

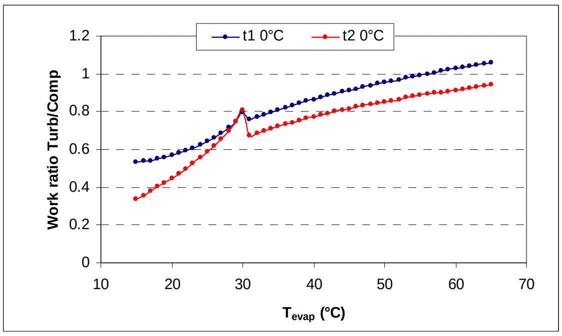

- e -

Figure 1.32: Variation of P_i, P_{gc}, CR, COP, COP and P_{gc} improvement, cooling capacity and compression work, turbine work to compression work ratio with gas cooler outlet temperature for RCC with isentropic expansion.
$\eta_{comp} = 1$, $\eta_{turbine} = 1$, $T_{SH} = 5$ K and $\Delta T = 0$ K.

5.3 Effect of the temperature difference between the intermediate temperature and the gas cooler outlet temperature

In order to evaluate the effect of ∆T, the temperature difference between the intermediate temperature and the gas cooler outlet temperature, on the performance of the refrigeration compression cycle with compressor cooling RCC, cycle calculations are done with $\Delta T = 15$ K for isenthalpic and isentropic expansion.

Simulation conditions: expansion is isenthalpic, the gas cooler outlet temperature is set at 3 different temperatures (35, 45, 55°C) .

Results

By comparing the P_{gc} of RCC_{15K} cycle to the conventional P_{gc}, the gas cooler outlet pressure variation $\%P_{gc}$ is positive and decreases with T_{ev}, so the HP of RCC is higher than the conventional cycle (Figure 1.33.a).

By comparing the COP of RCC_{15K} cycle to the conventional COP, the COP variation $\%COP_{RCC,15K}$ is positive and decreases with T_{ev} (Figure 1.33.b)., but the RCC_{15K} cycle improves the energy performance of the cycle lower than the RCC cycle with $\Delta T = 0$, so the energy performance decreases by increasing ∆T.

Simulation conditions: expansion is isenthalpic, the evaporating temperature = 0°C, the gas cooler/ condenser outlet temperature is varied and Figure 1.33.c is drawn.

Results

The gas cooler outlet pressure variation $\%P_{gc}$ is zero in sub-critical cycle (Figure 1.33.c). By comparing the COP of RCC_{15K} to the conventional COP, the COP variation $\%COP_{RCC,15K}$ is positive in sub-critical cycle and increases with T_{gc}, by 0% at $T_{gc} = 15$°C, and by 2% at $T_{gc} = 30$°C (Figure 1.33.c).

In transcritical cycle, by comparing the P_{gc} of RCC_{15K} to the conventional P_{gc}, the gas cooler outlet pressure variation $\%P_{gc,\ RCC,15K}$ is positive in trans-critical cycle and varies between 0% and 21% with T_{gc} (Figure 1.33.c).

By comparing the COP of RCC_{15K} to the conventional COP, the COP variation $\%COP_{RCC,15K}$ is positive and increases with T_{gc} from 3% at 31°C to 18% at 65°C, so the RCC_{15K} cycle improves less the energy performance of the trans-critical cycle compared to the RCC cycle (Figure 1.33.c).

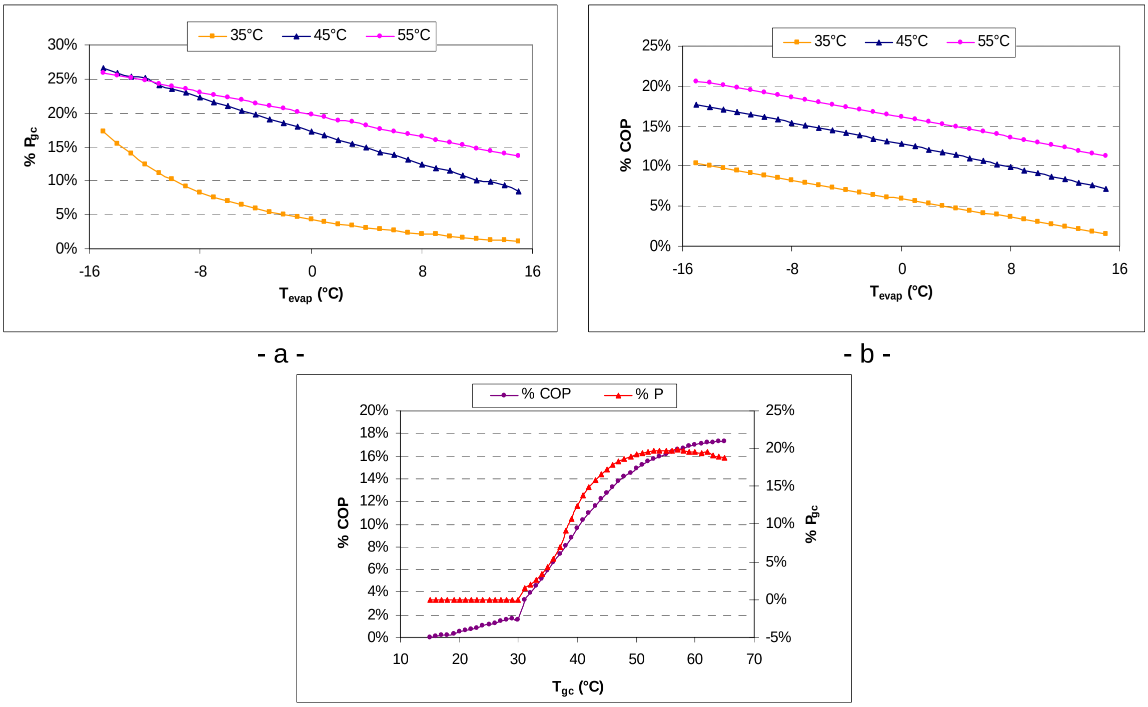

- a -

- b -

- c -

Figure 1.33: Variation of COP and P_{gc} improvement with evaporation temperature at constant T_{gc}, and with gas cooler outlet temperature at T_{ev} = 0°C for RCC.
($\eta_{comp} = 1$, T_{SH} = 5 K and ΔT = 15 K).

Simulation conditions: expansion is isentropic, the gas cooler outlet temperature is set at 3 different temperatures (35, 45, 55°C).

Results

By comparing the P_{gc} of RCC_{15K} cycle to the conventional P_{gc}, the gas cooler outlet pressure variation $\%P_{gc,RCC,15K}$ is positive and decreases with T_{ev}, so the HP of RCC is higher than the conventional cycle (Figure 1.34.a).

By comparing the COP of RCC_{15K} cycle with isentropic expansion to the conventional COP, the COP variation $\%COP_{RCC,15K,is}$ is positive and slightly decreases with T_{ev} (Figure 1.34.b), but the $RCC_{15K,is}$ cycle improves the energy performance of the cycle less than the RCC_{is} cycle with $\Delta T = 0$, so the energy performance decreases by increasing ΔT.

Simulation conditions: expansion is isentropic, evaporating temperature = 0°C, the gas cooler/ condenser outlet temperature is varied.

Results

In sub-critical cycle, the gas cooler outlet pressure variation $\%P_{gc}$ is zero.

By comparing the COP of $RCC_{15K,is}$ cycle to the conventional COP, the COP variation $\%COP_{RCC,15K,is}$ is positive and increases with T_{gc}, from 20% at T_{gc} = 15°Cto 75% at T_{gc} = 30°C (Figure 1.34.c).

In transcritical cycle, by comparing the P_{gc} of $RCC_{15K,\ is}$ cycle to the conventional P_{gc}, the gas cooler outlet pressure variation $\%P_{gc,\ RCC\ is,15K}$ is positive and varies between 0% and 20% with T_{gc}.

By comparing the COP of $RCC_{15K,is}$ to the conventional COP, the COP variation $\%COP_{RCCis,15K}$ is positive and increases with T_{gc} from 65% at 31°C to 185% at 65°C

(Figure 1.34.c), so the $RCC_{15K,is}$ cycle improves the energy performance of the cycle in trans-critical cycle, less (70% with ΔT = 0K) than the RCC_{is} cycle.

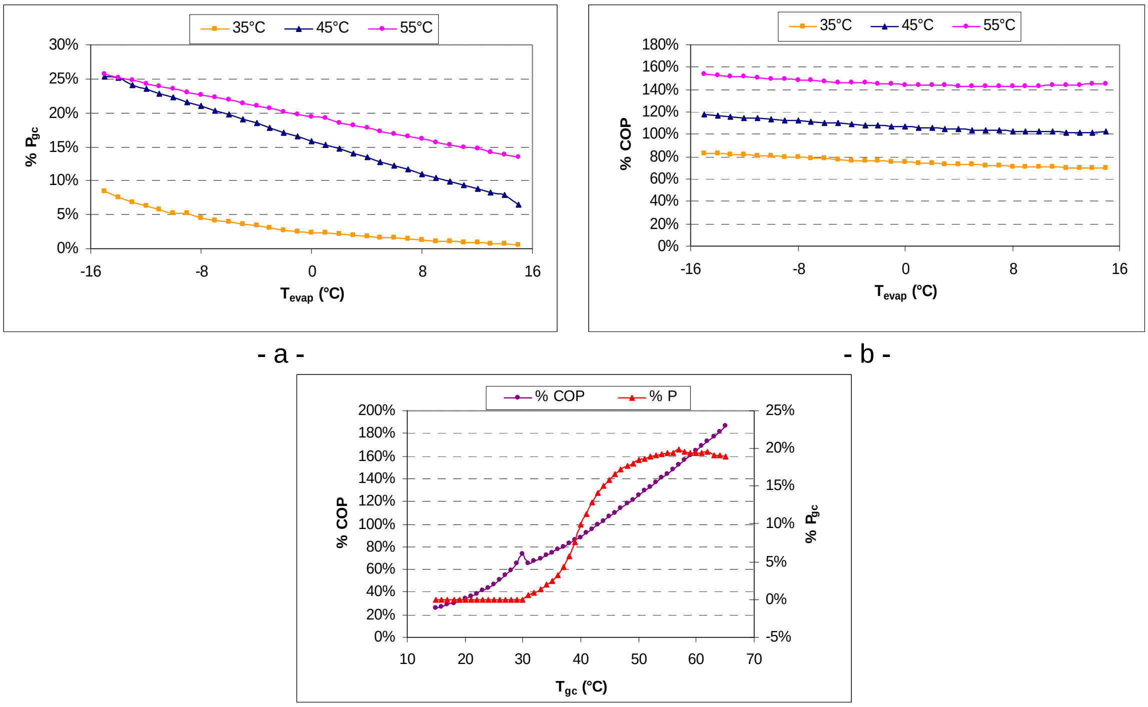

- a -

- b -

- c -

Figure 1.34: Variation of COP and P_{gc} improvement with evaporation temperature at constant T_{gc}, and with gas cooler outlet temperature at T_{ev} = 0°C for RCC cycle with isentropic expansion. ($\eta_{comp} = 1$, $\eta_{turbine} = 1$, T_{SH} = 5 K, ΔT = 15 K).

ANNEX 2. Ejector Computational Fluid Dynamics Analysis

The main objective of CFD modeling is to visualize the internal flow of the ejector. The distance between the nozzle outlet and the constant area chamber, the convergent and divergent angles, and the length of the constant area chamber cannot be represented by the 1D model. The CFD modeling gives quantitative and qualitative results on the influences of these parameters on the ejector operation. Since the two-phase flow cannot be analyzed by CFD, the vapor ejector will be characterized by CFD.

Building an ejector model requires:
- A proper definition of the geometry to be modeled.
- An appropriate choice of turbulence model.
- The choice of numerical techniques that ensure accurate results.
- A proper definition of boundary conditions.
- The choice of accurate physical models relevant to the case.
- The choice of reasonable convergence criteria.

1. Modeled ejector geometry

The ejector internal geometry where the vapor flows, has to be carefully drawn. The model can be drawn using software as "Gambit" or "AutoCad".

Since the ejector presents an axial symmetry, the ejector modeling becomes essentially two dimensional instead of being three dimensional.

2. Choosing a CFD model for the Ejector

The well established industry leading software, Fluent 6, was chosen as CFD code.

3. Conservation equations

The modeling of the ejector flow is based on conservation equations: the continuity, momentum, and energy equations. Those equations need to be written in the compressible flow form, and the geometry of the ejector makes it necessary to write conservation equations using the cylindrical coordinates system.

3.1 Continuity equation

The mass conservation principle yields the continuity equation.

$$\frac{\partial \rho}{\partial t}+\frac{\partial}{\partial x}\left(\rho v_x\right)+\frac{\partial}{\partial r}\left(\rho v_r\right)+\frac{\rho v_r}{r}=0 \tag{A2.1}$$

3.2 Momentum equation

The momentum conservation principle yields the momentum equation.

In the x direction:

$$\frac{\partial\left(\rho v_x\right)}{\partial t}+\frac{1}{r}\frac{\partial}{\partial x}\left(r\rho v_x v_x\right)+\frac{1}{r}\frac{\partial}{\partial r}\left(r\rho v_r v_x\right)=$$

$$-\frac{\partial p}{\partial}+\frac{1}{r}\frac{\partial}{\partial x}\left[r\mu\left(2\frac{\partial v_x}{\partial x}-\frac{2}{3}\left(\nabla\vec{v}\right)\right)\right]+\frac{1}{r}\frac{\partial}{\partial r}\left[r\mu\left(\frac{\partial v_x}{\partial r}+\frac{\partial v_r}{\partial x}\right)\right]+F_x \tag{A2.2}$$

In the radial direction:

$$\frac{\partial(\rho v_r)}{\partial t}+\frac{1}{r}\frac{\partial}{\partial x}(r\rho v_x v_r)+\frac{1}{r}\frac{\partial}{\partial r}(r\rho v_r v_r)=$$

$$-\frac{\partial p}{\partial r}+\frac{1}{r}\frac{\partial}{\partial r}\left[r\mu\left(2\frac{\partial v_r}{\partial r}-\frac{2}{3}(\nabla\vec{v})\right)\right]+\frac{1}{r}\frac{\partial}{\partial x}\left[r\mu\left(\frac{\partial v_x}{\partial r}+\frac{\partial v_r}{\partial x}\right)\right]-2\mu\frac{v_r}{r^2}+\frac{2}{3}\frac{\mu}{r}(\nabla\vec{v})+\rho\frac{v_x^2}{r}+F_r \qquad \text{(A2.3)}$$

where $\nabla\vec{v}=\frac{\partial v_x}{\partial x}+\frac{\partial v_r}{\partial r}+\frac{v_r}{r}$. (A2.4)

3.3 Energy equation

The energy equation in cylindrical coordinate system is:

$$\frac{\partial}{\partial t}(\rho E)+\nabla[\vec{v}(\rho E+p)]=\nabla\left[\kappa_{eff}\nabla T-(\bar{\tau}_{eff}\vec{v})\right] \qquad \text{(A2.5)}$$

In the above equation, the term E denotes the total internal energy defined as:

$$E=h-\frac{p}{\rho}+\frac{v^2}{2} \qquad \text{(A2.6)}$$

where the enthalpy h is defined as: $h=\int_{T_{ref}}^{T}c_p dT$ (A2.7)

The term κ_{eff} represents the effective thermal conductivity, defined as: $\kappa_{eff} = \kappa + \kappa_t$ where κ is the thermal conductivity of the fluid and κ_t is the turbulent thermal conductivity as defined by the turbulence model being used. The last term represents the viscous dissipation.

4. Turbulence Modeling

The high-speed flow and the extensive mixing processes that take place in ejectors make the flow highly turbulent. Therefore, accurate modeling of the flow requires the use of a proven turbulence model.

The renormalized group RNG k-ε model type is used in the study.

4.1 Standard k-ε Model

As shown first by Hanjalic and Launder (1972), the standard k-ε model is a semi-empirical turbulence model based on writing transport equations for the turbulence kinetic energy (k) and the turbulence dissipation rate (ε). Those two quantities can be expressed as follows:

$$k=\frac{1}{2}\overline{u_i' u_j'} \qquad \text{(A2.8)}$$

$$\varepsilon=2\frac{\mu}{\rho}\overline{e_{ij}' e_{ij}'} \qquad \text{(A2.9)}$$

where $e_{ij}=\frac{\partial u_i}{\partial x_j}+\frac{\partial u_j}{\partial x_i}$. (A2.10)

The standard k-ε model is only valid for fully turbulent flows since it is based on the assumption that the flow is fully turbulent, which makes the effect of molecular viscosity negligible.

The formulation of the standard k-ε model requires the writing transport equations for the turbulence kinetic energy, k, and the dissipation rate,ε.

$$\frac{\partial}{\partial t}(\rho k)+\frac{\partial}{\partial x_i}(\rho k u_i)=\frac{\partial}{\partial x_j}\left[\left(\mu+\frac{\mu_t}{\sigma_k}\right)\frac{\partial k}{\partial x_j}\right]+G_k-\rho\varepsilon-Y_M \qquad \text{(A2.11)}$$

$$\frac{\partial}{\partial t}(\rho \varepsilon)+\frac{\partial}{\partial x_i}(\rho \varepsilon u_i)=\frac{\partial}{\partial x_j}\left[\left(\mu+\frac{\mu_t}{\sigma_\varepsilon}\right)\frac{\partial \varepsilon}{\partial x_j}\right]+C_{1\varepsilon}\frac{\varepsilon}{k}G_k-C_{2\varepsilon}\rho\frac{\varepsilon^2}{k} \qquad \text{(A2.12)}$$

G_k represents the generation of turbulence kinetic energy due to the mean velocity gradients, and it is given by:

$$G_k=-\rho\overline{u_i' u_j'}\frac{\partial u_j}{\partial x_i}\,. \qquad \text{(A2.13)}$$

Y_M is a source term that represents the contribution of the fluctuating dilatation in compressible turbulence to the overall dissipation. This process is usually neglected in the formulation of k-ε models. Sarkar and Balakrisknan (1990) proposed the following model:

$$Y_M=2\rho\varepsilon M_t^2 \qquad \text{(A2.14)}$$

where $M_t=\sqrt{\frac{k}{a^2}}$. (A2.15)

$C_{1\varepsilon}$ and $C_{2\varepsilon}$ are constants. σ_k and σ_ε are the Prandtl numbers for k and ε respectively.

Using dimensional analysis, it can be shown that the turbulent cinematic viscosity, ν_t, may be expressed as: $\nu_t \propto V.\ell$, where V is a velocity scale and ℓ is a length scale. Using the definitions of k and ε ,V and ℓ can be expressed as: $V=k^{1/2}$ and $\ell=k^{3/2}/\varepsilon$. Therefore, the turbulent viscosity is expressed as: $\mu_t=\rho C_\mu\frac{k^2}{\varepsilon}$ (A2.16)
where C_μ is a constant.

The model constants $C_{1\varepsilon}$, $C_{2\varepsilon}$, C_μ, σ_k, and σ_ε are found empirically and optimized to yield good results for a wide range of applications. The optimized values are:
$C_{1\varepsilon} = 1.44$, $C_{2\varepsilon} = 1.92$, $C_\mu = 0.12$, $\sigma_k = 1.0$, $\sigma_\varepsilon = 1.3$.

4.2 Renormalized group (RNG) k-ε Model

The RNG based k-ε turbulence model was developed by Yakhot and Orszag (1986) using a mathematical technique called "renormalization group" method. The analytical derivation yields to transport equations that are similar to those of the standard k-ε model, but with different constants and additional terms and functions. The following description of this modeling technique has demonstrated its advantages over the standard k-ε model. The RNG k-ε model has the following form, similar to standard k-ε model:

$$\frac{\partial}{\partial t}(\rho k)+\frac{\partial}{\partial x_i}(\rho k u_i)=\frac{\partial}{\partial x_j}\left(\alpha_k\mu_{eff}\frac{\partial k}{\partial x_j}\right)+G_k-\rho\varepsilon-Y_M \qquad \text{(A2.17)}$$

$$\frac{\partial}{\partial t}(\rho \varepsilon)+\frac{\partial}{\partial x_i}(\rho \varepsilon u_i)=\frac{\partial}{\partial x_j}\left(\alpha_\varepsilon\mu_{eff}\frac{\partial \varepsilon}{\partial x_j}\right)+C_{1\varepsilon}\frac{\varepsilon}{k}G_k-C_{2\varepsilon}\rho\frac{\varepsilon^2}{k}-R_\varepsilon\,. \qquad \text{(A2.18)}$$

The quantities α_k and α_ε are the inverse effective Prandtl numbers of k and ε. μ_{eff} is the effective viscosity, and $C_{1\varepsilon}$ and $C_{2\varepsilon}$ are constants derived analytically from the RNG theory: $C_{1\varepsilon} = 1.42$, $C_{2\varepsilon} = 1.6\tilde{8}$.

Computing the effective viscosity is done through the scale elimination procedure in RNG theory. This procedure results in the following equations:

$$d\left(\frac{\rho^2 k}{\sqrt{\varepsilon\mu}}\right) = 1.72 \frac{\hat{v}}{\sqrt{\hat{v}^3 - 1 + C_v}} d\hat{v} \qquad \text{(A2.19)}$$

where $\hat{v} = \mu_{eff}/\mu$ and $C_v \approx 100$.

The solution of equation describes the relationship between turbulent viscosity and the effective Reynolds number. **Therefore, this model is able to handle both low-Reynolds-number and high-Reynolds-number situations**. In the high Reynolds number limit, the turbulent viscosity is: $\mu_t = \rho C_\mu \frac{k^2}{\varepsilon}$ (A2.20)

where C_μ is a constant.

The inverse effective Prandtl numbers, α_k and α_ε are computed using the following formula derived analytically by the RNG theory:

$$\left|\frac{\alpha - 1.3929}{\alpha_0 - 1.3929}\right|^{0.6231} \left|\frac{\alpha + 2.3929}{\alpha_0 + 2.3929}\right|^{0.3679} = \frac{\mu_{mol}}{\mu_{eff}} \qquad \text{(A2.21)}$$

where $\alpha_0 = 1.0$. In the high Reynolds limit, $\mu_{mol}/\mu_{eff} << 1$ therefore $\alpha_k = \alpha_\varepsilon \approx 1.393$.

The R_ε term is the main difference between the RNG and the standard k-ε models. It is given by:

$$R_\varepsilon = \frac{C_\mu \rho \eta^3 \left(1 - \eta/\eta_0\right)}{1 + \beta\eta^3} \frac{\varepsilon^2}{k} \qquad \text{(A2.22)}$$

where $\eta = S\,\kappa/\varepsilon$, $\eta_0 = 4.38$, $\beta = 0.012$.

The variable S is the modulus of the mean rate of strain tensor, given by:

$$S = \sqrt{2 S_{ij} S_{ij}} \qquad \text{(A2.23)}$$

Where S_{ij} is the mean strain rate defined as: $S_{ij} = \frac{1}{2}\left(\frac{\partial u_j}{\partial x_i} + \frac{\partial u_i}{\partial x_j}\right)$. (A2.24)

By rearranging the RNG ε equation, the equation becomes:

$$\frac{\partial}{\partial t}(\rho\varepsilon) + \frac{\partial}{\partial x_i}(\rho\varepsilon u_i) = \frac{\partial}{\partial x_j}\left(\alpha_\varepsilon \mu_{eff} \frac{\partial \varepsilon}{\partial x_j}\right) + C_{1\varepsilon}\frac{\varepsilon}{k}\left(G_k + C_{3\varepsilon} G_b\right) - C^*_{2\varepsilon}\rho\frac{\varepsilon^2}{k} \qquad \text{(A2.25)}$$

where $C^*_{2\varepsilon}$ is given by: $C^*_{2\varepsilon} = C_{2\varepsilon} + \frac{C_\mu \eta^3 \left(1 - \eta/\eta_0\right)}{1 + \beta\eta^3}$ (A2.26)

and $C_{3\varepsilon}$ is a constant.

In regions where $\eta < \eta_0$, the R_ε term makes a positive contribution, causing $C^*_{2\varepsilon}$ to become larger than $C_{2\varepsilon}$. For example, when $\eta \approx 3.0$, as is the case in logarithmic layer, it can be shown that $C_{2\varepsilon} \approx 2.0$. This value is close to that of $C_{2\varepsilon}$ in the standard k-ε model. Therefore, it can be concluded that RNG model yields results similar to those of the standard k-ε model for weakly to moderately strained flows.

However, in regions of large strain rate ($\eta > \eta_0$), the R_ε term results in a negative contribution, making the value of $C^*_{2\varepsilon}$ less than $C_{2\varepsilon}$, and eventually reducing k and the effective viscosity. As a result, in rapidly strained flows, the RNG model leads to a lower turbulent viscosity than the standard k–ε model.

Thus, the RNG model is expected to be more responsive to the effects of rapid strain and streamline curvature than the standard k-ε model, which explains the superior performance of the RNG model for certain classes of flows.

For more information about the k-ε model , consult the Fluent help.

5. Solver Type and discretization

The most appropriate solver type for ejector modeling is the coupled solver. The coupled solver solves the governing equations of continuity, momentum, and energy simultaneously as a set, or vector of equations. Governing equations for additional scalars will be solved sequentially, segregated from one another and from the coupled set. The segregated solver solves sequentially the governing equations.

5.1 Governing equation in Vector form

Many times, the governing equations are written in conservation vector form to describe mean flow properties. These equations can be integrated for any given control volume and written as follows:

$$\frac{\partial}{\partial t}\int_V \vec{W} dV + \oint \left[\vec{F} - \vec{G}\right] d\vec{A} = \int_V \vec{H} dV \ . \qquad \text{(A2.27)}$$

The vectors W,F and G are defined as:

$$W = \begin{Bmatrix} \rho \\ \rho u \\ \rho v \\ \rho w \\ \rho E \end{Bmatrix} \ ; \ F = \begin{Bmatrix} \rho v \\ \rho v u + p\vec{i} \\ \rho v v + p\vec{j} \\ \rho v w + p\vec{k} \\ \rho v E + p v \end{Bmatrix} \ ; \ G = \begin{Bmatrix} 0 \\ \tau_{xi} \\ \tau_{yi} \\ \tau_{zi} \\ \tau_{ij} v_j + q \end{Bmatrix} . \qquad \text{(A2.28)}$$

And the vector $\vec{H}$ contains source terms such as body forces and energy sources. The terms ρ, v, E and p are the density, velocity, total energy per unit mass, and the pressure of fluid respectively; τ is the viscous stress tensor, and q is the heat flux.

The total energy E is related to the enthalpy h by:

$$E = h + \frac{1}{2} v^2 - \frac{p}{\rho} \qquad \text{(A2.29)}$$

The integral form is suitable for use with the finite volume discretization approach used in Fluent. One of the problems encountered with expressing the Navier-Stokes equations in the integral form is the numerical stiffness when the Mach number is low. This stiffness is caused by the disparity between the fluid velocity v and the speed of sound c. The numerical stiffness of the equations under these conditions results in poor convergence rates. The CFD code overcomes this difficulty by employing a technique called time derivative preconditioning.

Time derivative preconditioning modifies the time derivative term by pre-multiplying it by a preconditioning matrix. This operation helps rescale the acoustic speed, or the Eigen value, of the system of equations being solved in order to eliminate potential numerical stiffness. The preconditioning matrix used in the CFD package is obtained from the work of Venkateswaran et al. (1992). To summarize this analysis, the preconditioning matrix is given by:

$$\Gamma\frac{\partial}{\partial t}\int_V Q dV+\oint\left[\vec{F}-\vec{G}\right]d\vec{A}=\int_V \vec{H} dV \tag{A2.30}$$

where:

$$\Gamma=\begin{bmatrix} \Theta & 0 & 0 & 0 & \rho_T \\ \Theta_u & \rho & 0 & 0 & \rho_T u \\ \Theta_v & 0 & \rho & 0 & \rho_T u \\ \Theta_w & 0 & 0 & \rho & \rho_T u \\ \Theta H-\delta & \rho u & \rho v & \rho w & \rho_T H+\rho C_p \end{bmatrix} \tag{A2.31}$$

$$\vec{Q}=\{p\ \ u\ \ v\ \ w\ \ T\}^T , \tag{A2.32}$$

$$\rho_T=\left.\frac{\partial\rho}{\partial T}\right|_p , \tag{A2.33}$$

$$\Theta=\left(\frac{1}{U_r^2}-\frac{\rho_T}{\rho C_p}\right). \tag{A2.34}$$

δ = 1 for ideal gas and δ = 0 for an incompressible fluid. The reference velocity U_r is chosen locally such that the Eigen values of the system remain well conditioned with respect to the convective and diffusive time scales.

The preconditioned coupled set of governing equations is discretized in time even when a steady state solution is sought. The steady state solution is obtained by marching the solution in time until convergence is reached. The reason for keeping the unsteady terms of the governing equations is that they ensure that the equations remain hyperbolic-parabolic as opposed to hyperbolic-elliptic. The latter are difficult to solve because hyperbolic equations require numerical techniques that are different from those required for elliptic equations. Discretization in time of the coupled equations as accomplished by either an implicit or an explicit time-marching scheme. These two algorithms are described below as documented by Fluent manual.

5.2 Explicit scheme

The explicit scheme utilizes a multi stage, time stepping algorithm to discretize the time derivative. The solution progresses from time step n to time step n+1 with an m-stage Runge-Kutta scheme, given by:

$$\vec{Q}^0=\vec{Q}^n ,\quad \Delta\vec{Q}^i=-\alpha_i\,\Delta t\,\Gamma^{-1}\vec{R}^{i-1} ,\quad \vec{Q}^{n+1}=\vec{Q}^m . \tag{A2.35}$$

Where $\Delta\vec{Q}^i=\vec{Q}^i-\vec{Q}^n$ and i = 1, 2, …, m is the stage counter for m-stage scheme. The parameter α_i is the multi stage coefficient for the i^{th} stage. The residual, R^i, is computed from the intermediate solution Q^i, and given by:

$$\vec{R}^i=\sum^{N_{faces}}\left(\vec{F}(\vec{Q}^i)-\vec{G}(\vec{Q}^i)\right)\vec{A}-V\,\vec{H}. \tag{A2.36}$$

The time step Δt is computed from the Courant-Friedrichs-Lewy (CFL) condition which was proposed by Courant et al.(1928):

$$\Delta t=\frac{CFL\Delta t}{\lambda_{max}} \tag{A2.37}$$

Where λ_{max} is the maximum of the local eigen values.

5.3 Implicit scheme

The implicit scheme discretizes the governing equations using a Euler implicit method combined with Newton type linearization of the fluxes to produce the following linearized system:

$$\left[D+\sum_{j}^{N_{faces}}S_{j,k}\right]\Delta\vec{Q}^{n+1}=-\vec{R}^n \tag{A2.38}$$

The center and off diagonal coefficient matrices, D and $S_{j,k}$ are given by:

$$D=\frac{V}{\Delta t}\Gamma+\sum_{j}^{N_{faces}}S_{j,i}\quad ; \tag{A2.39}$$

$$S_{j,k}=\left(\frac{\partial\vec{F}_j}{\partial\vec{Q}_k}-\frac{\partial\vec{G}_j}{\partial\vec{Q}_k}\right). \tag{A2.40}$$

And the residual vector $\vec{R}^n$ and time step Δt are defined same as explicit method.

5.4 Second order upwind scheme

In the finite volume approach, second order accuracy can be achieved at cell faces by performing a Taylor series expansion of cell centered solution about the center of the cell. Thus, for any variable, ϕ, the face value ϕ_f is computed using the following expression:

$$\phi_f=\phi+\nabla\phi.\Delta\vec{s}$$

Where ϕ is the cell centered value of the variable and $\nabla\phi$ is the gradient of the variable in the upstream cell, and $\Delta\vec{s}$ is the displacement vector from the center of upstream cell to the center of the face. Therefore, knowledge of ϕ_f requires that the gradient $\nabla\phi$ be computed in each cell. To do so, the divergence theorem in its discrete form needs to be applied as follows:

$$\nabla\phi=\frac{1}{V}\sum_{f}^{N_{faces}}\tilde{\phi}_f\,\vec{A} \tag{A2.41}$$

Where $\tilde{\phi}_f$ is an average value obtained by averaging ϕ from the two cells adjacent to the face.

6. Grid considerations

Successful application of a CFD model depends greatly on proper definition of a computational grid suitable for the geometry being modeled. Therefore, great care should be taken in defining a grid that would be appropriate and adequate for the flow situation and the geometry.

For two-dimensional geometries, the most common grid topologies are those based on triangular or quadrilateral cells. The triangular grid was used. The effect of grid size on the accuracy of modeling flow in ejectors should be studied, and a compromise should be taken between the grid size and the relative error between the results.

It is possible to consider many grid sizes in the geometry due to the phenomenon that occurs at every region of the grid. Thus, it is recommended that near the wall, where parameter variation is large, the grid size is smaller that the middle of the flow.

7. Boundary conditions

Once the appropriate grid is created for a certain geometry, it is important to define boundary conditions that accurately simulate actual physical conditions at those boundaries. There are four boundary conditions to define: ejector wall, primary stream inlet, secondary stream inlet, and the ejector exit.

7.1 Ejector wall

All the walls of the ejector are approximated as impermeable adiabatic walls. This assumption is common in refrigeration applications and is based on the fact that heat transfer per unit mass is low given the typically high flow capacity of an ejector. By comparing this assumption to the isothermal wall assumption, the results are almost identical.

7.2 Primary and Secondary stream inlets

These inlets are modeled as total pressure inlets, and not as mass flow or velocity. The temperature is also defined at the inlets for calculations pertaining to the energy equation.

7.3 Ejector exit

The ejector exit is modeled as a pressure outlet. In this case, only the pressure value is needed while the temperature is calculated using the energy equation. It is important to note that the CFD code would override the value of pressure at the exit if it is found to be inconsistent with the flow regime at the exit as computed by the code.

8. Physical properties

The density is considered variable with pressure and temperature, and it is calculated by the Ideal gas model. The heat capacity, the thermal conductivity, and the viscosity are expressed as functions of temperature under a polynomial form.

9. Convergence criteria and strategy for achieving convergence

A residual is the rate of change of the conserved variable $\vec{W}$. The RMS residual is the square root of the sum of the squares of the residuals in each cell of the domain:

$$R(\vec{W})=\sqrt{\sum_{n=1}^{N_{cell}}\left(\frac{\partial \vec{W}}{\partial t}\right)^2} \tag{A2.42}$$

When steady state CFD model approaches convergence, it is expected that the residuals will decrease and theoretically approach a zero value. However, the absolute value of the residuals may be misleading if they are not compared to previous residual. Therefore, the CFD code scales the residual of a variable using a scaling factor representative of that variable. This scaled residual is defined as: $\mathrm{Re}sidual\ \ ratio = \frac{R\left(\vec{W}\right)_{iteration\ N}}{R\left(\vec{W}\right)_{iteration\ 5}}$. (A2.43)

The denominator is the largest absolute value of the residual in the first five iterations.

Convergence is judged based on simultaneous observation of the scaled residuals and mass flow rate imbalance. A reasonable convergence criterion satisfy the two following conditions:

1- All scaled residuals must decrease by three orders of magnitude at least (10^{-3}).
2- The computed mass flow rate imbalance must be at most less than 0.1% of the mass flow rate at the ejector exit. Mathematically, this condition can be represented as follows: $\left|\frac{m_{exit} - \left(\dot{m}_{primary\ \mathrm{inlet}} + \dot{\mathrm{m}}_{\mathrm{secondary\,inlet}}\right)}{\dot{\mathrm{m}}_{\mathrm{exit}}}\right| \leq 0.001$. (A2.44)

The initial conditions of the model are very important for convergence criteria. So, at the iteration start, the control factors of the solution are decreased to low values less than 0.5, and when the error reaches $10^{-2,}$ the standard coefficients are re-used until convergence.

10. CFD modeling of two phase flow

The two- phase flow can be modeled using the Discrete phase modeling (DPM), sometimes called Lagrangian particle-tracking, a modeling technique which is readily available in Fluent. The objective is to examine the reliability of CFD techniques in modeling high speed two-phase flow in ejectors.

In simple terms, DPM solves transport equations for the continuous phase while it simulates a discrete phase, which consists of spherical particles, in a Lagrangian frame of reference. The trajectories of these discrete phase entities, as well as their impact on the continuous phase flow can be included.

Turbulent dispersion of particles can be modeled using a stochastic discrete particle approach. In this approach, turbulent dispersion of particles is predicted by integrating the trajectory equations for individual particles, using the instantaneous fluid velocity along the particle path during the integration. By computing the trajectory in this manner of a sufficient number of representative particles, usually called "number of tries", the random effects of turbulence on the particle dispersion may be accounted for.

The procedure used in implementing this technique was to first achieve a converged single-phase solution for the case to be studied. Water droplets are then introduced to the flow from the primary inlet in the form of injections. The assumptions used in this process are as follows:

- Liquid droplets are inert particles, so no phase change is allowed.
- Droplet size is constant, so no droplet breakup is allowed and no user defined droplet size distribution is given.
- Initial velocity of the droplets and the continuous phase are identical.

This two-phase modeling technique was carefully implemented by Ansary to simulate an air flow with liquid water droplets, however, reliable results were never achieved. Thus, since no phase change can be simulated with CFD models, experimentation is the only way to validate the 1D model and to adapt it.

ANNEX 3. Developed ejectors figures


Nozzle


Cylindrical separator


Body interior


Ejector body


3 nozzles : 0.75, 1 and 1.25 mm.

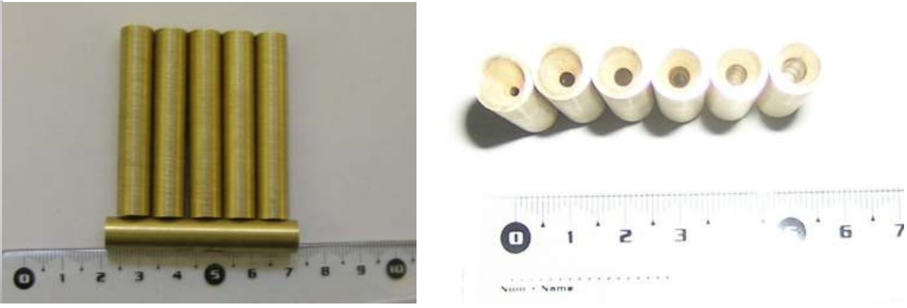
6 body interiors: 1.5, 2.0, 2.5, 3.0, 3.5, 4.0 mm


Assembly scheme of the ejector parts


The assembled ejector

ANNEX 4. Test bench

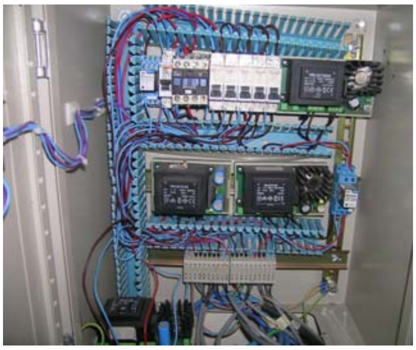

Electrical box

Acquisition system « Field Point »

Electrical motor control box

Liquid vapor separator

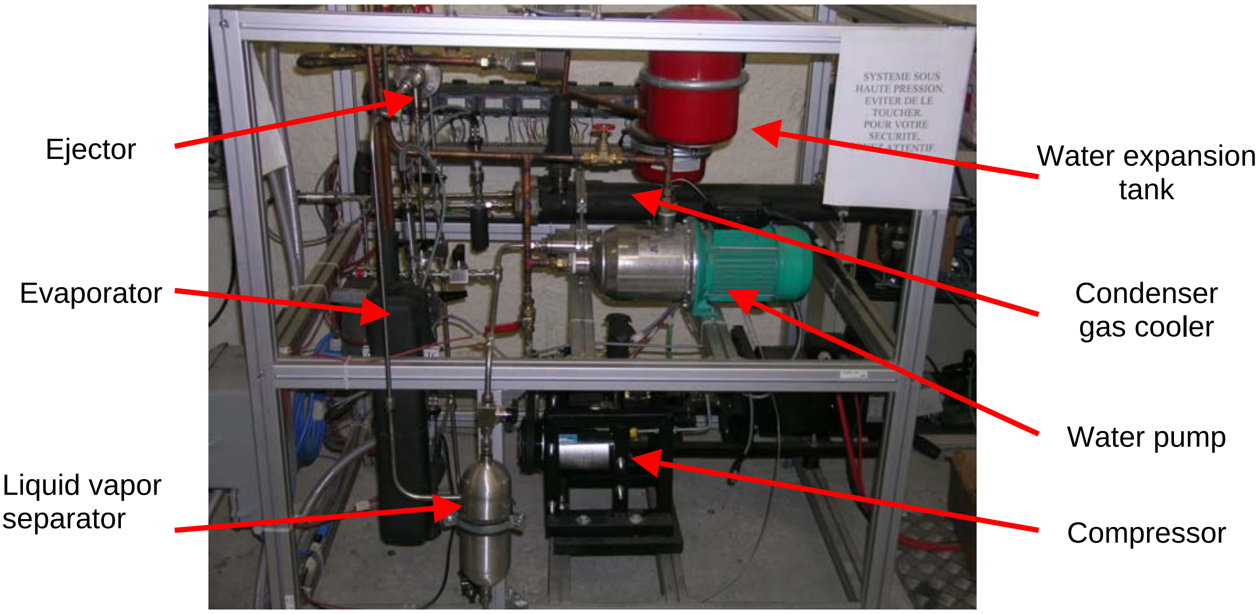

General view of the assembled test bench

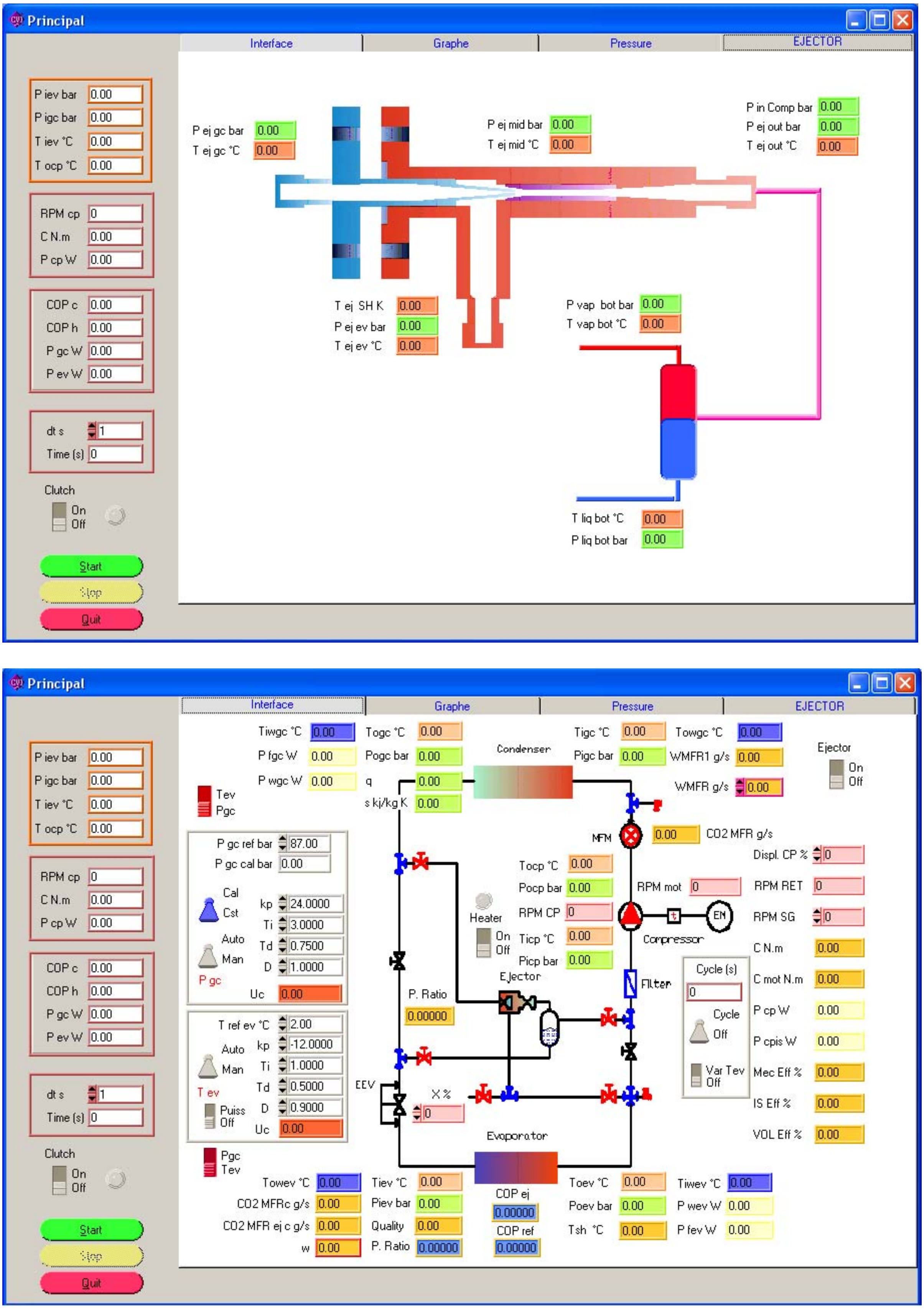

P iev bar 0.00
P igc bar 0.00
T iev °C 0.00
T ocp °C 0.00
RPM cp 0
C N.m 0.00
P cp W 0.00
COP c 0.00
COP h 0.00
P gc W 0.00
P ev W 0.00
dt s 1
Time (s) 0

P ej gc bar 0.00
T ej gc °C 0.00
P ej mid bar 0.00
T ej mid °C 0.00
P in Comp bar 0.00
P ej out bar 0.00
T ej out °C 0.00
T ej SH K 0.00
P ej ev bar 0.00
T ej ev °C 0.00
P vap bot bar 0.00
T vap bot °C 0.00
T liq bot °C 0.00
P liq bot bar 0.00

Tiwgc °C 0.00
P fgc W 0.00
P wgc W 0.00
Togc °C 0.00
Pogc bar 0.00
q 0.00
s kj/kg K 0.00
Tigc °C 0.00
Pigc bar 0.00
Towgc °C 0.00
WMFR1 g/s 0.00
WMFR g/s 0.00
Ejector On Off
CO2 MFR g/s 0.00
Displ. CP % 0
RPM RET 0
RPM SG 0
C N.m 0.00
C mot N.m 0.00
P cp W 0.00
P cpis W 0.00
Mec Eff % 0.00
IS Eff % 0.00
VOL Eff % 0.00
P gc ref bar 87.00
P gc cal bar 0.00
kp 24.0000
Ti 3.0000
Td 0.7500
D 1.0000
Uc 0.00
T ref ev °C 2.00
kp -12.0000
Ti 1.0000
Td 0.5000
D 0.9000
Uc 0.00
Tocp °C 0.00
Pocp bar 0.00
RPM CP 0
Ticp °C 0.00
Picp bar 0.00
RPM mot 0
Cycle (s) 0
P. Ratio 0.00000
X % 0
Towev °C 0.00
CO2 MFRc g/s 0.00
CO2 MFR ej c g/s 0.00
w 0.00
Tiev °C 0.00
Piev bar 0.00
Quality 0.00
P. Ratio 0.00000
COP ej 0.00000
COP ref 0.00000
Toev °C 0.00
Poev bar 0.00
Tsh °C 0.00
Tiwev °C 0.00
P wev W 0.00
P fev W 0.00

CVI acquisition interface to control the test bench.

ETUDE ET CONCEPTION DE SYSTEMES A EFFICACITE ENERGETIQUE AMELIOREE FONCTIONNANT AU CO_2 COMME FLUIDE FRIGORIGENE

Résumé

L'accroissement des émissions de gaz à effet de serre a amené l'Union Européenne à établir des politiques de réduction des émissions de ces gaz. Pour ce qui concerne la climatisation automobile, l'Union Européenne a décidé d'arrêter l'utilisation des fluides frigorigènes dont le GWP supérieur à 150 pour les nouvelles plate-formes à partir de 2011, et progressivement pour l'ensemble des véhicules neufs à partir de 2017.

Le CO_2 est un fluide candidat pour remplacer les fluides à GWP élevé. Les propriétés thermodynamiques du CO_2 impliquent un cycle frigorifique trans-critique à basses performances énergétiques pour une température de puits supérieure à 31°C. La haute pression peut être optimisée afin de maximiser le COP du système. L'analyse exergétique du cycle montre que les principales pertes de performances proviennent de la détente isenthalpique et de la compression. Le cycle de réfrigération à éjecteur diphasique (équivalent au cycle de réfrigération à deux étages de compression à injection totale avec détente isentropique) se présente comme une solution qui réduit ces pertes.

Un modèle 1D a été élaboré pour caractériser le fonctionnement de l'éjecteur et dimensionner des éjecteurs afin de les tester sur un banc d'essais. Des essais comparatifs ont été menés sur des cycles de réfrigération à CO_2 avec et sans éjecteur.

Les principaux résultats des essais sont :

- quatre stratégies de contrôle expérimentalement vérifiées pour réguler la haute pression et la température d'évaporation via le détendeur électronique et la vanne de contrôle externe du compresseur,
- la validation du modèle de la tuyère convergente
- la validation du modèle 1D en testant 18 éjecteurs différents.

Le modèle 1D développé a montré que l'éjecteur améliore jusqu'à 12% les performances énergétiques du cycle au CO_2. Les buses développées peuvent être couplées à une roue pour constituer une turbine à impulsion, organe de détente isentropique. Il serait intéressant d'utiliser l'éjecteur dans une boucle de climatisation à air pour évaluer ses performances. Dans le cadre de pompes à chaleur utilisées pour produire de l'eau chaude sanitaire à 60°C, l'éjecteur diphasique permet une amélioration des performances de l'ordre de 10 % comparativement au cycle classique au CO_2.

Mots clés : CO_2, cycles de réfrigération, exergie, stratégie de contrôle, régulation, éjecteur, échangeur, évaporateur, refroidisseur de gaz, condenseur.

STUDY AND DESIGN OF SYSTEMS WITH IMPROVED ENERGY EFFICIENCY OPERATING WITH CO_2 AS REFRIGERANT

Abstract

The increase in emissions of greenhouse gases led the European Union to establish policies aiming at the reduction of such emissions. For mobile air conditioning systems, the EU decided to ban the use of refrigerants with GWP > 150 for the new platforms starting in 2011, and progressively for all new vehicles as of 2017.

CO_2 is a candidate refrigerant to the replacement of high GWP refrigerants. The thermodynamic properties of CO_2 imply supercritical refrigerating cycle with low energy performance when the sink temperature is above 31°C. The high pressure of the system could be optimized in order to maximize the system COP. The exergy analysis of the cycle shows that the main irreversibilities are in the compression and isenthalpic expansion. The refrigeration cycle using two-phase ejector (equivalent to two-stage compression refrigeration cycle with total injection and isentropic expansion) is a solution to reduce irreversibilities.

A 1D model has been elaborated to characterize the operation of the ejector and to design ejectors to be tested on a test bench. Comparative tests have been performed on CO_2 refrigeration cycles with and without ejectors. The main test results are:

- 4 control strategies verified experimentally to regulate the high pressure and the evaporating temperature using the electronic expansion device and the compressor external control valve.
- Validation of the nozzle model.
- Validation of the 1D model by testing 18 different ejectors.

The 1D model revealed that a gain in energy efficiency of about 12% is possible using the ejector in the CO_2 cycle. The developed nozzles can be coupled to an impulse turbine wheel to become an isentropic expansion turbine. It could be interesting to use the ejector in an air refrigeration loop to evaluate its performances. The use of two-phase ejector in CO_2 heat pumps used to produce domestic hot water at 60°C leads to energy efficiency improvement of about 10% compared to CO_2 classical systems.

Key words: CO_2, refrigeration cycles, exergy, control strategies, regulation, ejector, heat exchanger, evaporator, gas cooler, condenser.

Laboratoire d'accueil : Centre Energétique et Procédés - Ecole des Mines de Paris
Paris : 60 Bd Saint-Michel - F-75272 Paris Cedex 06
Thèse présentée par : BOU LAWZ KSAYER Elias, **le 12 novembre 2007**
Discipline : « Energétique » - Ecole des Mines de Paris